



Delft University of Technology

Physics of broadband noise reduction by serrated trailing edges

Lima Pereira, L.T.

DOI

[10.4233/uuid:a7b16311-35f5-4819-9d95-5ff1f8cae84f](https://doi.org/10.4233/uuid:a7b16311-35f5-4819-9d95-5ff1f8cae84f)

Publication date

2023

Document Version

Final published version

Citation (APA)

Lima Pereira, L. T. (2023). *Physics of broadband noise reduction by serrated trailing edges*. [Dissertation (TU Delft), Delft University of Technology]. <https://doi.org/10.4233/uuid:a7b16311-35f5-4819-9d95-5ff1f8cae84f>

Important note

To cite this publication, please use the final published version (if applicable). Please check the document version above.

Copyright

Other than for strictly personal use, it is not permitted to download, forward or distribute the text or part of it, without the consent of the author(s) and/or copyright holder(s), unless the work is under an open content license such as Creative Commons.

Takedown policy

Please contact us and provide details if you believe this document breaches copyrights. We will remove access to the work immediately and investigate your claim.

**PHYSICS OF BROADBAND NOISE REDUCTION BY
SERRATED TRAILING EDGES**

PHYSICS OF BROADBAND NOISE REDUCTION BY SERRATED TRAILING EDGES

Proefschrift

ter verkrijging van de graad van doctor
aan de Technische Universiteit Delft,
op gezag van de Rector Magnificus prof. dr. ir. T.H.J.J. van der Hagen,
voorzitter van het College voor Promoties,
in het openbaar te verdedigen
op Woensdag 20 september 2023 om 15:00 uur

door

Lourenço Tércio LIMA PEREIRA

Master of Science in Mechanical Engineering,
Unversidade de São Paulo, Brazilië,
geboren te Poços de Caldas, Brazilië.

Dit proefschrift is goedgekeurd door de

promotoren: Prof.dr. F. Scarano, Dr. D. Ragni

copromotor: Prof.dr. F. Avallone

Samenstelling promotiecommissie:

Rector Magnificus,	voorzitter
Prof.dr. F. Scarano,	Technische Universiteit Delft, promotor
Dr. D. Ragni,	Technische Universiteit Delft, promotor
Prof.dr. F. Avallone,	Politecnico di Torino, IT, copromotor

Onafhankelijke leden:

Prof.dr. M. Azarpeyvand,	University of Bristol, UK
Prof.dr.ir. C. Schram,	Von Karman Institute, BE
Prof.dr.ir. M. Snellen,	Technische Universiteit Delft
Prof.dr. S. J. Watson,	Technische Universiteit Delft, reservelid
Dr.ir. S. Oerlemans,	Siemens Gamesa Renewable Energy, DK



This study is supported by the SMARTANSWER project (smart mitigation of flow-induced acoustic radiation and transmission for reduced aircraft, surface transport, workplaces and wind energy noise), part of the European Union's Horizon 2020 research and innovation programme under Marie Skłodowska-Curie grant agreement no. 722401.

Keywords: trailing-edge noise, trailing-edge serrations, aeroacoustics, experimental aeroacoustics

Printed by: Ridderprint

Cover: Illustration of serrations of different shapes and polar noise emission from different serration geometries.

Copyright © 2023 by L.T. Lima Pereira

An electronic version of this dissertation and data supporting it are available at dissertation: <http://repository.tudelft.nl/>

dataset: <https://doi.org/10.4121/uuid:46879b06-bbf5-49ed-9c83-5d286c3371df>.

*Viver e não ter a vergonha de ser feliz,
Cantar, a beleza de ser um eterno aprendiz...*

To live and not be ashamed of being happy,
To sing, the beauty of being an eternal apprentice...

O que é, o que é?, Gonzaguinha

CONTENTS

Summary	xi
Samenvatting	xv
1 Introduction	1
1.1 Trailing-edge noise mitigation	6
1.2 Thesis objectives and outline	9
2 Theory of trailing-edge noise and serrations	11
2.1 Principles of trailing-edge scattering.	12
2.2 Aerodynamics of the wall-pressure fluctuations at the trailing edge.	19
2.3 Wall-pressure fluctuations in the turbulent boundary layer	22
2.3.1 The wall-pressure spectrum (ϕ_{pp})	26
2.3.2 The convection velocity (U_c).	30
2.3.3 The correlation length (l_x)	31
2.4 Turbulent boundary layer trailing-edge noise.	32
2.5 Trailing-edge serrations for broadband noise reduction	33
2.5.1 Modelling of serrated trailing-edge noise	35
2.5.2 Impact of the serration geometry	40
2.6 The challenges of studying the noise from serrated trailing edges. .	42
3 Measurement techniques for aeroacoustics	47
3.1 Acoustic measurement techniques	48
3.1.1 Far-field microphone measurements	48
3.1.2 Microphone-array techniques	53
3.2 Acoustic measurements of airfoil self noise	60
3.2.1 Trailing-edge noise	60
3.2.2 Aeroacoustic wind-tunnel facilities	62
3.2.3 Wind-tunnels and background noise	63
3.2.4 Anechoic chambers.	66
3.3 Flow measurement techniques	67
3.3.1 Unsteady surface pressure sensors	67
3.3.2 Particle Image Velocimetry.	71
3.4 Conclusions	82

4	Description of Experiments	83
4.1	Isolated trailing-edge study	84
4.1.1	Model geometry	84
4.1.2	Flow facilities	85
4.1.3	Configurations and flow conditions	86
4.1.4	Instrumentation and measurement techniques	87
4.2	High-Reynolds airfoil study	92
4.2.1	Model geometry	93
4.2.2	Flow facility	93
4.2.3	Configurations and flow conditions	95
4.2.4	Instrumentation and measurement techniques	95
4.3	Sensitivity-based study of an airfoil with different serrations inserts	100
4.3.1	Model geometry	100
4.3.2	Flow facility	101
4.3.3	Configurations and flow conditions	101
4.3.4	Instrumentation and measurement techniques	105
5	Aerodynamic and acoustic properties of serrated trailing edges	109
5.1	Experimental setup and methodology	110
5.2	Flow and acoustic properties from isolated trailing-edge serrations .	111
5.2.1	Wall-pressure fluctuations over serrations	114
5.2.2	Vortex pairs and wall-pressure fluctuations	120
5.2.3	Far-field noise prediction	126
5.3	Wall-pressure fluctuations over a serrated trailing edge of an airfoil model	128
5.3.1	Mean flow conditions	128
5.3.2	Wall-pressure fluctuations at the serration root	130
5.3.3	Distribution of the wall-pressure fluctuations over the ser- ration without aerodynamic loading	134
5.3.4	Effect of the angle of attack on the wall pressure over the serration surface	136
5.4	Conclusions	139
6	Physics-based description of the flow over a serrated trailing edge	143
6.1	Objectives	144
6.2	Description and modelling of the wall-pressure over a serrated trailing edge	145
6.2.1	Impedance change at the trailing-edge boundary	145
6.2.2	Wake development and acceleration of turbulent structures	149
6.2.3	Aerodynamic loading effect	151

6.3	Experimental dataset	154
6.4	Results and discussions	157
6.4.1	Wall-pressure spectrum without loading	157
6.4.2	Wall-pressure spectrum with loading	160
6.5	Conclusions	167
7	Serration geometry and its implication on the emitted noise	169
7.1	Objectives	170
7.2	Results and discussions	171
7.2.1	General characteristics of trailing-edge serration noise	171
7.2.2	Sawtooth serration scaling	173
7.2.3	Serration geometry	179
7.2.4	Combed sawtooth design	181
7.3	Summary of parameter dependence	184
7.4	Conclusions	187
8	Conclusions and recommendations	189
8.1	Conclusions	190
8.2	Recommendations for future work	192
A	Validation of measurement techniques and acoustic noise estimations from isolated serrations study	195
B	Relation between wall-pressure fluctuations at the wall-bounded region and along the wall plane on the near wake	203
C	Wall-pressure fluctuations induced by turbulent flow over a span-streamwise oscillating flow field	205
D	Verification of analytical models with other datasets	209
	Bibliography	213
	Acknowledgments	227
	Curriculum Vitæ	231
	List of Publications	233

SUMMARY

Wind-turbine noise can restrict the growing implementation of renewable energy sources and their application close to urban environments. The largest contributor to the noise of modern turbines is the scattering of the turbulent fluctuations at the blade trailing edge. This source of noise is directly correlated with the turbine's extracted power. Therefore, operating in noise-restricted environments and at night times entails lower energy production. An extensively applied solution for reducing the noise of wind turbines is the use of trailing-edge serrations, i.e. imposing periodic variations in the geometry of the blade trailing edge. Serrations reduce the effectiveness of the scattering at the trailing edge as the turbulent fluctuations reach the trailing edge at different times along the blade span, consequently reducing the wind-turbine noise. Although extensive literature and knowledge exist on serrations, their measured performance does not compare with the predicted one. Even more problematic, the trends predicted for the geometric alterations of the serrations are not observed in reality. Notably, two things are worth mentioning: first, geometries shown as optimal by theory perform worse than other concepts, and second, the noise from serrations is affected by the angle between the insert and the flow. As a result, the design of trailing-edge serrations still requires dedicated experiments and numerical simulations, hampering the assessment of several geometries necessary for complete optimization of the serration design.

This work seeks a physical interpretation of the noise generation mechanisms of trailing edges with serrated add-ons. This interpretation is focused on understanding the underlying physical principles of the flow surrounding a serrated trailing edge. This is carried out in this work with three studies, respectively on the observation, modelling, and control of the flow and acoustic properties of serrated trailing edges.

The first study of this work is dedicated to the observations of the flow and acoustic properties of serrations. This is carried out experimentally with serrations mounted on both a zero-pressure gradient model and a benchmark airfoil section. The study discusses the properties of serrations at zero angle with respect to the flow and at an angle to the flow. In both cases, discrepancies exist between the measured and predicted noise levels. At zero angle, the acoustic noise reduction ceases at high frequencies, contrary to the asymptotic noise reduction predicted in theory. As the angle between the serration and the flow increases, the serration loses its ability to reduce noise and can even increase the trailing-edge noise. Observations

on the velocity field along the serration do not reveal significant modifications for the earlier condition, i.e. small serration angles, whereas, for the latter, the pressure differential between the two serration sides creates a pair of vortices that is formed from the pressure side and sits on the suction side of the serration surface. Observations of the wall pressure over the surface reveal three important effects. Without an angle with the flow, the wall-pressure fluctuations decrease from the root to the tip of the serration at low frequencies but increase at high frequencies. With an angle, the wall-pressure fluctuations are increased along the outer rim of the serrations. The latter effect correlates to the increase in the shear caused by the vortex pairs. A final assessment demonstrates that noise predictions using analytical models yield better comparisons when the variation of the wall-pressure fluctuations along the serration surface are taken into account. The latter indicates that considering the impact of the flow field along the serrations is necessary for a reliable description of the noise emitted by serrated trailing edges.

The second study focuses on a physics description and modelling of the wall-pressure fluctuations on a serrated trailing edge. Following the first study, three physics mechanisms are proposed. The first mechanism describes the reduction of the measured wall-pressure fluctuations at the tip of the serration for low serration angles with the flow. The impedance transition in the trailing edge creates a gradual change in the condition on the wall plane, resulting in a reduction of the wall-pressure fluctuations along the tip. This process is dependent on the scales of the turbulent structures and is more prominent at lower frequencies. At higher frequencies, a different physical mechanism is responsible for the increase of the wall-pressure fluctuations at the tip. This mechanism is related to the sidewise momentum transfer along the serration. The wake development along the gaps of the serrations causes an increase in the speed of the inner scales of turbulence, also observed on the surface of the serration. This increase in the mean velocity changes the scale, and consequently levels, of the eddies responsible for the wall-pressure fluctuations at a given frequency, consequently increasing the wall pressure along the serration tip. The final mechanism is associated with serrations at an angle with respect to the flow. The secondary shear imposed by the vortex pairs interacting with the incoming turbulent fluctuations from the boundary layer constitutes another source of wall-pressure fluctuations along the tip of the serrations. Analytical models are formulated to describe each of the physical mechanisms and results show the agreement between the predictions and measurements of the wall pressure over a serration surface, verifying the underlying physical mechanisms proposed in this work.

The third, and final, study described in this work pursues the relation between induced flow modifications and acoustic emissions of serrated trailing edges with different geometries. This study focuses on data from systematic modifications of

the serration geometry to describe both the effect of changing the serration size (wavelength, and height) and periodic geometry. The results propose an oriented discussion on the impacts that changes in the serration design have on the noise reduction. The discussion is built upon the frequencies where noise reduction starts and ends, and the maximum noise reduction achieved from the serration inserts. Results are separated between effects that are observed when serrations are placed at an angle with respect to the flow direction and effects that are present at every condition. This is used to create a discussion on the influence of serration angle with the flow on the noise reduction achieved. This work is concluded with a practical guideline and summary for the preliminary design and sizing of serrations for different applications.

SAMENVATTING

Het geluid afkomstig van windturbines kan de toenemende implementatie van duurzame energie in de buurt van stedelijke omgevingen beperken. De grootste veroorzaker van het geluid van moderne turbines is het ontstaan en verstrooiing van de turbulente fluctuaties aan de achterrand van het blad. Deze geluidsbron is direct gecorreleerd met de energie die de turbine onttrekt uit de wind. Het plaatsen van turbines in geluidsarme regio's of het alleen 's nachts mogen draaien, brengt een lagere energieproductie met zich mee. Een veel toegepaste oplossing om het geluid van windturbines te verminderen is het vertanden van de achterrand van turbine bladen, d.w.z. het gebruik van periodieke variaties in de geometrie van de achterrand van het blad. De zaagtanden verminderen de effectiviteit van de verstrooiing aan de achterrand, aangezien de turbulente fluctuaties de achterrand op verschillende tijdstippen bereiken over de spanwijdte van het blad. Hierdoor wordt het geluid van de windturbine verminderd. Hoewel er uitgebreide literatuur en kennis bestaat over deze zaagtanden, komen de gemeten prestaties niet overeen met de voorspelde waardes. Nog problematischer is dat het voorspelde gedrag voor de geometrische veranderingen van de zaagtanden in werkelijkheid niet worden waargenomen. Met name twee dingen zijn het vermelden waard: ten eerste presteren geometrieën die volgens de theorie als optimaal worden beschouwd slechter dan andere concepten, en ten tweede wordt het geluid van zaagtanden beïnvloed door de hoek tussen het oppervlak van de zaagtanden en de lucht stroming. Als gevolg hiervan vereist het ontwerpen van vertande achterranden nog steeds speciaal toegewijde experimenten en numerieke simulaties, wat de beoordeling van verschillende geometrieën belemmert die nodig zijn voor een volledige optimalisatie van de geometrie.

Dit werk focust op een fysieke interpretatie van de mechanismen in de stroming die het geluid veroorzaken, afkomstig van achterranden met zaagtanden 'add-ons'. Dit wordt in dit werk uitgevoerd met drie studies, respectievelijk over de waarneming, modellering en beïnvloeding van de stroming en akoestische eigenschappen van vertanding.

De eerste studie van dit werk is gewijd aan de waarnemingen van de stroming en akoestische eigenschappen van vertande achterranden. Dit wordt experimenteel uitgevoerd met vertandingen die zijn gemonteerd op zowel een nuldrukgradiënt-model als een benchmark-vleugelprofiel. De studie bespreekt de eigenschappen van vertande achterranden onder een hoek van nul graden ten opzichte van de

stroming en onder een hoek ten opzichte van de stroming. In beide gevallen zijn er afwijkingen tussen de gemeten en voorspelde geluidsniveaus. Bij de nulhoek stopt de akoestische ruisonderdrukking bij hoge frequenties, in tegenstelling tot de asymptotische ruisonderdrukking die in theorie wordt voorspeld. Naarmate de hoek tussen de zaagtanden en de stroom toeneemt, verliest de vertanding zijn vermogen om ruis te verminderen en kan zelfs het achterrangeluid toenemen. Waarnemingen van het snelheidsveld langs de vertande achterranden laten geen significante wijzigingen zien voor de eerdere toestand, d.w.z. kleine zaagtand hoeken, terwijl voor grotere hoeken het drukverschil tussen de twee vertande zijkanten een wervelpaar creëert die worden gevormd vanaf de onderrug tot aan de bovenrug van het zaagtand oppervlak. Waarnemingen van de wanddruk over het oppervlak laten drie belangrijke effecten zien. Zonder hoek met de stroming nemen de wanddrukfluctuaties bij lage frequenties af van de wortel tot de punt van de vertanding, maar neemt het toe bij hoge frequenties. Met een hoek worden de wanddrukfluctuaties vergroot langs de buitenrand van de zaagtanden. Het laatste effect correleert met de toename van de afschuiving veroorzaakt door de wervelpaaren. Een laatste beoordeling toont aan dat geluidsvoorspellingen met behulp van analytische modellen betere vergelijkingen opleveren, wanneer rekening wordt gehouden met de variatie van de wanddrukfluctuaties langs het vertande oppervlak. Dit laatste geeft aan dat rekening houden met de impact van het stromingsveld langs de zaagtanden noodzakelijk is voor een betrouwbare beschrijving van het geluid dat wordt uitgezonden door vertande achterranden.

De tweede studie richt zich op een fysische beschrijving en modellering van de wanddrukfluctuaties op vertande achterranden. Na de eerste studie worden drie fysische mechanismen voorgesteld. Het eerste mechanisme beschrijft de vermindering van de gemeten wanddrukfluctuaties aan het uiteinde van de zaagtanden voor kleine zaagtand hoeken. De impedantieovergang in de achterrand zorgt voor een geleidelijke verandering in de conditie op het wandvlak, wat resulteert in een vermindering van de wanddrukfluctuaties langs de punt. Dit proces is afhankelijk van de schaal van de turbulente structuren en is prominenter aanwezig bij lagere frequenties. Bij hogere frequenties is een ander fysiek mechanisme verantwoordelijk voor de toename van de wanddrukfluctuaties aan de punt. Dit mechanisme houdt verband met de zijwaartse impulsoverdracht langs de zaagtanden. De kielzorgontwikkeling langs de openingen van de zaagtanden veroorzaakt een toename van de snelheid van de binnenste turbulentschalen, ook waargenomen op het oppervlak van de zaagtanden. Deze toename van de gemiddelde snelheid verandert de schaal, en als gevolg de niveaus van de draaikolken die verantwoordelijk zijn voor de fluctuaties van de wanddruk met een bepaalde frequentie, waardoor de wanddruk langs de zaagtand punt toeneemt. Het laatste mechanisme wordt geassocieerd met zaagtanden onder een hoek ten opzichte van de stroming. De secundaire

afschuiving die wordt veroorzaakt door de wervelparen die in wisselwerking staan met de binnenkomende turbulente fluctuaties van de grenslaag, vormt een andere bron van wanddrukfluctuaties langs de punt van de zaagtanden. Er zijn analytische modellen opgesteld om elk van de fysische mechanismen te beschrijven en de resultaten tonen de overeenkomst tussen de voorspellingen en metingen van de wanddruk over een vertand oppervlak. Hiermee kunnen de onderliggende fysische mechanismen die in dit werk worden voorgesteld, worden geverifieerd.

De derde en laatste studie die in dit werk wordt beschreven, streeft naar de relatie tussen geïnduceerde stroomveranderingen en akoestische emissies van vertande achterranden met verschillende geometrieën. Deze studie richt zich op gegevens van systematische modificaties van de zaagtand geometrie om zowel het effect van het veranderen van de zaagtand grootte (golflengte en hoogte) als de periodieke geometrie te beschrijven. De resultaten presenteren een georiënteerde discussie over de effecten die veranderingen in het zaagtanden ontwerp hebben op de geluidsreductie. De discussie is gebaseerd op de frequenties waar ruisonderdrukking begint en eindigt, maar ook op de maximale ruisonderdrukking die wordt bereikt met de vertande inzetstukken. Resultaten worden gescheiden tussen effecten die worden waargenomen wanneer zaagtanden onder een hoek ten opzichte van de stroomrichting worden geplaatst en effecten die onder alle omstandigheden aanwezig zijn. Dit wordt gebruikt om een discussie op gang te brengen over de invloed van de zaagtand hoek met de stroming op de bereikte geluidsreductie. Dit werk wordt afgesloten met een praktische richtlijn en samenvatting voor het voorlopig ontwerp en de dimensionering van zaagtanden voor verschillende toepassingen.

1

INTRODUCTION

The growing energy consumption of modern society has created a push toward harvesting renewable sources of electricity, such as hydro-power, solar, and wind energy. The share of these sources to the total electricity production has passed 30% in 2022 [1]. In particular, wind sources of energy are especially prominent, growing by 17% between 2019 and 2020 to produce about 1,600 TWh (about 6% of the world's electricity consumption) in the latter year [1].

However, the installation and operation of wind turbines do not come without an impact on the society and on the environment. For example, the variation of the shadow produced by the blades causes a phenomenon known as shadow flickering and turbines must be installed far from houses to avoid these effects. Another source of disturbance from a wind turbine is noise [2]. For the latter, noise regulations exist to protect the communities. Thus, manufacturers and operators have to make sure their products abide by the environmental laws while trying to extract the maximum productivity out of their products.

This is a good example of how regulations can impact the design and operation of wind turbines. Although different from each country, noise restrictions are usually based on the level of emitted noise to the nearby communities. Table 1.1 summarizes some of these restrictions for different countries. Commonly, these restrictions vary according to the community type, i.e. residential or rural, and time of the day, i.e. during day or night periods. Based on this information, the power rating of the turbine and the minimum distance between the turbines and the population can be assessed.

The existing relation between noise and energy production is illustrated in Figure 1.1, which shows how the emitted sound pressure level (SPL in dBA) varies with the turbine-rated Annual Energy Production (AEP), and the distance to the community. The figure is based on a linear relation between the AEP of a wind turbine used in a given wind farm and the SPL produced by it. Restrictions from each country, according to Table 1.1, are also shown. The higher the AEP of the wind turbines and the closer they are to the community, the higher the noise emissions will be. The figure illustrates the impact of noise restrictions on the maximum energy production of a wind farm. Based only on acoustic restrictions, a reduction of 3 dB in the noise levels of the regulations would lead to a halving of the possible installed power, i.e., a 26% decrease in AEP for a change in restriction of 1 dB in sound pressure. For example, turbines installed 1000 m away from a rural population in Brazil could produce up to 6 GWh AEP. However, nighttime restrictions of 35 dBA can reduce this to around 2.0 GWh AEP, according to the figure. Besides, if these turbines are moved to 2000 m from the population, turbines with a rated AEP that is 4 times higher (8.0 GWh at night) could be installed. Electricity production is therefore hampered since either installed turbines must abide by the most restrictive night levels, or they must operate at lower acoustic

levels (low RPM) during the night, or they should be installed in remote locations. It is very important to point out that these values are based on the unrealistic scenario where only acoustic emissions are a concern, disregarding costs, space, and wake interaction. According to Oerlemans and Fuglsang [3], a typical constraint of noise would be around 3% AEP per dB, and a 5 dB night restriction would lead to a 15% reduction in the maximum energy production of the turbine.

Country		Residential [dBA]	Rural [dBA]
Netherlands	Day	45	40
	Night	35	30
Brazil	Day	50	40
	Night	45	35
Germany	Day	55	50
	Night	40	35
Denmark		40	45

Table 1.1: Noise regulation limits for equivalent sound pressure levels ($L_{A,eq}$) according to country, region, and time of the day. Data from [2] and [4].

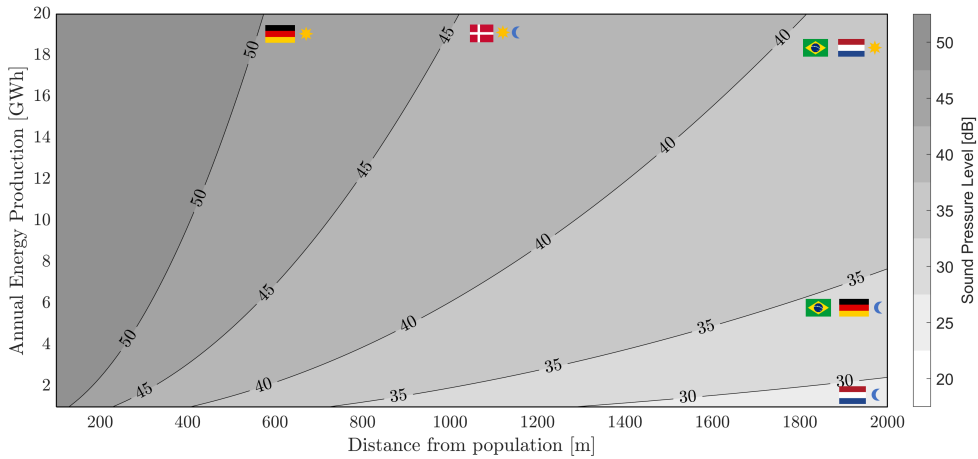


Figure 1.1: Noise levels (SPL) emitted by a wind turbine as a function of power output (AEP) and distance between the community and the wind turbine. Image based on [2–4].

These reasons have driven manufacturers to try assessing and mitigating noise from wind turbines. This starts with identifying the possible sources of noise. Several mechanisms are known to produce noise on a turbine. Figure 1.2 illustrate the fundamental sources identified, as described in the work of Oerlemans [5], and Wagner [2]. These are:

- Mechanical noise (A);
- Inflow turbulence:
 - Atmospheric turbulence (B);
 - Blade interaction noise (C);
 - Tower-blade interaction noise (D);
- Self noise:
 - Trailing-edge noise (E);
 - Blade-tip noise (F).

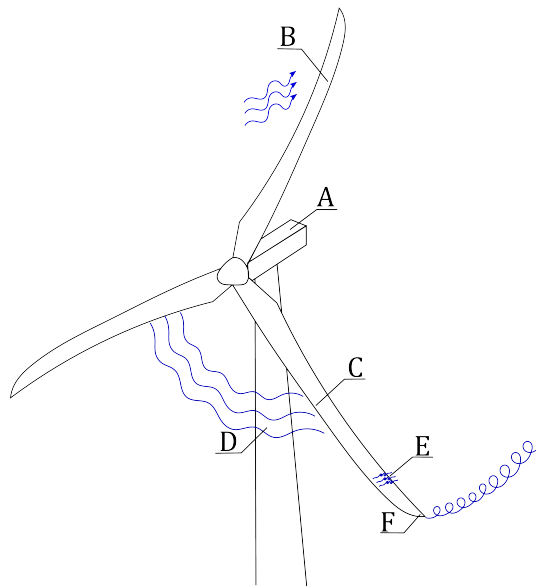


Figure 1.2: Illustration of the sources of wind turbine noise.

While the first mechanism is related to the wind-turbine machinery, the other sources of noise are of aerodynamic origin, i.e. aeroacoustic sources. Aeroacoustic sources are related to the character of the flow around the wind turbine and are either generated by the interaction between inflow turbulence and the wind turbine, or by the self-noise from the blades. The following paragraphs describe briefly the characteristics of each of these sources.

Mechanical noise: the mechanical noise is generally related to the many mechanical components inside the wind-turbine nacelle, such as the generator, the gearbox, cooling fans, and hydraulic actuators. This source is more intense

downstream of the nacelle, where the cooling exhausts are located and it can be treated by well-known engineering methods [2].

Atmospheric turbulence and blade interaction noise: interaction between the incoming turbulence and solid boundaries is a source of low-frequency noise from wind turbines. The inflow turbulence arising from the atmospheric boundary layer scatters when impinging on the rotating turbine blades. According to Buck et al. [6], this source of noise dominates the emissions from wind turbines at frequencies below 400 Hz and differs from others as it is sensitive to the characteristics of the atmospheric turbulence at the location where the wind turbine is operating.

Tower-blade interaction noise: the presence of the tower causes a non-uniform loading during the blade rotation. At the same time, the blade passing causes an unsteady flow to impinge on the tower. Due to the small RPMs that turbines operate, tower-blade interaction is a source of very low-frequency unsteadiness, in the order of a couple of Hz and far from the audible range [2]. However, this is a source of high-intensity pressure fluctuations and, under certain situations, the higher-order harmonics of the Blade-Passing Frequency (BPF) can be perceived as acoustic noise.

Trailing-edge noise: trailing-edge noise is generated when the turbulent flow over the blades reaches the sharp trailing edge, leading to the scattering of acoustic waves. This noise is of broadband type and is the most important contributor to the noise for wind turbines. It is even a more relevant source when considering that modern wind-turbine designs have evolved to high-diameter rotors and higher tip speeds. This is because this source scales with the wind speed with a power of 5 (U^5). Therefore, the faster the flow and rotational speed of the blade tip, the higher the emitted levels.

Blade-tip noise: blade tip noise is generated due to the interaction between unsteady flow from the blade-tip vortices, consequent flow separations, and the blade surface and trailing edge. This source is reduced for wind turbines since the aerodynamic shape of blade tips reduces the flow unsteadiness and interaction with the blade surface [7].

Table 1.2 shows a breakdown of the noise emitted by each of the sources of wind turbine noise for a 2MW turbine. According to the table, the sources of aeroacoustic noise are 0.8 dB above the mechanical ones for this turbine. These sources become more and more important as the blade diameter increases and the isolation of the mechanical noise is improved [2]. The noise of modern wind turbines is dominated by the trailing-edge sources along the blade tip [5].

Source	Level (dBA)
Hub (Mechanic)	98.4
Blades (Aeroacoustic)	99.2
Tower (Aeroacoustic)	71.2

Table 1.2: Breakdown of noise contribution per component of the wind turbine. Data taken from Wagner [2] for a 2MW wind turbine.

1.1 TRAILING-EDGE NOISE MITIGATION

Trailing-edge noise is generated by the scattering of unsteady aerodynamic fluctuations at the trailing edge of the blades. For applications in wind energy, these fluctuations come mostly from the turbulent flow beneath the boundary layer formed over the blade.

This source of noise can be reduced by the use of trailing-edge serrations. The devices consist of add-ons of periodic shapes placed at the trailing edge of the blades (Figure 1.3). According to Oerlemans et al. [8] an overall noise reduction of up to 3 dB can be achieved by the add-ons. Coming back to the discussion of Figure 1.1, if noise is reduced by 3 dB while keeping the same rated power, a more powerful wind turbine can be installed within the same restrictions. Following Oerlemans and Fuglsang [3], this noise reduction would allow the installation of a turbine that has an AEP 9% higher. This impact illustrates the importance of noise reduction on the production of energy in noise-restricted regions and on the whole wind-energy business.



Figure 1.3: Wind turbine blades retrofitted with trailing-edge serrations. Adapted from [9].

The working principle of serrations is based on creating a non-orthogonal

angle between the incoming flow and the trailing edge. According to Howe[10], the noise is more intense for straight trailing edges because turbulent fluctuations are, predominantly, aligned with the trailing-edge direction. With the use of serrations, the scattering is weakened since this alignment is avoided. This process is illustrated in Figure 1.4 where typical induced fluctuations from the turbulent flow are shown across a straight and serrated trailing edge. For the straight trailing edge, the scattering is happening only with negative fluctuations (illustrated in blue) while, for the serrated trailing edge, positive and negative scattering happens along the serration edge. The result is a reduction of the total scattering intensity and a reduction of the trailing-edge noise from the serrated trailing edges.

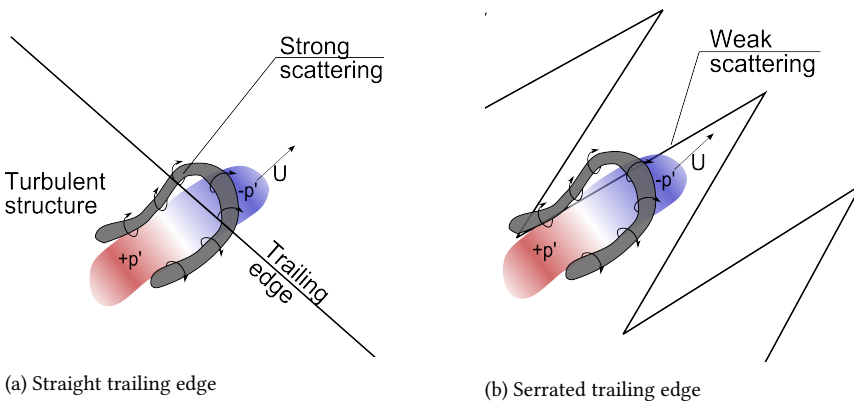


Figure 1.4: Illustration of the scattering of a turbulent structure at the trailing edge.

Although the principles of noise reduction from serrations are well understood, serrations have always performed, in practice, much poorer than predicted [11]. More problematic, the trends expected for modifications of the serration design do not always hold, hampering the use of these predictions to guide the design of serrated add-ons. For that, engineers must rely on unsteady Computational Fluid Dynamics (CFD) and Computational AeroAcoustics (CAA) simulations, and dedicated experimental techniques, with high associated costs and time, and with limited possibilities of testing.

More recent research has attributed these inconsistencies to the simplistic considerations of the flow surrounding the serrations. The predictions mentioned before assume that the properties of the incoming turbulent flow are the same for the straight and serrated trailing edge configurations. In reality, studies have demonstrated that the presence of the serrations alters the flow in the vicinity of the trailing edge [12–19].

These alterations can be divided into two categories, those that are observed under any flow condition and those that are only present when serrations are placed

at an angle with respect to the flow direction. Figure 1.5 illustrates the alterations mentioned and the possible modifications from the flow. The first set of alterations concerns the characteristics of the flow introduced by serrated trailing edges at any conditions. This mostly refers to the developing flow in the gaps between the serrations, as illustrated in Figure 1.5(a).

The latter alterations refer to when serrations create aerodynamic lift or loading, and each side of their surface represents a high- and low-pressure region. It encompasses conditions where serrations are placed at an angle relative to the blade airfoil, conditions of high angle of attack, or high airfoil camber. Due to the serration geometry, and the open gap between them, a pair of contra-rotating vortices will form and induce an outward movement of the flow on the pressure side and an inward one on the suction side, as illustrated in Figure 1.5(b). The formation of these vortices are correlated to the observed degradation of serration performance at high-loading conditions, i.e. the noise reduction obtained is deteriorated as the aerodynamic loading of the serration is increased [19].

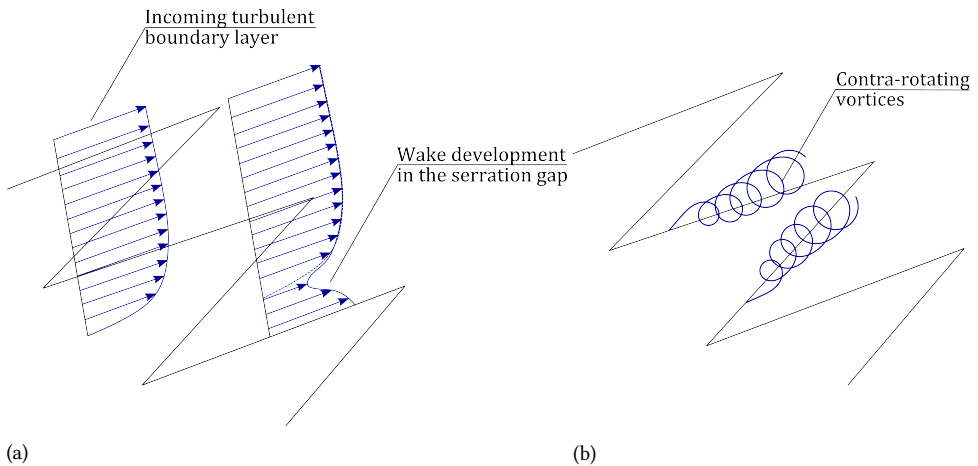


Figure 1.5: Illustration of the flow over a serrated trailing edge. The flow features observed for serrations under every condition is illustrated in (a) while the features observed only when serrations are placed at angle is illustrated in (b).

Although many works have already observed and mentioned these effects, there are still many questions that remain to be answered to improve the understanding and prediction of the impact of serrated trailing edges on reducing broadband noise from wind turbines. At first, the physics of the flow alterations across the serrations are not fully understood. The mechanisms behind these alterations need to be assessed to create a based discussion on how the flow modifications impact the scattered noise from serrated trailing edges. Finally, a full understanding of the driving physics of noise reduction from serrated trailing edges has practical

implications for the design of optimal serrations that could minimize the noise from wind-turbine blades.

1.2 THESIS OBJECTIVES AND OUTLINE

This work represents a step towards understanding in depth the physics of broadband noise reduction achieved with trailing-edge serrations. To accomplish that, experimental methodologies are explored to measure, explain, and model the aerodynamic and acoustic characteristics of trailing-edge noise emissions from serrated trailing edges. The work presented in this thesis has the four following objectives:

- Experimentation: make use and develop state-of-the-art techniques to study the aerodynamic and aeroacoustic behaviour of serrated trailing edges under representative conditions for wind-turbine applications;
- Analysis: determine the behaviour of the flow and noise in a wide variety of relevant conditions and extract the different physical mechanisms that play a role in the determination of serrated trailing-edge noise;
- Modelling: create physically-based models that describe these mechanisms and predict how the serrations impact the flow and acoustic emissions on the serrations;
- Design: synthesis of the influence of the different physical mechanisms on the design of serrations for obtaining maximum noise reduction.

A detailed description of the current theory of trailing-edge serrations and relevant measurement techniques for assessing acoustic and aerodynamic properties of serrations are given in Chapter 2, and 3 respectively. Chapter 4 describes the methodologies adopted in this thesis, validation results, and the setup of all the experiments used in this work. Chapter 5 is dedicated to assessing the acoustics and aerodynamics of serrated trailing edges under different flow conditions and relating it to the alterations of the flow surrounding the serrations. Chapter 6 proposes the physical mechanisms throughout which the relevant features of the turbulent flow are altered by the presence of the serrations. Chapter 7 discusses the impact of trailing-edge serration design on the broadband noise reduction achieved through a parametric study, and the optimal design of trailing-edge serrations. A full discussion is made based on the physical mechanisms observed in the previous work and on existing literature. A summary of the main conclusions of this work and recommendations for future studies is shown in Chapter 8.

2

2

THEORY OF TRAILING-EDGE NOISE AND SERRATIONS

A major contribution to the noise from wind turbines comes from the acoustic scattering at the trailing edge of the wind-turbine blades. In this chapter, the physical principles of trailing-edge scattering are described. Following, a discussion is made on the aerodynamic sources of unsteady flow that promote this scattering at the trailing edge. Attention is given to the sources of unsteadiness coming from the turbulent boundary layer as it constitutes the most relevant contributor to the wind-turbine noise. The wall-pressure fluctuations and, specifically, the wavenumber-frequency and the frequency spectra of it are explored in detail since these are the input variables for the models that describe trailing-edge noise.

A description of the physical principles of noise reduction from serrated trailing edges is given. This also includes the analytical modelling of the problem based on the formulations of Howe [10, 20], and Ayton [21, 22]. The models' main outcomes are discussed, and confronted against numerical and experimental results. The chapter ends with the critical review of the discrepancies between the analytical predictions and the measurements obtained in experimental campaigns. A discussion on the underlying causes of the differences, the current understanding of the problem, and the open questions on the physics of broadband noise reduction by serrated trailing edge close the chapter.

2.1 PRINCIPLES OF TRAILING-EDGE SCATTERING

As briefly described in the previous chapter, acoustic scattering happens by the interaction of advecting velocity fluctuations with the sharp trailing edge of wind-turbine blades. The mechanism is referred to as trailing-edge noise and is assimilated as the effect of advecting fluctuations across a semi-infinite plate, as demonstrated in Figure 2.1.

A first estimation of the effect of trailing-edge noise is due to Ffwoacs Williams and Hall [23], which has computed the Green's function for the semi-infinite plate by considering the impedance discontinuity at the trailing edge. The work has demonstrated an important characteristic of the noise scattered at the trailing edge, i.e. the scaling of the scattered noise with the flow velocity and turbulent length scales, in particular the boundary layer thickness (δ). The findings suggest that the intensity of trailing-edge noise scales with the flow speed (U) with the 5th power, and with the length scales of turbulence with the 2nd power according to equation 2.1. This constitutes a particularity of scattering noise and is valid for frequencies where the acoustic wavelength ($\lambda_{ac} = c_o/f$) is comparable to or lower than the chord dimension. The scaling with the flow speed with a power of 5 is lower than acoustic sources of pure turbulence, which scales with the free-stream velocity with the power of 8 [23], and compact body forces, which scales with the velocity with the power of 6 [24], indicating that this source of aeroacoustic noise is only dominant for low speed flows.

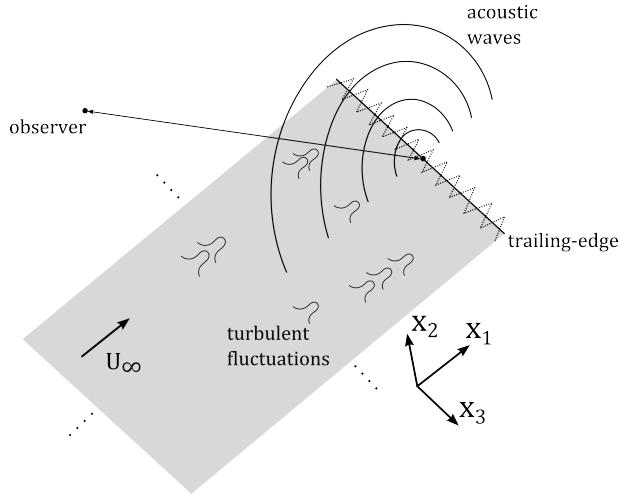


Figure 2.1: Synthesis of the acoustic scattering problem illustrated by the flow past a semi-infinite plate with a trailing-edge of a certain shape. Reference axes used through the work are also shown. The origin of the axes is commonly set to the mid-span along the trailing-edge line.

Several studies have demonstrated this 5th power scaling for trailing-edge noise or used it to confirm the nature of the sources measured. Particularly, the work of Oerlemans et al. [25] has demonstrated this property for the noise of a wind turbine, evidencing also the dominant trailing-edge scattering sources on the noise produced by a wind turbine.

$$I \propto \rho \frac{U^5 \delta^2}{c_o^2 R^2} \quad (2.1)$$

A convenient form of describing the problem mathematically is due to Amiet [26] who has modelled the scattering as a diffraction problem over a semi-infinite plate. Over this plate, an advecting perturbation, of aerodynamic nature, is represented as an incoming wall-pressure fluctuation. This wave is referred to as p_{aero} , and it moves at a speed U_c (convection velocity) along the streamwise direction. The diffraction problem describes the acoustic pressure induced by this advecting aerodynamic fluctuation input.

The acoustic pressure (p_{ac}) is governed by the wave equation 2.2, where U_∞ is the free stream velocity. To this equation, two conditions must be imposed. These conditions refer to the characteristics of the acoustic pressure along the semi-infinite plate, and along the wake downstream from the trailing edge.

At the wall, the non-penetration condition imposes that the acoustic pressure must have zero gradients along the wall-normal direction, represented as a Neumann boundary condition, i.e. $\frac{\partial p_{\text{ac}}}{\partial x_2} = 0$. At the wake region, the Kutta condition,

described in the work of Amiet [26], implies that the acoustic and aerodynamic pressure must be balanced (equation 2.3).

$$\nabla^2 p_{ac} - \frac{1}{c_0^2} \left(\frac{\partial}{\partial t} + U_\infty \frac{\partial}{\partial x_1} \right)^2 p_{ac} = 0 \quad (2.2)$$

$$p_{aero} + p_{ac} = 0. \quad (2.3)$$

The final set of boundary conditions to the equation are shown in 2.4. The function $g(x_3)$ describes the position of the trailing edge along the span.

$$\begin{cases} \frac{\partial p_{ac}}{\partial x_2}(x_2 = 0) = 0, & x_1 \leq g(x_3) \\ p_{ac}(x_2 = 0) = -p_{aero}, & x_1 > g(x_3) \end{cases} \quad (2.4)$$

The first solution to this problem is due to Amiet [27]. The solution is obtained for a straight trailing edge ($g(x_3) = 0$) perturbed by spanwise oriented advecting waves, in the form of

$$p_{aero}(t, x_1, x_3) = A e^{i(\omega t - k_1 x_1)} \quad (2.5)$$

where the streamwise wavenumber (k_1) is associated with the radial frequency (ω) according to

$$k_1 = \frac{\omega}{U_c}. \quad (2.6)$$

This set of equations is solved in the frequency domain for a 2-D acoustic wave along the spanwise direction, where the wave equation turns to the 2-D Helmholtz one, shown in 2.7, where P refers to the frequency decomposed acoustic pressure.

$$\beta^2 \frac{\partial^2 P}{\partial x_1^2} + \frac{\partial^2 P}{\partial x_2^2} + 2iKM \frac{\partial P}{\partial x_1} + K^2 P = 0. \quad (2.7)$$

In the above equation, the acoustic wavenumber K is defined as

$$K = \frac{\omega}{c_0}, \quad (2.8)$$

$\beta = \sqrt{1 - M^2}$ is the Prandtl-Glauert factor, and M represents the flow Mach number ($M = U_\infty/c_0$). Equation 2.7, subject to the same boundary conditions described in equation 2.4 for the pressure fluctuations on the frequency domain, constitutes the diffraction problem for the scattering at the trailing edge.

To obtain the solution, the following change of variables is required

$$P(x_1, x_2) = p(x_1, x_3) e^{i \frac{KM^2}{\beta^2} x_1} \quad (2.9)$$

along with a coordinate transformation represented by $y_1 = x_1$, and $y_2 = \beta x_2$. From that, the problem can be rewritten according to 2.10.

$$\frac{\partial^2 p}{\partial x_1^2} + \frac{\partial^2 p}{\partial x_2^2} + \mu^2 p = 0. \quad (2.10)$$

with boundary conditions given according to

$$\begin{cases} \frac{\partial p}{\partial y_2}(x_3 = 0) = 0, & x_1 \leq 0 \\ p(y_2 = 0) = -Ae^{-i\left(k_1 + \frac{KM^2}{\beta^2}\right)y_1}, & y_1 > 0 \end{cases} \quad (2.11)$$

where $\mu = \frac{KM}{\beta^2}$. This description is convenient for the application of the Schwarzschild solution, where $p(y_1, y_2 = 0)$, at the surface of the semi-infinite plate is given by

$$p(y_1, y_3 = 0) = -\frac{1}{\pi} \int_0^\infty F(y_1, \xi) p(\xi) d\xi \quad (2.12)$$

where the function $F(y_1, \xi)$ is defined as

$$F(y_1, \xi) = \sqrt{\frac{-y_1}{\xi}} \frac{e^{i\mu(\xi - y_1)}}{\xi - y_1} \quad (2.13)$$

The solution of this equation gives the acoustic pressure on the top of the plate surface

$$P(x_1, x_3 = 0) = -Ae^{-ik_1 x_1} \operatorname{erfc}\left(\sqrt{-i(k_1 + (1 + M\mu))x_1}\right), \quad (2.14)$$

where $\operatorname{erfc}(z)$ is the complementary error function (equation 2.15).

$$\operatorname{erfc}(z) = 1 - \operatorname{erf}(z) = \frac{2}{\sqrt{\pi}} \int_z^\infty e^{-t^2} dt. \quad (2.15)$$

From this solution, the far-field pressure on the observer's position $(x_{1,o}, x_{2,o}, x_{3,o})$ resulting from the disturbance of the wall pressure is given by the radiation integral along the model span and chord, following equation 2.16. It is valid to point out here that the integral is restricted to a certain model span (b), and chord (c), despite the considerations of semi-infinite plate during modelling.

$$P(x_{1,o}, x_{2,o}, \omega) = \frac{-i\omega x_{2,o}}{4\pi c_o S_o^2} \int_{-c}^0 \int_{-b/2}^{b/2} P e^{iKR_t} dx_3 dx_1, \quad (2.16)$$

where,

$$R_t = \frac{1}{\beta^2} (R_s - M(x_{1,o} - x_1)) \quad (2.17)$$

$$R_s = S_o \left(1 - \frac{x_{1,o}x_1 + \beta^2 x_{3,o}x_3}{S_o^2} \right) \quad (2.18)$$

$$S_o = \sqrt{x_{1,o}^2 + \beta^2 (x_{2,o}^2 + x_{3,o}^2)} \quad (2.19)$$

The work of Amiet (1976) [27] has provided an analytical solution for the acoustic pressure spectrum for an observer on the mid-span plane ($x_{3,o} = 0$), resulting in equation 2.20

$$S_{pp}(\mathbf{x}_o, \omega) = PP^* = \left(\frac{\omega x_{2,o}}{2\pi c_o S_o^2} \right)^2 \frac{\pi b}{U_c} |G(\omega, K, k_1, k_3)|^2 \Pi_{pp}(k_1, k_3 = 0). \quad (2.20)$$

In the equation, G is given by

$$G = \frac{1}{\Theta} \left((1+i) \left\{ \sqrt{\frac{1+M+k_1/\mu}{1+x_{1,o}/S_o}} E^*(2\mu[1+x_{1,o}/S_o]) e^{-i2\Theta} - E^*(2\mu[1+M]+k_1) \right\} + 1 \right), \quad (2.21)$$

where $\Theta = k_1 + \mu(M - x_{1,o}/S_o)$, and E^*

$$E^*(z) = \frac{1}{\sqrt{2\pi}} \int_0^z \frac{e^{-it}}{\sqrt{t}} dt, \quad (2.22)$$

and $\Pi_{pp}(k_1, k_3 = 0)$ is the two-wavenumber wall-pressure spectrum excited by the unsteady aerodynamic field. For simplicity, in the remainder of this work, the radiation integral and the function G are referred to as the acoustic transfer function, represented by L , such that the description of the equation is simplified to equation 2.23.

$$S_{pp}(\mathbf{x}_o, \omega) = |L(\omega, K, k_1, k_3, \mathbf{x}_o)|^2 \frac{\pi b}{U_c} \Pi_{pp}(k_1, k_3 = 0). \quad (2.23)$$

The solution is valid for the flow over a semi-infinite plate of span b . In theory, models with finite span will also have non-zero contributions from other wavenumbers, since the integral does not vanish to zero. For many applications, however, the model span is much larger than the scales of the boundary layer, and the secondary cut-on wavenumbers are not excited by the aerodynamic fluctuations with similar amplitude.

Another possible source of inconsistency of the model is the consideration of a large airfoil chord in comparison to the acoustic wavenumber. Roger & Moreau [28] proposed a correction of the scattering transfer function by considering the back-scattering of the acoustic waves at the model leading edge, such that $L = L_{TE} + L_{LE}$,

where L_{TE} is the acoustic transfer function from the work of Amiet, and L_{LE} the back-scattering of acoustic waves at the leading edge.

Figure 2.2 shows the polar directivity of the sources using the two different formulations of the acoustic transfer function for different wavenumbers. At small wavenumbers ($Kc \leq 1$), large wavelengths compared to the airfoil chord, the trailing-edge noise directivity resembles a dipolar emission pattern. This follows the assumption of a compact source at low frequencies. At this frequency range, the difference between the two assumptions is very evident. At intermediate wavenumbers ($2 < Kc \leq 4$), a cardioid-shaped directivity pattern is observed, where emissions are stronger upstream and the compact-source assumption is no longer valid. At high wavenumbers ($Kc > 4$), a more complex directivity pattern is observed with alternating regions of high, and low-intensity scattering. At these frequencies, the addition of the back-scattering does not yield significant differences with respect to considering only the trailing-edge scattering. Another important difference between the two conditions is the implication of compact sources at low frequencies ($Kc < 1$) and non-compact sources ($Kc > 1$). For example, the work of Curle [24] shows that the scaling of compact sources with flow speed is proportional to U^6 while non-compact sources scales with U^5 . This is also an observed difference between low-frequencies and high-frequencies sources of trailing-edge noise, since the former scales with U^6 and the latter with U^5 .

A more generic solution to the problem of trailing-edge scattering is shown in the work of Grasso et al. [29]. The solution is built for straight and oblique gusts, i.e. gusts convecting at angles not perpendicular to the trailing-edge direction ($k_3 \neq 0$), allowing the estimation of the acoustic transfer function for different combinations of wavenumber (k_1, k_3) .

The solution for each wavenumber-frequency mode represents the acoustic transfer function between an incoming aerodynamic fluctuation exciting that particular mode and the perceived acoustic fluctuation at a certain distance from the trailing-edge.

For a wing with an infinite span, only a single incoming wavenumber mode contributes to the scattered far-field noise, i.e. the one where the wavefronts are parallel to the trailing edge. As an example, for a slanted trailing edge, this wavenumber corresponds to $(k_1, k_3) = (\omega/U_c, \omega/U_c \tan \psi)$, where ψ is the trailing-edge sweep angle.

Figure 2.3 illustrates the process of predicting the trailing-edge noise from straight (top) and slanted trailing edges (bottom) for wings of large span. For a given frequency, the streamwise wavenumber is obtained based on the convection velocity ($k_1 = \omega/U_c$). From the streamwise wavenumber, the spanwise wavenumber is computed based on the trailing-edge sweep angle, defining the cut-on mode for the acoustic prediction. From the figure, it is clear that the cut-on mode correspond

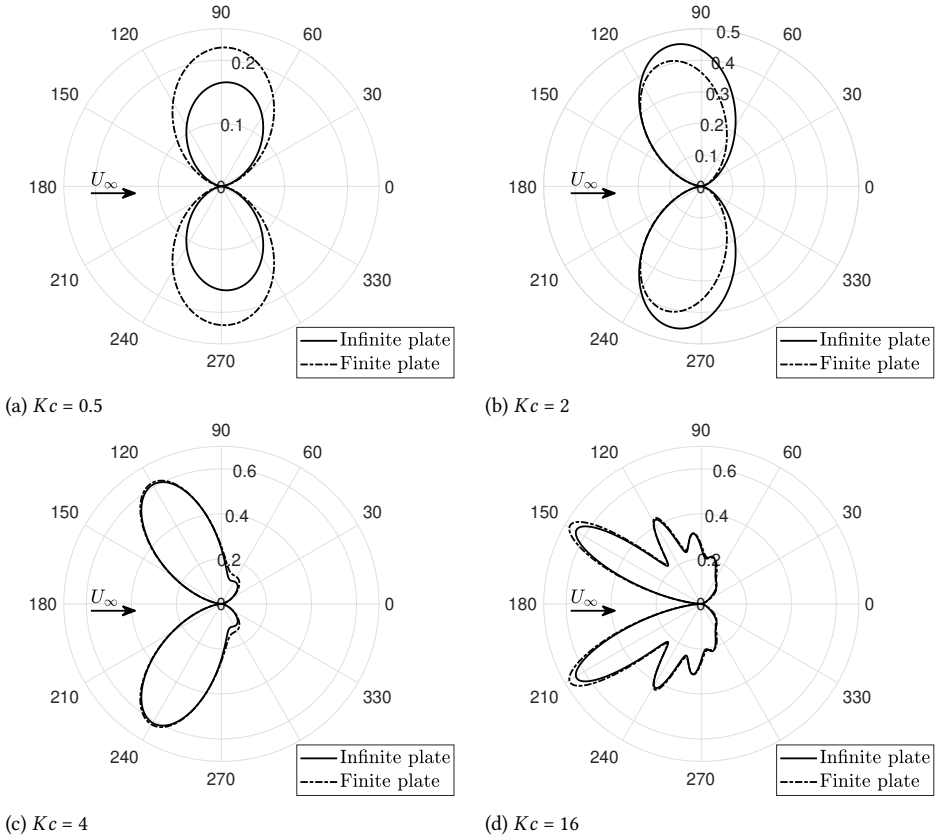


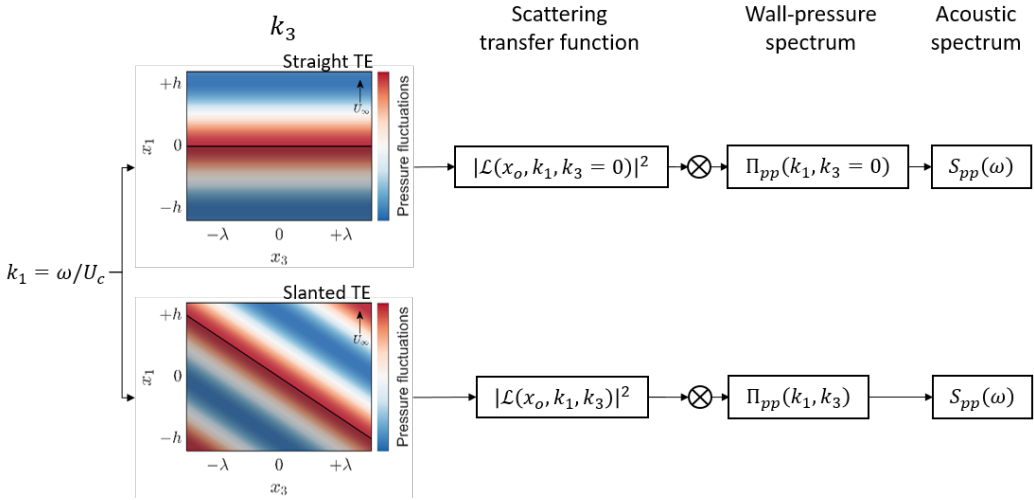
Figure 2.2: Directivity plot for the scattering of an infinite span wing with a straight trailing edge at $M = 0.2$ at different frequencies. The solid line represents the estimations without back-scattering, and the dashed lines with the back-scattering corrections.

to that where the wavefront is orthogonal to the trailing-edge line. Based on the pair (k_1, k_3) , the acoustic emissions are estimated by multiplying the computed acoustic transfer function $(L(\omega, K, k_1, k_3))$ by the input power spectrum from the aerodynamic fluctuations at that particular wavenumber $(\Pi(\omega, k_1, k_3))$, following equation 2.24.

$$S_{pp}(\mathbf{x}_o, \omega) = |L(\omega, K, k_1 = \omega/U_c, k_3 = \omega/U_c \tan \psi, \mathbf{x}_o)|^2 \frac{\pi b}{U_c} \Pi_{pp}(k_1 = \omega/U_c, k_3 = \omega/U_c \tan \psi). \quad (2.24)$$

Having a solution for the acoustic transfer function, the only required input to predict the noise from trailing-edge scattering is a description of the aerodynamic wall-pressure fluctuations. The following section explores the possible sources and

properties of these fluctuations.



2

Figure 2.3: Representation of the process of predicting the acoustic spectrum of a straight (above) and slanted (below) trailing edge of an infinite-span wing.

2.2 AERODYNAMICS OF THE WALL-PRESSURE FLUCTUATIONS AT THE TRAILING EDGE

According to the work of Brooks et al. [30], four different flow conditions over an airfoil can create the aforementioned aerodynamic pressure fluctuations necessary to produce trailing-edge noise, namely instabilities of the laminar boundary-layer flow; turbulent boundary-layer flow; boundary-layer separation; vortex shedding.

Figure 2.4 illustrates how the unsteady flow differs from each of the conditions. The following paragraphs discuss the properties of each of these possible sources of trailing-edge noise.

Instabilities of the laminar boundary-layer flow Laminar boundary layers are prone to flow instabilities which can reach the trailing-edge region, in turn creating scattering noise. Particularly, Tollmien-Schlichting waves [32] are known to generate trailing-edge noise. These are 2-D instabilities ($k_3 = 0$) and extend to a narrow range of wavenumbers and frequencies, depending on the evolution of the boundary layer along the airfoil chord and Reynolds number condition. The input in a narrow range of frequencies yields that the noise signature of laminar boundary-layer noise is also of narrowband nature.

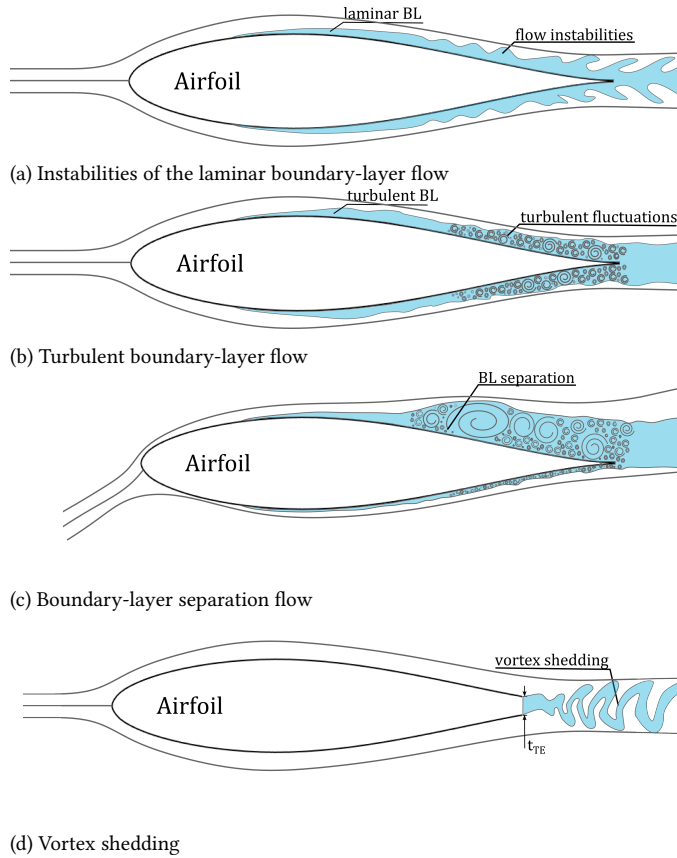


Figure 2.4: Illustrative representation of the sources of unsteady wall-pressure fluctuations on the flow over an airfoil. Adapted from the work of [31].

Besides, the scattered noise itself can excite the formation of the Tollmien-Schlichting waves, creating a feedback-loop mechanism that increases the levels of selected frequencies, generating a distinctive tonal noise source. These tones are known as laminar boundary layer trailing-edge tones. Several studies have addressed the incoming sources of this feedback and the possible mechanism behind it [33–36].

Turbulent boundary-layer flow In most engineering applications, and certainly for wind turbines, turbulent boundary layers are the dominating source of trailing-edge noise given the high flow-speeds and Reynolds numbers. The turbulent flow is a source of wall-pressure fluctuations in a broad range of frequencies, i.e. from low frequencies, represented by scales of the order of the boundary-layer thickness ($\propto \delta$), to the high frequencies represented by the scales on the dissipation range ($\propto \nu/u_\tau$). The wall-pressure turbulent fluctuations are responsible for exciting a full range of spanwise and streamwise wavenumbers, apart from the $k_3 = 0$ ones. Being this the dominating source of noise on a wind-turbine, and the focus of this work, Section 2.3 deepens the description of this source of noise.

Boundary-layer separation flow Separation is another source of large-scale turbulence and is known to increase trailing-edge noise by up to 10 dB with respect to turbulent boundary layers. According to [30], trailing-edge noise is the main source of separated flow noise when separation is restricted in the vicinity of the trailing-edge region. For large separations (deep stall conditions), the pressure fluctuations over the model surface also contribute to the overall noise.

Vortex shedding A last source of trailing-edge noise is the shedding of vortices due to the wake flow downstream from the trailing-edge. This source is especially important for small airfoil chords or thick trailing edges. According to the work of Blake [37], the noise from vortex shedding is observed in the far field for trailing edges that are thicker than 30% the boundary-layer displacement thickness (δ^*), according to equation 2.25.

$$t_{TE} \geq 0.3\delta^*. \quad (2.25)$$

The vortex shedding instability is a source of narrowband nature in which the noise is centred at a Strouhal number described by equation 2.26 [38], where t_{TE} is the trailing-edge thickness.

$$\frac{f t_{TE}}{U_\infty} \approx 0.1. \quad (2.26)$$

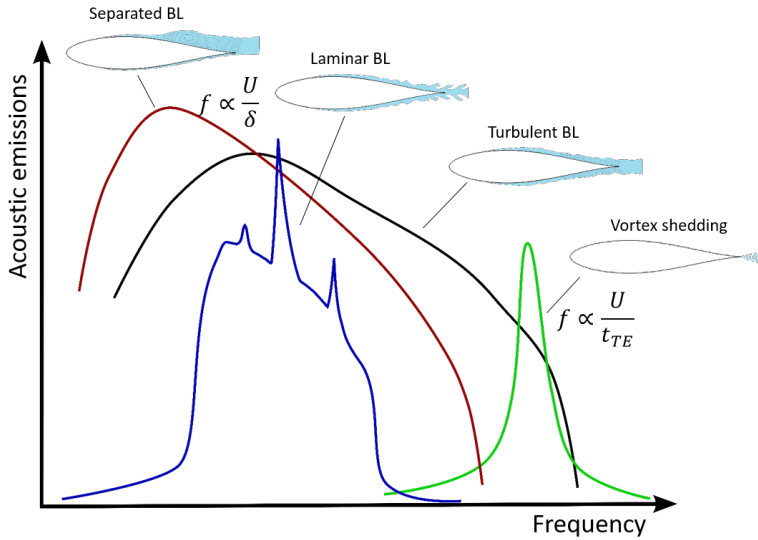


Figure 2.5: Illustration of the spectral shape of the acoustic scattering emissions obtained from the different aerodynamic sources of wall-pressure fluctuations at the trailing edge of an airfoil. With the exception of the vortex shedding noise, all other sources are proportional to the scales of the boundary layer at the trailing-edge.

Figure 2.5 illustrates the spectral shape of the trailing-edge noise emitted from each different type of aerodynamic input. The following section describes the properties of the wall-pressure fluctuations from a turbulent boundary layer.

2.3 WALL-PRESSURE FLUCTUATIONS IN THE TURBULENT BOUNDARY LAYER

A fundamental source of the wall-pressure fluctuations is represented by turbulent fluctuations from the boundary layer near the trailing edge. According to Wilmarth & Ross (1995) [39], the amplitude of these fluctuations correspond to about 0.35% of the flow dynamic pressure (equation 2.27).

$$p_{\text{rms}} \approx 0.0035 \frac{1}{2} \rho U_{\infty}^2. \quad (2.27)$$

The pressure fluctuations on a turbulent flow can be modelled by the Poisson pressure equation (eq. 2.28), obtained by taking the divergence of the Navier-Stokes momentum equation and using the incompressible continuity equation, followed by the Reynolds decomposition of the velocity into its mean-flow component (U_i) and its velocity fluctuations (u_i).

$$\frac{1}{\rho} \nabla^2 p = q = -2 \frac{\partial U_i}{\partial x_j} \frac{\partial u_j}{\partial x_i} - \frac{\partial}{\partial x_i \partial x_j} (u_i u_j - \overline{u_i u_j}) \quad (2.28)$$

The source element q contains two terms. The first term is denoted mean-shear and turbulence interaction, hereby referred to MS-T term, and represents the pressure fluctuations induced by the interaction between turbulent eddies and accelerations from the mean flow, or shear flow. The second term is referred to as turbulence self-interaction, referred to as the T-T term, and represents the self-produced pressure due to turbulence. On a turbulent boundary layer, the first term is dominant with respect to the second one. According to Kraichnan [40], the root-mean-square of the pressure induced by the MS-T sources is about 10 times larger than that of T-T sources. Other studies, however, have shown that the second term grows in significance at high frequencies [41].

For low frequencies, and consequently large scales of turbulence, the MS-T term can be considered the main source of pressure fluctuations in a turbulent flow. On a turbulent boundary layer of an infinite wing, the main contribution to the MS-T term comes from the mean shear generated by the gradient of the streamwise velocity along the wall-normal direction ($\frac{\partial U_1}{\partial x_2}$). This means that equation 2.28 can be approximated to equation 2.29. This equation demonstrates the important role of the wall-normal velocity fluctuations in the generation of pressure fluctuations on a turbulent boundary layer. Figure 2.6 illustrates the root-mean squared levels of the MS-T source term along the boundary-layer velocity profile. In the figure, the dashed turbulent eddies represent the mirrored condition imposed by the presence of the wall.

$$\frac{1}{\rho} \nabla^2 p = -2 \frac{\partial U_1}{\partial x_2} \frac{\partial u_2}{\partial x_1} \quad (2.29)$$

A solution for the wall-pressure fluctuation is based on the streamwise-spanwise wavenumber decomposition of the velocity and pressure fluctuations, following equation 2.30. The decomposed Poisson equation can be solved at the wall ($x_2 = 0$) using the appropriate Green's function formulation (G), shown in equation 2.31. This Green's function represents the wall-mirrored condition illustrated in Figure 2.6 and its choice is detailed in the work of Lilley [43]. The solution of the pressure in the wavenumber domain is given by 2.32.

$$\tilde{p}(k_1, x_2, k_3, t) = \frac{1}{4\pi^2} \iint_{-\infty}^{\infty} p(\mathbf{x}, t) e^{-ik_1 x_1} e^{-ik_3 x_3} dx_1 dx_3. \quad (2.30)$$

$$G(x_2, X_2, \mathbf{k}) = -\frac{e^{-\sqrt{k_1^2 + k_3^2} x_2}}{\sqrt{k_1^2 + k_3^2}}. \quad (2.31)$$

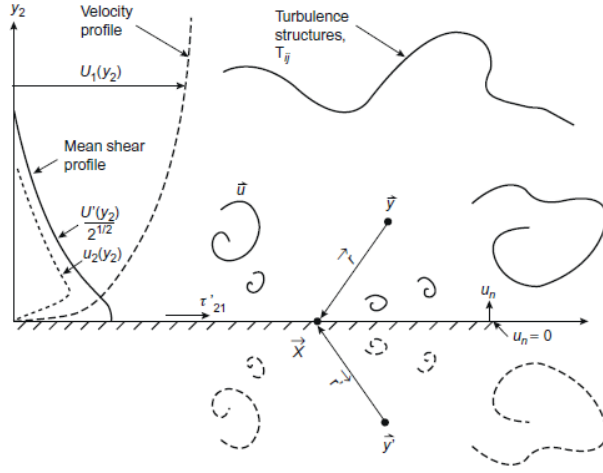


Figure 2.6: Representation of the MS-T sources of the pressure Poisson equation on a turbulent boundary layer [42]. The dashed eddies illustrate the mirrored condition imposed in the wall.

$$\tilde{p}(k_1, x_2 = 0, k_3, t) = -2\rho \int_0^\infty \frac{\partial U_1}{\partial x_2}(X_2) \frac{ik_1}{\sqrt{k_1^2 + k_3^2}} \tilde{u}_2 e^{-\sqrt{k_1^2 + k_3^2} X_2} dX_2. \quad (2.32)$$

The autospectrum of the wall-pressure $\Pi_{pp}(k_1, x_2 = 0, k_3, t)$ is obtained according to equation 2.33, where \tilde{p}^* represents the complex conjugate of the wavenumber-transformed wall pressure, and $S_{2,2}(k_1, k_3, X_2, X_2')$ is the wall-normal velocity cross-spectrum between points X_2 , and X_2' .

$$\Pi(k_1, k_3) = \overline{\tilde{p}\tilde{p}^*} = 4\rho^2 \iint_0^\infty \frac{\partial U_1}{\partial x_2}(X_2) \frac{\partial U_1}{\partial x_2}(X_2') S_{2,2} \frac{k_1^2}{k_1^2 + k_3^2} e^{-\sqrt{k_1^2 + k_3^2}(X_2 + X_2')} dX_2 dX_2'. \quad (2.33)$$

The first important insight that equation 2.33 gives is the dependence upon $\frac{k_1^2}{k_1^2 + k_3^2}$. This dependency indicates that for a certain value of k_1 , the wavenumber wall-pressure spectrum is maximum around $k_3 = 0$. This means that spanwise-aligned fluctuations of the wall-pressure carry the highest energy for a given k_1 . According to Blake [42], the two-wavenumber spectrum for the wall-pressure data filtered at a certain frequency ω has the characteristics shown in Figure 2.7. The figure shows the wavenumber spectrum of the wall-pressure fluctuations at a given frequency. The image shows on the left a cut of the spectrum along $k_3 = 0$, illustrating the maximum along the convective wavenumber, i.e. $k_1 = \omega/U_c$, where U_c is the convective velocity. The image on the right shows a contour plot of

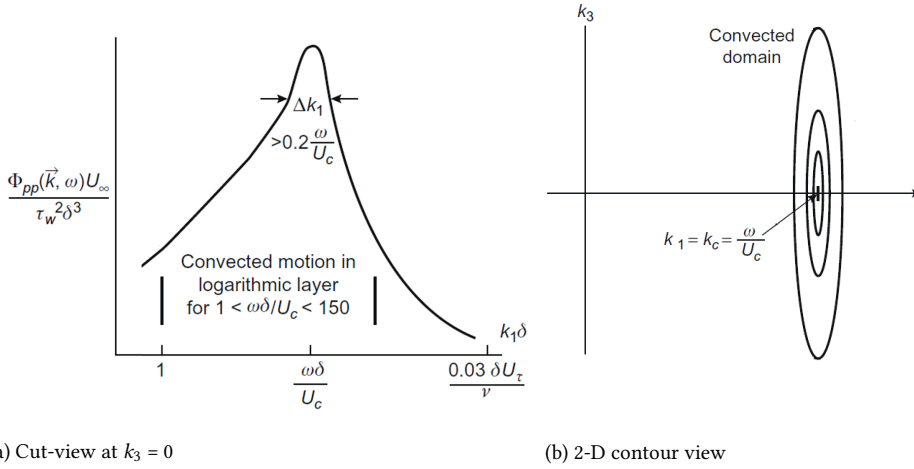


Figure 2.7: Representation of the shape of the frequency-filtered two-wavenumber spectrum of the compressible wall-pressure fluctuations beneath a turbulent boundary layer. Figure adapted from the work of [42].

the two wavenumbers, demonstrating that the maximum power is captured for spanwise-aligned waves ($k_3 = 0$).

The work of Corcos [44] has proposed a separation of the two-wavenumber spectrum between the convective component of the streamwise wavenumber spectrum and a shape function based on the nondimensionalized spanwise wavenumber (equation 2.34). The streamwise wavenumber spectrum is converted to the frequency spectrum using the convection velocity (U_c). The use of the wall-pressure frequency spectrum is a convenient choice as it represents the output from measurements of the pressure fluctuations in time at a single wall location.

$$\Pi_{pp}(k_1 = \omega/U_c, k_3) = \frac{U_c}{\pi} \phi_{pp}(\omega) \eta(k_3 l_{x3}). \quad (2.34)$$

Roger & Moreau (2005) [28] have proposed a simplified shape-function in the form of equation 2.35.

$$\eta(k_3) = \frac{l_{x3}}{1 + (k_3 l_{x3})^2}. \quad (2.35)$$

These equations highlight the three variables extracted from the wall-pressure fluctuations that govern the scattered noise, i.e. the frequency spectrum (ϕ_{pp}), the convection velocity (U_c), and the spanwise correlation length (l_{x3}). In the remainder of this work, the properties of these three parameters are extensively explored.

Therefore, the following sections describe important characteristics of each of the three mentioned variables.

2

2.3.1 THE WALL-PRESSURE SPECTRUM (ϕ_{pp})

The wall-pressure frequency spectrum, often referred to as only the wall-pressure spectrum, shows the energy distribution of the wall-pressure fluctuations for each frequency. Three different frequency, or scales, are observed for a turbulent boundary layer, namely the outer scales, the universal scales, and the inner scales. These three scales differ by the wall-normal location in the boundary layer where the source term is more intense, and consequently the mean-flow shear ($\frac{\partial U_1}{\partial x_2}$), turbulent fluctuations, and the scaling of the spectrum with frequency. From equation 2.33, the following can be inferred of the wall-pressure fluctuations according to Blake [42]:

- The outer scales: are due to the very large scales of the turbulent flow ($\omega\delta/u_\tau \leq 100$) produced at the wake region of the turbulent boundary layer, above the logarithmic range of the boundary layer [45]. These scales are associated to the wall-pressure fluctuations at the region of very low stream-wise wavenumber ($k_3 \gg k_1$) and frequency ($\omega = k_1 U_c$) where, according to equation 2.33, $\phi_{pp} \propto \omega^2$, i.e. the wall-pressure fluctuations increase with the square of the frequency;
- The inner scales: these turbulent scales are the smallest ones in the flow, starting at frequencies above $\omega > 0.3u_\tau^2/\nu$. Wall-pressure fluctuations created from these fluctuations are generated by the eddies inside the sub-viscous layer. The spectrum at this region decays with frequency following $\phi_{pp} \propto \omega^{-5}$;
- The universal scales: these scales represent the transition region in the mid-frequency range, where the sources of the wall-pressure fluctuations are contained in the logarithmic layer. Within this range, $\phi_{pp} \propto \omega^{-1}$. The size of this frequency range depends on the flow Reynolds number based on the boundary layer thickness, such that $f_{\text{end}}/f_{\text{start}} \approx 3 \times 10^{-3} Re_\delta$.

Figure 2.8 shows the basic shape of the wall-pressure spectrum beneath a turbulent boundary layer with zero pressure gradient. The figure shows that the spectrum reaches a maximum around $\omega\delta/u_\tau \leq 50$ and decays with $\propto \omega^{-1}$ in the universal scales. At the inner scales, the spectrum decays faster, with $\phi_{pp} \propto \omega^{-5}$.

Based on the analytical description of the wall-pressure spectrum beneath a turbulent boundary layer, several semi-empirical models were developed. The work of Lee et al. [47] described the models according to a generic equation (equation 2.36). In the equation, SS , and FS stand for spectrum and frequency scaling respectively, and R_t is the ratio between the turbulent (δ/U_e) and the viscous

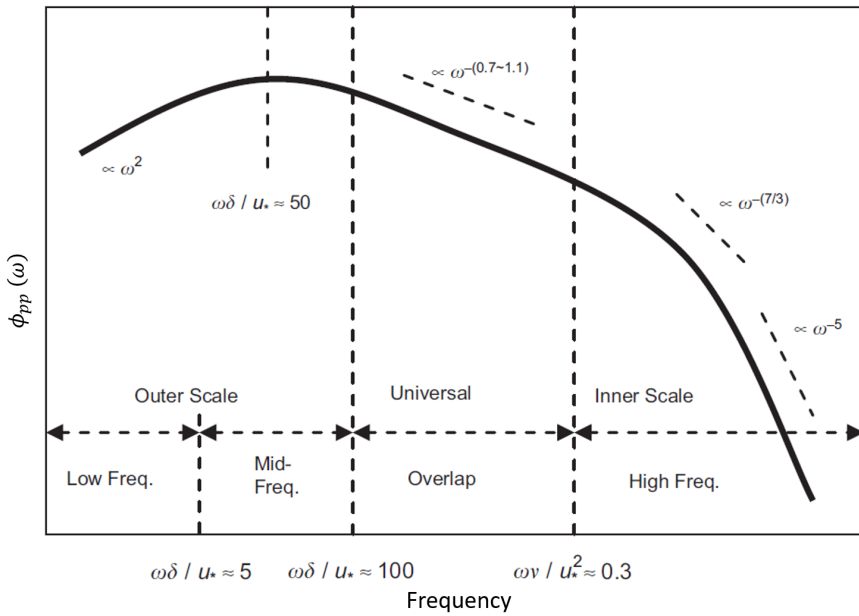


Figure 2.8: Representation of the general characteristics of the wall-pressure frequency spectrum (ϕ_{pp}) beneath a turbulent boundary layer without pressure gradient. Figure taken from [46].

(v/u_τ^2) time scales. The empirical parameters c_1 to c_4 , and n_1 to n_5 vary from the model chosen. Tables 2.1, 2.2, and 2.3, summarize these parameters for the models of Chase-Howe [10], Goody [48], Rozenberg [49], Kamruzzaman [50], Hu [51], and Lee [47].

The first two models are based on a zero-pressure gradient turbulent boundary layers. Chase-Howe model describes only the wall-pressure fluctuations from the outer ($\propto \omega^2$) and universal scales ($\propto \omega^{-(0.7-1.1)}$) of the flow. The model of Goody includes the inner scales ($\propto \omega^{-5}$) for the ZPG boundary layer. The other described models incorporate the effects of adverse and favourable pressure gradients (APG and FPG respectively) by considering different parameters of the boundary layer, i.e. the shape factor (H), the Zagarola Smit's parameter (Δ_*), the Clauser's equilibrium parameter (β_c), and the wake parameter (Π_w) from Coles [45]. The mathematical definitions of these parameters are shown from equations 2.37 to 2.42. It is worth mentioning that the model of Lee is based on a modification of Rozenberg's model and, as such, most of the parameters have similar values.

$$\frac{\phi_{pp}}{SS}(\omega) = \frac{c_1(\omega/FS)^{n_1}}{c_2[(\omega/FS)^{n_2} + c_3]^{n_3} + [(c_4 R_t^{n_4})(\omega/FS)]^{n_5}}. \quad (2.36)$$

Model	SS	FS	R_t
Chase	$\tau_w^2 \delta^*/U_e$	U_e/δ^*	-
Goody	$\tau_w^2 \delta/U_e$	U_e/δ	$(\delta/U_e)/(v/u_\tau^2)$
Rozenberg	$\tau_{\max}^2 \delta^*/U_e$	U_e/δ^*	$(\delta/U_e)/(v/u_\tau^2)$
Kamruzzaman	$\tau_w^2 \delta^*/U_e$	U_e/δ^*	$(\delta^*/U_e)/(v/u_\tau^2)$
Hu	$q^2 \theta/v$	U_e/θ	$(\delta/U_e)/(v/u_\tau^2)$
Lee	$\tau_w^2 \delta^*/U_e$	U_e/δ^*	$(\delta/U_e)/(v/u_\tau^2)$

Table 2.1: Summary of scaling parameters for different semi-empirical wall-pressure spectrum models following equation 2.36. These parameters are based on the works of [47], and [46].

Model	c_1	c_2	c_3	c_4
Chase	1	1	0.0144	0
Goody	3	1	0.5	1.1
Rozenberg	$[2.82\Delta_*^2(6.13\Delta_*^{-0.75} + c_3)^{n_3}][4.2(\Pi_w/\Delta_*) + 1]$	4.76	$4.76(1.4/\Delta_*)^{0.75}[0.375n_3 - 1]$	8.8
Kamruzzaman	$0.45[1.75(\Pi_w^2 \beta_c^2)^{0.5(H/1.31)^{0.3}} + 15]$	1	0.27	0.9609
Hu	$(81.0c_3 + 2.154) \times 10^{-7}$	1	$10^{-5.8Re_\theta H \times 10^{-5} - 0.35}$	7.645
Lee	$\max\{1, (0.25\beta_c - 0.52)c_{1,Roz}\}$	1	$\max\{1, 1.5c_{3,Roz}\}$	8.8

Table 2.2: Summary of the multiplicative parameters for different semi-empirical wall-pressure spectrum models following equation 2.36. These parameters are based on the works of [47], and [46].

Model	n_1	n_2	n_3	n_4	n_5
Chase	2	2	1.5	-	-
Goody	2	0.75	3.7	-0.57	7
Rozenberg	2	0.75	$3.7 + 1.5\beta_c$	-0.57	$\min(3, 19/\sqrt{R_t}) + 7$
Kamruzzaman	2	1.637	2.47	-2/7	7
Hu	1	87.9	0.0643	-0.411	6
Lee	2	0.75	$3.7 + 1.5\beta_c$	-0.57	$\min(3, 0.139 + 3.1043\beta_c, 19/\sqrt{R_t}) + 7$

Table 2.3: Summary of the power parameters for different semi-empirical wall-pressure spectrum models following equation 2.36. These parameters are based on the works of [47], and [46].

$$H = \frac{\delta^*}{\theta}. \quad (2.37)$$

$$\Delta_* = \frac{\delta}{\delta^*}. \quad (2.38)$$

$$\beta_c = \frac{\theta}{\tau_w} \frac{dP}{dx_1}. \quad (2.39)$$

$$2\Pi_w - \log(1 + \Pi_w) = \chi \frac{U_e}{u_\tau} - \log\left(\frac{\delta^* U_e}{\nu}\right) - \chi C^+ - \log(\chi). \quad (2.40)$$

$$\tau_w = \rho u_\tau^2 \quad (2.41)$$

$$\tau_{\max} = \max\left[\mu \frac{dU}{dx_2}(x_2)\right] \quad (2.42)$$

These semi-empirical models are all built with different datasets and applications in mind. Several studies exist on the advantages and disadvantages of each model for predicting the wall-pressure fluctuations [47, 50, 52, 53].

Another physically-based method is described in the work of Panton and Linebarger [54] in which equation 2.33 is integrated to create the wall-pressure spectrum. This method is referred to as Panton's method. Remmler et al. [55] described a numerical methodology for a computationally efficient calculation of the wall-pressure fluctuations. Opposed to the semi-empirical methods, the Panton model requires the profile of the mean streamwise velocity and of the wall-normal velocity fluctuations ($\overline{u_2}$). This information requires steady numerical simulations or experimental measurements using hot-wire anemometry or planar PIV techniques. Nevertheless, the method is still less costly when compared to dedicated unsteady simulations and measurement campaigns with unsteady pressure measurements, which could provide the wall-pressure fluctuations directly. Studies indicate that the

Panton model yields more consistent prediction of the wall-pressure fluctuations compared to the semi-empirical ones [53].

2.3.2 THE CONVECTION VELOCITY (U_c)

Besides the spectrum of the pressure fluctuations, the velocity with which these fluctuations travel, called the convective velocity (U_c), is another important parameter for the scattering at the trailing-edge. The convective velocity directly influences the aerodynamic input in equation 2.4. U_c is defined in time domain according to equation 2.43. The equation depends on the measurements of the wall-pressure fluctuations at two points along the streamwise direction, where Δx_1 is the distance between the points, and Δt_{\max} is the time delay where the cross-correlation (equation 2.44) between the wall-pressure ($\overline{p\overline{p}}$) captured in the two locations is maximum.

$$U_c = \frac{\Delta x_1}{\Delta t_{\max}}. \quad (2.43)$$

$$\overline{p\overline{p}}(\Delta x_1, \Delta t) = \int p(x_o, t) \cdot p(x_o + \Delta x_1, t + \Delta t) dt. \quad (2.44)$$

The convective velocity can also be defined in the frequency domain. This definition is shown in equation according to the work of Romano [56]. In the equation, $\frac{d\psi}{d\omega}$ is the derivative of the phase of the wall-pressure cross-spectrum between the same points spaced by Δx_1 with respect to the frequency.

$$U_c(\omega) = \Delta x_1 \left(\frac{d\psi}{d\omega} \right)^{-1}. \quad (2.45)$$

The convection velocity (U_c) is usually considered weakly dependent on the frequency [27] and it ranges from about 60-70% of the boundary-layer edge velocity (U_e). Nevertheless, U_c usually displays a small decay as the frequency increases. This happens as the wall-pressure at high frequencies is attributed to the small scales closer to the wall, which travel at a lower mean speed. The works of Smol'yakov et al. and Catlett et al [57, 58] provide a frequency-dependent estimation for the convective velocity. The latter has also proposed a relation between U_c and the boundary-layer shape factor (H). Lower values of H , associated with favourable pressure gradient boundary layers, yield a higher U_c , while higher H values, associated with adverse pressure gradient boundary layers, yield a lower U_c , according to equation 2.46. The shape-factor ranges from 1 to infinity and a typical value for a zero-pressure boundary layer is 1.4 [32].

$$\frac{U_c}{U_e} = 1.02 - 0.3H. \quad (2.46)$$

2.3.3 THE CORRELATION LENGTH (l_x)

The correlation length (l_x) is the last important parameter explored in this work to infer the noise emitted from trailing edges. Essentially, it provides the length of the turbulent wall-pressure structures in a certain direction and at a certain frequency. Its definition is similar to the one of the turbulent length-scales, differing for being based on the wall-pressure fluctuations and by the frequency-dependent representation.

Amiet [27] defines the correlation length (l_{xi}) according to equation 2.47, where i refers to the direction where the correlation length refers to. In the equation, $\gamma(\omega, x_0, x_0 + x_i)$ is the coherence coefficient of the wall-pressure fluctuations computed between points displaced by x_i . The streamwise (l_{x1}), and the spanwise (l_{x3}) correlation lengths are the most commonly used parameters for studies of trailing-edge noise.

$$l_{xi}(\omega) = \int_0^{\infty} \gamma(\omega, x_0, x_0 + x_i) dx_i. \quad (2.47)$$

Two models exist to estimate the correlation length. The first is based on the universal model of Corcos [44] for the wall-pressure cross-spectrum. According to it, the correlation length is inversely proportional to the frequency (ω) and directly proportional to the convective velocity of the flow, following equation 2.48. The semi-empirical constant α_{xi} can be determined experimentally. Hu & Herr [51] have obtained the values of 0.15, and 0.72 for the streamwise (α_{x1}), and spanwise (α_{x3}) correlation length constants respectively. The values indicate that the wall-pressure structures are about 5 times larger along the streamwise direction when compared to the spanwise one.

$$l_{xi}(\omega) = \frac{U_c}{\alpha_{xi}\omega}. \quad (2.48)$$

The latter model can correctly predict the behaviour of the correlation length in the universal and inner scales of the turbulence, i.e. its decay with frequency. This behaviour, however, is not observed for the outer scales of flow, where the correlation length increases with the increasing frequency [59]. Therefore, a second model based on the equation proposed by Efimtsov can be used to describe the correlation length at low frequencies (Equation 2.49). This equation turns into Corcos' model for $\beta_{xi} = 0$. The work of Palumbo et al. (2012) [59] used flight data to estimate the values of the constants, resulting in the ones shown in Table 2.4.

$$l_{xi}(\omega) = \frac{\delta}{\sqrt{\left(\frac{\alpha_{xi}\omega\delta}{U_c}\right)^2 + \frac{\beta_{xi}}{\left(\frac{\omega\delta}{u_r}\right)^2 + \zeta_{xi}}}}. \quad (2.49)$$

	Streamwise (l_{x1})			Spanwise (l_{x3})		
	α_{x1}	β_{x1}	ζ_{x1}	α_{x3}	β_{x3}	ζ_{x3}
Hu	0.15	0	-	0.72	0	-
Palumbo	0.06	25	25	0.77	67,600	4,225

Table 2.4: Summary of the semi-empirical parameters used for modelling the stream and spanwise correlation length based on equation 2.49.

2

2.4 TURBULENT BOUNDARY LAYER TRAILING-EDGE NOISE

Having discussed the properties of the acoustic scattering at the trailing edge and of the wall-pressure fluctuations beneath a turbulent boundary-layer flow, this section describes the expected characteristics of the trailing-edge noise induced by a turbulent boundary layer.

By using equation 2.23, 2.34, and 2.35, a model for the turbulent boundary layer trailing-edge noise is created (equation 2.50). This is the known solution from Amiet [27] for the turbulent boundary layer trailing-edge noise.

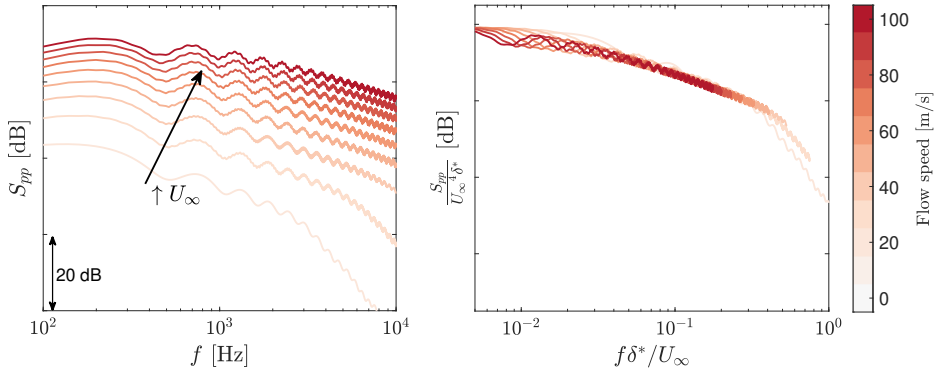
$$S_{pp}(\mathbf{x}_o, \omega) = |L(\omega, K, k_1 = \omega/U_c, k_3 = 0, \mathbf{x}_o)|^2 b \phi_{pp}(\omega) l_{x3}(\omega). \quad (2.50)$$

This model highlights some of the characteristics of the scattered noise mentioned before. At first, since $\phi_{pp} \propto U_\infty^3 \delta^*$, and $l_{x3} \propto U_\infty$ (Corcos' model), the resulting noise is proportional to the scales of the boundary layer according to equation 2.51. It is important to mention that the scaling is only valid for the power spectral density (PSD) of the acoustic emission. For the sound pressure level, given by the integration of the PSD in frequency bands (Δf), the proportionality changes back to U_∞^5 , as described in Ffowcs Williams & Hall [23], since $\Delta f \propto \Delta St U_\infty$.

$$S_{pp} \propto U_\infty^4 \delta^* b. \quad (2.51)$$

Secondly, the frequency spectrum of the scattered noise predominantly scales with the Strouhal number based on the boundary-layer displacement thickness ($St_{\delta^*} = f \delta^*/U_\infty$). This follows the scaling of the wall-pressure spectrum shown in the semi-empirical models (equation 2.36). Nevertheless, the scaling is also affected by the variations of the scattering transfer function and correlation length in frequency. The two latter parameters do not show proportionality only to St_{δ^*} . Other parameters such as speed of sound, and airfoil chord can affect this scaling.

Figure 2.9 shows predicted dimensional and non-dimensional spectra of turbulent boundary layer trailing-edge noise at different speeds obtained using the model of Goody for the wall-pressure spectrum and of Corcos for the correlation length. The non-dimensional spectra demonstrate the scaling of the frequency with the Strouhal number ($f \delta^*/U_\infty$) and of the levels with U_∞^5 .



(a) Dimensional trailing-edge noise spectrum (b) Non-dimensional trailing-edge noise spectrum

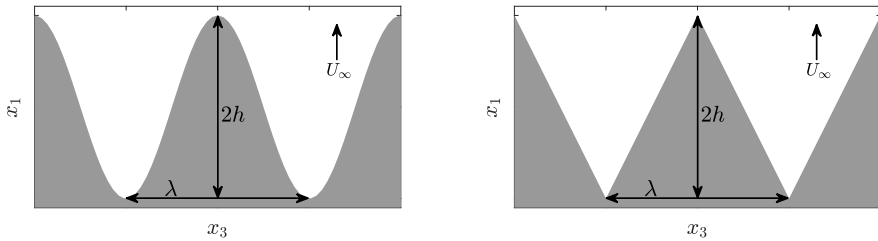
Figure 2.9: Variation of the predicted acoustic spectrum from the scattering of a flap plate of 1 m chord at different flow speeds.

2.5 TRAILING-EDGE SERRATIONS FOR BROADBAND NOISE REDUCTION

As discussed in the previous sections, trailing-edge noise is generated by the scattering of convecting aerodynamic fluctuations along the sharp trailing edge. In section 2.3, we have shown that the wavenumber spectrum of the wall-pressure fluctuations is, for a given frequency ω , always the maximum around $(k_1, k_3) = (\omega/U_c, 0)$. This particular wavenumber happens to be also the cut-on mode for a straight trailing edge, as shown in Figure 2.3. For this case, the wavefronts of the incoming wall-pressure are aligned with the trailing edge, i.e. it has the same phase along the entire model span. This means that the straight trailing edge represents the worst possible combination in regards to noise emissions. This is because the main cut-on mode for noise scattering coincides with the most energetic one excited by the turbulent boundary layer.

From that logic, it is reasonable to think that introducing a sweep angle on the trailing edge yields a reduction of the scattered noise [10]. By doing so, the dominant wavenumber for scattering is shifted to the ones where the incoming turbulent fluctuations have lower intensity. The recent work of Grasso et al. [29] provided analytical evidence that significant noise reduction can be expected by introducing a sweep angle to the trailing edge. Nevertheless, increasing the sweep angle is limited by other design constraints, such as manufacturing challenges or even aerodynamic ones, as the introduction of sweep leads to a reduction of the local lift coefficient and formation of cross flow.

Trailing-edge serrations come as a way to introduce a sweep angle by locally and periodically altering the sweep of the trailing edge [10]. By doing so, a much higher



(a) Sinusoidal-shaped serrations

(b) Sawtooth-shaped serrations

Figure 2.10: Illustration of the commonly applied sinusoidal (a), and sawtooth-shaped serrations. The two scaling parameters that define the design of serrations of the same shape, i.e. the serration height ($2h$), and wavelength (λ) are also shown.

sweep angle is possible with minimum impact on the structural and aerodynamic characteristics of the product. Two common examples of serration shapes are depicted in Figure 2.10, the sinusoidal and the sawtooth serrations respectively. The figure also shows the two parameters commonly used to describe the serrations, i.e. the serration height ($2h$), and wavelength (λ). Together with the serration shape, the height and wavelength constitute the design variables that can be modified in the serration geometry to modify its noise reduction.

The practicality of applying trailing-edge serrations lies exactly in the local modification that the serration design proposes. At first, the trailing-edge region does not represent a major contribution to airfoil lift, and modifications around this area have usually little impact on the overall lift of the airfoil. Secondly, streamlined and well-design serrations modify only the airfoil friction surface, resulting in a minor increase in drag. In comparison, other noise reduction technologies, such as porous or perforated materials, have shown a more significant impact on the pressure and friction drag [60]. Lastly, serrations can be built as add-ons to an existing system and installed on it according to the noise reduction demands. This is an important feature for wind-turbine manufacturers as it allows for a single design and manufacturing of the blades while a portfolio of configurations can be offered. This portfolio can include different serration designs which are varied to attend the different required noise levels. According to Oerlemans et al. [8], up to 4 dB noise reduction can be obtained by applying trailing-edge serrations on a wind-turbine blade. Figure 2.11 shows measurement results from the same reference for the noise spectrum of a wind turbine with and without serrated blades. The results demonstrate a peak noise reduction of up to 6 dB.

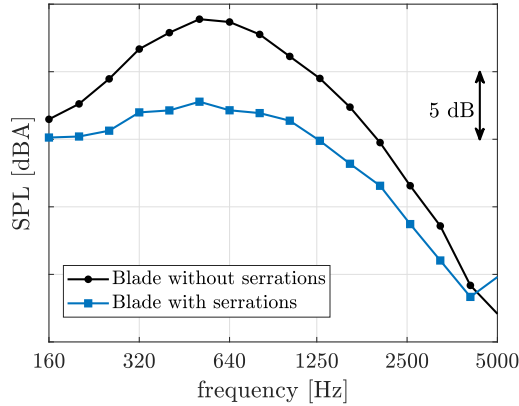


Figure 2.11: Example of noise spectrum measured for a wind turbine with and without serrated add-ons installed on the blades. Data is extracted from the work of Oerlemans et al. [8].

To exemplify the working principle of serrations, Figure shows the $k_3 = 0$ wavenumber interacting with a sawtooth serrated trailing edge. It is seen that, on the edges of the serrations, positive and negative acoustic scattering happens. The coexistence of positive and negative scattering reduces the efficiency of the scattering for this particular wavenumber. On the other hand, other wavenumbers turn cut-on modes, such as the $k_3 = \pm k_1 \frac{4h}{\lambda}$ where the wavefronts align with one of the sides of the sawtooth serration. These modes, however, are excited with lower intensity by the turbulent boundary layer. The combined effect points to a significant noise reduction from the serrated trailing-edge geometry when compared to the straight trailing-edge one.

The following subsections detail the modelling, prediction, and main findings regarding the noise reduction obtained by serrated trailing edges.

2.5.1 MODELLING OF SERRATED TRAILING-EDGE NOISE

Predictive models of serrated trailing edge noise date back to 1991, when Howe proposed models for sinusoidal and sawtooth serrated trailing edges [10, 20]. The solution is based on assumptions for high frequencies, where the aerodynamic wavelengths are smaller than the airfoil chord and the serration dimension. From that assumption, the Green's function for the scattering at a semi-infinite slanted trailing edge is used to first derive a solution for the noise reduction obtained by sinusoidal [10], and sawtooth [20] trailing edges.

The analytical equation obtained for the noise reduction for sawtooth trailing edges is shown in equation 2.52. The equation is based on the turbulent wall-pressure wavenumber spectrum of Chase [61], where $\epsilon \approx 1.33$. The procedures

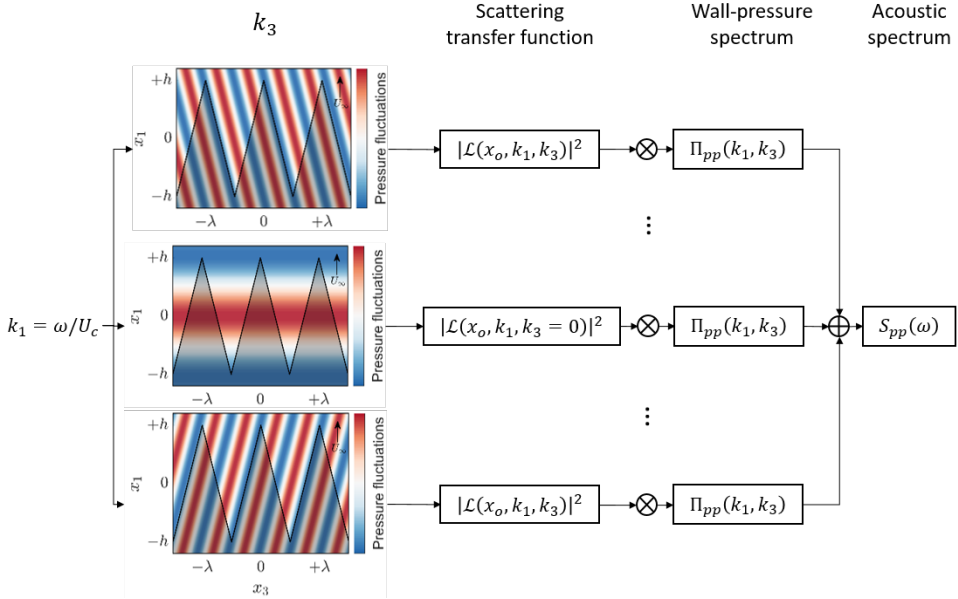


Figure 2.12: Representation of the process of predicting the acoustic spectrum of a serrated trailing edge. The resulting acoustic spectrum is dependent on an integral of all wavenumbers or a sum of the dominant cut-on wavenumbers.

of obtaining this solution are not shown as the simplifications differ from the established methodology of Amiet [27] for straight trailing edges. Nevertheless, this solution is a seminal one in the work of serrated trailing edges and its simplicity has proven useful to demonstrate trends and design guidelines for noise mitigation.

$$\frac{S_{pp,Serr}}{S_{pp,STE}}(\omega) = \frac{\left(\frac{\omega\delta}{U_c}\right)^2 + \epsilon^2}{\left(\frac{\omega\delta}{U_c}\right)^2 \left[1 + 4\left(\frac{2h}{\lambda}\right)^2\right] + \epsilon^2} \dots \quad (2.52)$$

$$\left[1 + \frac{16\left(\frac{2h}{\lambda}\right)^3 \left(\frac{\delta}{2h}\right) \left(\frac{\omega\delta}{U_c}\right)^2 \left\{ \cosh\left[\frac{\lambda}{2\delta} \sqrt{\left(\frac{\omega\delta}{U_c}\right)^2 + \epsilon^2}\right] - \cos\left(\frac{\omega 2h}{U_c}\right)\right\}}{\sqrt{\left(\frac{\omega\delta}{U_c}\right)^2 + \epsilon^2} \left\{ \left(\frac{\omega\delta}{U_c}\right)^2 \left[1 + 4\left(\frac{2h}{\lambda}\right)^2\right] + \epsilon^2\right\} \sinh\left[\frac{\lambda}{2\delta} \sqrt{\left(\frac{\omega\delta}{U_c}\right)^2 + \epsilon^2}\right]} \right]$$

Figure 2.13 shows, in black, the typical noise reduction spectrum obtained by a serrated trailing-edge design. From the figure, it is possible to observe that the noise reduction spectrum is negligible at very low frequencies. This happens for aerodynamic wavelengths that are much larger than the serration dimensions, i.e. $\frac{U_c}{f} \gg 2h$. At such conditions, the amplitude of the serration is much smaller than

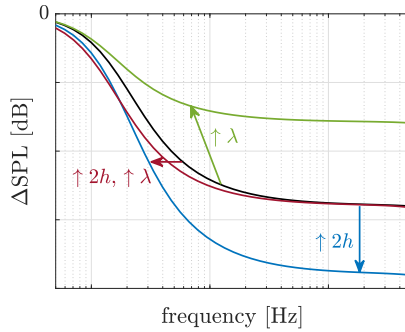


Figure 2.13: Example predicted variation of the noise reduction depending on the serration dimensions. The predictions are obtained with the rapid method from Lyu and Ayton 2020 [22]. The black line represents the reference noise reduction while the other lines illustrate the effect of different modifications of the serration geometry. Negative values of ΔSPL indicate noise reduction.

the incoming fluctuations, and no significant noise reduction is achieved. Within a certain range of frequencies, the serrations promote an increasing noise reduction, finally reaching an asymptotic noise reduction level for higher frequencies. It is important to mention that all analytical predictions so far [20–22, 62] have demonstrated this same behaviour, although at different levels.

The model of Howe [20] allows for a better analysis of the noise reduction trends. For example, it gives important information regarding the shape and scaling of the noise reduction spectrum. The equation 2.52 depends on two non-dimensional frequencies ($\frac{\omega\delta}{U_c}$, and $\frac{\omega 2h}{U_c}$). The latter is only associated with an oscillatory cosine term and promotes oscillations on the curve. This means that the spectrum of the serration noise reduction mostly scales with the non-dimensional frequency (Strouhal number) based on the boundary-layer thickness and flow speed, similar to what is observed for the turbulent boundary layer trailing-edge noise spectrum.

A second analysis that can be achieved from Howe’s model is the asymptotic maximum noise reduction levels. By taking the limit of $\omega \rightarrow +\infty$, an estimation of the maximum noise reduction achieved can be created. The limit causes the second term inside the parenthesis of equation 2.52 to vanish, resulting in equation 2.53 changed to decibel scaling for direct interpretation. This equation indicates that the maximum noise reduction is only a function of the serration aspect ratio ($\frac{2h}{\lambda}$). The higher the serration aspect ratio is, the higher the noise reduction achieved. This can be observed when comparing the black line in Figure 2.13 with the blue one. By increasing the serration height without changing its wavelength, the asymptotic noise reduction obtained is improved.

$$\Delta\text{SPL}_{\max} \approx -10 \log_{10} \left[1 + 4 \left(\frac{2h}{\lambda} \right)^2 \right]. \quad (2.53)$$

2

A final analysis can be made by estimating the frequency region where noise reduction reaches its asymptotic value. A cut-on frequency can be defined in which the noise reduction is half (+3dB) the asymptotic noise reduction, i.e.

$$\frac{S_{pp,\text{Serr}}}{S_{pp,\text{STE}}}(f_{\text{cut-on}}) = 2 \left(\frac{1}{1 + 4 \left(\frac{2h}{\lambda} \right)^2} \right), \quad (2.54)$$

by again considering high enough non-dimensional frequencies ($\frac{\omega\delta}{U_c} \gg \epsilon$), and serration aspect ratios ($\frac{2h}{\lambda} \gg \epsilon$), a simple estimation for this cut-on frequency is obtained according to equation 2.55. Here, the cut-on frequency is only dependent on the flow speed and the serration wavelength (λ). This indicates that, by modifying the serration wavelength, one can tune the serrations for reducing noise at different frequencies. This effect can be observed when comparing the black and red curves in Figure 2.13, where an increase of serration wavelength affects the frequency where noise reduction starts.

$$f_{\text{cut-on}} = \frac{2}{\pi} \frac{U_c}{\lambda}. \quad (2.55)$$

A fully analytical solution of equation 2.2 with boundary conditions for a periodic varying trailing edge is due to Ayton [21]. In the work, the problem, formulated as the 3D-Helmholtz equation, is solved with a Wiener-Hopf method. The general solution is obtained in the form of equation 2.56, where L represents again the transfer function between the intensity of the aerodynamic wall-pressure fluctuations in a particular wavenumber and the acoustic pressure at the observer location. It is important to point out that the radiation term shown in the equation of Amiet is also included inside the transfer function. The procedure of calculating this integral is illustrated in Figure 2.12.

$$S_{pp,\text{Serr}}(\omega) = \int_{-\infty}^{+\infty} |L(\omega, K, k_1, k_3, \mathbf{x}_o)|^2 \Pi_{pp}(\omega, k_1 = \omega/U_c, k_3) dk_3. \quad (2.56)$$

This solution, however, is not convenient for numerical implementation as the terms in the transfer function also require multiple integrations, yielding a computationally expensive procedure. The work of Lyu & Ayton [22] has produced an efficient approximation of this equation by summing only the cut-on modes, i.e. the ones where the wavelength is proportional to the serration dimension ($k_3 = n \frac{2\pi}{\lambda}$), yielding equation 2.57.

$$S_{pp, \text{Serr}}(\omega) = \sum_{n=-\infty}^{+\infty} \left| L \left(\omega, K, k_1 = \frac{\omega}{U_c}, k_3 = n \frac{2\pi}{\lambda}, \mathbf{x}_o \right) \right|^2 \Pi_{pp}(\omega, k_1 = \omega/U_c, k_3) dk_3. \quad (2.57)$$

The transfer function for this equation is given by 2.58, where $g(x_3)$ is the function that describes the serration geometry and has a maximum value of $+h$, and minimum one of $-h$. In the equation, θ_o is the elevation angle between the observer and the source, r_o is the distance to the observer, and $\bar{k}_1 = h(k_1 + (KM - k_1M^2))/\beta$.

$$L(\omega, K, k_1, k_3, \mathbf{x}_o) = \frac{1}{2\sqrt{\pi r_o}} \sin\left(\frac{\theta_o}{2}\right) \frac{\sqrt{-\bar{k}_1 - \bar{k}}}{\bar{k}_1 - \bar{k} \cos \theta_o} \int_0^\lambda e^{-i2n\pi \frac{x_3}{\lambda}} e^{i(\bar{k}_1 + k_3 \lambda g(x_3))} \frac{dx_3}{\lambda}. \quad (2.58)$$

To summarize, the following conclusions can be extracted from the methods discussed before:

- Serrations reduce noise by reducing the scattering efficiency of the stream-wise oriented wall-pressure fluctuations. These fluctuations are the ones that carry the highest energy on a turbulent boundary layer, and the ones responsible for the noise from straight trailing edges. By creating a non-orthogonal angle between the trailing-edge and these fluctuations the scattering is weakened and the noise reduced;
- The process of computing the noise from serrated trailing-edges involves the sum of the squared scattering transfer functions of all cut-on modes multiplied by the energy excited due to the turbulent flow for these modes. This process is based on the uncorrelated sum of the modes, as any phase interaction between the modes is neglected;
- According to the acoustic scattering theory, the noise reduction spectrum from serrated trailing edges is different from zero only after a certain frequency, where the aerodynamic wavelengths are comparable to the serration height ($U_c/f \sim 2h$). This noise reduction increases until it reaches an asymptotic value for high frequencies;
- The noise reduction spectrum scales in frequency (f) directly with the boundary-layer thickness (δ) and inversely with the convective flow speed U_c . A Strouhal number $St = \frac{f\delta}{U_c}$ can be used to describe the spectrum of noise reduction under different speeds and turbulent scales. The maximum noise reduction level (ΔSPL) is independent of the incoming flow conditions and scales mostly with the serration aspect ratio ($\frac{2h}{\lambda}$).

Having described the theory and basic properties of the noise scattered from trailing edges and its suppression by the use of serrations, the next sections focus on the insights that the theory provides for the design of trailing-edge serrations for broadband noise reduction.

2

2.5.2 IMPACT OF THE SERRATION GEOMETRY

The design of trailing-edge serrations is described by its periodic shape geometry, serration wavelength (λ), and serration root-to-tip height ($2h$). Different designs have been tested and used for serrations, and some works have discussed the impact of the serration geometry on the noise reduction obtained [63–65]. The following paragraphs describe some of the results from the analytical models regarding modifications of the serration geometry ($2h/\delta$, and λ/δ).

Effect of varying the serration height (constant λ): Following the works of [20, 64], increasing the serration aspect ratio ($2h/\lambda$) yields an improvement of the asymptotic noise reduction from the serrations (as depicted in equation 2.52). Also, according to the scattering models, changes in the serration height do not affect the frequency range where noise reduction happens (equation 2.55). This is shown in the blue line of Figure 2.13 where the modification of height only impacts the asymptotic predicted value of the noise reduction, without altering the frequency in which this value starts.

Effect of varying the serration wavelength (constant $2h$): Similar to the serration height, analytical scattering models predict that, by decreasing the serration wavelength, a higher asymptotic level of noise reduction is to be expected [64]. However, the serration wavelength influences the frequency at which the noise reduction reaches its asymptotic value, following equation 2.55. Therefore, the analytical methods suggest that the higher the serration wavelength the lower the noise reduction obtained is. Also, by doing that, the frequency where noise reduction starts is reduced, as illustrated by the green line in Figure 2.13.

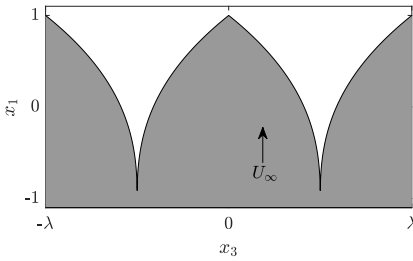
Effect of varying the serration scale (constant $2h/\lambda$): The serration scale ($2h/\delta$, or λ/δ) defines the frequency range where noise reduction starts. By increasing the serration height ($2h$), and wavelength (λ) while keeping $2h/\lambda$ constant, the noise reduction obtained is not expected to change but the frequency where the asymptotic noise reduction starts is lowered. This is illustrated by the red line in Figure 2.13, and indicates that the scaling of the serration can be tuned according to the desired frequency range where noise reduction is intended.

Effect of varying the serration geometry: The geometry of the serration is a way of modifying the shape of the noise reduction spectrum, many works have been dedicated to studying different serration geometries, including concave [16, 64], and combed-sawtooth [17, 65, 66]. It is important to mention that analytical noise reduction predictions are even with respect to the serration geometry. This means that the absolute value of $|L|^2$ is the same for a geometry $g(x_3)$, and $-g(x_3)$ ($|L(g(x_3))|^2 = |L(-g(x_3))|^2$). Therefore, according to the theory, serrations of a certain shape have the same noise reduction as their opposing geometry. This is illustrated in Figure 2.14 where two different pairs of serrations with the same noise (a, and b, and c, and d). However, it is very interesting to observe that serrations (a), and (c) are the ones described in [16, 17, 66] while (b), and (d) do not demonstrate practical applications. Kholodov et al. [63, 64] have explored the analytical optimization of the serration geometry. Both works have observed sawtooth-like shapes as optimal. This result was only not observed when dealing with boundary-layer scales outside the optimal range suggested in Gruber et al. [11]. For these cases, a concave-shaped serration (called Ogee-shape) performs slightly better. Therefore, many open questions still exist regarding the importance of the serration geometry, and whether an optimal geometry exists. For example, contrarily to what is predicted by the models, sawtooth serrations have shown to be outperformed by other geometries, such as concave serrations and combed-sawtooth serrations. Also, significant differences are observed between complementary serration geometries.

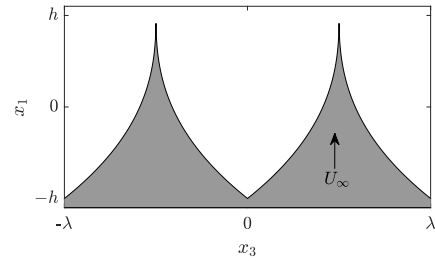
Table 2.5 summarizes the expected effects that changes in the serration sizes have on the maximum noise reduction and on the cut-on frequency of the noise reduction spectrum.

Design parameter	Maximum noise reduction	Cut-on frequency
$\uparrow 2h$	\uparrow	=
$\uparrow \lambda$	\downarrow	\downarrow
$\uparrow 2h, \lambda$ ($2h/\lambda$ constant)	=	\downarrow

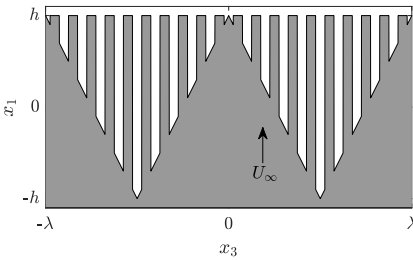
Table 2.5: Influence of the serration design parameters on the acoustic noise reduction obtained from serrated trailing edges.



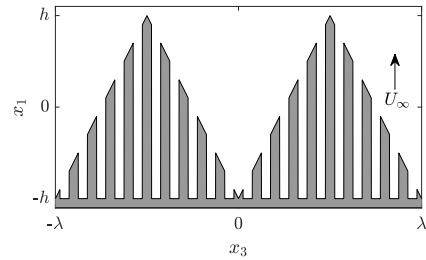
(a) Concave-shaped serrations



(b) Convex-shaped serrations



(c) Combed-sawtooth serrations



(d) Inverted combed-sawtooth serrations

Figure 2.14: Example of two pairs of different serration geometries with equal predicted noise reduction according to [21]. Serrations (a), and (b) have the same predicted noise levels. Similarly, serration geometries (c), and (d) have the same predicted noise levels.

2.6 THE CHALLENGES OF STUDYING THE NOISE FROM SERRATED TRAILING EDGES

Analytical models give important insights into the effects of trailing-edge serrations. However, experimental and numerical evidence have demonstrated big discrepancies with the predictions. Studies report a large discrepancy between the predicted and observed noise reduction levels. As shown in Figure 2.15 the analytical models overestimate the noise reduction by as much as 20 dB in comparison to experiments. The analytical models are only able to describe the frequency where noise reduction starts, and the maximum noise reduction is largely overestimated. Notably, the asymptotic noise reduction predicted by the models was never demonstrated by numerical or experimental evidences. In turn, the noise reduction obtained from serrations reaches a maximum level of noise reduction at a certain frequency and reduces at higher frequencies, with references even demonstrating noise increase

at higher frequencies [11, 67]. The inconsistencies hamper the use of the models for designing trailing-edge serrations and demand the use of computationally expensive numerical methods or dedicated experiments.

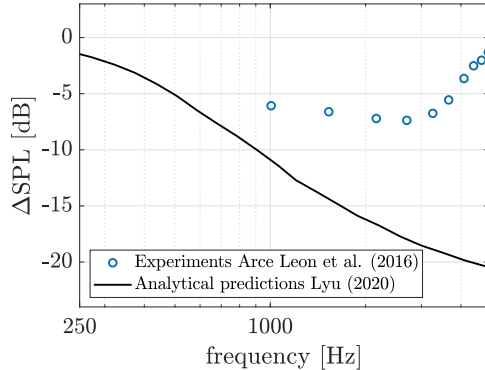


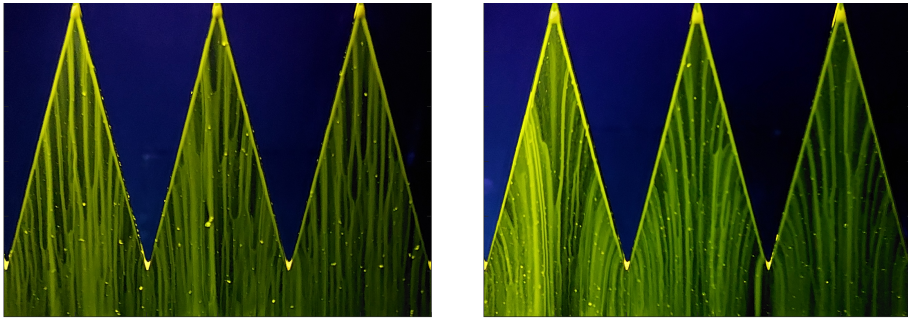
Figure 2.15: Comparison between measurements of the noise reduction obtained with serrated trailing edges from Arce Leon et al. (2016) [67], and predictions shown in the work of Lyu & Ayton (2020) [22].

An experimental parametric study conducted by Gruber et al. [11] has investigated the noise reduction achieved from different sawtooth serration designs. Among the points observed, the most important are:

- The noise reduction spectrum of a serrated trailing-edge design scales with the Strouhal number based on the boundary-layer thickness;
- The increase of noise reduction with increasing aspect ratio is only observed for serrations that are smaller than 2 times the boundary-layer thickness ($\frac{2h}{\delta} > 2$). Above this limit, no increase of noise reduction is observed;
- The large discrepancies between the predicted and measured noise reduction spectrum invalidated the use of the analytical models for the description of the results obtained.

This work has also pointed to the importance that flow modifications in the vicinity of serrations might have on the scattered noise. Theoretical models are based on purely advecting turbulence, known as Taylor's frozen turbulence assumption [68]. By the assumption, the turbulent flow is not modified in the vicinity of the serrations and, independent of serration size or flow condition, turbulence is only transported along the streamwise direction along the trailing edge. Gruber et al. [11] points to vortical formations along the serration edges to indicate that this assumption is unrealistic for serration noise prediction.

The experimental work of Arce Leon et al. [67] has used Particle Image Velocimetry (PIV) measurements to give a first figure of the flow conditions surrounding serrated trailing edges. The work demonstrated that under symmetric conditions, i.e. symmetric airfoil at zero degrees angle of attack ($\alpha = 0^\circ$) and serrations aligned with the airfoil chord, the mean flow and turbulent fluctuations are not significantly modified throughout the serration. However, when serrations are placed at angles to the flow direction, a pressure difference is formed between the upper and lower surface of the serrations, causing it to generate aerodynamic loading and, consequently, leading to the formation of side vortices along the serrations' edges. These side vortices cause first a modification of the mean flow direction, in which the flow is directed outwards on the pressure side and inwards on the suction side. Figure 2.16 shows the mean-flow direction along the serrations using a flow-visualization technique based on an oil tracer. The image demonstrates how the streaklines are distorted outwards for the flow under aerodynamic loading on the pressure side (Figure 2.16b). This secondary-flow formation also affects the turbulence levels surrounding the serrations. Under these conditions, the noise reduction obtained by the serrations highly deteriorates.



(a) Zero incidence

(b) At incidence, on the pressure side

Figure 2.16: Oil-flow visualization of the streaklines over a serrated trailing-edge.(a) shows the visualization obtained for serrations at zero incidence, i.e. without aerodynamic loading. (b) shows the visualization obtained for serrations at incidence, i.e. under aerodynamic loading, viewed from the pressure side.

The same work has first attempted to propose a correction of the analytical models by simply modifying the serration angle according to the one induced by the aerodynamic loading on the pressure side of the serrations. The results have concluded that, although predictions were improved, the simplifications cannot entirely describe the degradation of noise observed at angles of attack.

The work of Chong et al. [12] has measured the wall-pressure fluctuations on the surface of a serration mounted on the walls of a wind tunnel. The results have

demonstrated that the spectrum of the fluctuations is not constant and modify from the root to the tip of the serrations.

The conflicting results between predictions and experimental observations hamper the use of analytical methods for serration design. For example, analytical methods have always predicted maximum noise reduction for high and slender (high serration aspect ratio) serrations. However, experimental results, such as the one of Gruber et al. [11], have shown that this trend is limited to serrations higher than 4 times the boundary-layer thickness, and with wavelengths smaller than 40% of the boundary-layer thickness, i.e. $\frac{2h}{\delta} > 4$, and $\frac{\lambda}{\delta} < 0.4$.

Similarly, the possible optimality of the sawtooth serration geometry differs from some of the concepts being tested and used. In particular, two geometries have shown benefits with respect to sawtooth serrations. These geometries are the concave serrations, and combed-sawtooth serrations, shown in Figures 2.14(a), and (c) respectively. According to the numerical works of Avallone et al. [16, 17], these two geometries improve the noise reduction to the sawtooth geometry by more than 2 dB. The work also discusses how these different geometries interact with the turbulent flow at the trailing edge and infer the scattering properties of such geometries. Avallone et al. [17] demonstrates how combed-sawtooth serrations reduce secondary flow features, sustaining a streamwise oriented flow for further downstream. Besides, both works have pointed to the more intense scattering around the root of the serration at low frequencies. The latter is used to justify the improved performance from concave and combed-sawtooth serrations. In the former, the increased angle at the root reduces the scattering at the root. In the latter, the combs are responsible for moving the scattering region far downstream to the tip, where the wall-pressure fluctuations are less intense.

To summarize, the following inconsistencies and open questions exist in the theory of broadband noise reduction from serrated trailing edges:

- How do the observed alterations of the flow field affect the wall-pressure at the trailing edge?
- What are the underlying physical mechanisms from which the alterations of the flow impact the scattered noise at the trailing edge?
- Is it possible to reliably model and predict the scattered noise from serrated trailing edges?
- How can we use the knowledge of the acoustic and aerodynamic research on serrated trailing edges to design serrations for maximum noise reduction?

The current work intends to answer these questions or to advance towards an answer to them. While the next chapter (Chapter 3) describes the techniques used

for exploring those research questions, the remainder of this work is dedicated to address each of these problems.

3

3

MEASUREMENT TECHNIQUES FOR AEROACOUSTICS

This work has extensively used experimental techniques to assess the acoustic and aerodynamic properties of airfoils with serrated trailing edges. These techniques require dedicated flow facilities and experimental methodologies. In this chapter, a brief summary of these experimental techniques for aeroacoustics is given. For acoustic measurements, the properties of the transducers, and acquisition apparatus are first described. From that, microphone array and beamforming techniques are discussed. Besides, a discussion on the requirements for aeroacoustic measurements in a wind-tunnel facility, including background levels and acoustic condition, is also given. Two aerodynamic measurement techniques explored throughout this work are also described, namely Particle Imaging Velocimetry (PIV), and embedded unsteady pressure (microphone) sensors.

3.1 ACOUSTIC MEASUREMENT TECHNIQUES

Acoustic measurements are meant to assess the far-field emissions from a studied product. For the case of this thesis, the focus is given to measurements of noise emitted at the trailing edge of a 2-D airfoil or flat-plate model. This section describes the type of facilities, equipment, and techniques required for extracting the acoustic quantities required for the remainder of this work. It starts with a brief description of the far-field microphone measurements. A discussion on the expected levels of trailing-edge noise compared to other spurious sources expected during a wind-tunnel campaign follows. After, the properties of aeroacoustic testing facilities are described, ending with a description of microphone-array techniques used in this work.

3.1.1 FAR-FIELD MICROPHONE MEASUREMENTS

Far-field microphone measurements are a standard acoustic assessment technique. Modern measurement techniques rely usually on condenser-type microphone transducers, connected to a digital data acquisition system. The resulting data gathered consists of discrete pressure levels sampled at a determined Sample Rate (SR) for a given time (T_s), resulting in a number of samples $N_s = T_s SR + 1$, and a time discretization of $\Delta t = 1/SR$. The following sections describe the two parts of this system, i.e. the microphone transducer and the data acquisition system.

For inferring the acoustic levels perceived in the measurement location, the root-mean-square of the acquired pressure levels ($\sqrt{\overline{pp}}$) is converted to Overall Sound Pressure Levels (OASPL) following equation 3.1, where the reference pressure ($p_{\text{ref}} = 20 \mu\text{Pa}$) represents the threshold pressure of human hearing.

$$\text{OASPL} = 10 \log_{10} \left(\frac{\overline{pp}}{p_{\text{ref}}^2} \right). \quad (3.1)$$

A dedicated analysis of the acoustic content relies on the frequency spectrum decomposition of the pressure levels. When considering statistically stationary sources, this procedure can be carried with the Welch's method (equation 3.2), which takes the average fast-Fourier-transform (FFT) of chunks of N_{block} data points ($P_{i,\text{fft}}$). The resulting autospectrum of the microphone shows the energy density content (usually shown in Pa^2/Hz or $\text{Pa}^2 \cdot \text{s}/\text{rad}$) at a frequency band defined by $\frac{SR}{N_{\text{block}}}$ Hz. For the Fourier transform, a windowing function is applied, standard a Hanning window, to avoid the lack of periodicity induced by the truncated block size. The Hanning function affects the final spectral levels and a correction factor of $\frac{8}{3}$ must be applied to the data due to the spectral leak of the function. It is valid to point out that this correction factor is based on the assumption of broadband data. The correction factor must be altered to 4 when considering only tonal components, indicating a difference of 1.8 dB between the two considerations.

$$\overline{PP^*}(f) = \frac{8}{3} \frac{1}{N_{\text{average}} \Delta f} \sum_{i=1}^{N_{\text{average}}} P_{i,\text{fft}}(f) P_{i,\text{fft}}^*(f). \quad (3.2)$$

Further processing of the data, can include conversion to Sound Pressure Level by multiplying the spectral density by the frequency discretization, following equation 3.3. Another standard practice in acoustics is the spectral representation in octave scales (octave, third-octave, or twelfth-octave). This is obtained from the Welch's output by integrating the energy spectral density between the lower and upper frequency of each band.

$$\text{SPL}(f) = 10 \log_{10} \left(\frac{\overline{PP^*}(f) \cdot \Delta f}{p_{\text{ref}}^2} \right). \quad (3.3)$$

MICROPHONE TRANSDUCERS

Microphone transducers convert acoustic pressure fluctuations into electrical voltage ones. The transducers most commonly used for acoustic applications are condenser-type microphones, i.e. operated by fluctuations of capacitance given by a moving charged membrane inside the microphone capsule. This changing capacitance is usually conditioned to create the fluctuating voltage output required from the analog-to-digital converters (ADC) from the data acquisition system. The mechanical components and electrical conditioning of the microphones are exemplified in Figure 3.1.

All the mechanical components are packed inside the microphone capsules with the pre-conditioning system also integrated. Three external connections are required, i.e. the common ground voltage *gnd*, the external voltage that feeds the circuit (V_s), and the output voltage (V_o) that is read by the acquisition system. Apart from the possibility of conditioning illustrated in a, there are a second type

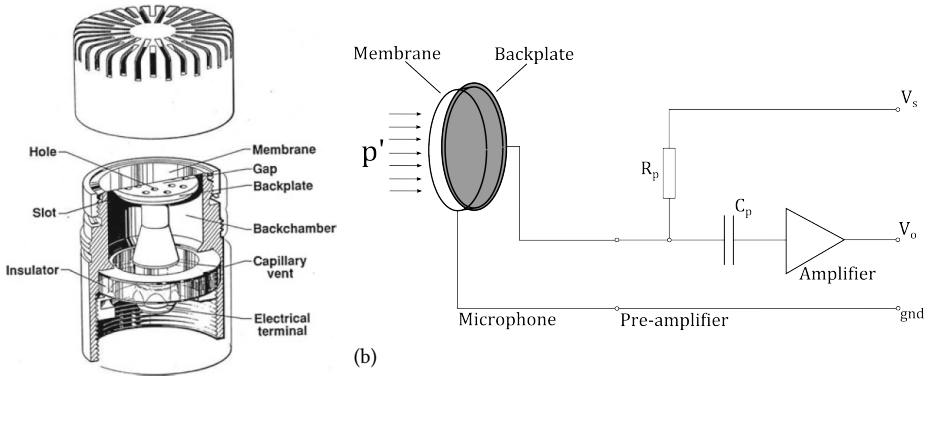


Figure 3.1: Cut-view of a B&K Type 4126 microphone [69] (a) and simplified electrical conditioning system for a non-polarized microphone.

that can be used, called pre-polarized microphones. This conditioning is based on the Integral Electronics Piezo-Electric (IEPE) standard and do not require a supply voltage input. These type of transducers allow for an easier connection since a coaxial cable can be used to connect the transducer directly to the acquisition system. This operation, however, requires dedicated acquisition systems, that operate in constant current mode (around 4 mA), to provide the necessary supply for pre-polarization and for the conditioning systems. Pre-polarized microphones are the standard practices for high-end acoustic measurements combined with the Transducer Electronic Data Sheet (TEDS) standard, which provides means for direct calibration and reading of the microphone data. The absence of the external supply cable is also beneficial for microphone-array applications, where the extra cables required between each microphone and the power supply are eliminated.

An important parameter of the microphone is its sensitivity (S) defined as the ratio between the output voltage V_o in the acquisition system and the input pressure on the microphone, given in mV/Pa. This quantity is dependent on the mechanical assembly of the microphone and the characteristics of the conditioning circuit. The higher the sensitivity the larger the signal obtained for the same acoustic input. Together with the sensitivity, microphones are also differentiated by their cut-on and cut-off frequencies, i.e. the range of frequencies where the response function of the microphone is linear and the sensitivity S is constant.

Figure 3.1 shows some properties of the basic mechanical and electrical system of the microphones. The first part of the mechanical design of a microphone is the sensitive membrane. The lower the mass and rigidity of the system, the higher the cut-off frequency (natural frequency of the mass-spring system), and

the amplitude of the signal. Nevertheless, the limited displacement, distortions, and plastic deformation of the membrane pose a mechanical end to the maximum pressure that can be measured, this is known as the microphone's upper dynamic range limit. Therefore, a trade-off exists between increasing sensitivity and reducing the upper dynamic range of pressures that can be measured.

Another important part of the microphone design is the vent and backplate. The vent equalizes the mean pressure inside the microphone which contacts with the membrane through the holes of the backplate. This is required as acoustic fluctuations are multiple orders of magnitude lower than fluctuations of the ambient pressure. Therefore, microphones are designed to be sensitive only to fluctuations of pressure above certain frequencies (usually 20 Hz) and not to absolute levels. The vents and holes in the backplate represent a mechanical high-pass filter, meant to equalize the ambient pressure. These vents must be designed to filter the acoustic fluctuations inside the microphone capsule, such that only the outside pressure fluctuations influence the membrane displacement. Microphones can have different vent configurations depending on the application. Side and back-vents are most common for far-field measurements, while front-vents are used for wall-mounted microphones, where the walls block the access for pressure equalization from the sides or back.

Electronically, the condenser microphones can be assimilated as non-ideal capacitors. The conditioning of non-polarized microphones consists of a filter and an amplification of the signal, as shown in Figure 3.1b. By amplifying the signal before it passes through the cables, the Signal to Noise Ratio (SNR) is increased. The microphone's internal noise and cabling, together with the internal friction of the membrane, determine the lower limit for microphone measurements, known as the lower dynamic range limit.

This description is valid for the so-called pressure-field microphones, in which the presence of the microphone won't affect the pressure field, e.g. wall-mounted microphones. Other applications require slightly different microphones. For example, far-field microphones are designed to have a response function that is carefully adjusted to compensate for the effect of high-frequency waves interacting with the microphone body itself, i.e. for frequencies above c_o/l_{mic} , where l_{mic} represents the length of the microphone. This correction is made through a tailored conditioning system that is adjusted for each microphone design.

Random-incidence microphones follow the same application as free-field microphones but are designed to reproduce the levels observed on a standard random incidence field, i.e. highly reverberating environments. Figure 3.2 exemplifies the three different applications of each microphone type. Throughout this work, far-field microphones are selected for assessing the acoustic emissions of the models and pressure microphones for the wall-pressure measurements.

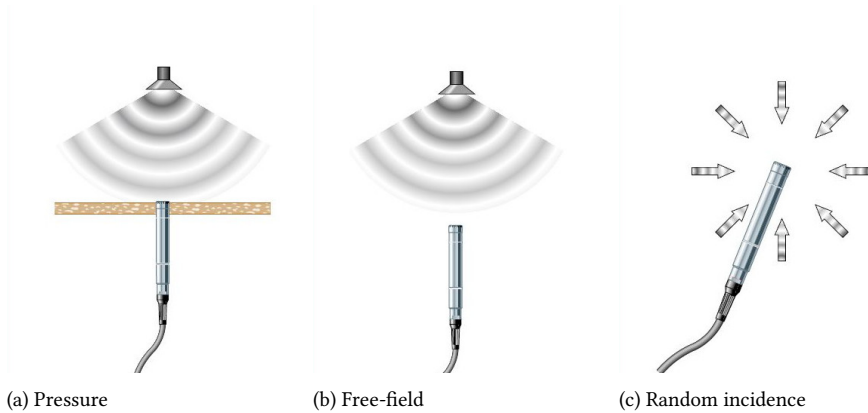


Figure 3.2: Different types of microphones and acoustic fields to each they are designed for. Images taken from G.R.A.S. sound and vibration website [70].

DATA ACQUISITION SYSTEMS

Digital data acquisition has greatly revolutionized measurement techniques, including acoustic ones. Its principle is based on sampling voltage differential in the input terminals, converting this voltage into digital format, and storing it. Four elements are of importance in this process: the preconditioning, the conversion, the clock, and the triggering.

Analog-to-digital converters (ADC) are based on the conversion of a signal with a certain maximum input voltage (commonly $V_{\text{ADC,max}} \pm 5$, ± 10 , or ± 20 V) into a digital signal with n_b bits of precision at a certain maximum sample rate (SR). This indicates that the digital signal has a minimum precision in the voltage conversion ($V_{\text{ADC,min}}$) given by equation 3.4. The higher the precision of the conversion, the lower the signal that the ADC is able to capture. On the other hand, ADCs are expensive and sensitive components and the price of the acquisition system is usually driven by the number and precision of the ADCs used. This is the reason why simpler acquisition systems of multiple channels commonly employ a single ADC with multiplexing of the channels instead of dedicated ADCs per channel. The latter configuration is reserved for sound & vibration types of acquisition boards, such as PXIe-4497, and 4499, LAN-XI 3053, and GBM Viper. These are some of the few options that are suitable for acoustic array applications, where data from multiple channels must be acquired synchronously.

$$V_{\text{ADC,min}} = \frac{2V_{\text{ADC,max}}}{2^{n_b} - 1}. \quad (3.4)$$

Preconditioning of the signal refers to any analog amplification or filtering of the signal before conversion. Signal amplification is beneficial for improving

the precision of the converted data. Since the regular ADC has a maximum input voltage and a minimum discrete voltage, amplification intends to adjust the range of the input signal to maximize the data resolution. This is carried out with a high-pass filtering to remove the steady level of the signal, usually of much higher magnitude than the fluctuations that the measurements are intended to capture. Acquisition systems such as the Viper 1.0 uses a variable gain system coupled with 16-bits ADCs to enhance measurement quality. Other systems, such as the PXIe-4499 give the option of 4 gains (offered as a variable voltage range ± 10 V, ± 3.16 V, ± 1 V, and ± 0.316 V) combined with a 24-bits ADCs. A second pre-conditioning of extreme importance for acoustic measurements is anti-aliasing filtering. This refers to the filtering of the signal for frequency contents above the sampled frequencies (Nyquist range $> SR/2$). This is a necessary step for acoustic measurements as undersampled high-frequency content leak into the spectrum of lower frequencies and affect the measurements, in a process referred to as aliasing.

Clock and triggering are required processes for data acquisition. The first refers to a series of pulse signals used to control the time instants of data acquisition, while the second refers to the signal that determines the starting moment of acquisition. These two processes are commonly taken as background ones for applications with single sensors but are keen for the synchronous acquisition of data. Data from multiple sensors are only considered synchronous if the clock and triggering signals are exactly the same for all the channels acquired.

The importance of considering this can be illustrated by the application of microphone array measurements. Available acquisition systems, such as the PXIe one, use a single clock signal for the whole chassis but individual triggering signals per acquisition board. Since each board can only acquire a maximum of 16 microphones (PXIe-4497 or 4499), applications with more than 16 microphones must specify that triggering signals come from a single source. In a more complex scenario, if multiple PXIe chassis are required during the measurements, the clock signal must also be communicated between the chassis.

3.1.2 MICROPHONE-ARRAY TECHNIQUES

The use of microphone arrays has emerged due to the fundamental benefits it provides to aeroacoustic testing. The concept is based on using multiple microphones at different locations to spatially filter the sources of noise coming from a desired point in space. This spatial filter is the most fundamental part of the microphone array technique that appeals to aeroacoustic experiments as sources from the desired Region of Interest (ROI) can be separated from other sources of noise such as wind-tunnel background sources and even secondary sources from the airfoil. Besides, for use on wall-mounted closed-test-section wind tunnels, microphone arrays can be a necessity as the turbulent boundary layer over the wall-mounted

microphones creates pressure fluctuations on the microphone location that are higher than the acoustic ones from the measured model.

The microphone-array technique is based on the time delay, or the phase in the frequency domain, between different microphones. Figure 3.3 illustrates the acoustic field from a single source on multiple microphones. By assuming the propagation path from an acoustic source, the information on the microphones can be used to locate these sources.

3

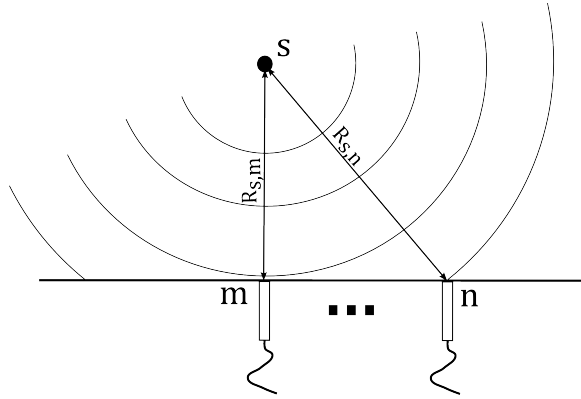


Figure 3.3: Illustration of the acoustic field created by a punctual monopole source at a distance R_s from an array of microphones.

A simple example of this processing is the delay-and-sum beamforming technique [71]. By assuming a source on a point \mathbf{x}_s , a microphone m at location $\mathbf{y}_{\text{mic},m}$, and a spherical propagation model (monopole source), the time delay between the generated sound at the source and the noise perceived by the microphone is given by equation 3.5, where $R_{s,m} = |\mathbf{x}_s - \mathbf{y}_{\text{mic},i}|$.

$$\tau_{s,m} = \frac{R_{s,m}}{c_0}. \quad (3.5)$$

For a monopole source, the relation between the pressure fluctuation caused by the source on a determined distance from the source (R_{ref}) and the one measured is given by equation 3.6. By having two microphones (m , and n), the reference sound pressure level can be estimated according to equation 3.7. The integral in the equation corresponds to the cross-correlation between the two microphones with a time delay $\Delta\tau_{s,ij} = \tau_{s,m} - \tau_{s,n}$, hereby referred to as $\overline{p p}_{mn}(\Delta\tau_{s,mn})$.

$$p_{\text{mic},m}(\mathbf{y}_{\text{mic},m}, t + \tau_{s,m}) = \frac{R_{\text{ref}}}{R_{s,m}} p_s(\mathbf{x}_s, t). \quad (3.6)$$

$$\overline{pp}_s = \frac{(R_{s,m} \cdot R_{s,n})}{R_{\text{ref}}^2} \frac{1}{T} \int_0^T p_{\text{mic},m}(\mathbf{y}_{\text{mic},m}, t + \tau_{s,i}) p_{\text{mic},n}(\mathbf{y}_{\text{mic},n}, t + \tau_{s,n}) dt. \quad (3.7)$$

In the process, the time delay is the essence of the technique as it allows for steering the measurement towards different source locations in space. Having multiple microphones is therefore required to create a non-unique time delay between microphones ($\Delta\tau_{s,mn}$). The same process for a single microphone measurement would give a null time delay for every spatial position, therefore not being able to differentiate the sources.

Still, by using only 2 microphones several positions over the space could result in the same time delay, as long as equation 3.5 produce the same $\Delta\tau_{s,mn}$. This means that the delay-and-sum process with 2 microphones is not able to distinguish two sources placed along this equal $\Delta\tau_{s,mn}$ space. An obvious solution to this problem is to measure the acoustic field in more locations and combining this information. By performing measurements with N microphones, this cross-correlation can be carried $\frac{1}{2}(N^2 - N)$ times, excluding auto-correlations and the permutation of the cross-correlations. By averaging the measurements from all of these combinations, an estimation of the sound pressure level can be obtained according to equation 3.8. The use of many microphones reduces the space where all combination of $\Delta\tau_{s,mn}$ is the same, making the spatial filter less conflicting.

$$\overline{pp}_s = \frac{2}{R_{\text{ref}}^2 (N^2 - N)} \sum_{m=1}^N \sum_{n=m+1}^N (R_{s,m} \cdot R_{s,n}) \overline{pp}_{mn}(\Delta\tau_{s,mn}). \quad (3.8)$$

This process requires the use of an array of microphones, based on multiple microphones placed at different locations and measuring simultaneously the same acoustic field. An emphasis is given to the simultaneous since this creates the need for simultaneous acquisition systems, which require dedicated ADCs for each microphone channel, as discussed previously. This requirement of simultaneous information demands dedicated and costly acquisition boards, which, combined with the cost of linear response microphones, contribute to the high cost of microphone arrays.

It is important to mention here that two are the fundamental reasons why microphone-array techniques are used for aeroacoustic research. The first is about finding noise sources on a model with unknown emission properties. In order to do so, a grid of points is defined along the model and the process in equation 3.8 is carried on, creating a contour map of the source level in space. A second use of microphone arrays for aeroacoustics relates to extracting the levels emitted from a defined location of the acoustic field. For example, on a setup for trailing-edge noise measurement of a 2D model, the location of the source is known, but, what is

desired from the microphone array is to extract the noise from a particular location in space, usually a portion of the trailing edge in the model mid span. As will be discussed in section 3.2.3, this is desired to eliminate the secondary and background noise sources from the measurements and to have the noise data in a region of the span where flow conditions are controlled, i.e. the model centre.

This discussion summarizes the importance and fundamentals of microphone array techniques, the following sections explore the current use of microphone arrays for applications in aeroacoustic research. It starts with the classic beamforming formulation (CBF), followed by a description of the Source Power Integration method (SPI), and finalizes with a discussion of the use and limitations of microphone-array techniques.

3

CLASSIC BEAMFORMING

The classic beamforming formulation is based on the application of equation 3.8 in the frequency domain. By doing so, the sound pressure level that a source s produces at the reference location at a certain frequency ($S_{pp}(\mathbf{x}_s, \omega)$) is given by equation 3.9. In the equation, $P_m P_n^*$ represents the cross-spectrum between the two microphone measurements, and $*$ is the Hermitian transpose of p .

$$S_{pp}(\mathbf{x}_s, \omega) = \frac{2}{R_{\text{ref}}^2 (N^2 - N)} \sum_{m=1}^N \sum_{n=m+1}^N (R_{s,m} \cdot R_{s,n}) e^{-i\omega\tau_{s,m}} P_m P_n^* e^{+i\omega\tau_{s,n}}. \quad (3.9)$$

This formulation is usually conveniently presented in a compact version by defining a cross-spectral-matrix (CSM), a $N \times N$ matrix in which the element $C(m, n)$ of the matrix contains the cross-spectrum between microphones m , and n . In this CSM, the elements of the main diagonal, the autospectra of the microphones, must be removed as the lack of phase information on the autospectra contaminates the map, see [72].

The exponential elements can be organized in a row vector, known as the steering vector (SV), where each element m corresponds to the phase delay and attenuation expected between the source and the microphone m , as shown in equation 3.10. The steering vector shown here follows formulation II from the work of Sarradj [73]. Note that the factor 2 from equation 3.9 is missed since this version includes the sum of the permutation of both cross-spectra, i.e. $P_m P_n^*$, and $P_n P_m^*$.

$$\mathbf{v}_m = \frac{R_{s,m}}{R_{\text{ref}} \sqrt{N^2 - N}} e^{-i\omega \frac{R_{s,m}}{c_0}}. \quad (3.10)$$

From these definitions, the beamforming process for a given source location and frequency reduces to equation 3.11. This is known as the frequency domain classical beamforming formulation.

$$S_{pp}(\mathbf{x}_s, \omega) = \mathbf{v} \cdot \mathbf{C} \cdot \mathbf{v}^* \quad (3.11)$$

As discussed before, beamforming provides a tool to spatially filter the noise levels at a given location. Nevertheless, this process is not perfect and two effects must be regarded when designing and operating a microphone array, these are the effects of the array beamwidth (BW) and the sidelobes (SL). The first has to do with the fact that the spatial filter is not perfect, i.e. if a source exists in the proximity of the focus point of the array, the calculated noise level might be affected by this source. One example can be seen by the beamforming source maps (frequently called beamforming maps) of a punctual source in Figure 3.4 at different frequencies for 3 different array designs. As it can be observed, the maps do not represent a punctual source but they rather show a continuous decrease of levels in the surroundings of the source location, where the noise peak is captured. The beamwidth (BW) is defined as the distance from this peak in which the estimated level is 3 dB lower than the peak level. From the figure, the lower the frequency is, the larger the beamwidth is as the phase difference between the microphones is smaller. According to Malgoezar et al. [74], the array beamwidth for a planar circular array can be related to the array design by equation 3.12, where d represents the distance from the source to the centre of the array, and D is the array diameter. It is interesting to observe here that the number of microphone or the organization of the microphones does not modify the beamwidth, but only the array diameter and proximity to the source do. Therefore, the first criterion for array design is specified, i.e. the size and distance from the source of the array must be such to meet the desired beamwidth for the lowest frequency that is to be analysed. The different array designs between Figure 3.4a-c (first row) and Figure 3.4e-g (second row) illustrate this phenomenon. The first line shows an array of 1.0 m diameter, while the second line shows an array of 2.0 m diameter. It is clear from the graphs how the beamwidth is reduced for the array with a larger diameter.

$$BW \approx 7.7 \frac{c_o}{\omega} \frac{d}{D} \quad (3.12)$$

A second important effect is the array sidelobes caused by regions where a similar phase shift is expected. As discussed for the two microphones arrangement, different positions of the field could have similar phase delays meaning that, if a source exists in one of these locations, the beamforming process will also predict high levels in the other ones. This can be observed in Figure 3.4 for high frequencies, where the source at the centre causes some secondary peaks in other regions. These sources are obviously non-existing and, depending on the measurement environment, can be misinterpreted as real ones. As discussed previously, a solution to this issue is to increase the number of microphones, therefore decreasing the

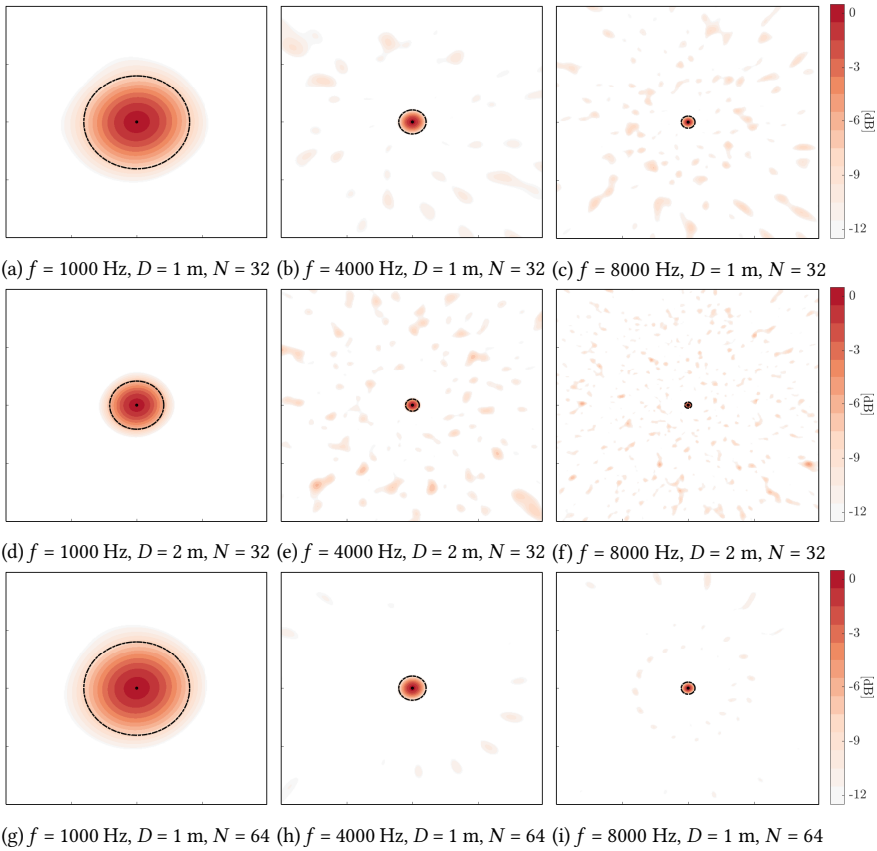


Figure 3.4: Acoustic source maps obtained at three different frequencies ($f = 1000, 4000,$ and 8000 Hz) for a monopole source at the centre of the map using three different array designs. a-c shows the source maps for an array with 1.0 m array diameter (D), and 32 microphones (N). d-f shows the source maps for an array with 2.0 m array diameter (D), and 32 microphones (N). g-i shows the source maps for an array with 1.0 m array diameter (D), and 64 microphones (N). Black dashed lines shows the expected beamwidth using equation 3.12.

presence and intensity of these sidelobes. This can be observed by the difference between the array design in Figure 3.4a-c (first row), and Figure 3.4g-i (third and last row). The latter array design has the double number of microphones and the sidelobes from the graphs are greatly reduced. Also, the disposition of the microphones can be optimized. Since adding more microphones have an important cost implication, several ways have been explored to improve the design of the array [75–77]. Typical design choices discussed are modified Archimedean spirals and random microphone locations.

The results from Figure 3.4 represent the so-called Point Spread Function (*PSF*)

of an acoustic array, defined as the acoustic map produced by an array due to a unitary point source. Although the shapes of the maps are somewhat dependent on the position of the source, the modifications can be neglected around the centre of the array and considered that the PSF is the same for different source positions. The *PSF* represents the spatial filtering of the microphone array, and a resulting source map can be thought of following equation 3.13. In the equation, the obtained source map ($S_{pp,array}$) is a convolution between the point spread function from the array and the real source distribution ($S_{pp,real}$).

$$S_{pp,array}(\mathbf{x}_s, \omega) = \int PSF(\mathbf{y}_s, \mathbf{x}_s, \omega) S_{pp,real}(\mathbf{y}_s, \omega) d\mathbf{y}. \quad (3.13)$$

SOURCE POWER INTEGRATION (SPI)

The previous section demonstrated how to obtain the sound pressure level from a single source in a determined location. However, when many sources exist in a region or when the determined location of the maximum is unknown, the process is not as simple. Therefore, a way of computing the sources on a Region of Interest (ROI) must be explored. This is important for aeroacoustic sources as some are not exact punctual sources, e.g. trailing-edge noise which can be assimilated as a line of incoherent sources.

Coming back to Figure 3.4, it is clear that integrating the map around the source location yields an overestimation of the source levels since the array beamwidth and sidelobes are also contributing to the integration. Source Power Integration (SPI) is a simple technique to overcome this problem. The technique consists of dividing the integrated level by the equivalent integral that a punctual source at the same position would have, i.e. the integral of the point spread function (*PSF*) at a given location, following equation 3.14. Although a simple technique, this has proven to produce coherent noise predictions as described in the benchmark studies of Sarradj et al. [78].

$$S_{pp}(\omega) = \frac{\iint_{ROI} S_{pp}(\mathbf{x}_s, \omega) dx_1 dx_2}{\iint_{ROI} PSF(\mathbf{x}_s, \omega) dx_1 dx_2}. \quad (3.14)$$

ADVANCED METHODS FOR MICROPHONE ARRAY

Knowing the limitations of the classic beamforming technique, other techniques have emerged attempting to improve beamforming maps or to increase the precision of the source level estimation. Some techniques try to extract a deconvoluted beamforming map from the classic beamforming map. These are the so-called deconvolution approaches. Famous deconvolution approaches are CLEAN-PSF, CLEAN-SC, and DAMAS. Other methods, called inverse methods, attempt to find the source distribution that would produce the measured cross-spectral-matrix. The

appeal of these methods is the incorporation of different acoustic source propagation behaviours, such as coherent sources, in exchange for increased complexity in the post-processing technique.

Other attempts, such as the so-called functional or robust beamforming, consist of modifying the spatial filter procedure [79]. With the method, a way of controlling the filter is given by controlling a power coefficient. This allows for reducing the beamwidth making the method more sensitive to errors or increasing it making the solution more robust for phase errors, source misalignment, or imperfections.

Each of these methods has their advantage and disadvantage and the choice of the most appropriate methods for each application is still an ongoing subject of discussion. Benchmarking activities have shown how no clear consensus exist on best practices for beamforming applications [78]. According to the results, the performance of the classical beamforming with source power integration is satisfactory provided that the signal-to-noise ratio is sufficient to separate the sources integrated.

3.2 ACOUSTIC MEASUREMENTS OF AIRFOIL SELF NOISE

Although the dominating noise source for many applications, airfoil self-noise, and especially turbulent boundary layer trailing-edge noise, is inherently a low-level source of noise at low Mach numbers. This means that measurements of trailing-edge noise require dedicated facilities with very low background levels and controlled incoming turbulence. These facilities are designed to have the maximum signal-to-noise ratio (SNR) between trailing-edge sources and other spurious sources of noise. Having described the measurement techniques that can be used for aeroacoustic measurement, this section explores the sources and levels of airfoil self-noise expected in a 2-D airfoil model in a wind-tunnel environment, and the noise and properties of wind-tunnel facilities, giving a explanation of the process of designing experiments for studying trailing-edge noise.

3.2.1 TRAILING-EDGE NOISE

As described in Chapter 2, the trailing-edge noise scales with the flow speed and the boundary-layer thickness at the trailing edge. The latter can be related to the flow speed as well considering the development of the turbulent boundary layer on a zero pressure gradient condition, following equation 3.15, where c represents the model chord.

$$\delta \approx 0.37 \frac{c^{4/5} \nu^{1/5}}{U_\infty^{1/5}}. \quad (3.15)$$

Combining this equation with equation 2.1 we obtain an scaling of the trailing-edge noise with the free-stream speed with a power of 4.8, with the chord with

a power of 0.8, and with the model span (b) with a the power of 1 (equation 3.16). This equation shows the scaling of the source that we seek to measure. The following sections describe the expected scaling of other spurious sources that can contaminate the measurements.

$$SPL_{TE} \propto 48 \log_{10} U_{\infty} + 8 \log_{10}(c) + 10 \log_{10}(b). \quad (3.16)$$

SECONDARY AIRFOIL NOISE SOURCES

Other airfoil sources also contribute to the measured noise. Understanding and controlling these sources is important in order to get the maximum SNR out of a 2-D airfoil experiment.

The primary source to be discussed is the leading-edge noise due to the scattering of the incoming turbulence on the model leading edge. This source of noise has the same dependency on the model span but it scales with U_{∞}^5 , with the turbulence intensity (TI^2) and with the incoming turbulence scales (L_f). The turbulence levels in a wind tunnel usually can be considered constant with the flow speed. This means that the leading-edge noise scales according to equation 3.17, with no dependency on the airfoil chord, and the free-stream velocity scaling with the power of 5. This suggests that big airfoil chords and lower speeds are preferable for increasing the SNR between trailing-edge noise and turbulence impingement noise. Besides, a low turbulence-intensity environment is desirable for the wind-tunnel facility.

$$SPL_{LE} \propto 50 \log_{10} U_{\infty} + 20 \log_{10} TI + 10 \log_{10}(L_f) + 10 \log_{10}(b). \quad (3.17)$$

Another important secondary source of noise from airfoils comes from the presence of the side walls where the 2-D model is mounted. The interaction between the incoming turbulent boundary layer in the side-plates wall and the model trailing and leading edge is a well-known source of spurious noise. First, the presence of the wall has the effect of doubling (+6 dB) the source in that region. Second, the boundary layer formed along the wind-tunnel walls is significantly thicker than the one formed over the airfoil, and the levels emitted at that region of the model differ from the ones at the model centre. Besides, at high angles of attack, the interaction of the boundary layer with the accelerating flow at the suction side can drastically increase the noise at this region, as observed in experiments with high-lift devices [80]. Here, increasing the model chord is a way of increasing trailing-edge noise SNR because the thicker boundary layer from the airfoil increases the trailing-edge noise while not modifying the one from the side walls. Another important strategy to mitigate this source of noise is to increase the model span. This is due to two

factors: first, the increasing aspect ratio of the model contributes to a more 2-dimensional flow distribution [80] and, second, by increasing the distance between the model centre, where the array measurements are focused, and the side walls, the influence of the noise from the boundaries on the measurements is reduced.

3.2.2 AEROACOUSTIC WIND-TUNNEL FACILITIES

Wind-tunnel experiments are the standard practice for experimental aerodynamic research. The increasing importance of aerodynamic sources of noise has created the demand for wind-tunnel facilities that allow for joint aerodynamic and acoustic assessment of the models. This often translates to reducing the background noise from the wind tunnel and improving the acoustic conditions at the test section to accommodate the acoustic measurement apparatus.

Regarding the last part, three configurations of wind-tunnel test section are commonly explored, i.e. open-jet facilities, closed test-section facilities, and hybrid facilities. The first one takes advantage of the outside-of-flow region in the test section to place the acoustic instrumentation. This gives two advantages: first, the sensors are not exposed to the flow, and second, the outside room can be acoustically isolated, creating a free-field condition (anechoic environment, with minimum reverberation) where acoustic measurements can be carried out. On the other hand, open-jet test sections are known to produce a less controlled aerodynamic field since the jet flow in the section is altered by the presence of the model. Brooks et al. [30] have created corrections that can be applied to the flow over a 2-D airfoil model on an open-jet facility. These corrections, however, are based on a vortex line replacing the airfoil pressure distribution. This means that errors are expected for airfoils with a large chord in comparison to the jet height, thick airfoils, or high circulations, where the expected flow distribution is compromised. Acoustically, the open-jets also present two disadvantages. First, the change in the flow velocity experienced by the acoustic waves travelling from the airfoil model to the microphone transducers causes a variation in the propagation direction from the source to the observer, which must be accounted for. Second, the shear-layer formed along the jet interacts with high-frequency acoustic waves, of similar wavelength to the size of the turbulent eddies, modifying the levels and phase of these waves, in a process called correlation loss.

Closed test section wind tunnels have a known aerodynamic behaviour and have been the standard practice for aerodynamic testing [81]. Wall corrections are well studied [82] and implemented for aerodynamic measurements. Nevertheless, this setup has very disadvantageous conditions for acoustic measurements. From start, the microphones cannot be placed outside the flow. Two options for microphone placement are possible. The first includes the microphone in the flow. This is only possible when nose cones [83] are placed on the microphone, diverting the flow from

impinging directly on the sensing membrane. Nose cones create an aerodynamic-shaped leading edge to the microphone body while a cavity protected by a mesh grid on the side keeps the membrane exposed to the acoustic pressure fluctuations. This cavity, however, affects the acoustic measurements for frequencies above 5.0 kHz [83]. Besides, the structure necessary for placing the microphones in the flow can also generate spurious sources of noise.

A second, and more often used, option is to place pressure-field microphones embedded in the wind-tunnel walls (Figure 3.5b) Still, by doing so, the microphones are exposed to the turbulent flow on top of the walls. This potentially hampers the acoustic measurements as the pressure fluctuations originating from the wind-tunnel's turbulent boundary layer are captured by the microphones. An alternative to that is to place the sensors in a cavity, where the fluctuations from the turbulent boundary layer are dampened at the microphone location. This yields a reduction of more than 10 dB on the measured signal from the turbulent boundary layer [84]. More practically, measurements on closed test section wind tunnels rely on the cross-correlation of synchronous measurements with multiple microphones, where the cross-correlation of microphones at distances above the turbulent length scale of the boundary layer on the walls is used to filter the acoustic signal from the spurious aerodynamic fluctuations. This alternative is the basis of beamforming, as it was explained in Section 3.1.2.

A third option for the design of the test-section attempts at combining the advantages of both facilities by introducing acoustically transparent materials on the wind-tunnel side walls. This concept is called hybrid aeroacoustic test sections (Figure 3.5c) and can be seen in facilities such as the one at Virginia Tech [85] or the Paul La Cour wind tunnel (PLC) in Denmark [86]. This concept creates the region outside the flow field where acoustic measurements can take place while still keeping flow conditions similar to the known ones at closed test-section wind tunnels. The transparent materials chosen are usually stretched Kevlar cloths [86] or perforated steel plates. Corrections of both the acoustic and the aerodynamic field are, however, required as these materials demonstrate acoustic absorption at high frequencies and flow permeability for high pressure gradients between the outside room and the flow field. A particular challenge for these facilities exists for the measurements of high-lift elements, where the extremely high suction peak causes local alterations of the flow penetration, and lower pressure coefficients than the ones achieved with hard-wall measurements [87].

3.2.3 WIND-TUNNELS AND BACKGROUND NOISE

Low-speed wind-tunnel background noise is commonly attributed to the noise from the fans, and motors. Achieving a low background facility comes from two practices: the design for low-noise wind-tunnel fans, and the absorption of this

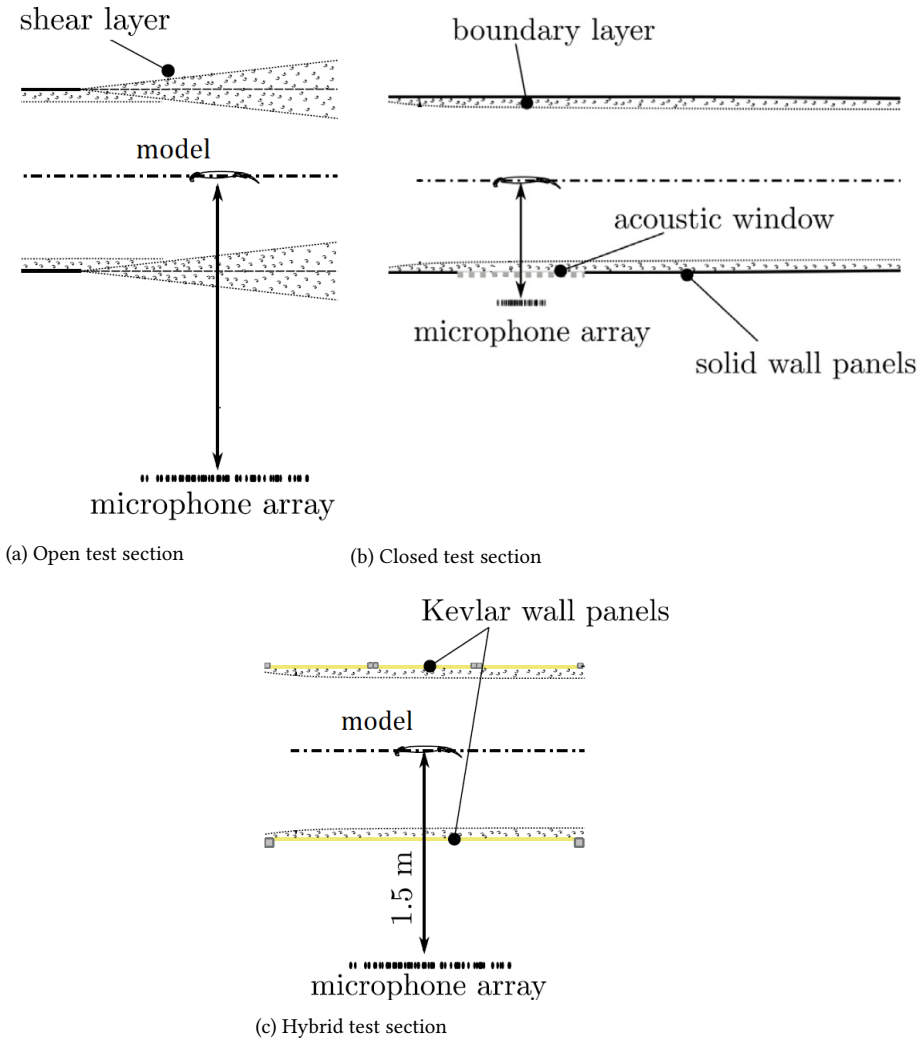


Figure 3.5: Illustration on the differences between the three test sections used for aeroacoustic measurements, i.e. open test sections (a), closed test sections (b), and hybrid test sections (c). Figure is adapted from [87].

noise along the wind-tunnel circuit. For example, low-noise fans have a higher number of blades (higher BPF and lower loading per blade) with possible leading- and trailing-edge sweep or serrations, to reduce scattered noise. On the absorption side, the fans are commonly isolated by acoustic silencers, these silencers can be separated from other parts of the circuit or integrated into it, as in the case of the acoustic turning vanes on facilities like DNW-LLF, DNW-NWB, and PLC wind

tunnels where elongated vanes covered with absorbing materials are selected to absorb the noise from the fans [88]. Other alternatives have included foam, and perforated materials on the side walls of the tunnels, acoustic cavities to reduce steady waves [86], and active noise reduction by speaker walls [89].

The study of Merino-Martinez et al. [90] has gathered the background noise from many wind-tunnel facilities. According to the study, the background noise of most aeroacoustic facilities can be studied by considering its total level normalized by the test section area, and flow speed, i.e. by analyzing the acoustic level versus the mass flow rate. Figure 3.6 shows the resulting noise levels from different wind-tunnel facilities. As it can be seen, noise levels scale with a power that is lower than U_∞^8 (free turbulence noise), and close to a power of U_∞^6 (surface loading noise). On average, the background noise from a wind tunnel can be approximated by equation 3.18. Variations from this prediction to the real facilities can be as high as ± 10 dB, emphasizing the importance of well-designed aeroacoustic facilities. Background noise is, for many applications, the most restrictive condition for realizing an experiment. This is because it represents the loudest source of noise and because it cannot be altered easily.

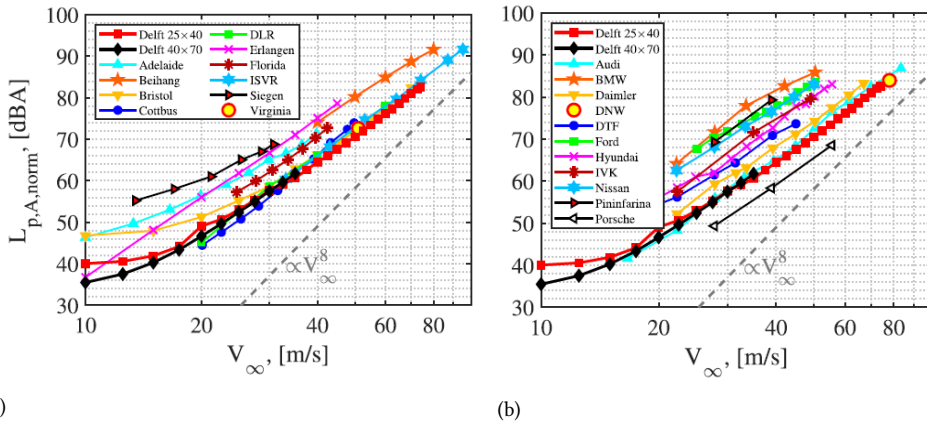


Figure 3.6: Comparison of the variation of the background noise levels with speed for several wind-tunnel facilities. The levels are shown in A-weighted overall sound pressure level made non-dimensional by the distance of the microphone from the centre of the test section and by the area of the test section. Figure is taken from [90].

$$L_{p,A} \approx -35 + 10 \log(A_{\text{section}}) + 60 \log(U_\infty). \tag{3.18}$$

The scaling with the power of 6 gives an interesting perspective on experiments of trailing-edge noise. By combining equations 3.18, and 3.16 and considering $A_{\text{section}} = b.h$ (test section span times the height), estimations of the dependencies

of SNR can be summarized in equation 3.19. First, the equation implies that the lower the velocity is, the higher the signal-to-noise ratio from the measurements. This logic is however limited as acoustic measurements at low-noise levels have compromised accuracy, and the low Reynolds number flow regime is less representative of application conditions. Besides, increasing the chord is an important way of increasing the SNR of trailing-edge scattering measurements. Lastly, another alternative for increasing the SNR is to decrease the nozzle height. This idea is based on lowering the required mass flow for the same speed, resulting in a lower noise from the fan. Again, this latter alternative is limited as decreasing the height affects the aerodynamic field, especially at angles of attack. Interestingly, the model span does not contribute to the SNR as the increasing noise from the trailing-edge is compensated by the increasing background due to the higher mass flow required. Still, it is valid to remember that a larger span can improve the spatial filtering for microphone array techniques and avoid spurious sources from the side walls.

$$SNR_{TE,measurements} \propto -12 \log(U_\infty) - 10 \log(h) + 8 \log(c). \quad (3.19)$$

3.2.4 ANECHOIC CHAMBERS

As discussed, the design of hybrid and open-section wind-tunnel facilities allows the placement of the microphones outside of the flow, preferably inside a non-reverberant acoustic environment, i.e. an anechoic chamber. The walls, floor, and ceilings on an anechoic chamber are designed to absorb fluctuations coming from the model, as illustrated in Figure 3.7. To accomplish so, acoustically absorbing materials are placed on the walls of the chamber. The simple rule of quarter wavelength (equation 3.20) can be followed to determine the thickness of the foam, i.e. t_{foam} must have at least one-quarter of the wavelength of the minimum frequency that the chamber is intended to absorb. Commonly selected materials are melamine foam, with high absorption coefficients but compromised flammability and decomposing characteristics, or natural wool with a lower absorption coefficient but more practical application.

$$t_{foam} \geq \frac{1}{4} \frac{c_0}{f}. \quad (3.20)$$

The properties of an anechoic chamber can be assessed by the reverberation and propagation test as described in the ISO 3745. The reverberation test assesses the delay time and amplitude occurring after a tap input. The propagation test studies the range of frequency where far-field propagation with respect to the distance from the source ($1/R$) is observed.

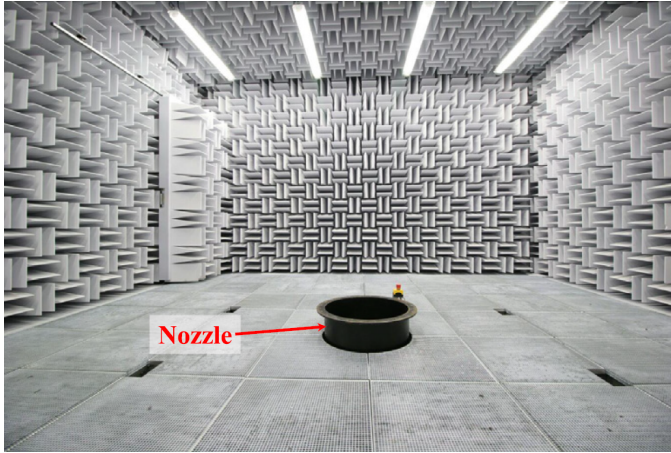


Figure 3.7: The anechoic chamber of the A-tunnel facility at the Delft University of Technology. Figure is taken from [90].

3.3 FLOW MEASUREMENT TECHNIQUES

In this work, two flow measurement techniques are explored for the study of the turbulent flow near the trailing-edge region. These are wall-mounted microphone sensors and Particle Image Velocimetry (PIV). This section describes the basic concepts of these two techniques.

3.3.1 UNSTEADY SURFACE PRESSURE SENSORS

Installing unsteady pressure sensors over a model surface is a known technique for assessing wall-pressure fluctuations. Nevertheless, limitations exist due to the difficult access and space inside the model to house the sensors and the required cabling.

In the past, research focused on the characterization of the wall-pressure fluctuations beneath a turbulent boundary layer. This means that measurements were carried on on the walls of a wind tunnel or on a single side of a model. For that, the sensors could interfere with the opposite side of the model or the wall as any interference from the other side could be disregarded. However, the study of the wall-pressure fluctuations on the surroundings of a trailing edge requires that the sensors should not interfere with any of the sides of the model. This poses an even more difficult problem as the small space close to the trailing edge restricts the allocation and routing of the sensors. For this reason, miniaturized sensors are commonly selected for these applications. Examples are piezoresistive Kulite sensors, and Micro Electro-Mechanical Systems (MEMS).

Kulite sensors are extremely dedicated piezoresistive pressure sensors. Piezore-

sistive sensors are suitable for large pressure differentials and, as such, Kulite sensors have started to be used for the study of unsteady aerodynamics. Advancements in the sensors have brought the pressure range down to 35 kPa (185 dB), in a cylindrical packaging of about 1.7 mm diameter, suitable for measurements of the wall pressure at low to medium subsonic applications. An aeroacoustic application of such sensors can be seen in the work of Murayama et al. [91], where a series of Kulite sensors were used to capture the pressure fluctuations inside the cove of the slat of a high-lift element wing.

The term MEMS describes a manufacturing technology responsible for creating electromechanical transducers in the micrometer scaling (0.001-0.1 mm). MEMS microphone sensors are of condenser type and normally available in a packaging of millimeter size with the sensitive element and conditioning system encapsulated. These types of sensors are used for current cellphone technology and offer significantly smaller costs compared to Kulite sensors. On the downside, these sensors have less controlled manufacturing, requiring the ability to check, calibrate, and test the sensors more often. MEMS sensors are also more sensitive to changes in conditions and may drift with variations of temperature or pressure during operation.

These two types of sensors are the most widely used for measurements of the wall-pressure fluctuations on a wind-tunnel model. To mount these sensors in the model, three strategies are usually explored, these are referred to as surface-mounted, cavity-mounted, and printed-circuit-board (PCB-mounted) sensors.

SURFACE-MOUNTED SENSORS

Mounting the sensors on the exposed surface of the model requires manufacturing the models with the proper spaces to house the sensors (Figure 3.8). This type of mounting is advantageous as the microphone readings are directly related to the wall-pressure on the model surface. However, the size of the sensors (in the order of a couple of millimeters) can interfere with the surface of the model. This can be especially restrictive close to the trailing-edge region. Another downside of this type of mounting is the fact that the sensors are exposed and it can be easily damaged during handling and storing of the model.

CAVITY-MOUNTED SENSORS

The disadvantages of surface-mounted sensors can be overcome by mounting the sensors inside a cavity as illustrated in Figure 3.8. This allows for reduced interference on the model surface as small pinhole-type mountings can be used. Besides, the placing and routing of the sensors are facilitated as they do not need to be placed exactly at the trailing-edge region.

However, the acoustic effects of cavity mounting must be taken into account. At first, the distance between the sensor location and the model surface can be

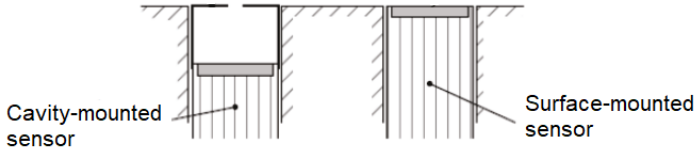


Figure 3.8: Cavity-mounted (left) and surface-mounted (right) unsteady pressure sensors. Figure adapted from Moreau [92].

assimilated as a tube with one closed end. Due to the steady waves formed on the tube, the transfer function between input pressure on the model surface and output pressure on the microphone membrane is not linear and depends on the frequency. This means that the measurements of the microphone sensor are not directly translated to the desired ones on the surface of the model. In order to avoid this effect, the size of the tube must be limited by the first cavity mode ($f_{\text{cavity}} = c_0/4L$) such that the desired frequencies of interest of the measurements ($f_{\text{meas.}}$) are below it, following equation 3.21.

$$L_{\text{cavity}} < \frac{c_0}{4f_{\text{meas.}}} \quad (3.21)$$

A second acoustic effect happens when a pinhole arrangement is selected. For that, the cavity with a restricted inlet can be assimilated as a Helmholtz resonator, with the cavity being the neck and the inside cavity as the plenum. Again, this means that the response of the microphone differs from the pressure at the model surface for frequencies above the resonance one. Using the same logic as previously described, the length and diameter of the cavity (L_c , and d_c respectively), as well as the pinhole ones (L_p , and d_p respectively) can be used to estimate the frequency in which Helmholtz resonance affects the measurements. Equation 3.22 shows the minimum condition for $f_{\text{meas.}}$ for cylindrical cavities and pinholes. In the equation, $L_{\text{eq}} = L_p + 0.3d_p$ is the equivalent length of the pinhole.

$$f_{\text{meas.}} < \frac{c_0}{2\pi} \frac{d_p}{d_c} \sqrt{\frac{1}{L_c L_{\text{eq}}}} \quad (3.22)$$

The effects of the cavity mounting can be compensated by tailored, frequency-dependent, calibrations of the data. However, when calibrating only the levels with respect to frequency, one must remember that the phase is also altered. This means that cross-correlations of microphones in different cavity arrangements might be compromised close to the frequency ranges described below. An alternative to that is to create the inverse transfer function of the cavity and apply it as a filter of the

time series. This can be done using equivalent models or with dedicated calibration followed by system identification techniques.

PRINTED-CIRCUIT-BOARD (PCB) MOUNTED SENSORS

A final possibility for the mounting of surface pressure sensors on wind-tunnel models is to mount the sensors on top of the model. This concept is applied to models that cannot be modified to accommodate the installation of the wall-pressure sensors and routing and where instrumentation with many sensors is desired. In order to accommodate the sensors, a strategy is to select PCB-mounted MEMS sensors, as illustrated in Figure 3.9. In this way, the PCB works both as the platform to which the sensors are attached and as the routing element. Modern flex-PCB designs can be as thin as 0.2 mm (2 layers) and can be used to route the signal with minimum interference to the flow (estimated $k^+ \approx 5$ for a 20 m/s flow speed, 0.6 m/s friction velocity), considered smooth flow regime according to [93].

As an example, G.R.A.S. sound and vibration has recently released the family of Ultra-Thin Precision microphones (UTP) in which an array of 4 to 8 sensors are placed together on a printed circuit board. The sensors are only 1 mm thick and can be used for full-scale vehicle testing and even large-scale wind-tunnel experiments. Martinez Rocamora Jr. et al. [94] has also demonstrated the use of PCB-mounted microphones on the vane of a fan-rig stator. The work of Sanders et al. [95] also placed a rigid PCB on the trailing-edge serrations of a 3D-printed airfoil model, showing the wall-pressure over the surface of the serrations. In the latter case, the airfoil was 3D-printed with the correct geometry to accommodate the PCB, which worked as a surface cover of the serrations.



Figure 3.9: PCB manufactured with 22 MEMS sensors to be mounted on the surface of a serrated trailing edge. The image shows the backside of the PCB with the sensors installed.

3.3.2 PARTICLE IMAGE VELOCIMETRY

The application of particle image velocimetry (PIV) has long been fundamental for studies of turbulent flows and aeroacoustics [96]. The technique provides instantaneous and time-averaged flow field in a plane or volume with a spatial resolution that is comparable to other state-of-the-art probes, such as hot-wires, or optical methods (laser doppler velocimetry, LDA).

Particle Imaging Velocimetry is based on inferring the flow velocity field from the movement of particles immersed in the flow field. The idea is based on the flow observation experiments carried out by placing particles tracers in the flow, such as dye or bubbles in water or oil drops in the air. The advancements in digital imaging and post-processing capabilities of the past decades have allowed extracting quantifiable velocities from these particle images. This is because, first, for the velocimetry of the tracers, a set of images with a suitable definition of the particles must be taken at short time intervals, such that the movement of these particles can be extracted. Second, an automated and robust way to extract this movement is required.

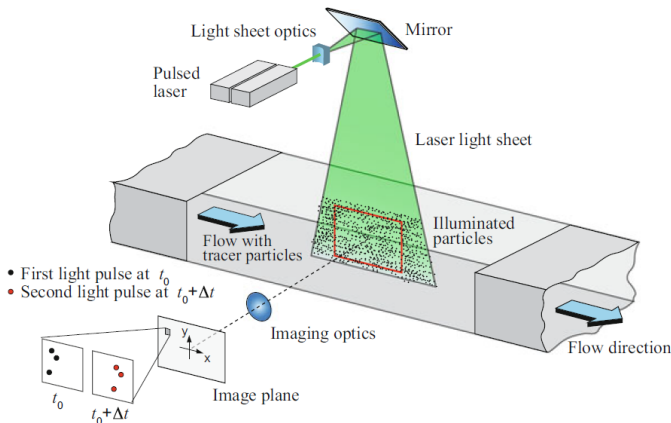


Figure 3.10: Example planar-PIV (2D2C-PIV) setup for a flow experiment. Image taken from Raffel et al. (2018) [96].

The importance of PIV data for turbulence and aeroacoustic studies has motivated a fast and escalating development of the measurement technique, giving rise to many different possibilities for PIV measurements. However, with the vast number of different procedures comes also the different nomenclature. To facilitate the reader throughout this work, Figure 3.11 breaks down some of the important nomenclatures that will be used in this work. They are differentiated by the type of triggering/timing of the images, spatial dimension (2D or 3D), number of velocity components of the retrieved information (2C or 3C, where C is the number of

velocity components), and post-processing technique used for the procedure. The next paragraphs describe the basic principles of PIV and the differences between the methodologies mentioned.

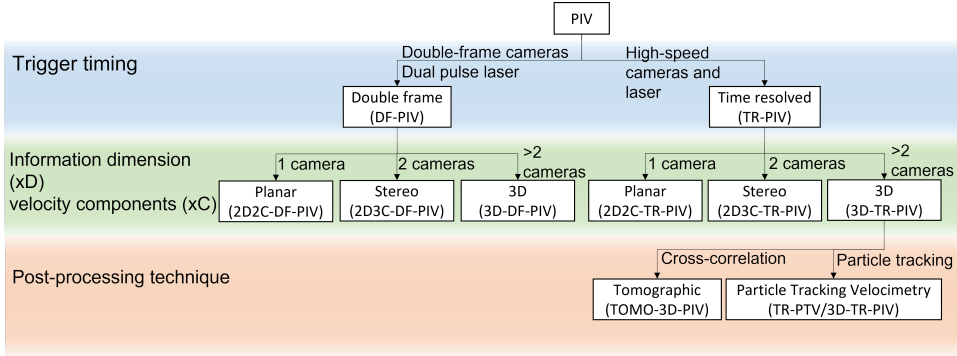


Figure 3.11: Nomenclature and difference between Particle Imaging Velocimetry (PIV) techniques followed in this work.

The simplest example of PIV application is the planar PIV (2D2C), where a single camera, most commonly, is used to extract the two components (2C) velocity information on a plane (2D) in the flow. Figure 3.10 shows a schematic arrangement for such a technique. For carrying out the measurements, 3 elements are required, i.e. particles mixed to the flow, a source of illumination, and a camera system. The following paragraphs discuss some of the required hardware.

Particles: two criteria must be looked at when selecting the particles to be mixed with the flow. These are the particles' ability to follow the flow and their light-scattering properties. Following the work of Raffel et al. [96], the equation of motion of the particle is governed by its acceleration (or material derivative, $\frac{DV_p}{Dt}$), specific mass (ρ_p), and diameter, according to equation 3.23, where F_b and D are respectively the fluid buoyancy and drag over the particle. Under small enough Reynolds numbers based on the differential velocity ($V_p - V_f$), and particle diameter (d_p), the drag force can be estimated by the Stokes drag and the equation represents a first order system with respect to the particle velocity (equation 3.24), where $F(V_f)$ is the forcing function imposed by the the fluid flow. This system has a time response τ_p given by $\tau_p = \frac{(\rho_p - \rho)d_p^2}{18\mu}$. The inverse of this time response represents the frequency cut-off of the particle response (equation 3.25), i.e. the maximum frequency where the particle movement is in phase and amplitude with the fluid one.

Tracer	Particle size (μm)	Density (kg/m^3)	Time response (μs)	$f_{\text{cut-off}}$ (kHz)	Scattering index ($\propto d_p^2$)
DEHS	1	750	2.0	80	1
HFSB	400	1.1	20.0	8	1.6×10^5

Table 3.1: Summary of properties of the two types of flow tracing particles used in this work. Data taken from the work of [97].

$$F_b + D = \rho \frac{1}{6} \pi d_p^3 \frac{DV_p}{Dt}. \quad (3.23)$$

$$\frac{(\rho_p - \rho) d_p^2}{18\mu} \frac{DV_p}{Dt} + V_p = F(V_f). \quad (3.24)$$

$$f_{\text{cut-off,particle}} = \frac{1}{2\pi\tau_p} = \frac{9\mu}{\pi(\rho_p - \rho) d_p^2}. \quad (3.25)$$

The closer the particle time response is to zero the better the tracer particle is to describe the fluid dynamics. This means that the particle can react to fluctuations of higher frequencies (higher $f_{\text{cut-off,particle}}$). It is important to point out that this frequency response relates to the flow and particle material acceleration (Lagrangian reference, moving with the particle), and not to the time derivative of the flow in an Eulerian reference (fixed position). The equation shows two approaches to reduce τ_p , i.e. decreasing the particle diameter (d_p) or using particles with a more similar density (ρ_p) to the fluid (ρ).

A second important characteristic of the seeding particles for PIV is their ability to scatter light. The higher the scattered energy, the lower the required illumination power required to image the particles. The intensity of light scattering is proportional to the square of the particle diameter [96]. This latter characteristic goes against the strategy of reducing particle size as, by doing so, the illumination power required is increased.

Among the many tracers used for air-flow measurements, two types of tracers are reported here, i.e. DEHS, and Helium Filled Soap Bubbles (HFSB). Table 3.1 shows the properties of both particles. It is interesting to observe that these two tracers follow different concepts to achieve a small time response. While the oil particles rely on small-sized drops of a high-density element, the HFSB is based on neutrally buoyant particles of a significantly larger size. As demonstrated by the table, although the HFSB has a slightly higher time response, its scattering is about 5 orders of magnitude higher than the one of DEHS particles.

Illumination: the required illumination properties for PIV depend on the type of technique to be applied. For planar PIV (2D2C) the particles within a plane must be illuminated. This requires a pulsed laser, which can be shaped into a thin light sheet by the appropriate set of optics. For volumetric measurements, lasers or LED arrays can be used.

3

Particle image recording: the camera system is responsible for imaging the particles in the fluid. These usually constitute black and white cameras with a high number of pixels and intensity accuracy. The two requirements are necessary to capture the light scattered by the tiny particles and to have enough pixel resolution to describe the particle displacement. Two types of camera systems are used for modern PIV applications, namely double-frame and high-speed cameras. The latter is the most simplistic application of PIV in which all images recorded are sequential in time and the delay between frames is small enough to allow the tracing of the particles (Figure 3.14b). A double-frame camera system allows a pair of consecutive images to be recorded and stored. This is realized by setting the shutter of the camera exposed according to Figure 3.14a. This strategy, combined with two short laser pulses (also in the figure), creates a pair of images where the time between laser pulses is not restricted by the camera repetition rate (in the order of 10 Hz), enabling the particle tracing without the use of high-speed cameras. This technique greatly reduces the requirements for the cameras. Although the instantaneous velocity field is captured, the temporal evolution of the flow is usually not captured. Time synchronous data can only be achieved with high-speed cameras, referred to as time-resolved PIV.

A second relevant aspect of the camera setup is the number and arrangement of the cameras. Using a single camera, only the two in-plane (2D) velocity components (called 2C) can be obtained. However, the third flow component (the out-of-plane one) can be obtained by adding a second camera and combining both camera views. This process is referred to as stereo-PIV (2D3C-PIV) [98]. In this process, the difference in the displacement observed between the two cameras is used to infer the out-of-plane motion of the particles. Another option of multiple camera setup is for three-dimensional PIV measurements (3D-PIV). For this technique, the view of multiple cameras is combined to identify the particle location in a 3-dimensional space. This can be carried out by either reconstructing the 3D particle field using tomographic reconstruction techniques [99] or by triangulating the particle position from the images [100]. The latter technique is used in particle tracking methods. 3D-PIV techniques require volumetric illumination and at least 2 cameras recording the same flow volume. The work of Scarano [101] showed that a satisfactory quality of the flow reconstruction is only achieved for setups with 3 or more cameras.

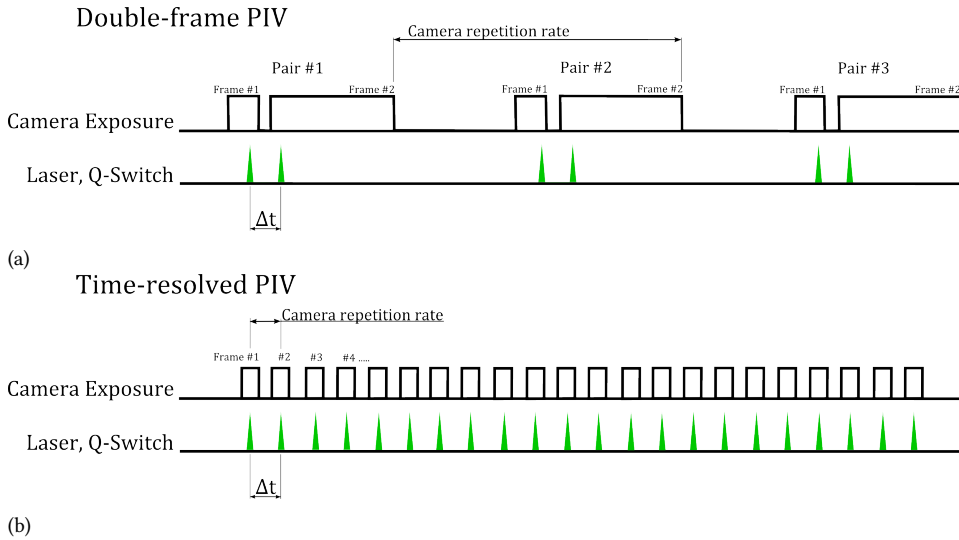


Figure 3.12: Illustrative camera exposure and Laser Q-switch timing for (a) double-frame PIV and (b) time-resolved PIV measurements.

VELOCIMETRY THROUGH IMAGE CORRELATION

The images obtained from the PIV must be pre-processed to extract the velocity field in the region of interest. This translates to obtaining the particle displacement within the frames. Two techniques are possible for extracting the displacement, namely cross-correlation, and particle-tracking techniques. The former is the standard practice for PIV processing. It is based on splitting the image in small domain windows of size $n_n \times n_m$ pixels, where cross-correlation is used to identify the mean displacement of the particles inside this window.

The discrete cross-correlation analysis, defined in equation 3.26, is carried between two consecutive frames (I_1 , and I_2). The cross-correlation R indicates the levels of similarity between two frames displaced in $(\Delta m, \Delta n, \Delta k)$. This process is carried out for every combination of $(\Delta x_1, \Delta x_2)$ within the interrogation window, covering possible particle displacements between the frames. A correlation map between the two images is created.

$$R(\Delta m, \Delta n) = \sum_{m=1}^{n_m} \sum_{n=1}^{n_n} I_1(m, n) I_2(m + \Delta m, n + \Delta n). \quad (3.26)$$

The cross-correlation map yields a peak corresponding the average particle displacement between the two frames ($\overline{\Delta x}$), Figure 3.13 illustrates the process. The velocity field in the window is estimated according to equation 3.27, where Δt is the time interval between the images. This process is carried out for every window

in the image, to create the velocity field in the region of interest. The windows are selected to form a Cartesian grid. Overlapping between the windows is often used to increase the spatial resolution of the velocity field obtained.

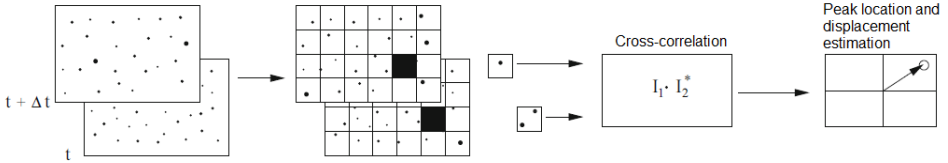


Figure 3.13: Procedure for motion analysis based on the cross-correlation between two image frames. Adapted from Raffel et al. [96].

$$\bar{U} = \frac{\overline{\Delta x}}{\Delta t} \quad (3.27)$$

The particle travelling distance between frames must be controlled during experiments to ensure the quality of the correlation maps. This first translates to controlling the number of particles per pixel in the image. Raffel et al. [96] suggests that a window must contain about 5 particles to be correlated, i.e. particles that do not enter or exit the window between the frames. The recommended density of particles-per-pixel, referred to as ppp, depends on the type of post-processing carried on. For planar and stereo applications, such density is not critical. For 3D PIV, instead, it is recommended not to exceed ppp 0.1. The higher the ppp, the smaller the window size that can be selected, hence the higher the spatial resolution of the measurements.

The displacement of the particles between frames affects the quality of the cross-correlation map. A small displacement, close to the image pixel, yields a small accuracy of the particle movement. On the opposite side, increasing excessively the displacement cause the decorrelation of the images. A general rule of thumb tells that the particle displacement between frames must lie around 10-20 pixels [96].

VELOCIMETRY THROUGH PARTICLE TRACKING

A second alternative for the pre-processing of the images is called particle tracking. This alternative aims at improving the resolution of measurements by creating an automated way of locating individual particles and tracking their movement. Three minimum steps are required for particle tracking, namely particle identification, pairing, and velocity estimation. These steps are described in the following paragraphs.

Particle identification: a state-of-the-art particle identification technique is based on the Iterative Particle Reconstruction (IPR, [102]). The technique aims at identifying all individual particles in the image. The technique is based on a description of the imaging of the particle by the cameras, called the Optical Transfer Function (OTF). The process of particle tracking is carried out by finding the local maximum intensity in the figure, which is assumed as the particle location. The image of that particle is reconstructed based on the OTF. This particle image is then subtracted from the real image, creating a new image where that specific particle is removed. This process is carried in loop until all particles are found and removed from the image.

Particle pairing: pairing the particle consists in identifying the same particles within the different frames in order to compute the particle displacement. Tracking is carried out by a minimization of the acceleration among time frames. This process starts with an initialization based on the particles on two frames. From that, the position of the tracked particle in the next frame is taken as the one which minimizes acceleration, i.e. the particle positions in time that produces minimum particle acceleration is taken as the trajectory point of that particle.

Trajectory model and velocity estimations: having the discrete positions of the particles, several techniques can be used to retrieve velocity information. The simplest form is the use of a finite differences method with the particle position. Another commonly used technique is the fitting of the particle tracks using different methodologies. The latter is more adequate to reduce the influence of errors in the particle position. Possible fitting methods are least-squared polynomial fitting, Splines, and B-Splines.

SHAKE-THE-BOX PARTICLE TRACKING

Many particle-tracking algorithms exist, being the currently most used one the so-called Shake-the-Box method [100]. The particularity of this method lies in the particle identification part, where an iterative step is taken to accelerate particle tracking. After identifying the particle tracks in previous time steps, the location of the particles is predicted based on an extrapolation of the particle position. From the estimated particle location, the position is iterated to minimize the image residual. This process is called "shake". With the particles that were already tracked in previous iterations identified, the new particles that enter the field of view are triangulated from the several camera views. By avoiding the triangulation of the previously tracked particles, and the tomographic reconstruction of the field (required for cross-correlation-based approaches), shake-the-box is extremely less

computationally expensive than other 3D-PIV techniques (around 5 times faster than standard tomographic PIV techniques [100]).

Particle identification is still the main drawback of particle tracking algorithms, and many can only identify the particles from images with small particle densities. According to Schanz et al. [100], the Shake-The-Box can correctly track the particles from noisy images with about 0.05 ppp, similar to tomographic-PIV applications, which indicates that Shake-The-Box promises an increased spatial resolution compared to cross-correlation.

The outcomes of a particle-tracking algorithm are the positions and time derivatives of each tracked particle. For velocimetry application, the particle velocity and position are the most important data. Still, the scattered data obtained from the algorithm creates difficulties for the analyses. Especially, since the particles change position within time steps, the obtained scattered velocity fields in time have also different reference positions, hampering the calculation of velocity gradients and Eulerian time derivatives when needed.

DATA ASSIMILATION TO AN EULERIAN GRID

Different possibilities exist for interpolating the particle velocity data, known as Lagrangian data, into an Eulerian grid. These are known as data assimilation techniques. Some techniques are based on simple interpolation methods, while others try to incorporate flow physics to enhance the quality of the assimilated data. Some of these methods are described in the paragraphs below:

Data binning: binning is equivalent to a nearest interpolation. This process only assimilates, to the grid point, the data from the particles nearest to it. This technique is most effective to create time-averaged velocity fields from a large number of snapshots;

Linear interpolation: linear interpolation, or trilinear interpolation (for 3D data) consists of assimilating the data at the grid point according to a tent basis function. From a mathematical perspective, linear interpolation is gradient-free to the second order, meaning that the conservation of mass is kept in the interpolated field.

Vortex-in-cell method (VIC+, and VIC#): some methods attempt to increase resolution and robustness of the reconstruction by using flow physics information in a fitting procedure aiming at assimilate the particle tracking information. This is the case of VIC+ [103], and VIC#. These methods are based on finding the gridded vorticity field (ω_g) that reproduces best the particle velocity and velocity

acceleration from the measurements (represented by the subscript m). This translates, mathematically, to the minimization problem shown in equation 3.28, where J_u is the relative error in the velocity between the gridded and the particle data (equation 3.29), J_{Du} is the error in the particle acceleration (equation 3.30), and α_v is the weighting coefficient that compensates the acceleration error and the velocity error.

$$\min_{\omega_g} [J_u(\omega_g) + \alpha_v^2 J_{Du}(\omega_g)]. \quad (3.28)$$

$$J_u = \frac{\sum_{p,i=1,2,3} (u_{m,p,i} - u_{g,p,i})^2}{\sum_{p,i=1,2,3} (u_{m,p,i} - \bar{u}_{m,p,i})^2}. \quad (3.29)$$

$$J_{Du} = \frac{\sum_{p,i=1,2,3} \left(\frac{Du_{m,p,i}}{Dt} - \frac{Du_{g,p,i}}{Dt} \right)^2}{\sum_{p,i=1,2,3} \left(\frac{Du_{m,p,i}}{Dt} - \frac{D\bar{u}_{m,p,i}}{Dt} \right)^2}. \quad (3.30)$$

The process starts with a given vorticity field. This is used to obtain the velocity field from the solution of the Poisson equation 3.31 with the appropriate boundary conditions. The vorticity and velocity fields in the gridded data are used to obtain the Eulerian time derivative of the vorticity field using the vorticity-transport equation (equation 3.32). The latter variable is then input in the time derivative of the Poisson equation 3.31, to obtain the Eulerian time derivative of the velocity field (equation 3.33). Finally, the process is concluded by estimating the material derivative of the velocity (Lagrangian velocity derivative, or particle acceleration) using equation 3.34. After this process, a velocity, and velocity material derivative gridded field is obtained from the vorticity field. These fields are then interpolated to the particle positions and compared against the experimental particle velocity and acceleration. A radial-basis-function representation is used to speed-up the numerical process and improve the interpolation. The minimization problem is solved with a gradient-based method using an adjoint method. Figure 3.14 shows a flowchart of the VIC+ technique.

$$\nabla^2 \mathbf{u}_g = -\nabla \times \omega_g. \quad (3.31)$$

$$\frac{\partial \omega_g}{\partial t} = (\omega_g \cdot \nabla) \mathbf{u}_g - (\mathbf{u}_g \cdot \nabla) \omega_g. \quad (3.32)$$

$$\nabla^2 \frac{\partial \mathbf{u}_g}{\partial t} = -\nabla \times \frac{\partial \omega_g}{\partial t}. \quad (3.33)$$

$$\frac{D\mathbf{u}_g}{Dt} = \frac{\partial \mathbf{u}_g}{\partial t} + (\mathbf{u}_g \cdot \nabla) \mathbf{u}_g. \quad (3.34)$$

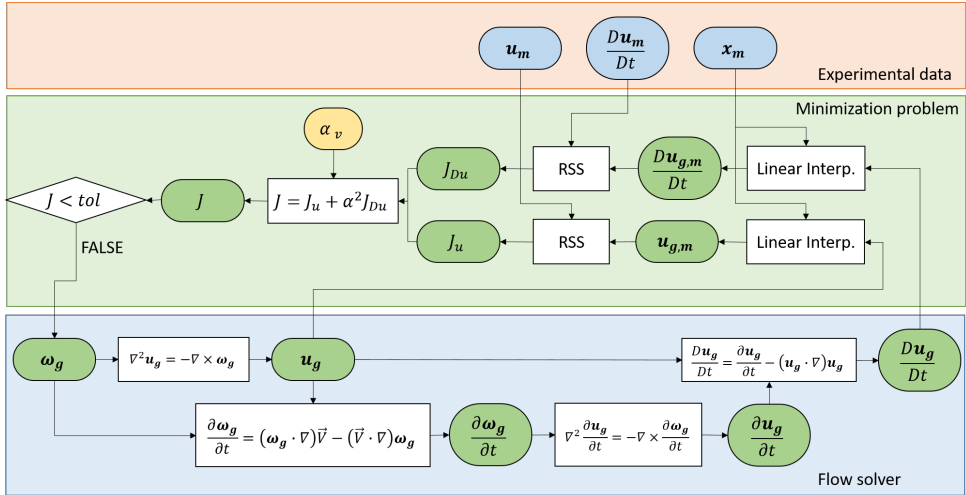


Figure 3.14: Information flowchart of the Vortex-In-Cell based data-assimilation technique (VIC+).

FlowFit: flowFit follows a similar procedure to VIC+, and VIC#, where a fitting procedure based on a field that follows certain physical properties is sought. In this case, however, a B-spline is used to represent the velocity field, and possibly the pressure field as well. To this velocity field, the minimization is constructed as the sum of different errors, e.g. the velocity error with respect to the measurements, the error in the velocity divergence, and the error in the momentum equation. In that sense, differently from VIC+ and VIC#, neither the physical properties nor the measured velocity field is enforced on the assimilated data and the weights of the cost function drive which of the errors is more important.

The data-assimilation techniques differ in quality of reconstruction, robustness to wrong particle information, and computational cost. Attempts to compare the methodologies are due to the Data-Assimilation Challenge, where numerical particle data with different particle concentrations and with different noise on the particle position are given as input for assimilation. Figure 3.15 shows the velocity wavenumber spectrum obtained with different assimilation techniques, including linear interpolation, VIC+ (labelled TUD VIC+), VIC# (labelled LaVision 3D), and flowFit (labelled DLR). The results show how including more physical information in the assimilation yields a field with an energy spectrum that agrees better with the numerical data for smaller structures.

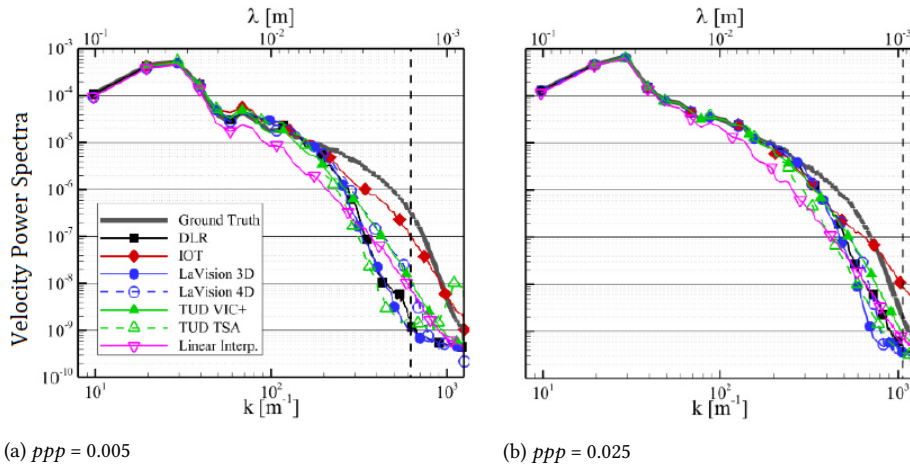


Figure 3.15: Comparison of the wavenumber spectra of the velocity fluctuations obtained from numerical simulation (ground truth), and different data-assimilation techniques. Image from the work of Sciacchitano et al. [104] for different particle concentrations. The dashed line shows the mean distance between particles.

PRESSURE FROM PIV

As discussed in chapter 2, the theory of trailing-edge noise is based on the diffraction of the advecting wall-pressure fluctuations along the trailing edge. This means that an oriented discussion of the sources of scattering noise requires the analysis of the pressure surrounding the trailing-edge region. The pressure is not a direct output from particle image velocimetry measurements however, alternatives exist to extract the pressure from PIV measurements.

The most common technique is based on the numerical solution of the Poisson equation for pressure (equation 3.35). In the equation, the source term is different from the one of equation 2.28 as the latter represents the pressure fluctuation after the Reynolds average process. Besides, the time derivatives of the source term are represented in Lagrangian form. This is done so as, according to Violato et al. [105], this is proven to be a more robust form to obtain the source term from time-resolved experimental measurements. The Lagrangian acceleration is obtained from the tracking of the particle movement within the measurements and the further interpolation of this track for obtaining the required material derivatives.

$$\nabla^2 P = -\rho \nabla \cdot \frac{DU}{Dt}. \quad (3.35)$$

From the source term on a regular grid, an implicit finite-differences approach is used to solve the equation. This partial differential equation requires appropriate boundary conditions. At regions of uniform flow, a Dirichlet boundary condi-

tion can be used based on Bernoulli's equation (3.36). Solid boundaries and flow interfaces are treated with Neumann boundary conditions, where the inviscid momentum equation is used, following equation 3.37 where the subscript n indicates the direction normal to the interface.

$$P = p_\infty + \frac{1}{2}\rho(U_{\text{ref}}^2 - \mathbf{U} \cdot \mathbf{U}). \quad (3.36)$$

$$\frac{\partial P}{\partial x_n} = -\rho \frac{DU_n}{Dt}. \quad (3.37)$$

Other methodologies for pressure reconstruction are the use of flowFit [106], or the direct integration from the particle tracking output [107].

3.4 CONCLUSIONS

This chapter has discussed several experimental techniques that can be explored for aeroacoustic measurements. The techniques are divided between those for the assessment of the acoustic emissions from an aerodynamic source and those for the assessment of the properties of the flow surrounding a model. Acoustic techniques are focused on microphone methods, especially, microphone-array techniques. A discussion on the background levels from wind tunnels, and the suitability of wind-tunnel facilities for trailing-edge noise studies is also given.

Aerodynamic measurement techniques are focused on microphones mounted on the model for the wall-pressure assessment, and particle image velocimetry techniques. These techniques are extensively used during the remainder of this work. The work of chapter 5 combines time-resolved 3D-PIV, and surface mounted sensors to create a description of the flow over the serrations. Acoustic measurements using the microphone array complement the study. Chapter 6 uses the surface mounted sensors on a high-Reynolds airfoil model to demonstrate the hypothesized physics of the wall-pressure fluctuations on top of serrated trailing edges. Stereo(2D3C)-PIV measurements complement the data with information on the incoming boundary layer. Chapter 7 describes the influence of the serration geometry on the acoustic field captured with microphone array techniques. The fundamentals, nomenclatures, advantages, and disadvantages of each of these methods explained here are important for following the discussions presented in the next chapters.

4

DESCRIPTION OF EXPERIMENTS

4

This chapter describes the three different experimental methodologies that were carried out to create the studies shown in the remainder of this thesis. The first study is dedicated to the assessment of the isolated effect of trailing-edge serrations. The second study focus on the turbulent fluctuations on over serrated trailing edges mounted on an airfoil operating at high-Reynolds numbers. The third, and final, study focus on the effects of the serration geometry on the noise reduction achieved. To accomplish this goal, an experimental campaign based on the same airfoil described before is conducted where different serration geometries are tested.

The following sections describe each of the studies, the goals, and the measurement techniques employed.

4

4.1 ISOLATED TRAILING-EDGE STUDY

This study intends to first assess the measurement techniques that will be employed throughout this study, namely the time-resolved 3D-PIV based on particle tracking, and the wall-mounted unsteady pressure sensors on the serration surface. From the validated techniques, the experiments also aim at studying the properties of high-Reynolds flows surrounding an isolated serrated trailing edge and, especially, how these properties varies with the serration aerodynamic loading, i.e. when the serrations are placed at an angle with respect to the flow, creating a pressure difference between both sides of the serrations. The obtained results from this campaign are described in Chapter 5.

With this goal in mind, a wind-tunnel model consisting of a long flat plate with trailing-edge flaps is chosen. The choice follows first the controlled condition to the development of the turbulent boundary layer. The measurements of the turbulent boundary layer upstream from the trailing edge are used for a first validation of the PIV and wall-mounted microphone sensors techniques. The trailing-edge section can be tested with different serration inserts, and the trailing-edge flap allows for controlling the aerodynamic loading over the serrations. Details of the model, the wind-tunnel facilities used, flow conditions, and the measurement techniques employed during the campaign are given in the following sections.

4.1.1 MODEL GEOMETRY

As mentioned, the model is a flat plate with the differential of a trailing-edge flap where different trailing-edge inserts can be placed (Figure 4.1). The plate is manufactured in Plexiglas and features an elliptical leading edge. The model has 0.4 m span, 1.0 m chord, and 20 mm thickness. Boundary-layer transition is forced after the leading edge with two staggered rows of obstacles of 10 mm height and 30 mm pitch. The thick transition device follows the work of [113] and is meant to induce a thick boundary layer (approximately 60 mm height) at the measurement

region. At the model end, the thickness reduces through a symmetric wedge (8° half-deflection) providing the transition to a 2 mm thickness trailing-edge insert made of Plexiglas. The edge thickness complies with the limit suggested by Blake [42] of $t/\delta^* < 0.3$ that avoids the onset of a vortex-shedding regime. The choice of a transparent material is important because it allows optical access (for PIV) on both sides of the trailing edge. The trailing-edge flap consists of a pivot (150 mm apart from the trailing edge) and two side brackets to control the flap angle (δ_f) within $\pm 15^\circ$ by 2.5° steps. The model is installed between side plates. The serration height ($2h = 1\delta = 60$ mm) is selected to produce noticeable noise reduction and to permit the PIV measurements at a desirable spatial resolution. Following previous works [18], the serration wavelength is equal to half of its height ($\lambda = 30$ mm).

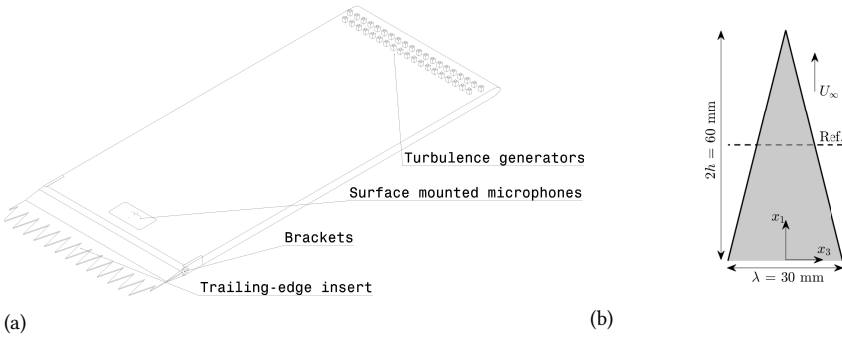


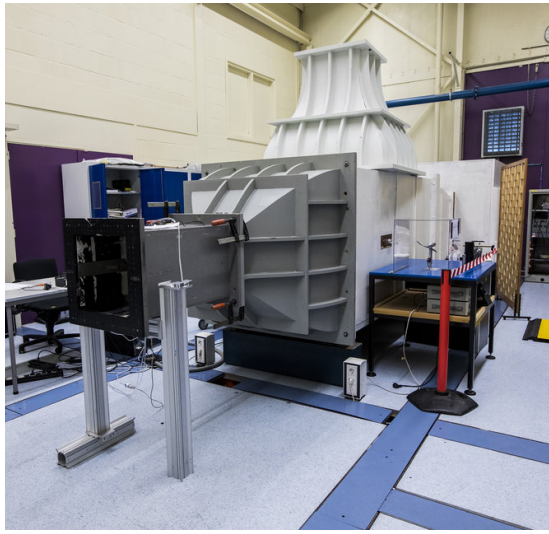
Figure 4.1: Experimental setup of the flat-plate model used (a) and the trailing-edge geometries tested (b). In the last picture, Ref. refers to the position of the baseline straight trailing edge at $x_1 = 1h$ used. The same picture also shows the coordinate system and origin adopted in the remainder of the study.

4.1.2 FLOW FACILITIES

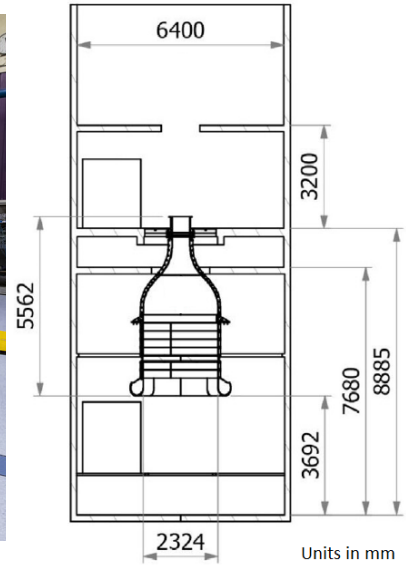
Experiments are conducted in two low-speed wind tunnels of the Aerospace Engineering laboratories at TU Delft. The W-Tunnel facility is used for the time-resolved 3D-PIV measurements, where a HFSB seeding particle generator can be installed in the settling chamber. The W-Tunnel is a blower-type, open-jet flow facility with a contraction ratio of 14, and a 400×400 mm² operating section (Figure 4.2a). Turbulence intensity is quoted below 0.5% however, with the seeding generator installed, the free-stream normalised turbulence intensity is verified to be within 0.6% of the free-stream velocity.

Wall-pressure and acoustic measurements are instead carried out in the anechoic A-Tunnel (free-stream turbulence $< 0.1\%$, [90]). The A-Tunnel is a vertical closed circuit, open test-section wind tunnel (Figure 4.2b). Variable nozzles can be used to control the flow speed and size of the model. For this experiment, a nozzle of 400×700 mm is selected, with a maximum achievable speed of 35 m/s. To ensure

that conditions on both tunnels are equivalent, hot-wire measurements are carried out during the A-tunnel testing for verifying that the turbulent boundary layer develops with similar characteristics in both facilities.



(a) W-Tunnel



(b) A-Tunnel

Figure 4.2: Wind-tunnel facilities used for the isolated serration study.

4.1.3 CONFIGURATIONS AND FLOW CONDITIONS

Experiments are carried out at a free-stream velocity of 10 m/s. The incoming boundary-layer conditions, measured with PIV at $\delta_f = 0^\circ$ and $\delta_f = 10^\circ$, are summarized in Table 4.1. The velocity profile within the boundary layer presented in Table 4.1 is here extracted from the PIV measurements. The correct wall position (within ± 0.5 mm of the reference one) and friction velocity (u_τ) are estimated from the fit of the velocity profile with the logarithmic law of the wall [114], considering $\chi = 0.41$ and $C^+ = 5$. Integral quantities, displacement (δ^*), and momentum thickness (θ) are then computed. The law of the wake and the wake parameters (Π_w) are obtained from the formulation proposed by Coles [45]. The pressure gradient is estimated from the edge velocities (U_e) obtained at the location where the variation of the spanwise vorticity in the wall-normal direction becomes negligible, following the procedure adopted in [67] (based on the work of Spalart and Watmuff [115]). A full description of the procedures followed to estimate the boundary-layer properties at those angles along with the characterization of the incoming wall-pressure

Parameter	Symbol	$\delta_f = 0^\circ$	$\delta_f = 10^\circ$ (suction side)	$\delta_f = 10^\circ$ (pressure side)
Edge velocity	U_e [m/s]	10.5	11.0	9.4
BL thickness	δ [mm]	57	60	53
BL displacement thickness	δ^* [mm]	9.3	10.7	6.6
BL momentum thickness	θ [mm]	6.7	7.4	5.1
Reynolds number	Re_c	670,000		
	Re_{δ^*}	6,600	7,900	4,300
BL shape factor	$H = \delta^*/\theta$	1.39	1.44	1.29
Friction velocity	u_τ [m/s]	0.42	0.44	0.41
Zagarola & Smits' parameter	Δ_*	6.1	5.5	8.0
Wake parameter	Π_w	0.36	0.52	0.11
Pressure gradient	dP/dx_1 [Pa/m]	-8.5	45.8	-53.9
Clauser's parameter	$\beta_\theta = \left(\frac{\theta}{\tau_w}\right) \frac{dP}{dx_1}$	-0.27 (ZPG)	1.45 (APG)	-1.36 (FPG)

Table 4.1: Mean boundary-layer parameters measured with the straight trailing-edge insert.

spectrum and far-field noise of the straight trailing edge is provided in Appendix A.

It is important to mention that flow separation is not observed on the suction side for any of the conditions tested. This is also verified with flow visualization techniques in both wind-tunnel facilities used.

The different inlet heights between the two facilities used (0.4 m at the W-Tunnel and 0.7 m at the A-Tunnel) can lead to small discrepancies in the induced angle due to the deflection of the jet flow. Estimations using thin airfoil theory and the corrections of Brooks et al [30] result in discrepancies below 2° for $\delta_f = 15^\circ$.

4.1.4 INSTRUMENTATION AND MEASUREMENT TECHNIQUES

PARTICLE IMAGE VELOCIMETRY

Time-resolved volumetric PIV (4D-PIV) is performed for the flap angles of $\delta_f = 0^\circ$, and 10° using HFSB [97] as seeding particles. The HFSB seeding system at TU Delft features 206 nozzles installed on 11 rakes aligned vertically and covering a cross-section of 1.0 m \times 0.5 m, which yields a particle density of about 2 particles per cubic centimetre in the free stream. The tracers have a mean diameter of 0.4 μm and a time response of about 20 μs [116]. Illumination is provided by a high-speed Quantronix Darwin Duo laser (2 \times 25 mJ per pulse at 1 kHz). The laser beam enters the measurement domain from the spanwise direction (Figure 4.3) expanding in both directions. The domain of illumination is truncated making use of a knife-edge filter along the wall-normal direction to a height of approximately 100 mm on each side of the model (twice the expected boundary-layer thickness) avoiding light scattering from particles outside of this range. Imaging is provided by three

CMOS Photron FASTCAM SA1.1 cameras (12 bits, 1024×1024 pixels at 5,400 fps). The cameras are placed along the streamwise direction subtending an arc of 40° at approximately 1 m distance from the trailing edge. Each camera is equipped with a 105 mm focal length objective, resulting in a field of view of about 80 mm along the streamwise and the spanwise directions. The range in the wall-normal direction is determined by the illumination and depth of focus of the imaging system and is approximately 60 mm on each side of the trailing edge. Illumination, imaging, and acquisition are synchronised with a LaVision Programmable Timing Unit (PTU 9) controlled by LaVision DaVis 10 software.

4

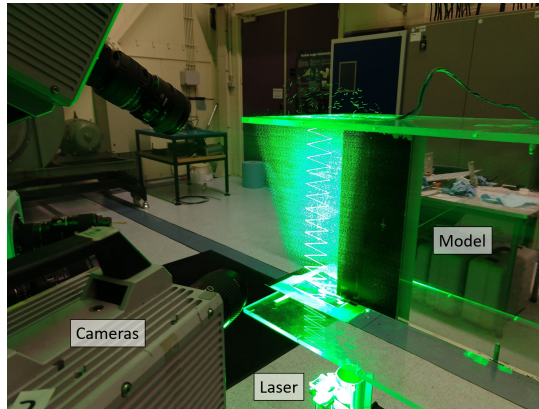


Figure 4.3: Experimental set-up for the 3D-PIV measurements carried at the W-Tunnel facility.

Images of the tracers are recorded at 5,400 frames per second. The trajectory of each tracer is evaluated with the Lagrangian Particle Tracking algorithm Shake-The-Box [100] from DaVis 10. The velocity measured along the particle's track is reduced to a regular Cartesian grid by data assimilation using the VIC+ technique [117]. The technique also estimates the velocity gradient and its temporal derivative, needed for pressure reconstruction and the remainder of the analyses. The process is schematically illustrated in Figure 4.4 along with the methodologies used at each step, which are further described in the remainder.

The VIC+ reconstruction is used, yielding data on a Cartesian grid with a spacing of $\Delta x = 2.5$ mm (Table 1). The spacing is based on the grid discretization criterion of $1/4C^{-1/3}$, where C is the mean particle concentration. At the solid wall, no-slip boundary condition is imposed for the boundary-layer case. In the wake of the trailing edge, no boundary condition is imposed.

The instantaneous flow pressure is reconstructed in the three-dimensional domain solving the inviscid Poisson equation for pressure. The source term of the Poisson equation is computed with a Lagrangian approach using a stencil of 5 points in time, as described in Ghaemi et al. [118]. Pressure from PIV is used

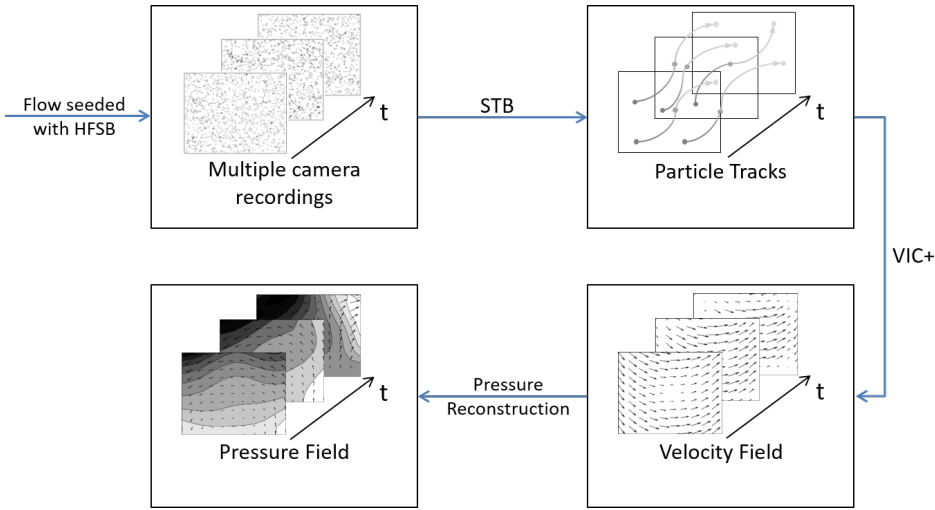


Figure 4.4: Flowchart for the data processing of the raw recordings with 4D-PIV and reconstruction of dense velocity field with data assimilation. The analysis is concluded with instantaneous pressure estimation

to estimate the convection velocity and correlation length with a higher spatial resolution than that available from the surface pressure sensors, mainly for the characterization and verification of the incoming TBL conditions. Details are given in Section A.

The main parameter governing the spatial resolution of the PIV measurements with HSFBS is the average distance between neighbouring particles. The latter dictates the spatial resolution through the VIC+ grid spacing one-quarter criterion [117] (velocity field reconstructed on a Cartesian mesh with vector spacing no smaller than $\frac{1}{4}$ of the average particle distance). In the present case, given the varying particle density inside the measurement volume, a more conservative choice of the grid spacing ($\Delta x_1 = 2.5$ mm), approximately one-third of the particle mean distance, is made. The grid spacing defines the maximum wavenumber that can be resolved, in turn also limiting the maximum resolved frequency to about 1,000 Hz according to equation 4.1, where u_c is the convection velocity and the constant 0.4 is a function of the VIC+ interpolation scheme.

Uncertainty of PIV: the uncertainty of the velocity measured from a single particle track depends on the particle position error (here taken as the distance between glare points of the same particle), the number of exposures composing a trajectory, and the time separation between frames. When a polynomial regression is applied to describe the particle positions in time (track), neglecting truncation

Parameter	Units	Value
Particle size	mm	0.4
Particle concentration	#/cm ³	2.5
Digital imaging resolution	px/mm (px/ δ)	10.2 (610)
Numerical aperture		$f/32$
Recording rate	Hz	5,400
Number of images recorded		5,400
Measured volume ($x_1 \times x_2 \times x_3$)	cm ³	$7 \times 10 \times 7$
	δ^3	$1.2 \times 1.7 \times 1.2$
Maximum particle displacement	px (mm)	21 (2)
VIC+ velocity vector grid spacing	mm (δ)	2.5 (4%)
Uncertainty in velocity measurements	m/s (U_∞)	0.04 (0.4%)
Uncertainty in pressure measurements	Pa	0.3
Uncertainty in convection velocity	m/s (u_c)	0.3 (5%)
Uncertainty in the $MS - T$ terms	Pa/m ² ($\rho U_\infty^2 / \delta^{*2}$)	1,700 (0.001)
Frequency limit*	Hz (U_∞ / δ^*)	1,000 (1.0)

Table 4.2: Summary of PIV measurement parameters for the flow around the trailing-edge region.

errors, the velocity random error follows equation 4.2 [119], where d_b represents the bubble diameter (the glare points distance is approximately $d_b / \sqrt{2}$), N the number of exposures considered by the polynomial stencil, and Δt the time separation between subsequent frames. For this experiment, a 2nd order polynomial obtained from a 9-time-step stencil yields an estimate of the instantaneous velocity uncertainty of about 0.04 m/s (0.4% of free-stream).

$$f_{VIC+} \approx 0.4 \frac{u_c}{\Delta x_1}. \quad (4.1)$$

$$\epsilon_u = \frac{d_b / \sqrt{2}}{\Delta t} N^{-3/2} \approx 0.4\% U_\infty. \quad (4.2)$$

The procedure to estimate the measurement uncertainty for the instantaneous pressure is explained in Lima Pereira et al. [108]. The uncertainty on the estimations of the mean-shear turbulence ($MS - T$) interaction term, discussed in this work, depends on the uncertainty on the velocity estimations. As for the estimations of the convection velocity (u_c), it depends on the fitting procedure based on the work of [56]. A summary of the main PIV measurement and post-processing parameters is presented in Table 4.2.

SURFACE MOUNTED MICROPHONE SENSORS

The wall-pressure fluctuations on the serration are measured with an array of 10 surface-mounted sensors. The O8AC03 MEMS sensors are installed on a printed circuit board (PCB) 0.2 mm thick (Figures 4.5b,c), attached over the Plexiglas for

Parameter	Units	Value
Average sensitivity	mV/Pa	18.2
Frequency limit	Hz (U_∞/δ^*)	5,000 (5)
Uncertainty in pressure measurements	Pa (dB)	0.02 (0.5)
Uncertainty in convection velocity	m/s (u_c)	0.1 (2%)
Uncertainty in the correlation length	mm (δ)	2 (3.4%)

Table 4.3: Summary of the parameters of the microphones used for the wall-pressure measurement over the serration surface.

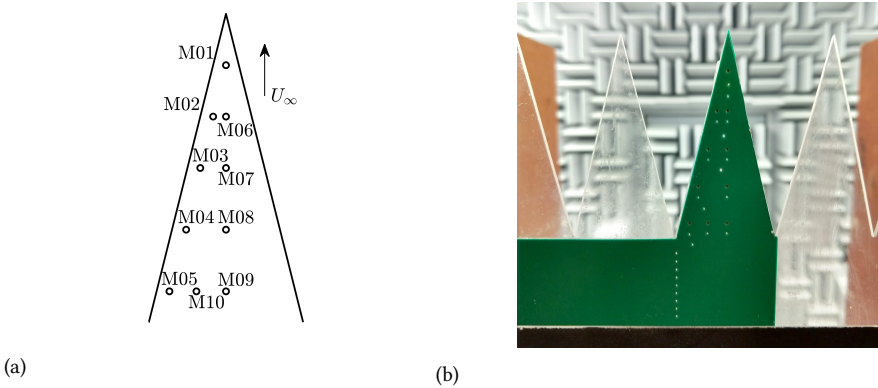


Figure 4.5: Schematic description of the surface pressure sensors on the trailing-edge sawtooth (a). Photograph of the PCB integrated with the trailing-edge insert (b).

non-intrusive instrumentation of the serration. Sensors are calibrated against a reference LinearX M51 microphone by measuring simultaneously an acoustic field band-passed within 50 Hz and 5 kHz (microphone linear range). The sensitivity of the microphones in average is of 18.4 mV/Pa with a variance in the estimations for each sensor in the order of 0.14 mV/Pa. This level of variance points to an uncertainty on the pressure estimations of ± 0.5 dB (95% reliability). It is important to highlight that this level of uncertainty is modified by other factors, such as temperature variations and the post-processing technique, e.g. the Welch's method. Table 4.3 summarizes the main characteristics and uncertainties on the analyses carried out with the sensors. Surface pressure data are recorded at a rate of 51.2 kHz during 30 seconds using a National Instruments cDAQ-9189 chassis and NI-9234 boards.

FAR-FIELD ACOUSTIC ARRAY

Acoustic measurements are carried out with a 64-microphone array, visible in Figure 4.6. The array features a modified Underbrink spiral configuration, optimized to reduce beamwidth and minimize sidelobe levels for applications in the A-Tunnel

[77]. The array uses G.R.A.S. 40PH microphones connected to a dedicated National Instruments PXIe system equipped with 4 PXIe-4499 boards. Data is acquired at 51.2 kHz for 30 seconds. The centre of the array is placed at 1 m distance from the model half-chord, resulting in an angle of 25° between the central microphone and the trailing edge. Post-processing is carried out with the conventional beamforming technique (CBF) described by Sijtsma [72]. The time series is converted into a matrix of cross-spectral terms (CSM) to estimate source levels at desired locations within the model mean plane using the steering vector formulation I from the work of Sarradj [73]. Correction of the effect of the flow velocity on the acoustic wave propagation is carried out based on the average velocity between the source and the microphone [72]. The spurious noise produced by the tripping device is eliminated by removing the main diagonal of the CSM, containing the microphone auto-spectra. This process is important to reduce uncorrelated sources but also to avoid the contamination of the source maps by other acoustic sources [72]. Sound power levels at the trailing-edge region are estimated by the source power integration (SPI) procedure [120] in a $100 \times 100 \text{ mm}^2$ area centred around the trailing-edge position ($x_1 = 1h$).

4

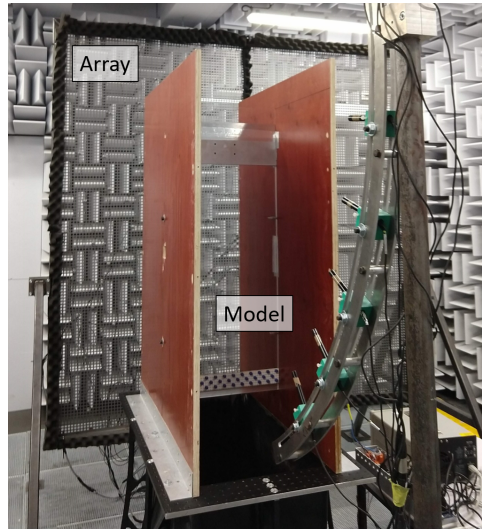


Figure 4.6: Experimental set-up for the acoustic microphone array measurements at the A-Tunnel.

4.2 HIGH-REYNOLDS AIRFOIL STUDY

This study aims at describing the properties of the wall-pressure on the surface of a serrated trailing edge mounted on an airfoil at high Reynolds number conditions, representing flow conditions similar to the ones observed at the tip of the blade

during the operation of a wind turbine. The experiments are carried together with the benchmarking efforts from the BANC workshop shown in Luesutthiviboon [112]. The measurements of the wall-pressure fluctuations over the serrations under different flow conditions are used to first assess the turbulent conditions past a serrated trailing edge in Chapter 5, and to propose a physical description for the variation of the wall-pressure fluctuations across the surface of the serration surface shown in Chapter 5.

4.2.1 MODEL GEOMETRY

The NACA 63₃-018 airfoil profile is symmetric with a maximum thickness-to-chord ratio of 0.18 at $x_1 = 0.66c$. This airfoil profile is chosen due to its similarities with wind-turbine blade airfoil sections and the advantages of testing with a symmetric airfoil. The wing model is manufactured for the model has a span of $b = 2.22c$ and it was manufactured by *Deharde* using sheet metal skins covering rib and stringer structures [112]. The model has a chord of 0.9 m and a span of about 2.0 m, limited in the wind tunnel as the section is only 1.25 m high. The trailing-edge of the model is of $1\%c$, corresponding to 0.9 mm. Figure 6.5a shows the model mounted inside the Kevlar test section of the wind tunnel.

A sawtooth serration of 90 mm height ($2h$), 45 mm wavelength (λ), 1 mm thickness, and 2 mm radius around the edges is manufactured by laser cutting and bending of a steel sheet. Since the model was not manufacture for testing with trailing-edge serrations, the add-ons are fixed from one side of the model, and the bend angle corresponding to the trailing-edge one (3.2°) is created to align the serrations with the airfoil chord. The size chosen for the serration follows the work of Gruber et al. (2011) [11], that suggests that meaningful noise reduction is achieved for serrations of $2h/\delta > 2$, and $2h/\lambda = 2$.

4.2.2 FLOW FACILITY

The Low-Turbulence Tunnel (LTT) facility of TU Delft is a closed-circuit wind tunnel with a contraction ratio of 17.8 (Figure 4.8). Without model, the wind tunnel can create stable flow conditions between 20 and 70 m/s, the turbulence intensity varies from 0.015% to 0.07% [121]. The model is mounted on a built-in turntable of the exchangeable octagonal test section which is integrated into the LTT circuit. The test section has the width, height, and length of $2.00c$, $1.39c$, and $2.88c$ (1.8, 1.25, 2.5 m), respectively. Since the airfoil span of 2 m could not fully fit in the section, the span is constrained by the test section height. The actual aspect ratio of the airfoil therefore became 1.4, with the remaining portion of the span outside the flow.

For this particular test section, the wall panels were treated with Kevlar-covered melamine wedges to minimize acoustic reflections. An acoustically transparent



Figure 4.7: BANC NACA 63₃-018 2D wing model mounted inside the Kevlar test section of the LTT wind tunnel.

Kevlar window was installed on the side panel of the section where a microphone array was placed. Figure 6.5a shows the airfoil mounted in the LTT section. Acoustic results from this campaign are not shown in the remainder of this work. Those can be found in the benchmark work of Luesutthiviboon et al. (2022) [112], which also includes background noise properties of the wind tunnel facility and studies of the transmission loss properties of the acoustically transparent window.

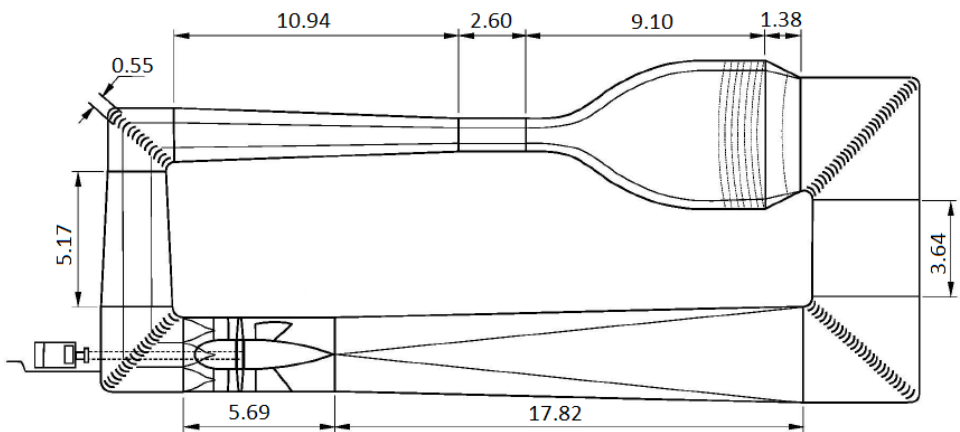


Figure 4.8: Low Turbulence wind Tunnel (LTT) circuit.

U_∞ [m/s]	Re_c	α [°]
17	1,000,000	[-10:1:10]
34	2,000,000	[-10:1:10]
51	3,000,000	[-10:1:10]

Table 4.4: Flow conditions selected and available dataset of the NACA 63₃-018 LTT wind tunnel campaign.

4.2.3 CONFIGURATIONS AND FLOW CONDITIONS

The model is tested at speeds of 17, 34, and 51 m/s, corresponding to Reynolds numbers of 1, 2, and 3 million, and at angles of attack (α) from 0 to 10° in steps of 1°. For the benchmark activities, lower Reynolds numbers are achieved with a smaller sized model at the A-tunnel in Delft University of Technology [90], and higher ones at the Poul la Cour facility in DTU. The smaller model corresponds to the one used in the third campaign described in this chapter. For the analysis carried in this work, the model is tripped at 5% c at the pressure side with 0.8 mm zig-zag trip and at the suction side with 0.4 mm zig-zag trip. Laminar-to-turbulent transition at the tripping location is verified under all conditions with an stethoscope. Table 4.4 summarizes the available data conditions obtained from the campaign.

4.2.4 INSTRUMENTATION AND MEASUREMENT TECHNIQUES

SURFACE PRESSURE AND WAKE RAKE MEASUREMENTS

Steady surface pressure distributions were measured via built-in static pressure taps. The model has a total of 197 pressure taps. Due to the model installation in the LTT test section, the center of the main pressure tap row was not exactly in the middle of the test section, but at about 1 c from the bottom wall. This main row has 101 pressure taps with a spanwise angle of 10°, to avoid flow interference from the upstream taps to contaminate the measurements.

The main row is used to assess the distribution of the pressure coefficient (c_p) along the airfoil and to compute the lift coefficient from this campaign. Three other streamwise-oriented rows spaced of 0.28 c from the main row with 16 taps are used to confirm the two-dimensional properties of the flow along the span. The pressure taps are connected to a DTC pressure system featuring 6 ESP-HD scanners with selected ranges for the application (± 2 Pa). The lift coefficient c_l is computed from the closed line integral of the pressure coefficients c_p along the airfoil outline s , following equation (4.3)

$$c_l = \frac{\hat{\mathbf{n}}_\alpha}{c} \cdot \oint_s c_p \hat{\mathbf{n}}_s ds, \quad (4.3)$$

in the equation $\hat{\mathbf{n}}_\alpha$ and $\hat{\mathbf{n}}_s$ represent the unit vectors that are orthogonal to the

airfoil angle of attack and to the airfoil surface respectively.

To estimate the drag from the model, a wake rake is used. The drag coefficient is obtained from the momentum deficit in the wake downstream of the model according to equation 4.4. In the equation, c_p denotes the pressure coefficients at the wake rake location, the subscripts s and t in $c_{p,s}$ and $c_{p,t}$ refers to the measured static and total pressures, respectively.

$$c_d = \frac{2}{c} \int_{\text{wake}} \sqrt{c_{p,t} - c_{p,s}} \left(1 - \sqrt{c_{p,t}}\right) dx_2 = 2 \frac{\theta_{\text{wake}}}{c}, \quad (4.4)$$

The equation is equivalent to the momentum thickness across the wake (θ_{wake}) normalized by the chord, as shown in the equation.

4

The wake rake used in the LTT facility has 67 total pressure and 16 static pressure tubes and is placed $x_1 = 0.67c$ downstream from the trailing edge. A traverse system is used to center the rake with the wake and, during acquisition, to average the drag along the span of the model ($\pm 0.16c$). The distance between the total pressure tubes varies along the rake, and, in the center, the tubes are spaced by 3 mm, with the whole rake spanning for 500 mm.

Aerodynamic corrections are applied to the measurements following the works of Timmer and Garner et al. [82, 121]. Nevertheless, results concerning different angles of attack mostly refers to the geometrical angle of attack. Still, the modifications applied to the test section wall to improve its acoustic properties may affect the flow conditions and are therefore assessed. Aerodynamic measurements of the baseline airfoil are carried with both Kevlar and hard-wall configurations. Of major concern, while one side (the wall facing the suction side at positive angles of attack) of the test section is a Kevlar-Melamine panel with a solid back plate for the absorption of the acoustic waves, the opposite side (the wall facing the pressure side at positive angles of attack) is left with a single Kevlar panel in order to allow access for the microphone array measurements. This can cause asymmetry between the positive and negative angles of attack tested. Figure 4.9 shows the comparison of the c_p distributions and c_l curve obtained in both test sections. Predictions from X-Foil are also shown in the figures. From Figure 4.9a where c_p distributions at $\alpha_{\text{eff}} \approx \pm 8^\circ$ are compared, a slightly smaller suction peak is captured with the Kevlar walls. The permeable walls of the Kevlar section leak air from the ambient room to the test section when the pressure difference is significant, consequently reducing the suction peak. The difference between positive and negative angles of attack is also shown. Using the hard walls as reference, the Kevlar walls cause a small decrease in the lift (c_l in Fig. 4.9b) for angles above $\alpha_{\text{eff}} \approx 10^\circ$ at the negative condition caused by the relatively lower suction peak. Observable difference in c_l can only be found at $\alpha_{\text{eff}} < -10^\circ$. This is beyond the range of angles considered in the analysis of Chapters 5, and 6.

Additionally, the influence of the serration on the pressure distribution, lift, and drag of the model must be assessed. Figure 4.10 shows the c_l , c_d , and c_p distribution for conditions with and without the serrations. It can be observed that, apart from conditions of high loading ($\alpha_{\text{eff.}} \geq 8^\circ$), where the lift of the serrations modify the pressure distribution and lift, the presence of the serrations do not affect significantly the aerodynamic characteristics of the airfoil. It is important to note that the c_l shown in the graph is obtained from the integration of the pressure over the airfoil surface, and so the lift of the serration is not included. Nevertheless, the presence of the serrations seem to delay separation and increase the lift for effective angles above 10° .

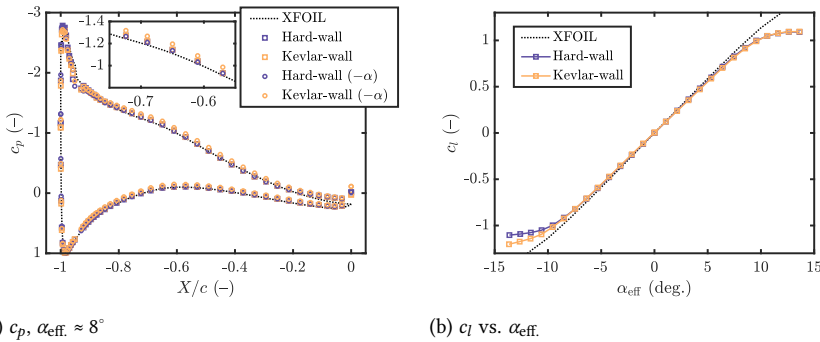


Figure 4.9: Comparison of c_p distribution (a), and c_l (b) from the LTT test with hard-walls and Kevlar-walls of the baseline NACA 633-018 airfoil at $Re_c = 3 \times 10^6$.

EMBEDDED MICROPHONE SENSORS

22 Sonion P8AC03 unsteady pressure sensors are placed over the sawtooth serrations as shown in Figure 4.11. The sensors capture the pressure fluctuations on the surface of the serrations, used for building the spectral and correlation statistics shown in Chapters 5, and 6. A 0.4 mm thick printed circuit board (PCB) is mounted on top of the trailing-edge insert. The insert is manufactured to house the sensors inside, avoiding interference from both sides of the model. The multiple sensors and selected coordinates allow for the following analyses:

- Wall-pressure spectrum around the serration edges, using the sensors along the edge;
- Streamwise correlation and convective velocity, from the streamwise oriented central row;
- Spanwise correlation length, from the 4 spanwise rows along the serration;

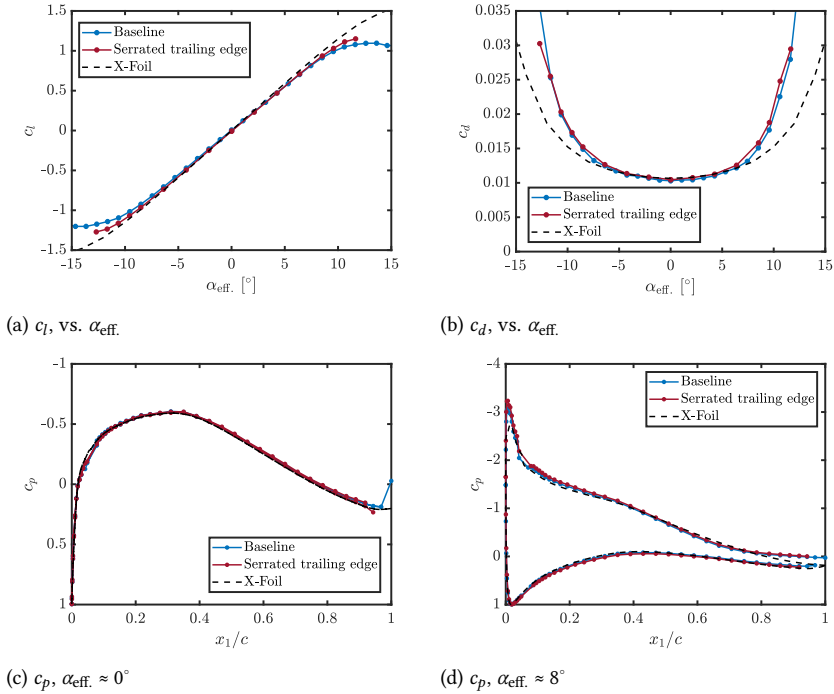


Figure 4.10: Comparison between conditions with and without trailing-edge serrations. (a) c_l , vs. α_{eff} , (b) shows the c_d , vs. α_{eff} . (c) and (d) shows the pressure distribution along the airfoil surface for angles of $\alpha_{eff} \approx 0^\circ$, and $\alpha_{eff} \approx 8^\circ$ respectively. Measurements are taken at $Re_c = 3 \times 10^6$. X-Foil estimations are also provided for reference.

- Distribution of the wall-pressure fluctuations over the serrations, from the data of the sensors interpolated over the serration surface (symmetry is assumed along the x_3 axis).

The calibration of the sensors is carried out with a Linear-X M51 microphone measuring an acoustic field close to the serrations. The Linear-X microphone is previously calibrated with a G.R.A.S. 42AA pistonphone. Acquisition is performed with NI cDAQ-9234 boards attached to a synchronous NI cDAQ-9189 chassis. The data is sampled at a rate of 51,200 samples per second for 20 seconds.

PARTICLE IMAGE VELOCIMETRY

A stereo PIV technique is used to capture the flow field near the trailing edge, used to extract the boundary-layer properties at the trailing-edge region. Two Imager sCMOS cameras (double shutter with 120 ns interframe time, 16 bits, 5MP) are placed outside the test section, 0.8 m apart from the illumination plane, one aligned with the trailing-edge line, and the second one forming an arc 20° upstream of

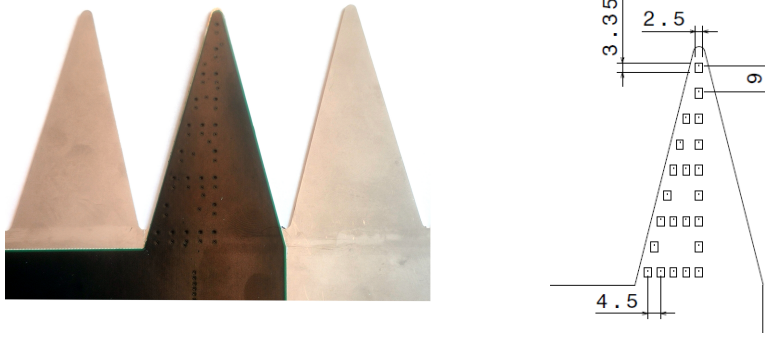


Figure 4.11: Instrumented trailing edge mounted on top of the model trailing edge and location of the unsteady pressure sensors at the trailing-edge serration.

the first. Imaging access is given by placing a Plexiglas wall on the turn-table. A Quantel Evergreen double pulsed laser (200 mJ, 15 Hz) is fixed on one of the side walls and a laser sheet is created normal to the model plane. Measurements are carried out for the baseline at $\alpha = 0^\circ$, and 4° geometrical angles of attack in order to extract the boundary-layer profiles at the trailing edge. Figure 4.12 shows an illustration of the PIV setup and Table 4.5 summarizes the characteristics of the PIV technique employed.

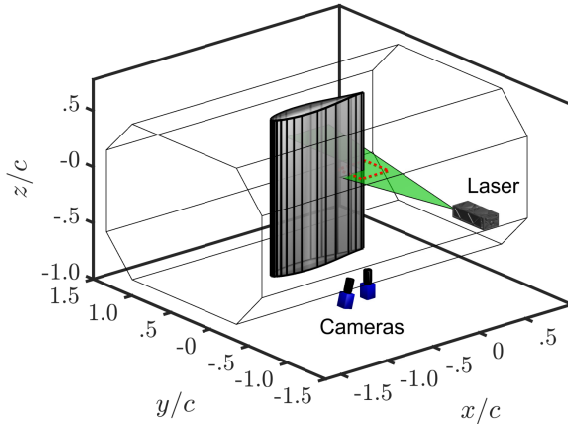


Figure 4.12: BANC NACA 633-018 test setup illustration with model, test section, and PIV setup.

Table 4.5: Description of the Stereo PIV setup for the measurement campaign.

Parameter	Value	
Digital image resolution	18	px/mm
Numerical aperture	$f/11$	
Field of view ($x_1 \times x_2$)	150×100	mm
Number of images recorded	1,000	
Maximum particle displacement	15	px
Vector resolution	0.3	mm
Uncertainty in instantaneous velocity	0.7	% U_∞

4

4.3 SENSITIVITY-BASED STUDY OF AN AIRFOIL WITH DIFFERENT SERRATIONS INSERTS

This study assesses the acoustic emissions of an airfoil fitted with trailing-edge serrations of different geometries. Focus is given on creating a sensitivity-based study where serrations with different geometries are manufactured and tested under different flow speeds and airfoil angles of attack. Acoustic measurements are carried for each condition and configuration to create the data that is basis for the parametric study shown in Chapter 7.

4.3.1 MODEL GEOMETRY

The model used is based on the same symmetric 2D NACA 63₃-018 airfoil but with 200 mm chord and 400 mm span. This airfoil is chosen following the same efforts to create facility-validated benchmark data [112]. Besides, the model symmetry allows assessing the radiated noise from the trailing edge without aerodynamic loading conditions on the serrations (airfoil at $\alpha = 0^\circ$) and comparing it with conditions with aerodynamic loading. Besides, the low trailing-edge angle (δ_{TE}) of about 3.2° is appropriate to reduce installation effects in the wedge junction between the serration and the airfoil trailing edge. The trailing-edge section is separated at 80% c to allow the installation of different inserts. An insert with the baseline airfoil straight trailing edge is used as the reference configuration while another insert with two clamps is used to allow the serrated trailing edges to be tested. The baseline insert has a trailing-edge thickness of about 0.15 mm, while the serrated trailing-edges inserts are 1 mm thick. The serrations have their centre aligned with the baseline trailing-edge location and are manufactured via laser cutting of a steel sheet. Figure 4.13 shows a schematic of the setup and the model installed in the wind-tunnel facility.

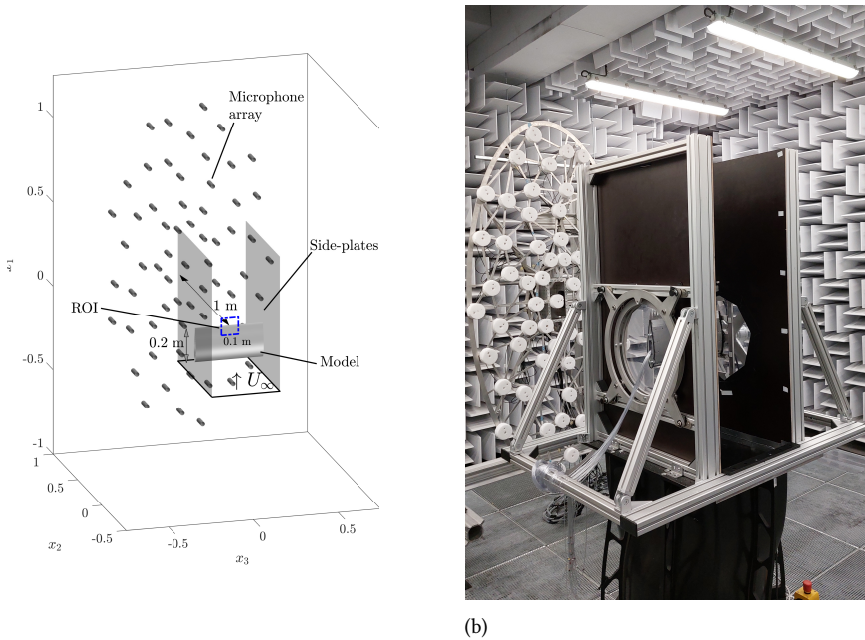


Figure 4.13: Experimental setup for acoustic measurements. (a) Schematic of the experiment, and (b) picture of the model mounted in the wind-tunnel facility.

4.3.2 FLOW FACILITY

Experiments are conducted in the aeroacoustic wind-tunnel facility of the Delft University of Technology (A-Tunnel, Figure 4.2b). The open test section wind tunnel has an option of exchanging nozzles that allows controlling maximum speed and model dimensions. In this campaign, a rectangular 400×700 mm nozzle is selected, resulting in a maximum flow speed of 35 m/s. The test section is enclosed by an anechoic chamber where the acoustic measurements are carried out. The chamber is designed to avoid reflections from frequencies higher than 150 Hz. More details about the facility are shown in [90].

4.3.3 CONFIGURATIONS AND FLOW CONDITIONS

A zig-zag tripping tape of 0.6 mm height is placed at $5\%c$ on both sides of the model to force the laminar-to-turbulent transition location at all tested conditions, following the benchmark work of Luesutthiviboon (2022) [112]. For most of the analyses carried out, the model is tested at three different flow speeds (15, 20, and 30 m/s). Measurements are taken at angles of attack (α) from 0° to 10° in steps of 1° , and from 10° to 20° in steps of 2° . This study mostly refers to the geometric angle of attack of the model. It is important to have in mind that open test sections have

strong influence on the flow and the effective angle of attack of the section (α_{eff}) is, in turn, much smaller. According to Luesutthiviboon (2022) [112], the effective angle of attack is compared to the geometric one (α) according to equation 4.5.

$$\alpha_{\text{eff}} \approx 0.67\alpha. \quad (4.5)$$

To capture the acoustic emissions from both the suction and the pressure sides, the measurements are carried out for positive and negative angles of attack. Table 4.6 summarizes the conditions of test.

U_∞ [m/s]	Re_c	α [°]
15	200,000	[-20:2:-12 -10:1:10 12:2:20]
20	270,000	[-20:2:-12 -10:1:10 12:2:20]
30	400,000	[-20:2:-12 -10:1:10 12:2:20]

Table 4.6: Flow conditions selected and available dataset of the acoustic campaign carried out.

A series of different trailing-edge serration geometries and sizes are tested during this campaign. The serrations are varied by modifying their scaling (height, and wavelength based on a sawtooth design), geometry (for the analysis of sawtooth vs. concave-shaped serrations), and comb size (for the analysis of combed-sawtooth serrations). A reference serration design is defined with a height $2h = 30$ mm, and a wavelength $\lambda = 15$ mm ($2h/\lambda = 2$). The reference serration dimension follows Arce Leon et al. (2016) [122], which has demonstrated adequate noise reduction levels for serrations with $2h/\delta \approx 4$ (δ based on the $\alpha = 0^\circ$ condition), and $2h/\lambda = 2$. The other geometries are built upon variations of this reference geometry, creating a sensitivity-based study using a one-factor-at-a-time approach.

Table 4.7 shows the designs used for the study of the geometric scaling of the sawtooth serrations. For the analyses, three parameters are chosen, namely the serration height ($2h$), wavelength (λ), and aspect ratio ($2h/\lambda$). For each of the parameters, 4 serrations exist where its value remains the same while the other parameters are changed individually. This means that 4 geometries have the same height ($2h = 30$ mm) but different wavelengths and aspect ratios, other 4 have the same wavelength ($\lambda = 15$ mm) but different heights and aspect ratios, and other 4 have the same aspect ratio ($2h/\lambda = 2$) but different heights and wavelengths.

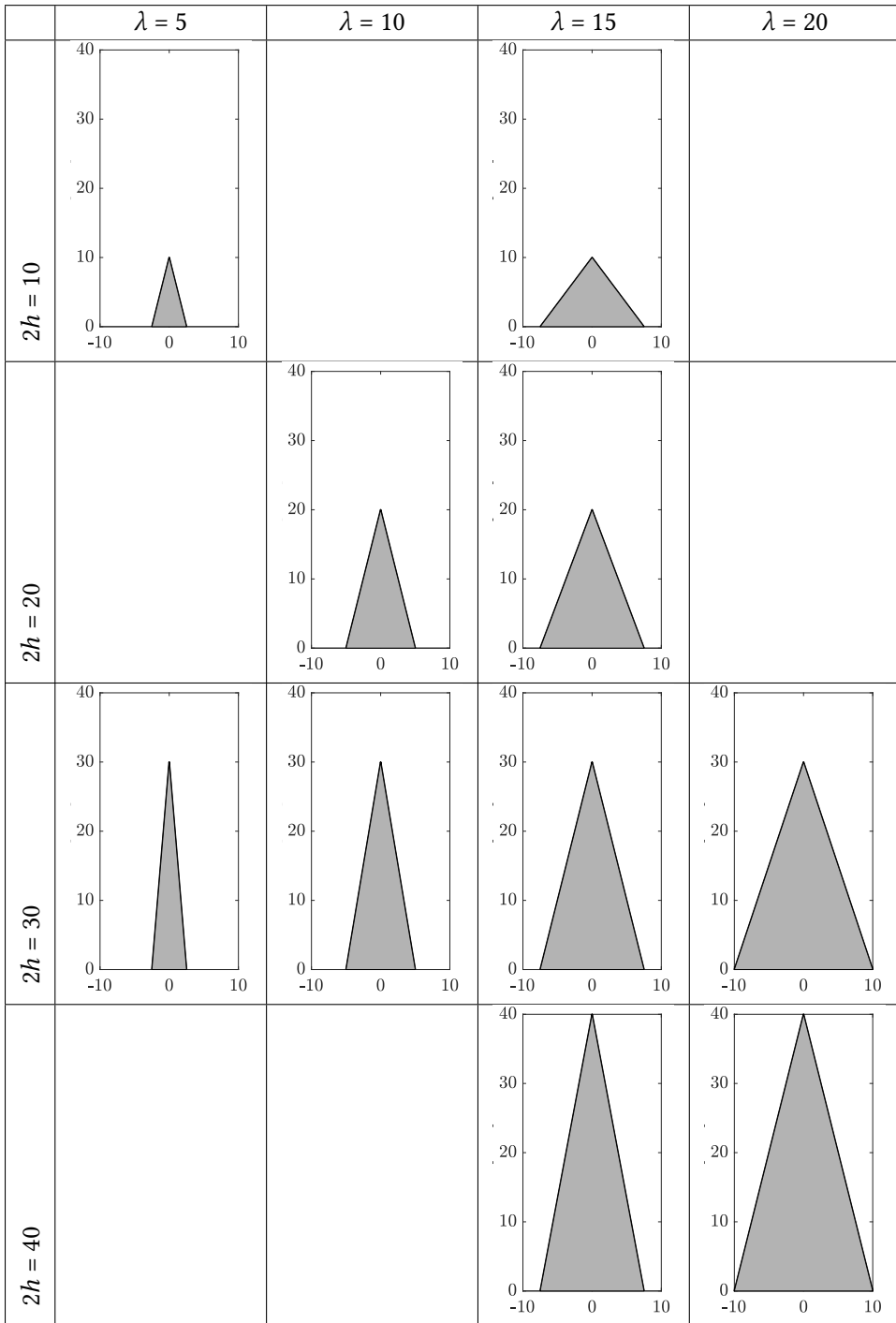


Table 4.7: Geometry of the sawtooth serrations selected for the scaling study of trailing-edge serrations shown in Chapter 7. Dimensions are shown in millimeters.

The geometric changes are based on the concave-shaped serrations (ogee-shaped serrations) described in Avallone et al. (2017)[16], and Kholodov et al. (2020)[64]. The geometries are generated following equation 4.6. In the equation, the parameter n controls the geometry of the serration. According to the equation, $n = 1$ results in the sawtooth design. If $n < 1$, the serration presents a concave shape, i.e. the angles at the root are higher than at the tip. If $n > 1$, the serration presents a convex shape with angles at the tip higher than the ones at the root. In turn, n is controlled based on the desired percentage of surface area compared to the total area of the trailing edge, referred to in this work as the solidity factor (SF), following equation 4.7. Similarly to the previous study, 4 different geometries are selected, with solidity factors of 0.2 (convex-sawtooth serrations), 0.5 (reference sawtooth serrations), 0.7, and 0.8 (concave-sawtooth serrations). Table 4.8 shows the geometries selected.

$$x_1(x_3) = \begin{cases} 2h \left(\frac{2x_3}{\lambda} + 1 \right)^n, & -\frac{\lambda}{2} \leq x_1 \leq 0 \\ 2h \left(-\frac{2x_3}{\lambda} + 1 \right)^n, & 0 < x_1 \leq \frac{\lambda}{2} \end{cases} \quad (4.6)$$

$$SF = \frac{\int_{-\lambda/2}^{\lambda/2} x_1 dx_3}{2h\lambda} = \frac{1}{n+1}. \quad (4.7)$$

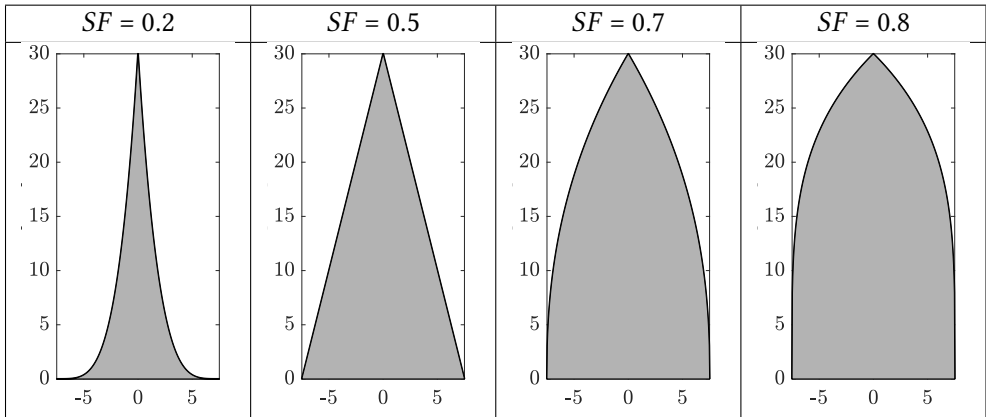


Table 4.8: Concave vs. convex serration geometry parametrization based on the solidity factor (SF) described in equation 4.7. Dimensions are shown in millimeters.

For the combed sawtooth design, two parameters are selected for the study, namely the number of combs per wavelength (N_{teeth}), and the ratio between the comb pitch and the open pitch. The latter affects the solidity factor (SF) more significantly and is described using the latter parameter. Geometries are created

for each of the two parameters as shown in Tables 4.9 and 4.10. It is important to highlight that the combed-sawtooth designs corresponding to $N_{\text{teeth}} = 5$ in Table 4.9, and $SF = 0.75$ in Table 4.10 are the same.

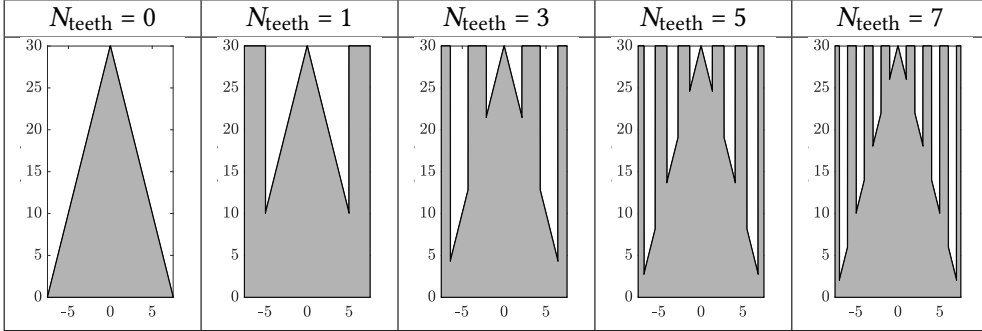


Table 4.9: Combed-sawtooth geometric parametrization based on the number of combs per wavelength (N_{teeth}). Dimensions are shown in millimeters.

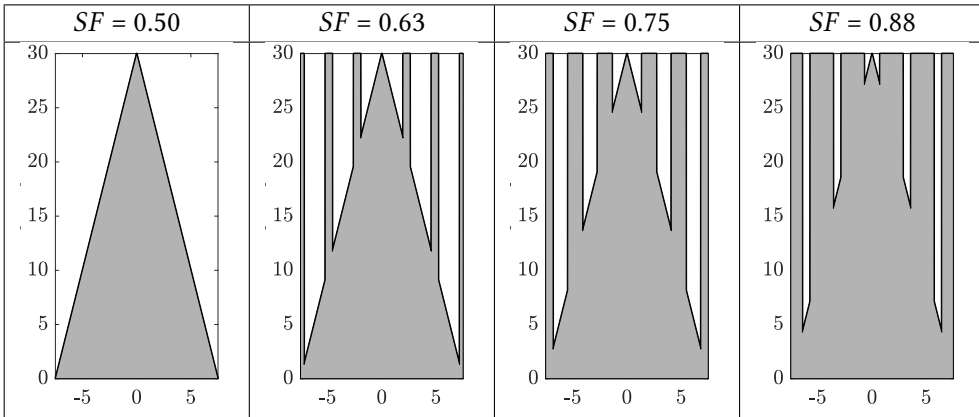


Table 4.10: Combed-sawtooth geometric parametrization based on the solidity factor (SF) for $N_{\text{teeth}} = 5$. Dimensions are shown in millimeters.

4.3.4 INSTRUMENTATION AND MEASUREMENT TECHNIQUES

SURFACE PRESSURE AND BOUNDARY-LAYER PITOT RAKE

A pitot rake is installed at the model to measure the boundary-layer properties at the trailing-edge region. The rake contains 12 total pressure tubes along the wall-normal direction and 2 static tubes on each side of the model (upper and lower side). The measurements are used to assess the boundary-layer velocity profile at mid-span and 90% c location for the baseline configuration. The effect of the

tubes in proximity to the airfoil walls is corrected following the work of Bailey (2013) [123]. Figure 4.14a shows the setup of the measurement and Figure 4.14b the resulting boundary-layer displacement thickness from the experiment. The displacement thickness is used in the remainder of this work to characterize the acoustic emissions at the trailing edge.

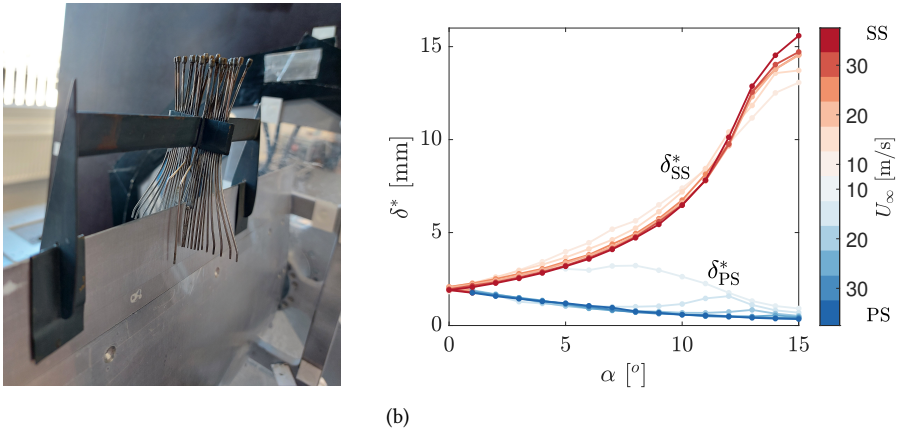


Figure 4.14: Experimental setup of the pitot-rake (a), and measured boundary-layer displacement thickness (b).

FAR-FIELD ACOUSTIC ARRAY

The noise levels of the serration designs are assessed through measurements with a microphone array. The schematic in Figure 4.13a shows the setup for the acoustic measurements. The microphone array used consists of 64 G.R.A.S. 40PH microphones connected to a PXIe system with 4 PXIe-4499 acquisition boards. Details of the apparatus and data acquisition parameters are reported in Table 4.11.

Number of microphones	64
Microphone type	G.R.A.S. 40PH
Frequency range	50 Hz to 20 kHz
Acquisition system	NI PXIe
Acquisition board	PXIe-4499 (x4)
Voltage range	± 10 V
ADC converter precision	24 bits
Array x -span	2.0 m
Array y -span	1.0 m

Table 4.11: Setup of the acoustic array measurement and acquisition system.

The data acquired are processed with the conventional beamforming technique described in Sijtsma (2010) [72]. The steering vector formulation number I from Sarradj (2009) [124] is selected and the effect of the flow velocity is corrected following the simplification proposed in Sijtsma (2010) [72]. Resulting source maps of the baseline serration are shown in Luesutthiviboon et al. (2022) [112]. The trailing-edge sources can be observed for frequencies from 400 to 5,000 Hz.

To better isolate the noise from the trailing edge, a source power integration (SPI) procedure is used. Sources on the mid-span of the trailing edge are integrated inside a region of $100 \times 100 \text{ mm}^2$ ($0.5c \times 0.5c$). For conditions under angles of attack, the spectra presented are averaged from the results taken from both the pressure and suction side, following the procedure discussed in Ref. [125].

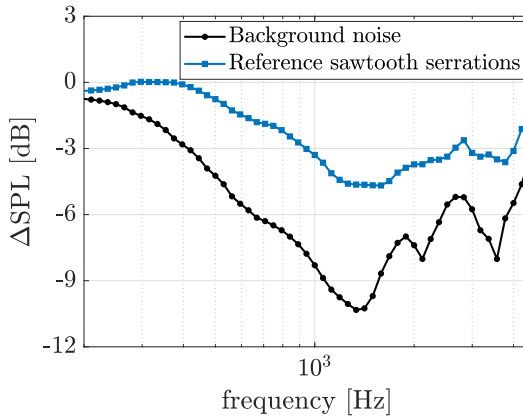


Figure 4.15: Measured difference between background noise and baseline noise levels (black curve) obtained with source power integration from the centre span region. The difference between the reference sawtooth serration design and the baseline noise levels is shown in blue. Negative values of ΔSPL indicate noise reduction. Background noise measurements are obtained by removing the model from the test section while measuring at the same flow speed.

Figure 4.15 shows the difference between the noise levels of the baseline airfoil and the same measurements carried out for the test section without the model, taken here as the reference background noise. The spectra are presented in twelfth-octave bands. Negative values indicate that the background noise is lower than the baseline noise of the airfoil (black line in the graph). The black line represents the noise reduction floor for the measurements. Measurements of serrations that would reduce more noise than the background levels are compromised due to the background noise. In the same figure, the noise reduction obtained with the reference serration geometry is shown in blue. The results show that the noise levels from the serrated trailing edge are still 2-3 dB above the background ones, indicating that the measurements are not hampered or affected by the facility

background levels within the frequency range of interest.

5

AERODYNAMIC AND ACOUSTIC PROPERTIES OF SERRATED TRAILING EDGES

5

This chapter covers the second objective of this thesis, which is to assess the main secondary flow features that are introduced when serrations are retrofitted on the trailing edge of a model. For that, aerodynamic and acoustic measurements are conducted on a sawtooth-shaped trailing edge installed on a zero-pressure gradient model and on a NACA 63₃-018 airfoil. The first study aims at measuring the flow over the serrated trailing edge under a controlled environment while the second focuses on the observed behaviour of serrations on a realistic setup. Focus is given to the variations of the wall-pressure fluctuations on top of the serration surface as, following Chapter 2, this is the flow quantity directly related to the scattered noise by the work of Amiet (1976) [27]. For the first study, the turbulent flow across the trailing edge is inspected by time-resolved three-dimensional velocity field measurements obtained from 4D-PIV, while the wall-pressure fluctuations are measured with surface-embedded microphones. For the second model, surface-embedded microphone sensors are used to confirm the observations on a representative and high-Reynolds measurement. Results discuss the relation between the velocity fluctuations over the serrations, the surface pressure fluctuations, and the far-field noise spectra. Focus is given to the modification between the cases without aerodynamic loading, and with aerodynamic loading, induced by changing the angle between the incoming flow and the serrations, representative of a change in the flap angle of the serrations installed or of a change in the angle of attack of the airfoil model. The aerodynamic analysis discusses the effect of counter-rotating vortex pairs, generated by the pressure imbalance across the edges of the serrations under loading. It is shown that the interaction of these vortices with the incoming turbulence affects the intensity of the wall-pressure spectrum at the outer rim of the serration surface. On the suction side, the intensity of the pressure fluctuations from the incoming boundary layer dominates over that induced by the vortex pairs. On the pressure side, instead, the velocity gradient prescribed by the vortex pairs produces a significant increase in the wall-pressure fluctuations around the edges. The resulting spatial distribution of the wall-pressure fluctuations directly affects the far-field noise. Scattering predictions carried out with the wall-pressure fluctuations in the centre and root (on the suction side) are used to describe the comparison between measured noise and flow field over the serration surface.

5.1 EXPERIMENTAL SETUP AND METHODOLOGY

In the first part of this work (Section 5.4), the isolated behaviour of the flow over a serrated trailing-edge is assessed. This is realized from the measurements over serrated trailing-edges mounted on a flat-plate model, as described in Section 4.1. An assessment of the validity of the results obtained in the first study is carried out from a high-Reynolds study of an airfoil equipped with trailing-edge serrations, shown in Section . This study follows the experimental efforts with the benchmark

airfoil model NACA 63₃-018 tested at Reynolds numbers from 1 to 3 million, as described in Section .

5.2 FLOW AND ACOUSTIC PROPERTIES FROM ISOLATED TRAILING-EDGE SERRATIONS

The overall contribution of the serration on the far-field noise measurements is presented and compared to the straight configuration (Figure 5.1). As can be seen from the results, the serrated trailing-edge geometry is responsible for reducing the far-field noise compared to the straight trailing edge at almost all the tested conditions. Noise reduction over the entire frequency range is observed for both the $\delta_f = 0^\circ$, and the $\delta_f = 10^\circ$ cases. However, for the largest value of the flap angle ($\delta_f = 15^\circ$) the noise from the serrated trailing edge increases when $f\delta^*/U_\infty > 0.3$. This result is consistent to previous works from Arce León et al [67], and Gruber et al. [11] who ascribe it to the alterations of the flow caused by the serrations under loading.

An indication of the physical cause of the noise alterations is given by the time-averaged flow field over the trailing-edge serrations at $\delta_f = 0^\circ$, and $\delta_f = 10^\circ$, plotted in Figure 5.2. Planar contours of the time-averaged velocity magnitude in the centre of the serration are plotted together with iso-surfaces of positive and negative streamwise vorticity.

Three main flow regions can be identified, i.e. the incoming turbulent boundary layer over the serration surface, the developing wake along the gaps in-between the serrations, and the trailing vortices at the serration edges. At $\delta_f = 0^\circ$, streamlines deflection is barely observed. When the serrations are loaded ($\delta_f = 10^\circ$), the pressure mismatch between the suction and pressure side induces a pair of streamwise vortices along the serration edges. These vortices are visible in the figure from approximately 25% of the serration height. Similar to what was shown by Avallone et al. [15], the vortices are formed along the edges in the centre of the serration and are approximately aligned with the free-stream direction.

A visible deflection of the streamlines with respect to the $\delta_f = 0^\circ$ case is therefore introduced, indicating that the flow presents accelerations. As a consequence, velocity gradients are generated along the spanwise and wall-normal directions. Contrary to the wall-normal deflection, the spanwise one is relatively small to be seen from the pictures. To improve the visualization of this component, the regions where the streamlines have a spanwise velocity above $U_3 = +0.04U_\infty$ are represented in red, while the regions where this velocity component is smaller than $U_3 = -0.04U_\infty$ are represented in blue. For $\delta_f = 10^\circ$, on the pressure side, the streamlines deflect towards the gap of the serration because of the higher pressure along the serration centre line; on the suction side, the exact opposite happens

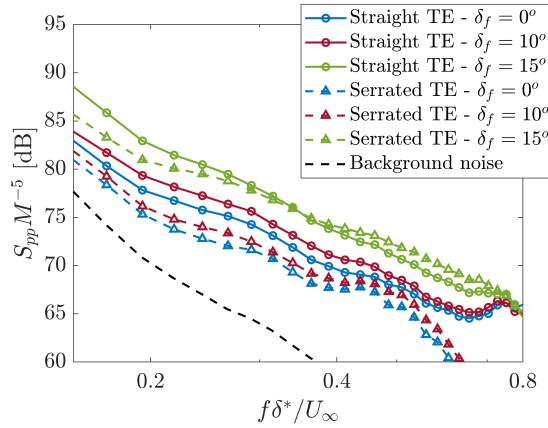
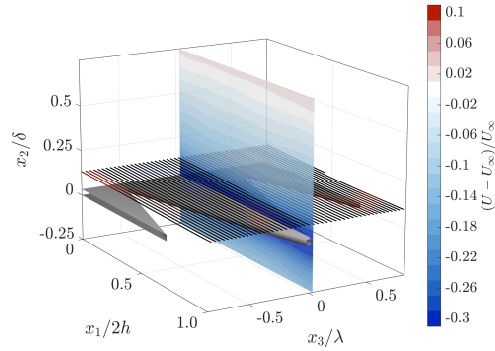


Figure 5.1: Acoustic noise levels estimated from the SPI procedure of the CBF maps. Measurements are performed with a straight and a serrated trailing-edge insert at $\delta_f = 0^\circ$, 10° and 15° .

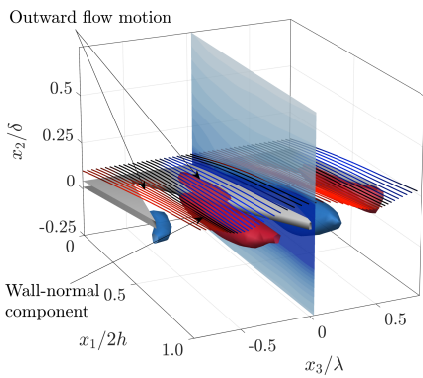
5

with a deflection towards the centre line of the serration region, highlighted by the inversion of the streamline colour pattern. The alterations of the streamlines demonstrate the presence of spanwise velocity gradients, which are accentuated along the edges of the serration. At this region, the flow direction is modified, with respect to the incoming flow direction, by about 4° along the spanwise direction and by about 6° along the wall-normal direction in the gap region. These deflections were observed by Arce León [67], who concluded that the noise increase cannot be explained by simply considering the altered flow direction on the scattering function of Howe [20]. From the work of Arce León [67], the increase in noise observed at high loading conditions was conjectured to have a direct relation with the flow distortions induced by the trailing vortices on the fluctuations near the edges of the serrations.

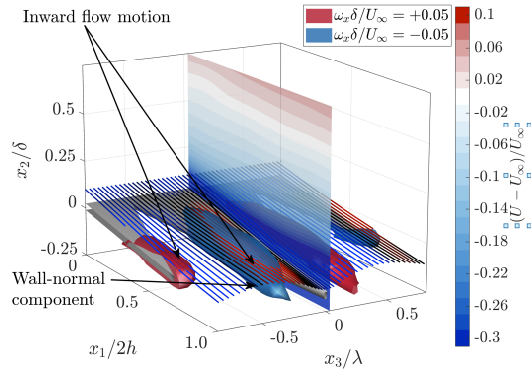
The spatial distribution of the turbulent intensity (TI) over the serration can be visualized in Figure 5.3 for $\delta_f = 0^\circ$, and $\delta_f = 10^\circ$. The plot shows two streamwise aligned planes, one at 25% and another at 75% of the serration height. At $\delta_f = 0^\circ$ the turbulence intensity near the wall attains about $8\%U_\infty$. From root to tip only a small dissipation occurs and no significant variation along the spanwise direction is captured. At $\delta_f = 10^\circ$ a region of high turbulence intensity emerges at the gap in between the serration. The intensity of the turbulent fluctuation at this region is stronger at the root and dissipates towards the serration tip, as observed in the numerical studies of Jones and Sandberg [14]. Turbulence intensity is as high as $15\%U_\infty$, about $2\%U_\infty$ higher than the one captured around the centre of the serration. Previous works [14, 67] concluded that the interaction between this region of increased turbulent flow and the accelerating vortex pairs field, ultimately



(a)



(b)



(c)

Figure 5.2: 3D visualization of the mean flow over the trailing-edge serration at $\delta_f = 0^\circ$ (a) and $\delta_f = 10^\circ$ from the pressure (b) and suction side (c). Isosurfaces of streamwise vorticity are shown in red ($\omega_x \delta^* / U_\infty = +0.05$) and blue ($\omega_x \delta^* / U_\infty = -0.05$). Streamlines of the flow at $x_2 / \delta = 0.1$. Black streamlines are undistorted, red and blue correspond to $U_3 \geq 0.04 U_\infty$ and $U_3 \leq 0.04 U_\infty$ respectively.

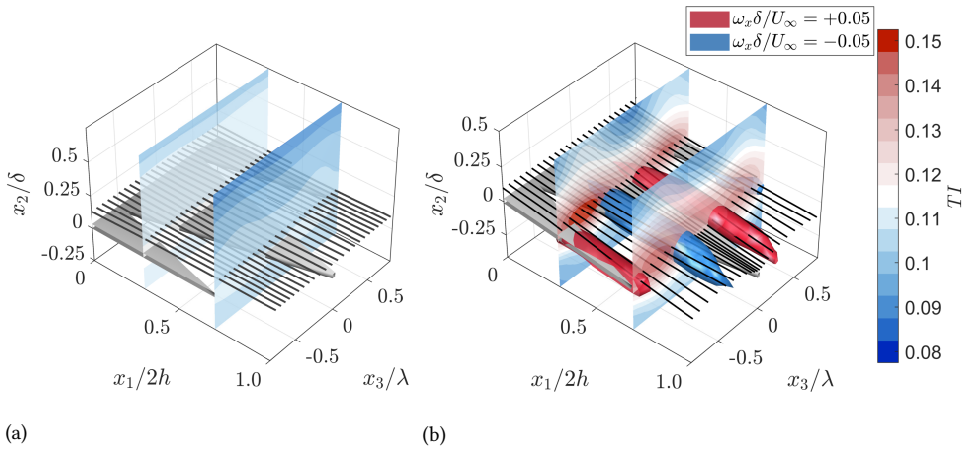


Figure 5.3: Spatial distribution of turbulence intensity (TI) at $\delta_f = 0^\circ$ (a) and $\delta_f = 10^\circ$ (b) by cross-sections at $x_1/2h = 0.25$ and 0.75 . Isosurfaces of streamwise vorticity as from Figure 5.2. Black lines show the streamlines of the flow at 8 mm from the wall.

5

affects the distribution of the wall-pressure fluctuations over the serration, causing the increase in noise observed for trailing-edge serrations under loading.

5.2.1 WALL-PRESSURE FLUCTUATIONS OVER SERRATIONS

The spatial distribution of the surface pressure fluctuations obtained from the installed microphones is illustrated in Figure 5.4. Columns correspond to varying incidence of the trailing-edge insert from $\delta_f = 0^\circ$ to $\delta_f = 15^\circ$ (both on the pressure and suction side). The analysis is presented for three selected frequency bandwidths. The chosen values of the frequency expressed in non-dimensional form are $f\delta^*/U_\infty = 0.1, 0.2,$ and 0.4 respectively. Data are reported in terms of the difference of Sound Pressure Level (ΔSPL) between the signal at each microphone and M09, i.e. the microphone located at the root of the serration ($x_1/2h = 0.1, x_3/2h = 0$), taken as a reference for the incoming wall pressure from the turbulent boundary layer. The graphs represent an illustration of the spatial distribution of the wall-pressure fluctuations on the serration surface. For visualisation purposes, the data points are spatially (linearly) interpolated such to yield the visualization with colour-contours. Linear extrapolation is applied towards the outer edges. Moreover, symmetry is assumed to complete the spatial distribution over the serration surface. The visualization clearly indicates a spatial variation of the surface pressure fluctuations along the streamwise as well as the spanwise direction. The latter indicates that assuming frozen turbulence is inadequate to accurately model the overall noise reductions from loaded serrations. It is hereby assumed that the modifications captured from the wall-pressure sensors are mostly caused by the modification

of the aerodynamic flow conditions. Given the low Mach number and the large separation between aerodynamic and acoustic wavenumbers, the acoustic field over the serrations is expected to remain uniform within the serration length.

At $\delta_f = 0^\circ$, only mild variations of pressure fluctuations are observed on the main body of the serration (up to the half-height). Towards the tip of the serration, a marked reduction of the pressure fluctuations is observed. Similar behaviour was reported by Avallone et al. [16] for the pressure RMS fluctuations. This behaviour is observed at almost all conditions and is ascribed to the diminished wall effect when flow structures are only partly bounded by the solid wall.

The trend is accentuated when considering the suction side for the $\delta_f = 10^\circ$ case and for Strouhal numbers $f\delta^*/U_\infty < 0.2$. At this condition, the higher incoming pressure fluctuations, compared to the $\delta_f = 0^\circ$ case, rapidly decrease from the root of the serration towards the serration edges because of the decreasing pressure gradients along the serration gap. On the pressure side, a noticeable increase of the pressure fluctuations with respect to the incoming one is captured at the edges of the central portion of the serration. This increase corresponds to the location of the vortex pair and mostly impacts the pressure fluctuations at 25-75% of the serration height. In the condition of highest loading ($\delta_f = 15^\circ$), this effect is most pronounced with significantly higher wall-pressure fluctuations along the edges of the pressure side and a minor increase also noted on the suction side.

The above discussion stresses the role played by the different flow regimes around the serration whereby three types of flow may be identified, namely the incoming turbulent boundary layer, the near wake region in-between the serrations, and the vortex pairs along the serration edges. When the aerodynamic loading is small, the pressure over the serration is ascribed only to the turbulent boundary-layer flow and the influence of the gap region. This yields a reduction in the pressure spectrum along the edges and tip of the serrations, as captured for the $\delta_f = 0^\circ$ case and on the suction side for the $\delta_f = 10^\circ$ test case.

At higher loading conditions, the increasing pressure fluctuations induced by the trailing vortices dominate over those transported within the turbulent boundary layer, and new regions with higher pressure fluctuations emerge along the edges of the serration. These regions appear to be concentrated at the central portion of the serration at lower frequencies, while they become stronger and extend towards the tip at higher frequencies, e.g. $f\delta^*/U_\infty = 0.4$. The influence of the vortex pairs is clear for the $\delta_f = 10^\circ$ case on the pressure side and for the $\delta_f = 15^\circ$ on both sides. The combination of these two patterns, viz. reducing wall pressure towards the tip and increasing levels along the edges, determines the distribution of wall-pressure fluctuations observed in the present experiments. The velocity gradients induced by the vortex pairs forming on the pressure side combined with the lower incoming pressure fluctuations from the FPG boundary layer, leads to a

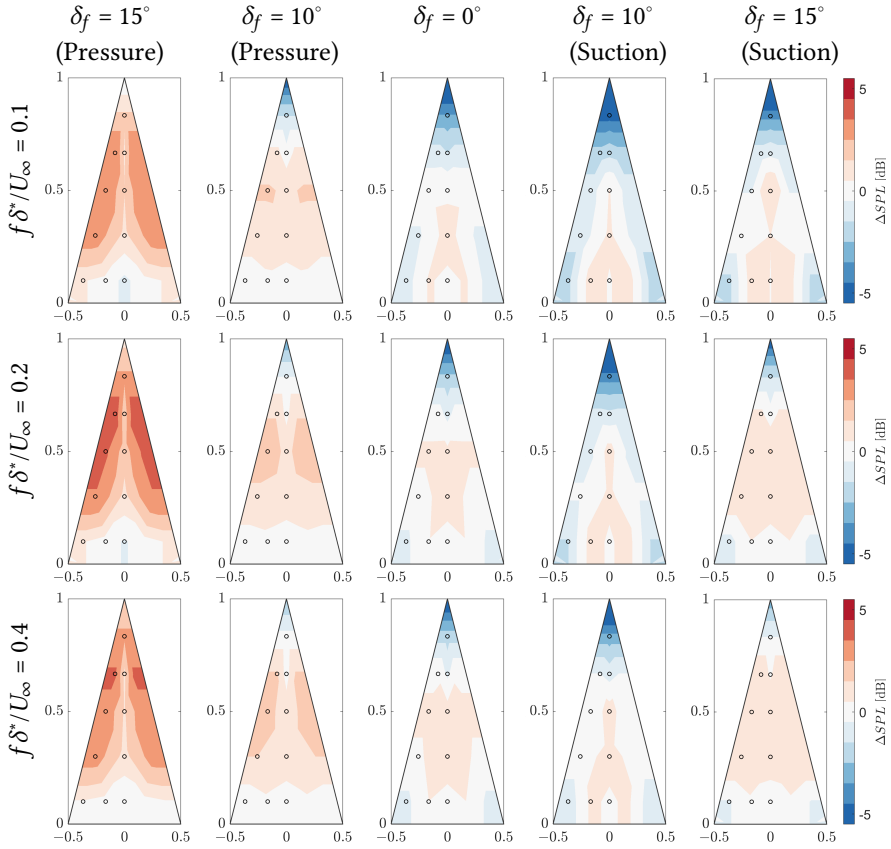


Figure 5.4: Surface pressure fluctuations along the trailing-edge serration relative to the incoming level (reference Mic 09). Trailing-edge incidence angle δ_f varies along columns. Strouhal number varies across rows. The circles represent the position of the sensors.

stronger spatial alteration of the wall-pressure fluctuations at this side, as discussed in Jones and Sandberg [14], and Arce León et al. [67]. On the other hand, the suction side perceives the influence of the shear along the edges only at extreme loading conditions ($\delta_f = 15^\circ$).

The effect of the aerodynamic mechanisms presented above on the spectral distribution of the wall pressure can be observed in Figure 5.5 where the wall-pressure spectra are presented for different values of the flap angle. Figures 5.5 (a, b, and c) show the pressure spectra at $x_1/2h = 0.1$ (root), $x_1/2h = 0.5$ (centre) and $x_1/2h = 0.8$ (tip) normalised by the freestream velocity and boundary-layer displacement thickness at the ZPG condition. The sensors closer to the edge are selected as the scattering is more strictly related to the wall-pressure fluctuations at the edge. Figures 5.5d and 5.5e show the variation of the pressure spectrum ($\Delta\phi_{pp}$)

with respect to the root region (sensor M05).

Here an increase of the wall-pressure spectrum at the serration centre followed by a decrease at the tip for the $\delta_f = 0^\circ$ case become apparent. However, at the tip, an increase in the levels is noted in the high-frequency range. This was also observed in previous studies with numerical simulations [17] where it was hypothesized to be due to the development of additional small structures generated in the wake around the serration tip.

At $\delta_f = 10^\circ$, the APG boundary layer on the suction side exhibits an overall increase of the pressure fluctuations while the FPG one on the pressure side exhibits a low-frequency increase followed by a decrease for $f\delta^*/U_\infty > 0.1$. This observation is expected for conditions of mild pressure gradient turbulent boundary layers, as demonstrated by Hu and Herr [51]. As the flow advances along the edges of the serration, the amplitude of the pressure fluctuations on both sides slowly converge to the ZPG condition, as can be seen in Figures 5.5b, and c. This indicates that the high overall levels on the suction side decrease more rapidly compared to the ones on the pressure side ($f\delta^*/U_\infty > 0.1$).

Results at $\delta_f = 15^\circ$ differ from the $\delta_f = 0^\circ$, and 10° case. The overall levels at the root are increased on both sides, with the suction side dominating the amplitude of the pressure fluctuations. Along the edges, the vortex pairs seem to induce a significant increase in the wall-pressure levels, which can be observed by comparing the variation in Figures 5.5d and e with respect to the $\delta_f = 10^\circ$. This overall increase of the wall-pressure fluctuations along the edges of the serration affects the levels measured at the centre and tip of the serration, where the suction and pressure sides reach similar levels, with the pressure side dominating the pressure fluctuations in the frequency range above $f\delta^*/U_\infty = 1.0$.

The previous observations can be used to attempt a first description of the overall effect of aerodynamic loading on the distribution of the wall-pressure fluctuations over the serration surface. The footprint of the pressure fluctuations at zero or mild loading displays a maximum at the root and centre of the serration and a decrease along the serration edges. At these conditions, the influence of the open region beneath the serrations progressively reduces the pressure fluctuations, consequently reducing the pressure fluctuations at the edge. As the loading increases, the onset of the vortex pair increases the shear along the edges of the serration and consequently the pressure-fluctuation levels around this region.

As mentioned in Chapter 2, besides the wall-pressure spectrum levels, the study of the spatial distribution and convective properties of the wall-pressure fluctuations along the serration is necessary to fully represent the parameters playing a role in the modelling of the scattered noise. The convection velocity estimated from the sensors (lines) along the centreline of the serration is presented in Figure 5.6. Estimations from PIV measurements along the serration edges are

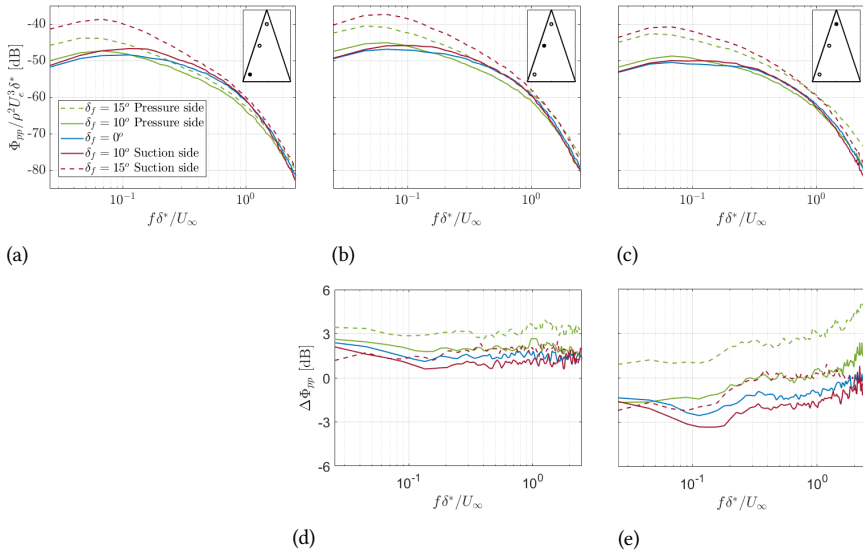


Figure 5.5: Variation of the wall-pressure spectrum along the serration edge and relative change in relation to $x_1/2h = 0.1$ at $x_1/2h = 0.1$ (a), $x_1/2h = 0.5$ (b and d), and $x_1/2h = 0.8$ (c and e).

presented too (filled marks). The agreement between the microphone- and the PIV-based estimations indicates that the convection velocity does not change significantly along the spanwise direction. At zero pressure gradient, the advection of the pressure fluctuations is sustained at 59% of the free stream velocity. Following the boundary-layer velocity profile on the pressure side, a higher velocity closer to the wall is due to the effect of the locally favourable pressure gradient. This is responsible for increasing the velocity with which the turbulent eddies that cause the wall-pressure fluctuations are transported, consequently increasing the convection velocity. Conversely, on the suction side, the fluctuations near the wall are transported at a lower mean velocity. Therefore a lower convection velocity is expected for the wall-pressure fluctuations, as observed from the measurements. From the root to the tip, u_c increases on the pressure side and decreases on the suction side. Avallone et al. [15] have also observed an increase in the convection velocity under similar conditions.

Compared to the baseline value of $u_c/U_\infty = 0.6$, the maximum flap angle causes a decrease of the convection velocity to 0.4 on the suction side and an increase to 0.8 on the pressure side. These modifications impact the correlation length of the flow structures on the serrations at a given frequency. Following the formulation of Corcos [44], the stream and spanwise correlation lengths are proportional to the convection speed. Therefore, the higher u_c is, the higher the correlation length

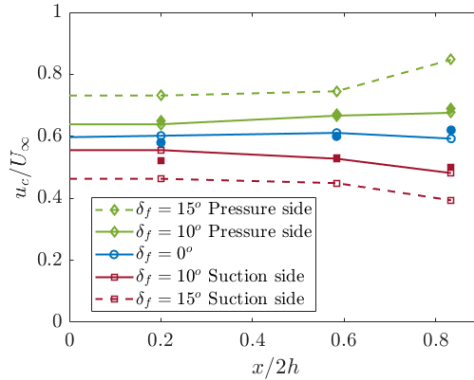


Figure 5.6: Wall-pressure convection velocity estimated along the centre of the serration. Filled marks represent estimations from PIV measurements.

of structures at a given frequency and, consequently the energy scattered at the trailing edge.

Figure 5.7 presents the correlation lengths in span and streamwise direction (calculated from the wall-mounted sensors) at the root of the serration. Overall, results seem to agree with Corcos [44] formulation (see Appendix A for direct comparisons), and larger correlation lengths are captured on the pressure side and lower ones on the suction side for the same Strouhal numbers. A fitting process with the obtained curves using Corcos [44] formulation yields a constant $\alpha_{x_1} \approx 0.17$ for the streamwise correlation length and $\alpha_{x_3} \approx 0.70$ for the spanwise correlation length, similar to the values described by Hu and Herr [51], ($\alpha_{x_1} = 0.15$, and $\alpha_{x_3} = 0.72$).

The increased length of the coherent structures on the pressure side indicates that, although the captured levels at this side are overall lower, the structures are correlated throughout a larger extension. This implies that the coherent scattering from such structures at the trailing edge is stronger and should be considered together with the wall-pressure levels.

A final assessment of the contribution from the correlation length and pressure levels to the trailing-edge noise can be carried out with the highest wavenumber-frequency wall-pressure spectrum mode ($\Pi_{pp}(\omega, k_2 = 0) \propto \phi_{pp}(\omega) l_{x_2}(\omega)$) along the serration (Figure 5.8). The plot combines the variations of the wall-pressure spectrum (Figure 5.5) with the ones of the spanwise correlation length (Figure 5.7) at different regions of the serration. Figures 5.8a, b, and c show the wall pressure at the root, centre, and tip of the serrations respectively. Figures 5.8d, and e show the difference in levels ($\Delta\Pi_{pp}$) with respect to the condition at the root (sensor M05).

At $\delta_f = 0^\circ$, the value of Π_{pp} reaches a maximum in the centre (higher pressure and convection velocities) and decreases at the tip, indicating that noise, in this

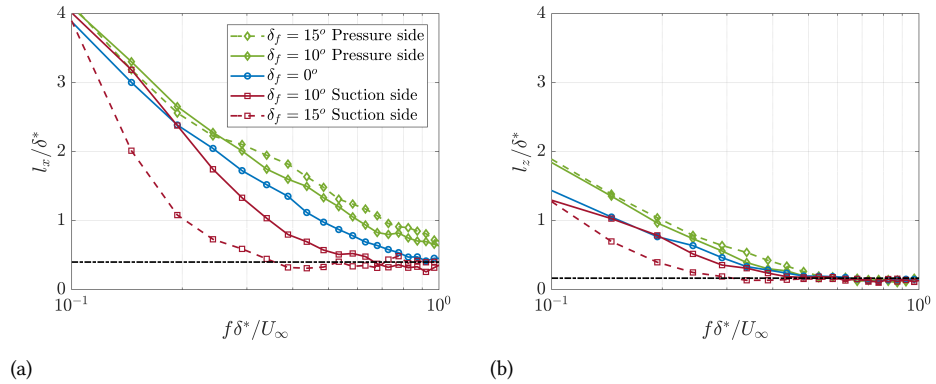


Figure 5.7: Measured streamwise and spanwise correlation length along the trailing-edge serration from the surface microphone sensors at $\delta_f = 0^\circ$, 10° and 15° . The black dot-dashed lines represent the limit of the measurement technique considering coherence levels below 0.05 for two adjacent microphone sensors.

5

condition, is primarily dominated by the scattering of acoustic waves at the edges of the serrations located at the root and central portion of the serration. Nevertheless, the small differences captured along the serration surface suggest that the contribution from the other portions of the serration is not negligible.

The wall-pressure fluctuations from the pressure side are significantly impacted by the effect of the vortex pairs. The increasing levels in the centre and tip of the serration and the extended length of the turbulent structures are responsible for bringing the wall-pressure levels on the pressure side closer or even higher than the conditions on the suction side. In the centre of the serration, the pressure side dominates the scattering at very low ($f\delta^*/U_\infty < 0.1$, $\delta_f = 10^\circ$) and very high frequencies ($f\delta^*/U_\infty > 1.0$, both flap angles). At the tip, Π_{pp} is higher on the pressure side for both flap angles tested.

It can be confirmed from the study that, at low and mid-frequencies ($f\delta^*/U_\infty < 0.2$), the scattering on the serration is dominated by the conditions at the serration root and centre whereas the tip becomes important only at high frequency, as also suggested in the numerical work of Avallone et al. [17]. Moreover, the suction side is seen to dominate the wall-pressure fluctuations at the root and centre while the pressure side increases its importance in the centre while dominating the noise generation at the serration tip, as previously indicated by Arce León et al. [19].

5.2.2 VORTEX PAIRS AND WALL-PRESSURE FLUCTUATIONS

The previous results have been used to characterize the flow near the trailing-edge serration and the spatial and temporal distribution of the wall-pressure fluctuations.

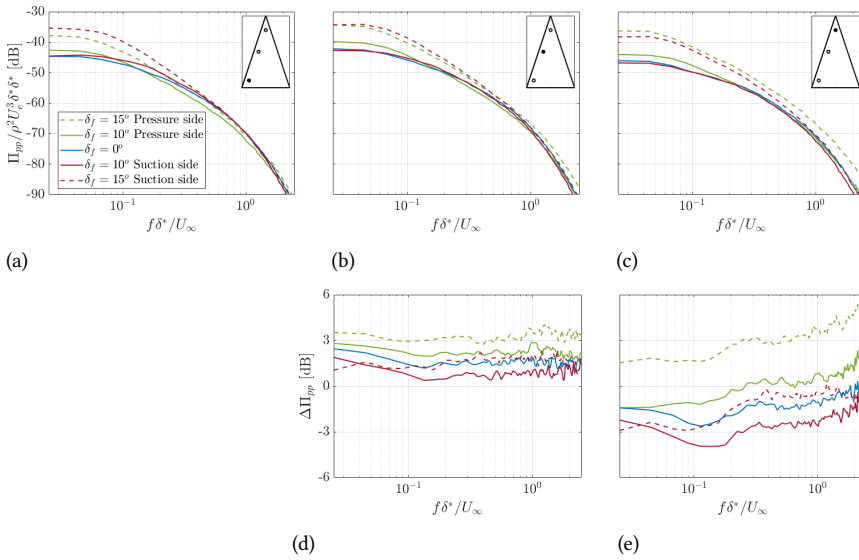


Figure 5.8: Variation of the scattering energy spectrum along the serration edge and relative change in relation to the root ($x_1/2h = 0.1$), at $x_1/2h = 0.1$ (a), $x_1/2h = 0.5$ (b and d), and $x_1/2h = 0.8$ (c and e).

A qualitative comparison is presented here, whereby the three-dimensional flow field and the surface pressure distribution are examined with the aim to identify the effect of streamwise vortices on the wall-pressure distribution. Here, the Poisson equation for pressure is invoked (equation 2.28), which relates the pressure fluctuations with regions of accelerating turbulent flow at its surroundings. This section analyses the variations in the MS-T source term. It is hereby assumed that the variations of the MS-T term are solely related to the variations on the intensity of the pressure fluctuations. This analysis seeks for indications of the causes for the modifications of the wall-pressure observed in the previous section. It is important to highlight that the MS-T is related to the wall-pressure by a volume integration, according to [43], and this analysis provide only an indication of the regions where the MS-T variation are more intense.

Iso-surfaces of the MS-T source term (equation 2.28) can be visualized in Figure 5.9 together with the associated pressure fluctuations at the wall measured from the surface-mounted microphones (taken from Figure 5.4) for $\delta_f = 10^\circ$. The data are bandpass at $f\delta^*/U_\infty = 0.4$. The regions with higher pressure fluctuations can be correlated to those of high MS-T fluctuations on the flow. This supports the conjectures of Section 5.4 between the formation of secondary flow structures and their relation to the pressure fluctuations. In particular, the MS-T fluctuations attain a maximum at approximately one momentum thickness above the surface, where

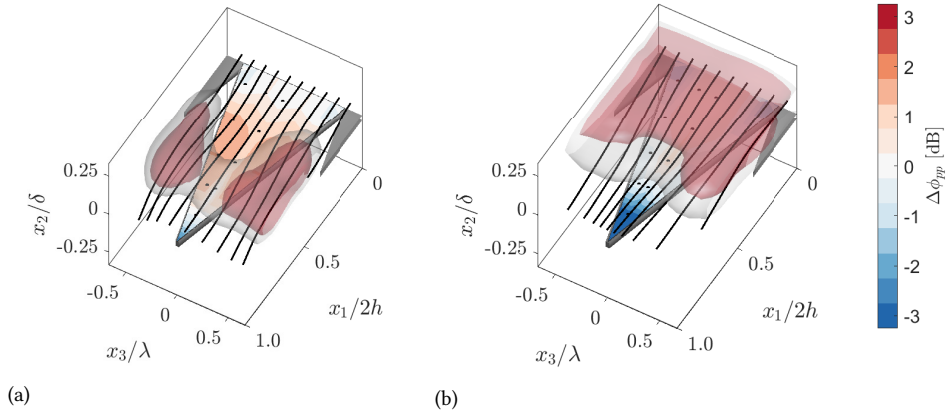


Figure 5.9: Iso-surfaces of the MS-T term (bandpass filtered at $f/\delta^*/U_\infty = 0.4$) compared against the surface pressure measurements from the microphones on the pressure (a) and suction side (b) of the flat plate at $\delta_f = 10^\circ$. The iso-surfaces represent non-dimensional levels MS-T of 0.025 (grey surface) and 0.04 (red surface). Pressure fluctuations are taken from Figure 5.4.

5

the mean-flow gradients of the turbulent boundary layer interact with the stronger velocity fluctuations.

The pressure side exhibits overall low MS-T levels with respect to the $\delta_f = 0^\circ$ case and pressure fluctuations are only increased along the edges of the serration, where the vortex pairs are active, following the regions where the streamlines are more strongly deflected.

On the suction side, high values of MS-T are observed at the root and central portion of the serration, following the high incoming turbulence levels from the adverse pressure gradients observed in Figure 5.3b. This behaviour was also reported by Avallone et al. [15] for the suction side of a sawtooth serration at 4° angle of attack. A secondary region of increased MS-T is captured along the gaps of the serration and is linked to the spanwise accelerations imposed by the vortex pairs along the edge, also in agreement with the region of high-pressure fluctuations.

In the present work, a connection between the pressure and the velocity field is attempted considering the flow field distortions featured by the serrated trailing edge under aerodynamic loading. To this purpose, the terms of the Poisson equation for pressure (Panton and Linebarger [54], equation 2.28) are studied using the velocity inputs from the PIV data. In the equation U_{i1} and u_i represents the mean and fluctuating velocity components respectively, $(\overline{u_i u_j})$ the Reynolds stress tensor components, and ρ the flow density. In the modelling from Panton and Linebarger, the two terms on the right-hand side are named mean shear and turbulence interaction (MS-T) and the turbulence self-interaction (TT) respectively. The latter

term can usually be neglected [40, 43] as demonstrated by Jaiswal et al. [41] for the flow inside a turbulent boundary layer. The MS-T term represents the pressure fluctuations that are caused by the interaction between the velocity fluctuations and the mean flow gradients. This can be further simplified, as presented by Panton and Linebarger [54], for a turbulent boundary-layer flow, where the streamwise velocity derivatives along the wall-normal direction dominate ($\frac{\partial \bar{U}_1}{\partial x_2} \frac{\partial u_2}{\partial x_1}$).

The previous results indicate that the distribution of the wall-pressure fluctuations over the serration surface is a direct consequence of the velocity gradient imposed by the mean flow on the incoming turbulent fluctuations (MS-T term) near the wall. Theoretical predictions of the wall-pressure fluctuations on a turbulent boundary layer are based on the dominant wall-normal shear (MS-T $\approx -2\rho \frac{\partial \bar{U}_1}{\partial x_2} \frac{\partial u_2}{\partial x_1}$). Nevertheless, the MS-T term ($-2\rho \frac{\partial \bar{U}_i}{\partial x_j} \frac{\partial u_j}{\partial x_i}$) still comprises the sum of 9 different terms. Thus, a breakdown of each component of the MS-T interaction term can be used to indicate the contribution of the secondary velocity components to the wall-pressure fluctuations along the serration seen in Figure 5.9, and the validity of the previous assumption for the flow over the serration.

Figure 5.10 shows each of the 9 terms with respect to the total root mean squared value obtained at three different points of the edge of the serration (root, centre, and tip of the serration) for $\delta_f = 10^\circ$. The values are obtained at one momentum thickness above the wall, following the region of more intense MS-T fluctuations observed in Figure 5.9. In the figures, the terms are varied in i along the horizontal axis and in j along the vertical one. The overall sum does not equal 1 since this procedure neglects the coherent contribution of the components. Nevertheless, a maximum deviation of 30% of the total MS-T root mean square term is observed, indicating that the uncorrelated sum still holds most of the energy content in the domain.

The $\delta_f = 0^\circ$ case shows the dominance of the $\frac{\partial \bar{U}_1}{\partial x_2} \frac{\partial u_2}{\partial x_1}$ term all over the serration, in agreement with the studies of Lilley and Hodgson [43]. The latter term also dominates the Poisson source term on the suction side of the $\delta_f = 10^\circ$ case, although a significant contribution of the $\frac{\partial \bar{U}_1}{\partial x_1} \frac{\partial u_1}{\partial x_1}$ and $\frac{\partial \bar{U}_2}{\partial x_2} \frac{\partial u_2}{\partial x_2}$ terms is captured at the tip (totalizing 45% of the total term root-mean-square). The finding is associated with the acceleration of the flow in the stream and wall-normal directions along the central portion of the serration (induced by the adverse pressure gradient) and the consequent changes in the corresponding velocity fluctuations captured. The results suggest that a description of the boundary layer and wake flow near the serration root suffices for the modelling of the wall-pressure fluctuations on the suction side under mild loading conditions. Besides, the predominance of the $\frac{\partial \bar{U}_1}{\partial x_2} \frac{\partial u_2}{\partial x_1}$ term indicates that current models of the wall-pressure spectrum can still be used.

This scenario is different for the pressure side. The reduced fluctuations from the favourable pressure gradient conditions hinder the influence of the wall-normal component ($\frac{\partial \bar{U}_1}{\partial x_2} \frac{\partial u_2}{\partial x_1}$) while the significant span and wall-normal accelerations of the mean-flow field along the serration lead to an increasing contribution from the secondary terms.

At the root and tip, the gradients of the velocity components in the streamwise direction also increase the importance of the $\frac{\partial \bar{U}_1}{\partial x_1} \frac{\partial u_1}{\partial x_1}$ term. However, the central portion of the serration is also influenced by the spanwise derivative components. Particularly, the increasing spanwise velocity along the edge due to the presence of the vortex pairs causes the terms $\frac{\partial \bar{U}_1}{\partial x_3} \frac{\partial u_3}{\partial x_1}$, and $\frac{\partial \bar{U}_3}{\partial x_3} \frac{\partial u_3}{\partial x_3}$ to contribute to 30% of the total MS-T fluctuation. These observations, coupled with the increased MS-T term along the serration edges, suggest that the increase in pressure fluctuations captured on the pressure side occurs due to the compression of the turbulence eddies in the streamwise direction. This process is strengthened at the sides of the serration due to the stretching of these eddies in the spanwise and wall-normal directions prescribed by the vortex pairs.

In summary, the conclusions that can be drawn from the above discussion are:

1. Pressure fluctuations are significantly modified throughout the serration and, as the loading over the serration is increased, so are the overall wall-pressure levels on the suction side and the local levels around the edges on the pressure side.
2. The fast distortion of the turbulent fluctuations by the mean flow is at the origin of the changes in the pressure spectrum along the serration, following the estimated MS-T term presented in Figure 5.9. Without loading, the amplitude of the pressure fluctuations decays progressing from the root to the tip (as also seen in [17]). This is a consequence of the wall-free condition in the gap region. On the suction side, a similar behaviour is observed. The higher incoming pressure fluctuations on the APG boundary layer are strongly dampened from the root to the tip of the serration.
3. The trailing vortices increase the shear along the edges. On the pressure side, vortex pairs interaction with the incoming fluctuations dominates the wall pressure. The streamlines deflection along the edges induces a spanwise eddy stretching and increases the pressure fluctuations across the edges. The vortex pairs also contribute to the pressure fluctuations along the suction side (Figure 5.4) for highly loaded conditions.

Figure 5.11 summarises the above conjecture about the stretching mechanisms induced by aerodynamic loading. The regions of increased pressure fluctuations

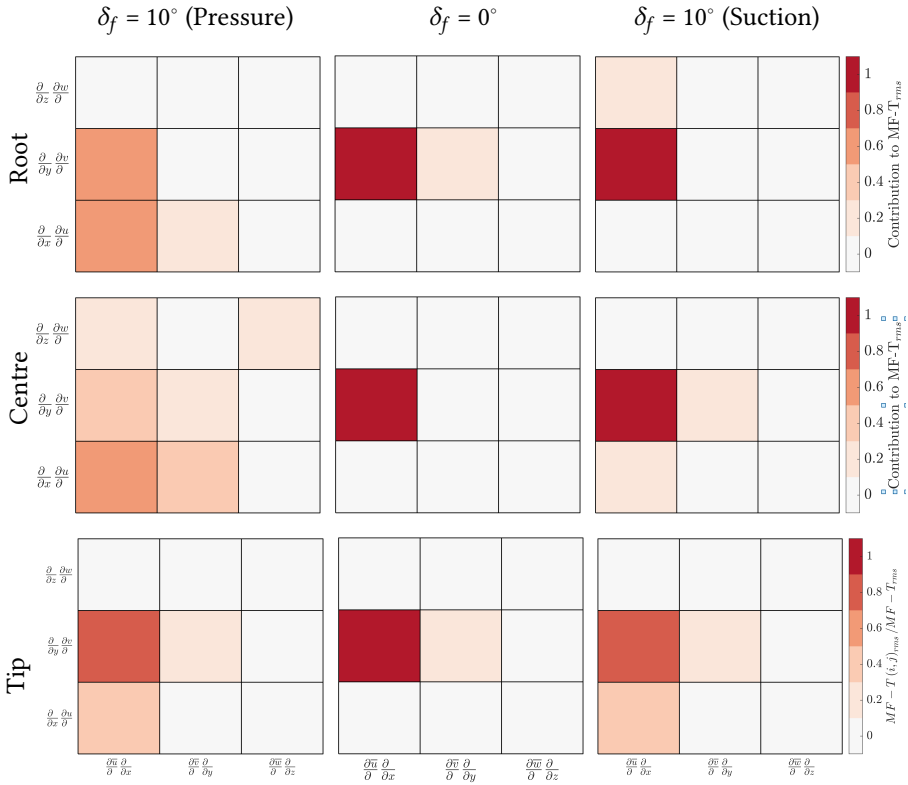


Figure 5.10: Relative contribution of the root-mean-squared of each component $\frac{\partial \overline{U}_i}{\partial x_j} \frac{\partial u_j}{\partial x_i}$ to the mean shear-turbulence (MS-T) interaction term of the pressure Poisson equation estimated along the edges of the serration (one momentum thickness above the wall). Different flap angles, $\delta_f = 0^\circ$ (b, e, and h) and $\delta_f = 10^\circ$ on the pressure (a, d, and g) and suction sides (c, f, and i) are represented.

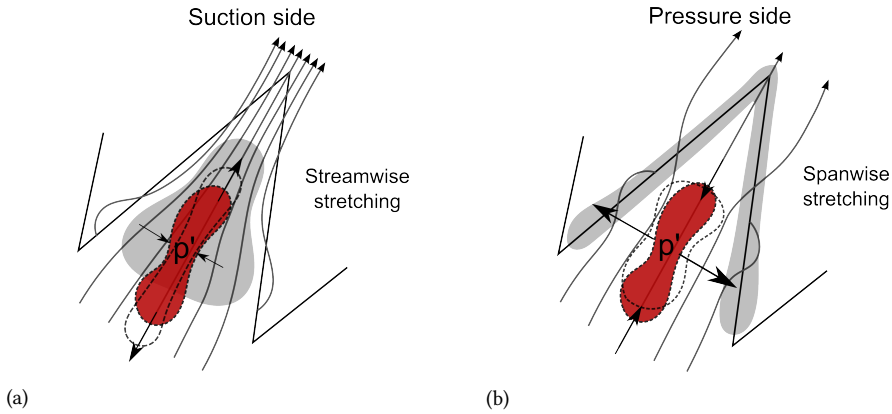


Figure 5.11: Illustration of the flow mechanism acting on the suction (left) and pressure (right) side of an aerodynamically loaded serrated trailing edge. The red curve surface and arrows represent the eddy stretching mechanism, responsible for the associated increase in pressure fluctuations. The grey shades represent the regions where higher pressure fluctuations were captured in the measurements.

5

(grey areas) and the direction of the distortion mechanism are represented in the figure. On the suction side, the higher wall-pressure fluctuations at the serration centre are associated with the streamwise stretching of the adverse pressure gradient boundary layer. On the pressure side, this occurs around the outer rim of the serrations, given the spanwise stretching imposed by the vortex pairs.

5.2.3 FAR-FIELD NOISE PREDICTION

The noise reduction achieved with the serrations with respect to the straight trailing edge is presented in Figures 5.12a, b, and c. Along with the measurements, estimations for the noise reduction are performed with the model of Ayton [22]. The predictions are made in order to illustrate the impact that considering different distributions of the wall-pressure fluctuations has on the predicted noise reduction from trailing-edge serrations. The wall-pressure fluctuations measured at the root, centre, and tip of the serration are selected as input to the model. The model of Ayton requires the input of the incoming wall-pressure fluctuations, supposed uniform throughout the entire serration surface. By using a different input to the model, it is here considered that the entire serration surface will experience the levels of wall-pressure fluctuations of the root, centre, and tip respectively. Another curve, named STE, is proposed that considers all the scattered energy from the tip as if it would behave like a straight trailing edge (STE), is also reported. This curve follows the study of Avallone et al. [17] who conjectured that, at high frequency, the serrations scatter noise as a straight trailing edge with higher pressure fluctuations along the serration tip.

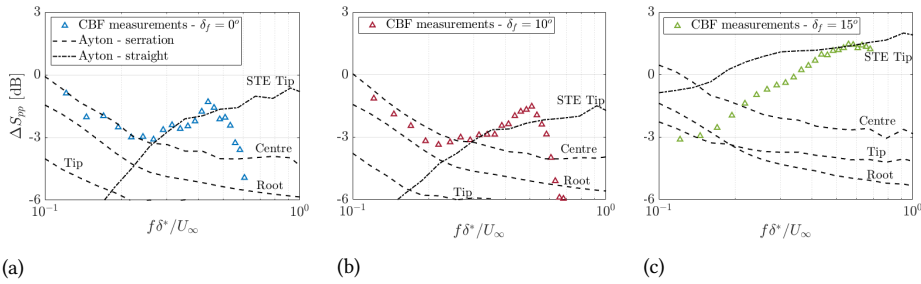


Figure 5.12: Illustration of the flow mechanism acting on the suction (left) and pressure (right) side of an aerodynamically loaded serrated trailing edge. The red curve surface and arrows represent the eddy stretching mechanism, responsible for the associated increase in pressure fluctuations. The grey shades represent the regions where higher pressure fluctuations were captured in the measurements.

The maximum noise reduction measured is of about 3 dB and is captured at $f\delta^*/U_\infty \approx 0.25$ for 0° . As the flap angle is increased, this frequency is reduced. This Strouhal number is similar to that reported by Arce León et al. [67], and Avallone et al. [17]. In this frequency range, the wall-pressure levels are higher in the centre of the serration and, therefore, the scattered noise is dominated by the conditions at this region. This is indicated by the noise estimations using Ayton's method. Predictions using the wall-pressure levels in the centre of the serration yield better comparisons with the measured noise reduction at low frequencies.

The predictions indicate that the low-frequency noise contributions, generated by turbulent structures larger or comparable to the serration wavelength, are not affected by the secondary flow and scatter noise following the conditions assumed in Ayton [21]. On the other hand, smaller flow structures (approximately $l_{x3} < \lambda/6$, or $l_{x1} < 2h/3$) are more affected by the secondary flow motions and depart from the assumptions of the frozen turbulence. The experimental data exhibit a good fit of the frequency where the maximum noise reduction is attained, according to equation 5.1, provided that the smallest convection velocity from the two sides (suction side) is selected, which represents the smallest structures (lower u_c) for a chosen frequency.

$$f_{\max} \approx 3.1 \frac{u_c}{2h}. \quad (5.1)$$

For $f\delta^*/U_\infty > 0.25$, noise reduction is seen to decrease for all curves. The flow structures corresponding to this frequency range are significantly smaller in comparison to the serration dimensions and the highest scattering energy levels are quoted from the pressure side at the tip of the serration. The agreement with the analytical model in this frequency range is best for estimations given at the tip region but considering a straight trailing-edge geometry (STE curves in Figure 5.12).

Two aspects support the above hypothesis: first, the noise reduction is much poorer at the edges in comparison to the central region (slanted angle); furthermore, the small turbulent structures on the pressure side are more prone to the distortions imposed by the flow over the serration, resulting in a lower equivalent edge angle. The combined effect poses a limit for the noise reduction that can be obtained from serrations. This limit can be compared against the noise of a straight trailing edge with pressure fluctuations dominated by the levels at the serration tip. This assumption seems to produce accurate predictions up to $\delta_f \leq 10^\circ$ and departs from them at $\delta_f = 15^\circ$, where the low-frequency region exhibits noise reduction levels in between the sawtooth and the straight trailing-edge predictions. The discrepancies at such extreme angles can be linked to the more pronounced difference between the sawtooth and the straight trailing-edge estimations. The measured noise emissions lie in between the curves of the sawtooth and the straight trailing-edge prediction. The latter confirms that the assumption of frozen turbulence in a condition of strongly varying flow, such as in serrations under aerodynamic loading, leads to inaccurate noise predictions.

5

5.3 WALL-PRESSURE FLUCTUATIONS OVER A SERRATED TRAILING EDGE OF AN AIRFOIL MODEL

This section focuses on the verification of the observations from the flat plate on a more representative airfoil model and under flow conditions (Reynolds number) that are representative of wind turbine applications. The model chosen is of the NACA 63₃-018, used in the benchmark work of Luesutthiviboon [112]. Measurements of the wall-pressure fluctuations on the serration surface under different conditions are used to create the discussions in this section. First results are dedicated to an assessment of the wall-pressure fluctuations at the root and centre of the serration, taken as the reference condition and mostly caused by the incoming flow and the turbulent boundary layer at the trailing-edge of the airfoil.

5.3.1 MEAN FLOW CONDITIONS

The pressure distribution over the model is compared to data obtained from X-Foil in Figure 5.13. As observed, for angles from 0 to 8°, the pressure distribution compares well with the predictions. The presence of the sawtooth serration does not influence the flow along the airfoil indicating the correct alignment with the airfoil symmetry line. It is therefore supposed that the turbulent boundary layer develops similarly for both the baseline and serrated case, as also observed in Avallone et al. [17]. This former confirmation is relevant for the analyses as results are often non-dimensionalized with respect to the properties of the boundary layer predicted without the presence of the serration.

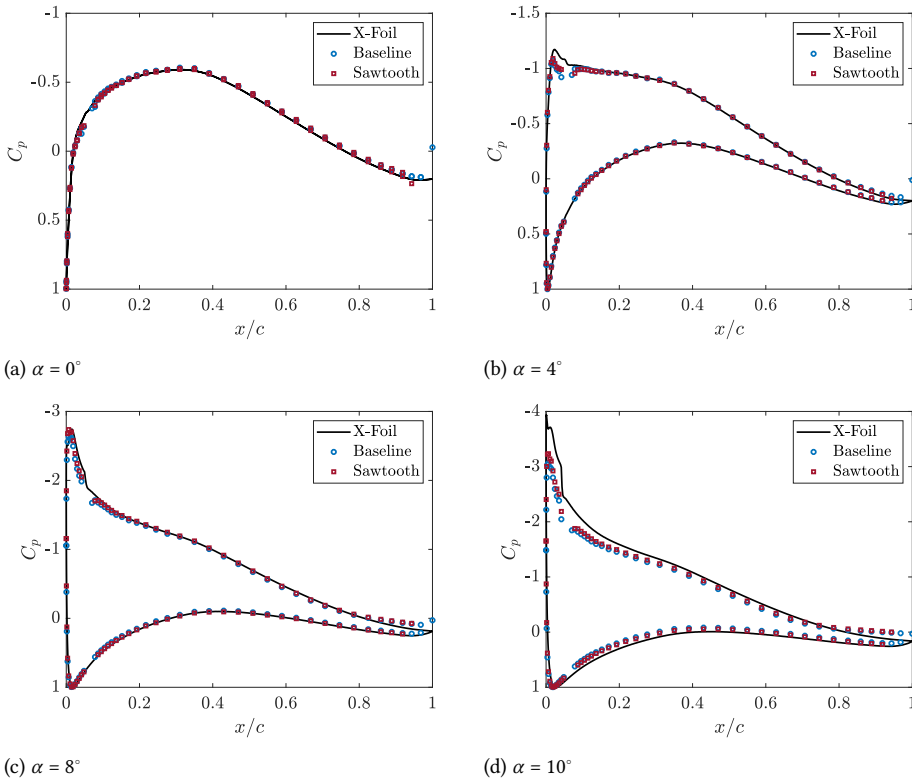


Figure 5.13: Pressure distribution at different angles of attack compared against X-Foil predictions ($Re = 2,000,000$).

Figure 5.14 shows the flow field captured near the trailing edge from the PIV measurements. The flow is measured for 0° and 4° . The boundary-layer profiles are extracted at $98\%c$ (indicated with the wall-normal lines in Figure 5.14) to avoid possible errors caused by the reflections at the exact trailing-edge region. Figure 5.15 shows the 3 boundary layer profiles extracted ($\alpha = 0^\circ$, $\alpha = 4^\circ$ suction and pressure side) in wall units. Using Clauser's approach [114] the friction velocity u_τ can be estimated. The wake profile [45], represented by the dashed colored lines, improves the predictions for the different pressure gradient boundary layers, and is known to impact the wall-pressure fluctuations in adverse pressure gradients boundary layers [126]. Table 5.1 lists the parameters of the boundary layers extracted from the PIV technique and compares them with the predictions from X-Foil. The comparable results obtained with X-Foil indicate that the predictions from the software are reasonably in agreement with the data and can be used for the non-dimensionalization of the variables at other conditions, where the boundary layer

integral parameters are not collected (e.g. other angles of attack).

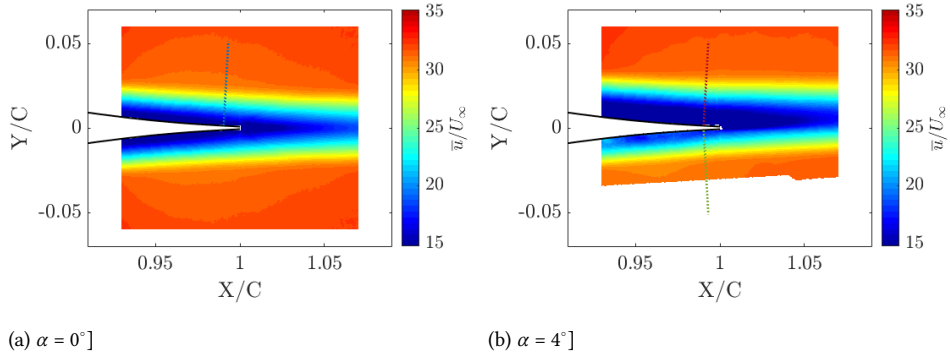


Figure 5.14: Flow field near the trailing edge for the baseline case at $\alpha = 0^\circ$ (a), and $\alpha = 4^\circ$ ($Re = 2,000,000$). Wall normal lines denotes the region where the boundary-layer profile was extracted.

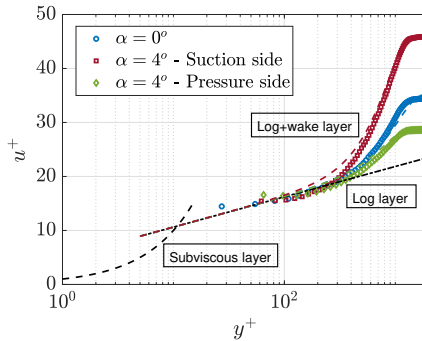


Figure 5.15: Boundary-layer profile near the trailing edge for the baseline case at $\alpha = 0^\circ$ (a), and $\alpha = 4^\circ$ ($Re = 2,000,000$). Linear, logarithmic and logarithmic + wake laws are plotted.

5.3.2 WALL-PRESSURE FLUCTUATIONS AT THE SERRATION ROOT

In this section, the properties of the wall-pressure fluctuations at the serration root are shown. The data at the serration root are taken as reference incoming flow conditions. Further sections study the deviations on the wall-pressure fluctuations with respect to the root conditions.

Figure 5.16 shows the variation of the pressure spectrum with the angle of attack captured at the root of the serration. The blue shades represent the spectrum measured at the pressure side (PS) and the red ones at the suction side (SS). Figure 5.16a shows the captured spectra versus dimensional frequency while Figure 5.16b

Table 5.1: Boundary-layer parameters captured with the PIV measurements at $Re = 2,000,000$. Values in parenthesis indicate predictions from the X-Foil code.

Parameters	$\alpha = 0^\circ$	$\alpha = 4^\circ$ (SS)	$\alpha = 4^\circ$ (PS)
U_e [m/s]	31.5	31.5	31
U_e/U_∞	0.89	0.89	0.88
δ_{99} [mm]	27	30	17
δ^* [mm]	6.1 ((5.3))	9.0 (8.4)	3.4 (3.6)
θ [mm]	3.9 (3.4)	4.8 (4.7)	2.8 (2.6)
Re_δ	56,700	63,200	35,100
H	1.59	1.87	1.29
Δ_*	4.4	3.3	5.0
u_r [m/s]	0.91 (0.94)	0.69 (0.78)	1.08 (1.08)
Π	2.45	4.79	1.41
β_θ	-1.18 (FPG)	7.28 (APG)	-0.24 (FPG)

shows the data scaled according to the predicted boundary layer properties. As the angle of attack increases, the amplitude at the suction side progressively increases at the lower frequencies while decreasing at the higher frequencies. The opposite trend is observed at the pressure side (PS), i.e. increase in the higher frequencies and decrease in the lower ones. The results follow the expected scaling of the wall-pressure spectrum as the thicker boundary layers on the suction side show higher amplitudes at larger scales (lower frequencies) while the thinner ones on the pressure side show higher amplitudes at smaller scales (higher frequencies) [46].

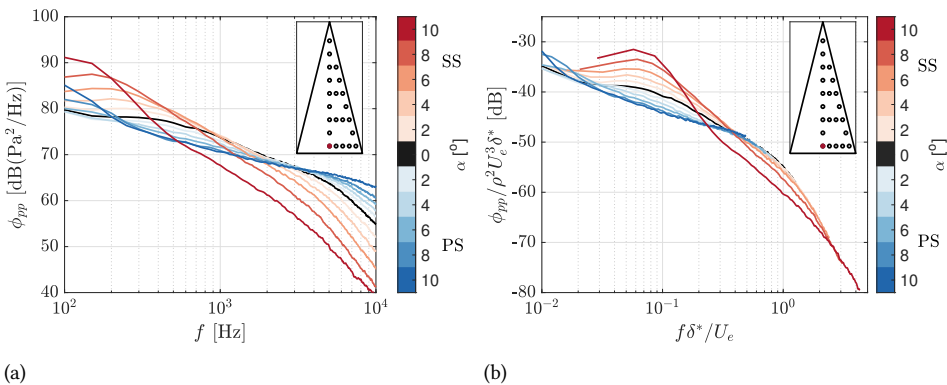


Figure 5.16: Variation of the pressure spectrum at the root of the serration with frequency and Strouhal number for different angles of attack ($Re = 2,000,000$).

Besides the energy of the wall-pressure fluctuations, their average advection speed also influences the scattered noise. This parameter can be estimated with the time delay of maximum coherence between two streamwise spaced microphones, or, in the case of this work, with the derivative in the phase of the cross-spectrum of the same microphones with respect to the frequency, following the procedure described in Romano [56] (eq. 5.2). Figure 5.17 depicts the variations in the mean convection velocity at the serration root with the angle of attack. Figure 5.17(a) shows how the convection velocity increases at the pressure side and reduces at the suction side. The favourable pressure gradient in the pressure side is responsible for a boundary layer velocity profile with higher momentum flow closer to the wall. As a consequence, the surrounding velocity fluctuations that affect the wall pressure are advected at a higher speed, thus resulting in a higher convection velocity of the wall-pressure fluctuations. At the suction side, the same velocity fluctuations closer to the wall are subjected to a smaller mean velocity and, consequently, the captured convection velocity is reduced.

5

$$U_c = 2\pi\Delta x_1 \frac{d\psi^{-1}}{df} . \quad (5.2)$$

The variation of the convective velocity with the boundary layer profile can be well described with its dependency on the boundary layer shape factor (H) in Figure 5.17b, similarly to the work of [57]. Data is shown in all three Reynolds numbers tested ($Re = 1,000,000, 2,000,000, \text{ and } 3,000,000$) to demonstrate the consistency of the trends. As mentioned before, it can be seen that lower convection velocities are usually associated with higher boundary-layer shape factors (lower speed flows near the wall) and higher convection velocities with lower shape-factors (higher speed flows near the wall). This relationship can be expressed according to equation 5.3. An experimental exponential fit is proposed combining the obtained convective velocities and boundary layer shape factors at the three Reynolds numbers tested. The proposed fit yields a representation of the convective speed for this experiment at the full range of boundary layer shape factors.

$$\frac{U_c}{U_e} = e^{-\left(\frac{H-1}{1.5}\right)^{3/4}} . \quad (5.3)$$

From the wall-pressure spectrum and the convection velocity one can already describe the wall-pressure fluctuations as a wavenumber frequency spectrum [28], following the requirements for analytical noise predictions [21, 62, 127]. Nevertheless, the correlation length is another fundamental quantity that impact trailing-edge noise [62]. It gives a measure of the average size of the wall-pressure structures in the boundary layer. This parameter determines the particular extension of the trailing edge that scatters noise coherently [27]. The analytical estimations of

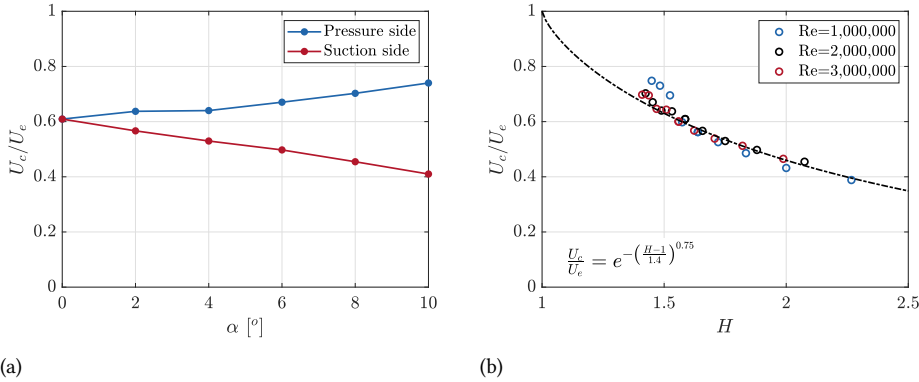


Figure 5.17: Measured convective velocity at different angles of attack at $Re = 2,000,000$ (a) and fitting of the convective velocity with the boundary layer shape factor, H (b).

serration require the assumption of $l_x > 2h$ and, therefore, predictions obtained for smaller correlation lengths (higher frequencies) are less accurate.

The correlation length is defined by the integral of the coherence function γ in frequency domain along the span or streamwise direction [27] (equation 5.4). In this work, this integral is computed after the fitting of the coherence values with an exponential function, following the assumption provided in Corcos [44]. This procedure improves the accuracy of the extracted quantities as it is more robust to noise and avoids truncation errors. The values of l_{x_1} , and l_{x_3} are commonly predicted to be directly proportional to the convection velocity and inversely proportional to the frequency ($l = U_c/k\omega$) [44], where k is estimated in 0.15 and 0.7 for the stream (l_{x_1}) and spanwise (l_{x_3}) correlation length respectively [51].

$$\begin{cases} l_{x_1}(\omega) = \int_0^\infty \gamma(\omega, \Delta x_1) dx_1, \\ l_{x_3}(\omega) = \int_0^\infty \gamma(\omega, \Delta x_3) dx_3. \end{cases} \quad (5.4)$$

Figure 5.18 shows the measured stream and spanwise correlation lengths at the serration root for different angles of attack. At the Reynolds numbers investigated, the predictions of Corcos [44] are only valid at high frequencies (as observed in Figures 5.18c and 5.18c using the k values proposed by Hu & Herr [51]). A local maximum is captured for both correlation lengths, following the Efimtsov curve shape used in the work of Palumbo [59]. Nevertheless, the value and frequency of maximum correlation length seem to vary with the angle of attack. Besides, this maximum correlation length varies differently for the spanwise and streamwise correlation lengths, indicating that the two are not dependent on the same parameters. For the streamwise correlation length (l_{x_1}), all angles of attack tested seem to follow

the trend predicted by Hu & Herr [51]. The local maximum is higher at the suction side and smaller at the pressure side. However, scaling the correlation length with the boundary layer displacement thickness show a nice collapse of the curves. The local maximum on the pressure side happens at a lower non-dimensional frequency and it corresponds to a higher ratio l_{x_1}/δ^* .

The spanwise correlation length follows a similar trend, i.e. lower maximum correlation lengths at the pressure side and higher ones at the suction side. Nevertheless, the non-dimensional plot reveals some important differences. At first, the trend proposed by Hu & Herr [51] is only valid for the $\alpha = 0^\circ$. The suction side presents higher relative correlation lengths (l_z/δ^*) while the same value decreases at the pressure side with the angle of attack. Contrarily to the streamwise correlation length, the local maximum is constrained to values around $l_{x_3}/\delta^* = 3$ for all conditions tested.

In the streamwise direction, the Corcos equation using the empirical parameter $k = 0.15$ [51] yields good predictions for both favourable and adverse pressure gradient conditions. The maximum correlation length, however, seems to be relatively higher (l_{x_1}/δ^*) at favourable pressure gradient conditions.

In the spanwise direction (l_{x_3}), the high frequency decrease depends on the pressure gradient condition and the proposed $k = 0.7$ [51] is only valid for $\alpha = 0^\circ$. The local maximum, however, is restricted to a non-dimensional value around $l_{x_3}/\delta^* = 3$.

5.3.3 DISTRIBUTION OF THE WALL-PRESSURE FLUCTUATIONS OVER THE SERRATION WITHOUT AERODYNAMIC LOADING

Following the discussed properties of the incoming wall-pressure fluctuations, this section focuses on the description of the variations of the wall-pressure spectrum along the serration surface. These variations can be directly related to the discrepancies between measured and predicted far-field noise reduction since the former considers that the wall pressure is exactly the same over the entire serration surface. This section attempts to assess the captured modifications in the wall pressure observed when the serrations are not aerodynamically loaded, i.e. without any effect caused by the vortex pairs formed around the serration edges [122].

Figure 5.19 shows the spectra captured at the sensors along the centre of the serrations. The figure demonstrates the variations of the wall pressure along the serration. At the root, the amplitude is higher at low frequencies and lower for higher frequencies. As one progresses from the root towards the tip the low frequency ($f < 2.0$ kHz) levels are reduced while the high-frequency ones increase. [16, 17] have reported a decrease in the wall-pressure root mean square from the root to the tip. This is also in agreement with the present observations as the higher overall amplitude in the low-frequency content contributes strongly to the root

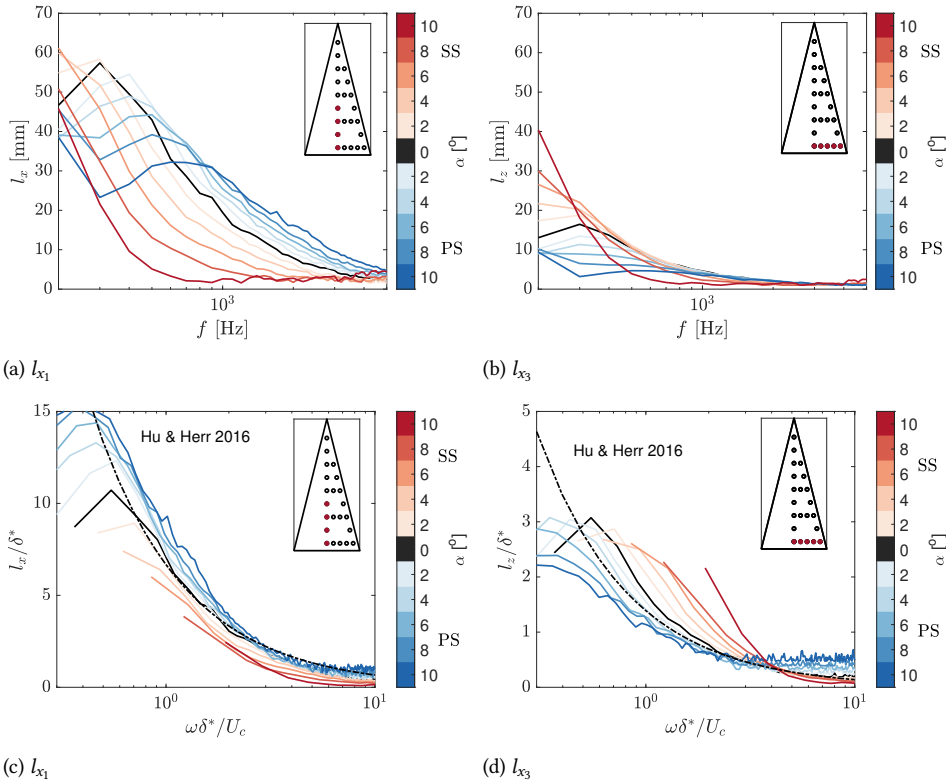


Figure 5.18: Variation of the stream (a and c) and spanwise (b and d) correlation length at the root of the serration with frequency and Strouhal number for different angles of attack ($Re = 2,000,000$).

mean square values and, therefore, the decrease from the root to the tip of the serration dominates the analysis. Nevertheless, the high-frequency energy is also noted in the same references. The increase in high frequencies is related to the cut-off in the noise reduction obtained from trailing-edge serrations. Avallone et al. [16] have suggested that the noise is predominantly generated at the root of the serration in low frequencies and at the tip in high frequencies. This assumption follows the different locations of higher wall-pressure fluctuations at low frequencies (serration root) and at high frequencies (tip).

The variations of the wall pressure can be better observed from the interpolated distribution over the serration surface for different frequencies in Figure 6.8. In the images, the sensor at the centre root is taken as the reference. Shades of blue indicate a reduction while shades of red indicate an increase of the wall-pressure fluctuations with respect to the incoming ones.

The images show the modifications discussed previously. At lower frequencies,

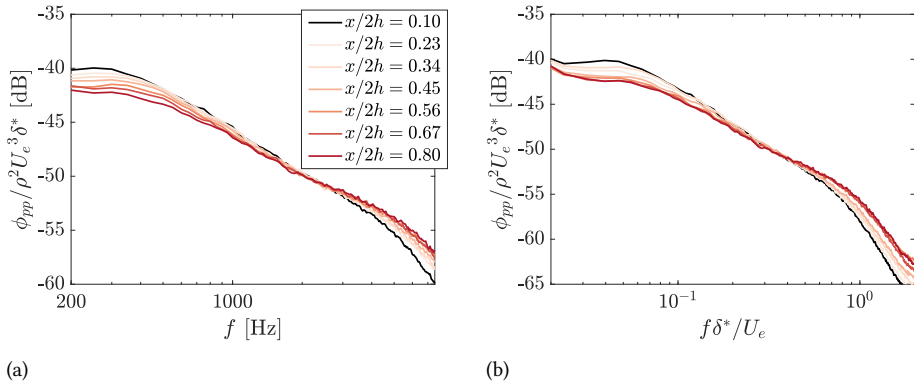


Figure 5.19: Variation of the pressure spectrum along the serration centre with frequency (a) and Strouhal number (b) for $\alpha = 0^\circ$ and $Re = 2,000,000$.

5

the overall spectrum reduces from the centre root to the tip of the serration. This reduction is more intense and spread over the serration surface at lower frequencies (Figures 5.20a, 5.20b) and becomes milder and restricted to the serration edges at higher frequencies (Figure 5.20c). At even higher frequencies (Figures 5.20e, 5.20f) a different trend is observed. The pressure fluctuations increase from root to tip. This latter trend is only dependent on the streamwise position and no significant variations are observed along the spanwise direction.

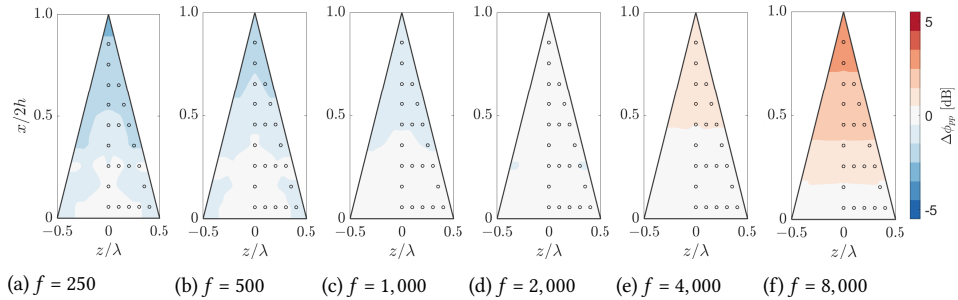


Figure 5.20: Wall-pressure fluctuations over the serration surface at $\alpha = 0^\circ$ and $Re = 2 \times 10^6$. Reference is set to the sensor at the centre root of the serration.

5.3.4 EFFECT OF THE ANGLE OF ATTACK ON THE WALL PRESSURE OVER THE SERRATION SURFACE

Having analyzed the distribution of the wall-pressure fluctuations without the presence of aerodynamic loading, this section focuses on the alterations of these wall-pressure fluctuations caused by the aerodynamic loading and the vortex pairs

generated on the serration edges.

Figure 5.21 shows the progressing modification of the wall-pressure fluctuation distribution with the angle of attack at $f = 500$ Hz. Fig. 5.21 (a) to (f) show the data obtained at suction side while Figure 5.21 (g) to (l) show the one obtained at the pressure side. From the graphs it is clear that the observed tendency at $\alpha = 0^\circ$ is sustained for small angles (up to $\alpha = 4^\circ$ at the suction side and $\alpha = 6^\circ$ at the pressure side). At such conditions, aerodynamic loading does not seem to affect the wall-pressure spectrum and the surface distribution follows the trend described in Section 5.3.3 at low frequencies. For higher angles, a visible increase of the wall-pressure fluctuations along the serration edges is captured. The increase is at first restricted to the tip of the serration for mild angles, e.g. $\alpha = 6^\circ$, but it spreads towards the serration root for higher angles, e.g. $\alpha = 10^\circ$. The effect is observed for angles of attack higher than 6° along the suction side and only at 10° at the pressure side. This difference is demonstrated later in the work and relates to the frequency dependency of these pressure fluctuations induced by the aerodynamic loading. For the selected frequency ($f = 500$ Hz), the fluctuations at the suction side are stronger than the ones at the pressure side.

The captured increase in the wall-pressure fluctuations due to the aerodynamic loading is often related to the formation of a vortex pair at the serration edge and to the increase in noise from serrated trailing edges at an angle [19, 122].

This increase in the wall-pressure levels along the serration edge is also frequency dependent. Figure 5.22 depicts how the measured spectrum modifies along the serration edge at $\alpha = 10^\circ$ for frequencies from 250 to 8000 Hz. Again, Figures 5.22(a) to (f) show the wall-pressure fluctuations at the suction side and Figures 5.22(g) to (l) at the pressure side.

The distribution of the wall-pressure levels analyzed in different frequencies shows that the effects of the aerodynamic loading are frequency-dependent and also that it varies from the suction to the pressure side. The effects are generally concentrated on a narrow band of frequencies. On the suction side, stronger modifications are observed around $f = 250$ Hz. On the pressure side, the same is only observed around $f = 2000$ Hz.

These discrepancies are attributed to the different scales and velocities of the convecting pressure fluctuations that interact with the vortex pairs. On both sides, the non-dimensional Strouhal number based on the boundary layer displacement thickness $f\delta^*/U_c$ in which the effect is stronger yields similar values (0.20 and 0.18 at the pressure and suction side respectively). This similarity between the two values indicates that the phenomenon depends also on the properties of the incoming turbulent boundary layer. This means that the accelerations of the mean flow influence the larger and slower structures from the suction side and the smaller and faster ones from the pressure side. This influence gets stronger with the

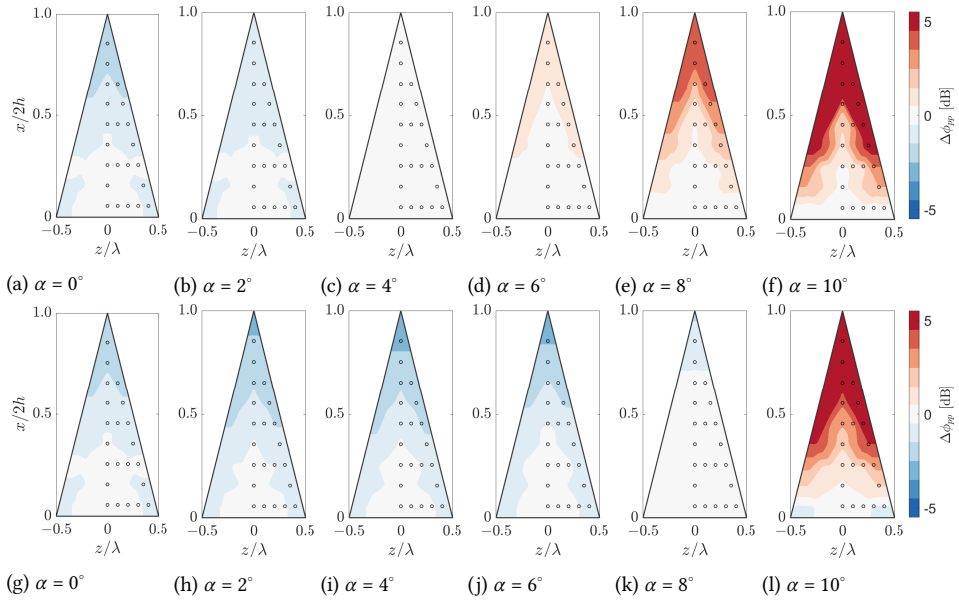


Figure 5.21: Wall-pressure fluctuations over the serration surface for $f = 500$ Hz at different angles of attack and $Re = 2 \times 10^6$. Reference is set to the sensor at the centre root of the serration. Figures (a) to (f) shows the measured wall-pressure levels at the suction side and figures (g) to (l) at the pressure side.

aerodynamic loading of the serration, indicating that the interaction between the vortex pairs and the incoming turbulent structures is responsible for the increased pressure fluctuations on the serration edges.

This effect can increase the pressure fluctuations by more than 5 dB on the edge of the serrations. Such values are in the order of the quoted trailing-edge noise in many applications [11] and indicate how the vortex pairs can influence the scattered noise.

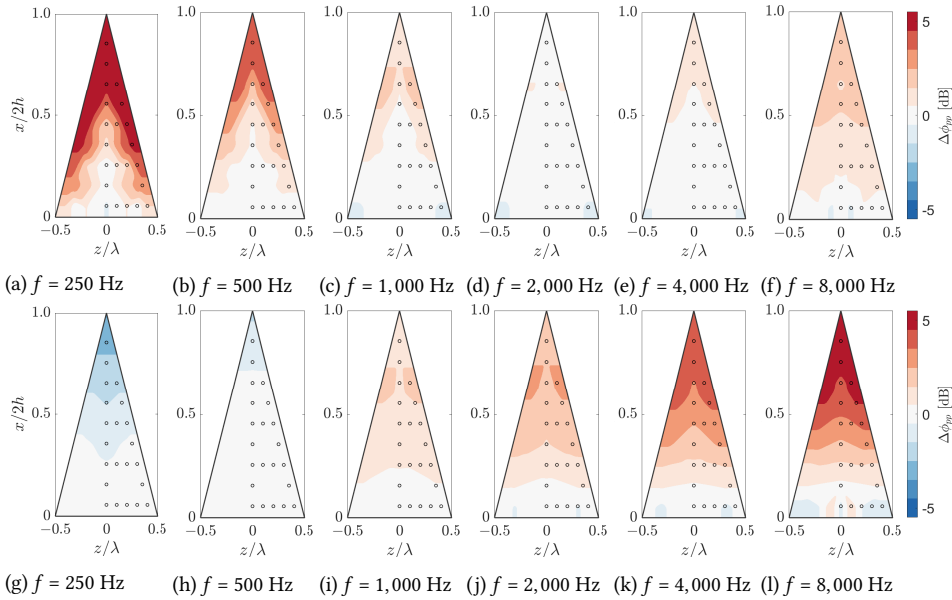


Figure 5.22: Wall-pressure fluctuations over the serration surface for $\alpha = 10^\circ$ and $Re = 2 \times 10^6$. Reference is set to the sensor at the centre root of the serration.

5.4 CONCLUSIONS

Measurements of the flow around a serrated trailing edge are studied to understand the effects of aerodynamic loading on the turbulent boundary layer trailing-edge noise reduction. A flat-plate model with a trailing-edge flap is used to control the aerodynamic loading condition. Time-resolved 3D-PIV measurements are complemented with non-intrusive surface pressure measurements to diagnose velocity and wall-pressure fluctuations over the serrations. Acoustic measurements with phased array technique complete the study with far-field predictions of the noise reduction.

The onset of streamwise vortices from approximately 25% of the serration height generates spanwise deflections that accelerate the flow towards the centre of the serration on the suction side and towards the gap region on the pressure side. The interaction of this secondary flow structure with the incoming turbulent flow from the boundary layer represents the major contribution to the increasing wall-pressure fluctuations along the serration. This effect is particularly strong on the pressure side, where the lower incoming fluctuations from the FPG flow are increased by the spanwise accelerations of the flow. The levels of the pressure fluctuations around the edges of the serration on the pressure side increase, with the maximum located around 60% of the sawtooth height. On the suction side, the

vortex cores only impact the pressure fluctuations for highly loaded conditions. The variation of the wall-pressure spectrum over the serration surface is in the order of ± 4 dB and indicates that considering the amplitude of the wall-pressure fluctuations constant along the serration surface is not representative of the flow over trailing-edge serrations undergoing aerodynamic loading.

These results also reveal that noise estimations only based on the flow over the suction side might lead to inaccurate results. The suction side represents a critical region of low and mid-frequency noise, and results have shown that predictions based on the incoming turbulent boundary-layer conditions do not yield large deviations. Nevertheless, the flow alterations on the pressure side yield an increase in the noise levels at higher frequencies. The latter is dependent on the 3D characteristics of the flow and is a function of the flow angle and loading conditions, deviating increasingly from the predicted pressure fluctuations using the incoming boundary layer as the serration flap angle is increased.

5

The connection between the wall pressure and the velocity fluctuations at the vortex is analysed from the MS-T term, specifically at one boundary-layer momentum thickness above the serrations. The region of increased MS-T is driven by the acceleration of the stream and spanwise components of the flow velocity, which, in combination with the increased velocity fluctuations, lead to the wall-pressure fluctuations captured along the serration edges.

Acoustic measurements have shown the noise reduction provided by the serrated trailing edge under the different conditions tested. In agreement with the literature, noise reduction is maximum at about $f\delta^*/U_\infty = 0.25$ for no pressure gradient condition. This Strouhal number is shifted towards lower frequencies as the angle of the flap is increased and is bounded by the size of the coherent structures within the boundary layer in comparison to the serration geometry. Noise estimations using the model of Ayton [21] reveal that pressure conditions taken at the central part of the suction side of the serrations yield better comparisons with beamforming measurements at low to mid frequencies. At higher frequencies, noise reduction follows the predictions for an equivalent straight trailing edge. It is speculated that the small structures on the pressure side generate noise predominantly at the tip of the serration. The reduced scattering effectiveness of this portion of the serration bound the noise reduction achieved by the equivalent straight edge.

The observed behaviour on the isolated trailing edge is verified on conditions close to application with an study with a high-Reynolds airfoil with serrated trailing edges. Measurements of the wall-pressure fluctuations on the surface of a serrated trailing edge of the benchmark NACA 63₃-018 airfoil are carried out. Results show the properties of the incoming wall-pressure fluctuations at the serration root and their modifications along the serration surface under different flow conditions.

Without aerodynamic loading, the wall-pressure fluctuations are higher at the root of the serration and decrease progressively as one moves towards the tip of the serration. This pattern is more strongly observed in low frequencies and gets milder as the frequency increases. At very high frequencies this trend is reverted and pressure fluctuations are higher at the tip than at the root of the serrations. Results are in agreement with other observations [16, 17] and point to a stronger scattering at the serration root with respect to the one at the serration tip at lower frequencies and the inverse to happen at higher frequencies, i.e. conditions at the tip of the serration dominate the scattered noise.

The aerodynamic loading causes an increase in the wall-pressure fluctuations at the outer rim of the serration. This increase is stronger around $f\delta^*/U_e \approx 0.2$ and is related to the accelerations of the flow imposed by the trailing vortices formed at the serration interacting with the incoming turbulent boundary layer fluctuations. Again, these modifications can be related to decreasing efficiency of the serration devices observed in other references [67].

Overall, it is shown that meaningful variations occur in the wall-pressure fluctuations along the serration surface. Deviations from the measurements at the root are as large as 5 dB, similar to the quoted noise reductions achieved with serrated devices. Consequently, accurate noise predictions from serrated trailing-edge noise are dependent on a proper description of those deviations, and predictions based solely on the incoming wall-pressure fluctuations from the turbulent boundary layer are prone to major deviations from the measurements. The results presented in this work also contribute to the future BANC activities by providing experimental data of the wall-pressure fluctuations over the serration surface. The data could contribute to further attempts of modelling or simulating the present benchmark configuration.

6

PHYSICS-BASED DESCRIPTION OF THE FLOW OVER A SERRATED TRAILING EDGE

6.1 OBJECTIVES

Even though serrations are widely used, the prediction of trailing-edge serra-
tion noise [10, 20–22, 62] is still an ongoing subject of research, given that large deviations between experiments and analytical predictions are often reported [11, 22, 122]. Consequently, predictions of noise reduction from wind turbine with serrations still require dedicated experiments or numerical simulations, whereas a fast assessment and physical interpretation could be provided by more advanced analytical methods that can capture the dominant effects introduced by the serrations. Available predictive methods are based on the solution of the acoustic scattering problem from an incoming gust prescribed in the form of a wavenumber-frequency fluctuation of the wall pressure [21]. The fluctuations are therefore considered to be advected towards the trailing-edge serration, i.e. frozen turbulence is assumed [68]. However, many experimental [11, 12, 15, 18, 38, 122], and numerical [14, 16, 17] studies have pointed out that the mean-flow pattern is distorted along with the distribution and intensity of the turbulent fluctuations surrounding the trailing-edge serrations, indicating that the assumption of frozen turbulence does not hold true.

Two different conditions are consistently studied in the literature, corresponding to the flow in the absence or in the presence of aerodynamic loading over the serration, the latter caused by the misalignment between the serrations and the flow. At low angles of attack, numerical simulations [16, 17] and experiments [12, 18] have shown a reduction of the pressure fluctuations from the root to the tip of the serration at low and mid frequencies and an opposite trend at higher frequencies, i.e. increasing wall-pressure fluctuations at the serration tip. Also, the formation of vortex pairs along the serration edges, when the serrations are under aerodynamic loading, is often ascribed to be the cause of the noise-reduction degradation at increasing airfoil angle of attack [19, 122].

The wall-pressure fluctuations are primarily used as input for the modelling of trailing-edge noise generation [27], but they have only been studied in recent works [12, 16–18, 108]. Although the above works have illustrated the overall distribution of the wall pressure on the surface of serrations, the underlying causes of its distortions have not yet been established. Thus, improving the analytical modelling of serrated trailing-edge noise requires fundamental understanding of the underlying mechanisms that govern the aerodynamic wall-pressure fluctuations over the serration surface.

This chapter proposes a description of the dominant flow mechanisms relevant to the modification of wall-pressure fluctuations over a serrated trailing edge. Wind tunnel experiments are conducted on a NACA 63₃-018 airfoil model at chord Reynolds numbers from 1 to 3 million retrofitted with trailing-edge serrations of height ($2h$) 90 mm and wavelength (λ) 45 mm. The detailed distribution of the wall-pressure fluctuations on the serrated trailing edge with varying airfoil

incidence is obtained with a wall-mounted printed circuit board (PCB) containing embedded microphone sensors. Steady aerodynamic measurements are carried out with surface pressure taps and stereoscopic-PIV.

The flow mechanisms proposed follow semi-empirical models that encapsulate their physical principles. Section 6.2 describes the physical mechanisms that modify the spatial distribution and intensity of the wall-pressure fluctuations on the serration surface and the models proposed for them. The experimental setup and the properties of the flow are presented in Section 6.3. Results shown in 6.4 compare the measurements with the proposed models. Main conclusions are summarized in 6.5.

6.2 DESCRIPTION AND MODELLING OF THE WALL-PRESSURE OVER A SERRATED TRAILING EDGE

In this section, the physical mechanisms responsible for the modification of the wall-pressure statistics on the surface of a serrated trailing edge are postulated, described and modelled. Three effects are presented based on a critical analysis of literature and the current experimental data, those are: i.) the change in the impedance at the edge of the serration; ii.) the sidewise momentum exchange between free wake and boundary layer along the serration surface; iii.) the streamwise vortices generated by serration under aerodynamic loading. Each of the above effects is described separately in this section.

6.2.1 IMPEDANCE CHANGE AT THE TRAILING-EDGE BOUNDARY

The discontinuous change in impedance from the airfoil solid surface to the fluid flow region at the trailing edge is known to be responsible for the scattering of acoustic waves [27]. This discontinuity also affects the aerodynamic pressure fluctuations at the wall plane as the impedance, defined here as the ratio between the pressure fluctuations (p) and the wall-normal velocity fluctuations (u_2) on the wall ($x_2 = 0$), changes from an infinite value at the wall to a finite one downstream from the trailing edge. On a serrated trailing edge, this process occurs, along streamwise locations, more gradually than for the straight edge. Therefore, modifications of the wall-pressure fluctuations are observed from the root to the tip of the serration surface.

The influence of this change on the wall-pressure fluctuations can be formulated as a modification of the boundary conditions along the chord line of the model. The presence of the wall forces the wall-normal velocity to be zero $u_2(x_2 = 0) = 0$, differently from the unbounded region, exhibiting non-zero wall-normal velocity fluctuations. On the other hand, in the unbounded flow, velocity fluctuations from both sides influence the pressure captured along the chord line. This process is

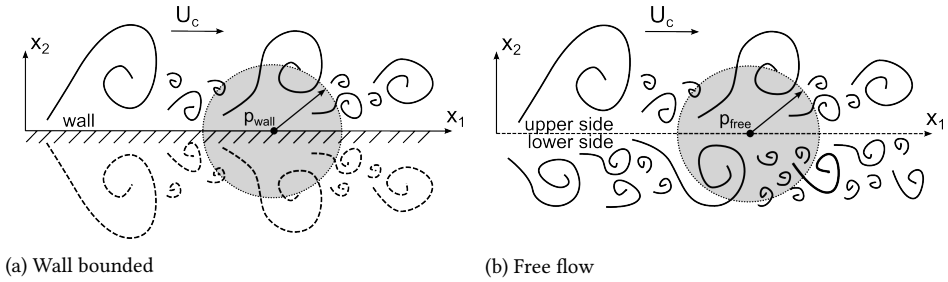


Figure 6.1: Schematic representation of the velocity fluctuations at the wall and along the symmetry region in the near-wake. In grey, the sphere illustrates the region of influence of the velocity fluctuations that affect the pressure at a certain location.

illustrated in figure 6.1. Two schematics are presented in the figure to explain the flow in the presence and in the absence of a wall. The pressure at a certain location of the wall plane is dependent on the velocity fluctuations at its surroundings [54], as illustrated by the grey area in the figures. The wall-bounded flow is equivalent to a mirrored condition (figure 6.1a), where the fluctuations below the wall are exactly coherent with the ones on top. Similarly, in the free flow (figure 6.1b), both sides contribute to the wall-pressure fluctuations at the chord line. However, in this case, the velocity fluctuations on both sides, supposedly incoming from the turbulent boundary layer developed in the upper and lower side of the model, are not correlated in the near wake.

Assuming that turbulent fluctuations from the top and bottom boundary layers are uncorrelated in the free-flow region, a relation describing the pressure spectrum (ϕ_{pp}) along the symmetry line ($x_2 = 0$) in the absence of the wall is formulated (equation 6.1), where $\phi_{pp,free}$ results from a combination of the measured wall-pressure spectrum on the upper ($\phi_{pp,upper}$) and lower ($\phi_{pp,lower}$) side of the solid surface. The mathematical process that leads to equation 6.1 is expanded in Appendix B. The 1/4 factor comes from the doubling of the pressure fluctuations in the wall region, as also pointed out by Howe [128].

$$\phi_{pp,free}(x_2 = 0) = \frac{1}{4}\phi_{pp,upper} + \frac{1}{4}\phi_{pp,lower} \quad (6.1)$$

As an example, considering the incoming wall-pressure fluctuations from both sides to be of equal amplitude, a consequence of equation 6.1 is that the pressure fluctuations at the symmetry line drop by half (-3 dB) with respect to the value at the wall. This mechanism can also be visualized from the illustration in figure 6.1 where the presence of the wall mimics a free region with pressure fluctuations coherent from both sides, whereas the free region combines non-coherent fluctuations. The difference between such cases is 3 dB when both sides have the same level of

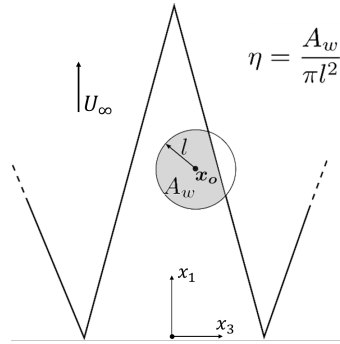


Figure 6.2: Representative view of the radius of influence of the wall-bounded region in a point $\mathbf{x}_o = (x_{1,o}, x_{3,o})$ and the procedure applied to compute the factor η over a serrated trailing-edge.

velocity fluctuations. In the case where no fluctuations are present on the lower side, this difference reaches 6 dB (pressure fluctuations at the symmetry line outside the wall are a quarter of the ones measured at the wall).

These results describe the expected change from the wall-bounded region to the unbounded one. It is therefore intuitive that, near the trailing edge, a transition between these two conditions occurs, as discussed in Howe [128]. This process is especially important for serrated trailing edges since its geometry causes the change of impedance to happen progressively from the root, where the neighbouring region is bounded by the wall, till the tip, where the unbounded flow is dominant. The idea translates to a natural decrease of the pressure fluctuations from the root to the tip of the serration depending on the considered flow scales. This phenomenon has been reported already in recent works from Avallone et al. [16, 17] and Ragni et al. [18], based on numerical simulations and experiments respectively. In all three studies wall-pressure fluctuations were observed to reduce to about half (-3 dB) from the root to the tip of the serrations. Similarly, the experimental work of Chong and Vathylakis [12] for a serrated plate with flow only from one side captures a reduction of about -6 dB in the wall-pressure fluctuations of the serration tip.

This modification of the wall-pressure fluctuations is dependent only on the geometry of the trailing edge and on the size of the turbulent structures inside the boundary layer. Therefore, even in the absence of variations of the flow properties on the surrounding of the trailing-edge region, the wall-pressure fluctuations in the surroundings of the trailing-edge are altered. Here, a semi-empirical relation is proposed to describe the wall-pressure fluctuations near the complex geometry of trailing-edge serrations. The model takes into account the above discussed variation of impedance within a radius l , as illustrated in figure 6.2.

The geometry of the serration can be represented, in the plane $x_1 x_3$, by its function g , such that $x_1 = g(x_3)$. $H(x_1, x_3)$ represents the model surface and is a

Heaviside function defined according to equation 6.2.

$$H(x_1, x_3) = \begin{cases} 1, & x_1 \leq g(x_3) \\ 0, & x_1 > g(x_3) \end{cases} \quad (6.2)$$

The factor η is introduced according to equation 6.3 for a point $\mathbf{x}_o = (x_{1,o}, x_{3,o})$ that accounts for the portion of the circle that overlays the solid wall (grey shaded in figure 6.2).

It is here hypothesized that the factor l depends only on the size of the turbulent structures locally. This hypothesis follows the dependency of wall-pressure fluctuations on the correlation of the velocity fluctuations [54]. This translates to the relation shown in equation 6.4, where the radius of influence l is proportional to the aerodynamic wavelength and the size of the turbulent structures, i.e. directly proportional to the convection velocity (U_c) and inversely proportional to the frequency (ω). This assumption makes the proposed model frequency-dependent. The constant C_i needs to be determined from experiments and follows the definition of the correlation length from the work of Corcos [44].

$$\eta(\mathbf{x}_o) = \frac{\iint_0^{|x-x_o|=l} H(\mathbf{x}) d\mathbf{x}}{\pi l^2} \quad (6.3)$$

$$l = C_i \frac{U_c}{\omega}. \quad (6.4)$$

The parameter η is then used to establish a linear relationship that describes the wall-pressure fluctuations (ϕ_{pp}) along the upper side of the serration surface, resulting in equation 6.5, where $\phi_{pp,\text{upper}}^o(\omega)$ and $\phi_{pp,\text{lower}}^o(\omega)$ represent the wall-pressure spectrum measured sufficiently upstream from the trailing edge.

If $\eta = 1$ the pressure at that location corresponds to that of the wall-bounded case ($\phi_{pp}(\mathbf{x}, \omega) = \phi_{pp,\text{upper}}^o(\omega)$). Conversely $\eta = 0$ pertains to a point sufficiently far from the wall, where the mentioned -3 dB correction should apply, i.e. $\phi_{pp}(\mathbf{x}, \omega) = \frac{1}{4}\phi_{pp,\text{upper}}^o(\omega) + \frac{1}{4}\phi_{pp,\text{lower}}^o(\omega)$.

$$\phi_{pp}(\mathbf{x}, \omega) = \frac{1}{4} [1 + 3\eta(\mathbf{x}, \omega)] \phi_{pp,\text{upper}}^o(\omega) + \frac{1}{4} [1 - \eta(\mathbf{x}, \omega)] \phi_{pp,\text{lower}}^o(\omega) \quad (6.5)$$

The above equation models the reduction of the wall-pressure fluctuations close to the trailing-edge region and predicts the distribution of the wall-pressure fluctuations over any trailing-edge geometry. For lower frequencies, the larger extent of the turbulent structures (larger radius of influence, l) imposes a more gradual change of the parameter η and thus the wall-pressure fluctuations are

modified from a larger distance to the edge. Instead, at higher frequencies, (smaller radius of influence l) the change remains confined to the near edge region. This aspect is demonstrated by experiments and discussed in more detail in the results section. The model proposed is valid for both serrated and non-serrated trailing edges. The latter geometry is also expected to present a reduction of the pressure fluctuations near the vicinity of the edge. However, this reduction does not vary over the span as it happens with a serrated trailing edge.

6.2.2 WAKE DEVELOPMENT AND ACCELERATION OF TURBULENT STRUCTURES

Besides the natural decrease of the wall-pressure fluctuations imposed by the change in the impedance across the trailing edge, the sidewise interaction between the free and the wall region along the serration also affects the distribution of the wall-pressure fluctuations. Specifically, the near-wake developing in the serration gaps modifies the properties of the flow on the serration surface. Studies in the literature report increasing wall-pressure fluctuations at the tips of serrations, especially at higher frequencies [16, 17]. An explanation put forward involves the modifications of the turbulent flow near the serrations, consequently leading to an increase of the scattered noise from the serrated trailing edges at high frequencies [11].

According to Haji-Haidari and Smith [129] the modifications of the flow field in the near wake captured within 25 times the boundary-layer momentum thickness (θ) downstream of the trailing edge are restricted to the inner-layer. This downstream distance is several times longer than the serration height ($2h$). Thus, the influence of the developing near wake on wall-pressure fluctuations must also remain restricted to the inner scales ($\omega v/u_\tau^2 > 0.3$, [46]). The most important aspect of this flow development is the increasing mean velocity within the inner scales. The work of Ghaemi and Scarano [130] shows that, within less than 5θ from the trailing edge, the velocity along $x_2 = 0$ has evolved to about 50% that in the free-stream. Hayakawa [131] have shown that, across the near wake, the wall-normal velocity fluctuations are only mildly modified. Haji-Haidari and Smith [129] too have concluded that turbulence is not impacted in the near wake, the main effect being the rapid increase of momentum in the inner layer region.

The above indicates that the near-wake development along the serration mostly affects the mean flow velocity near the wall. It is therefore conjectured that the observed increase in high frequencies of the wall-pressure fluctuations follows a modification of the convective velocity, while the energetic content of the fluctuations remains the same. Such increase of convective velocity was already observed by Avallone et al. [15] from the root to the tip. Furthermore, a similar trend is observed in the current experiments.

Early works [20, 44] have suggested that the convective velocity approaches $0.6\text{--}0.7U_e$ for a turbulent boundary layer, while values higher than $0.8U_e$ are often reported for a near wake flow [132]. Thus, an increase of convection velocity from root to tip is to be expected, following the different values in the wake (free) and wall-bounded region. Considering that the wavenumber spectrum is not altered, this acceleration causes a shift of the energy of the smaller structures in the inner layer, resulting in an increase of the wall-pressure spectrum levels at high frequencies.

Therefore, a correction for the high-frequency increase can be derived from the semi-analytical wall-pressure formulation of Goody [48], shown in equation 6.6. The equation is slightly modified so that the frequency normalization uses the convection velocity instead. The model proposed in equation 6.7 considers the ratio between the levels occurring at the root ($U_c = U_c^o$) and at a position \mathbf{x} ($U_c = U_c(\mathbf{x})$), applying the limit to higher frequencies and considering the terms of lower magnitude close to 1. The correction affects only the inner scales ($\phi_{pp} \propto \omega^{-5}$) and can be used for predicting the high-frequency increase of the wall-pressure fluctuations. In the limit of $\omega \rightarrow \infty$, the correction tends to $\phi_{pp}/\phi_{pp}^o(\mathbf{x}) = (U_c(\mathbf{x})/U_c^o)^5$, indicating that a maximum increase is observed at high frequencies. This increase starts with the inner scales of the turbulent boundary layer, which frequency can be estimated according to equation 6.8. It is important to note that the $\phi_{pp} \propto \omega^{-5}$ is a theoretical condition elaborated for low pressure gradient boundary layers [42]. The works of Rozenberg et al. [126], Catlett et al. [57], and Lee and Villaescusa [47] propose different scalings that depend on the pressure gradient and boundary-layer properties. Introducing these models can produce more precise predictions for highly adverse pressure gradient conditions.

$$\frac{\phi_{pp} U_e}{\tau_w^2 \delta}(\omega) = \frac{C_2 \left(\frac{\omega \delta}{U_c} \right)^2}{\left[\left(\frac{\omega \delta}{U_c} \right)^{0.75} + C_1 \right]^{3.7} + \left[C_3 R_t^{-0.57} \left(\frac{\omega \delta}{U_c} \right) \right]^7} \quad (6.6)$$

$$\frac{\phi_{pp}}{\phi_{pp}^o}(\mathbf{x}, \omega) = \frac{1 + C_3^7 R_t^{-4} \left(\frac{\omega \delta}{U_c^o} \right)^5}{1 + C_3^7 R_t^{-4} \left(\frac{\omega \delta}{U_c(\mathbf{x})} \right)^5} \quad (6.7)$$

$$f_{\text{wake}} = 0.05 \frac{u_\tau^2}{\nu}. \quad (6.8)$$

The above correction depends only on the estimation of the convection velocity along the serration. In this work, the convective velocity is estimated from the wall-pressure measurements on the serration centre. Further investigations can

explore an analytical description of the convection velocity along the serration surface.

6.2.3 AERODYNAMIC LOADING EFFECT

A third important aspect that affects the distribution of the wall pressure along the serrations is the aerodynamic loading. When serrations are at an angle with respect to the flow direction, a pair of streamwise vortices emanates from the serrations, as a result of the pressure difference between the two sides of the serrations. The presence of these vortices is commonly associated with the loss of acoustic performance of trailing-edge serrations under loading [19, 122].

Recent studies have demonstrated that the vortices cause an increase of the wall-pressure fluctuations along the outer rim of the serration surface [109]. An assessment of the mean-shear turbulence terms has pointed out that the acceleration of the mean flow interacting with the incoming turbulent fluctuations from the boundary layer is directly related to the modification of the wall-pressure fluctuations captured.

The presence of the vortex pairs modifies the velocity field, in turn generating new velocity gradients along the stream and spanwise direction. Arce Leon et al. [122] showed that the flow accelerates on the suction side in the central portion of the serration while on the pressure side the flow accelerates in the gap region. A spanwise flow component is induced that deflects the streamlines inwards on the suction side and outwards on the pressure side. The intensity of these streamwise vortices is determined by the aerodynamic loading, whereas, their size by the width of the serration. The incoming velocity fluctuations from the turbulent boundary layer interact with the mean flow velocity gradients from the streamwise vortices, thus modifying the pressure fluctuations captured at the wall, following the mean-shear interaction term of the pressure Poisson equation [54].

Therefore, the process can be thought of as the interaction between the incoming velocity fluctuations from the turbulent boundary layer and a space-periodically varying mean flow.

In this work, the mean flow caused by the aerodynamic loading is simplified as a stream-spanwise oscillation in the form of a Taylor-Green vortex, following equation 6.9.

$$\begin{cases} U_1(x_1, x_3) = U_o + iA_o \left(e^{-i\bar{k}_1 x_1} e^{i\bar{k}_3 x_3} - e^{-i\bar{k}_1 x_1} e^{-i\bar{k}_3 x_3} \right) \\ U_3(x_1, x_3) = iA_o \frac{\bar{k}_1}{\bar{k}_3} \left(e^{-i\bar{k}_1 x_1} e^{i\bar{k}_3 x_3} + e^{-i\bar{k}_1 x_1} e^{-i\bar{k}_3 x_3} \right) \end{cases} \quad (6.9)$$

In the equation, \bar{k}_1 and \bar{k}_3 define the wavenumbers excited in streamwise and spanwise directions respectively. A physical value for these quantities can be taken

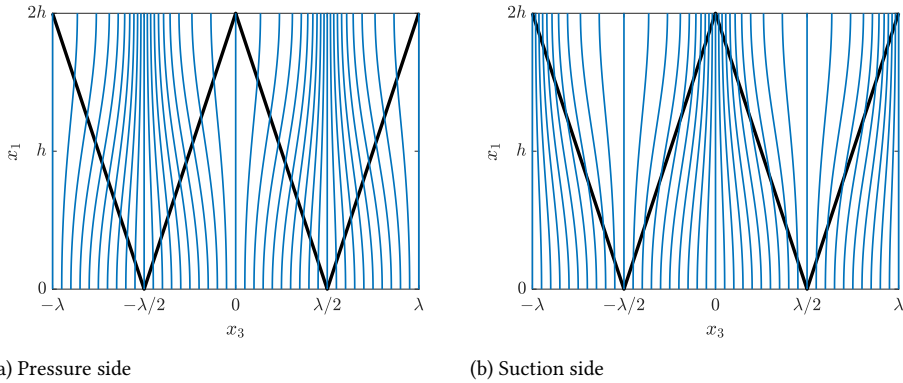


Figure 6.3: Illustrative streamlines of the flow created by the superposition of a Taylor-Green vortex with wavenumbers defined as $\bar{k}_1 = \pi/2h$ and $\bar{k}_3 = 2\pi/\lambda$ to the uniform flow.

as $\bar{k}_1 = \pi/2h$ and $\bar{k}_3 = 2\pi/\lambda$. The values represent qualitatively the accelerations experienced by the flow towards the centre of the serration on the suction side and towards the gap region on the pressure side. Figure 6.3 gives an example of the idealized flow conditions created from the Taylor-Green vortex. In the figure, the deviation of the streamlines towards the gap region on the pressure side and towards the centre of the serration surface on the suction side is demonstrated.

A model for the wall-pressure fluctuations due to the mean flow accelerations can be derived following the same procedure applied for the prediction of the wall-pressure fluctuations past a turbulent boundary layer [42]. This procedure is detailed in Appendix C. The equation mentioned in the Appendix does not have a closed analytical form. Its numerical integration is used to derive a final and simplified formulation that describes the solution in mid and high frequencies (equation 6.10). The low-frequency solution ($f < \frac{1}{2}U_c/2h$) is disregarded given that it predicts the wall-pressure fluctuations from turbulent structures that are in fact larger than the serration dimension. At such conditions, the periodic mean-flow oscillation idealized does not represent the actual flow modified only locally by the presence of the serrations. In the equation $St_{\delta^*} = f\delta^*/U_c$, where δ^* is the boundary-layer displacement thickness, and α_s represents the angle between the serration and the zero-lift serration angle in radians. For the case of the flow over a symmetric airfoil with serrations aligned with the chord line, the angle α_s corresponds to the airfoil angle of attack ($\alpha_s = \alpha$). The semi-empirical constant C_v determines the level of the wall-pressure fluctuations created by the vortex pairs and must be inferred from the experiments.

$$\frac{\phi_{pp}(St_{\delta^*})}{\rho^2 U_c^3 \delta^*} = C_v \alpha_s^2 \left[\left(\frac{2h}{\lambda} \right)^2 + \frac{1}{4} \right] \left(St_{\delta^*} - \frac{1}{4} \frac{\delta^*}{2h} \right)^2 \operatorname{erfc} \left[2.5 \left(St_{\delta^*} - \frac{1}{4} \frac{\delta^*}{2h} \right) \right]. \quad (6.10)$$

The model proposed above features the same power dependence ($St_{\delta^*}^2$) as that proposed by Goody [48] while the high-frequency decay follows a complementary error function (erfc), which comes from the adopted Gaussian velocity cross-spectrum. The resulting equation indicates that the effect of the vortex pairs does not differ from that of the turbulent boundary layer. Important modifications are the frequency shift, represented by the $(St_{\delta^*} - \frac{1}{4} \frac{\delta^*}{2h})$ term, the dependence on the serration lift, and the absence of a universal range. On a boundary layer, the universal range represents the migration from the wall-pressure fluctuations caused by the turbulent structures in the outer layer to the ones caused by the turbulent structures in the inner layer [42]. Contrary to the wall-pressure fluctuations induced on a turbulent boundary layer, the spanwise and streamwise accelerations adopted in this work are not modified within the layers, and hence the source term is not altered, resulting in no universal layer.

Figure 6.4 depicts how the spectrum predicted by equation 6.10 varies as a function of the ratios, δ^*/λ and $\lambda/2h$. Figure 6.4a describes the effect of modifying the boundary-layer height for a given serration height and wavelength ($\lambda/2h = 0.5$). The spectrum attains a maximum around $St_{\delta^*} = 0.4$ and decays rapidly for higher frequencies. Following equation 6.10, the St_{δ^*} where the effect of the vortex pairs is maximum is dependent only on the ratio $\delta^*/2h$ and can be estimated with equation 6.11:

$$St_{\delta^*}^{\max} = \frac{1}{4} \frac{\delta^*}{2h} + \frac{\sqrt{\pi}}{5}. \quad (6.11)$$

As the boundary-layer height is increased with respect to the serration, the energy of the wall-pressure fluctuations is restricted to a narrower band around $St_{\delta^*} = 0.4$ as the two wavenumbers excited (\bar{k}_1 , and \bar{k}_3) approach the smaller scales of the boundary layer. At low values of $\delta^*/2h$, \bar{k}_1 becomes smaller, and the velocity fluctuations excite a broader range of frequencies. In figure 6.4b the effect of modifying λ , while keeping the serration height and the boundary-layer thickness constant is shown. As observed, by increasing λ the amplitude of the pressure fluctuations decreases without altering the spectral shape. This happens because the serration wavenumber dictates the intensity of the vortex pairs and the smaller λ is, the more intense the vortex and consequently the induced wall-pressure fluctuations.

Overall, the boundary-layer displacement thickness (δ^*) seems to influence the location of maximum and the frequency of the decaying spectrum, while the

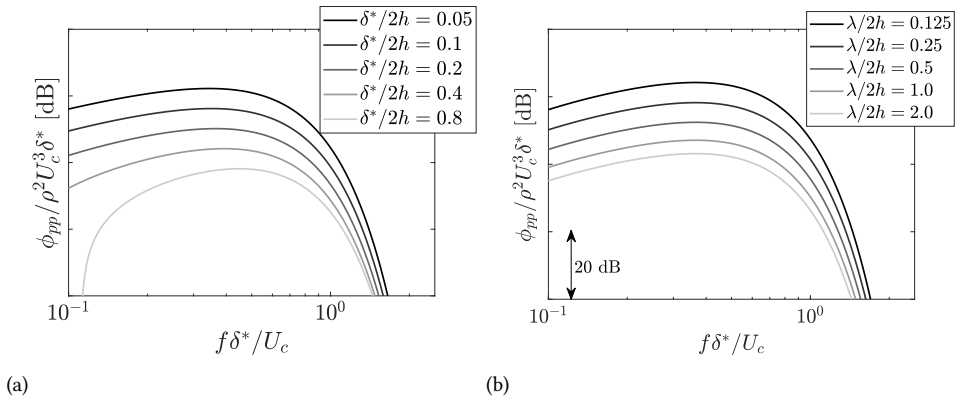


Figure 6.4: Predicted wall-pressure spectrum due to the presence of vortex pairs for different values of $\delta^*/2h$ (a), and of $\lambda/2h$ (b).

serration height and wavelength modify the cut-on and the energetic content of the large scales.

6

6.3 EXPERIMENTAL DATASET

The semi-empirical models presented in Section 6.2 are compared and tuned with experimental data of the wall-pressure fluctuations on the surface of a serrated trailing edge. The experiments are conducted in the Low Turbulence wind Tunnel (LTT) at the Delft University of Technology using the 2D NACA 63₃-018 airfoil model described in Section . Figure 6.5a shows the model installed inside the section.

A sawtooth-shape serration of $2h = 90$ mm, $\lambda = 45$ mm, thickness of 1 mm, and 2 mm radius at junctions and tips was manufactured in steel. This design is chosen following the criteria proposed in Gruber [133] of $h/\delta > 1$, and $2h/\lambda = 0.5$. The thickness (t) of the insert is selected to be the same as the airfoil trailing-edge thickness, following $t/\delta^* < 0.3$ [134]. Figure 6.5b depicts the serration main geometry. The add-on is attached to one side of the model and a bend angle of 3.2° (equivalent to the airfoil trailing-edge angle) is given to the piece so that the serration is aligned with the airfoil chord.

The boundary-layer parameters obtained from the measurements are summarized in Table 6.1. The values in brackets show the predictions obtained with X-Foil. The agreement between the measurements and the predictions serves as a verification of the code for the current setup. The boundary-layer values at each angle of attack used in the remainder of the analyses are taken from the software results.

The convective velocity across the serration centre, necessary for the correc-

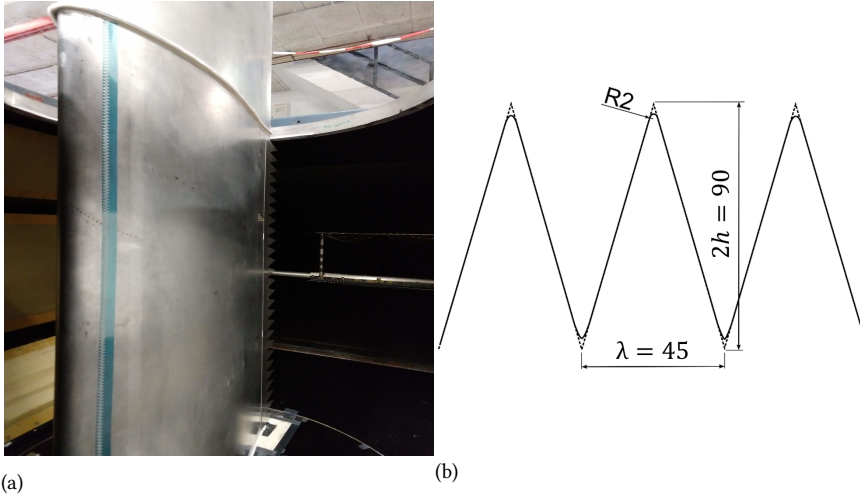


Figure 6.5: BANC-X NACA 633-018 2D wing model mounted inside the LTT wind tunnel with Kevlar test section and serration geometry used (dimensions are shown in mm).

Table 6.1: Boundary-layer properties measured at the trailing edge of the airfoil model. Values in parenthesis indicate the predictions using the X-Foil software.

U_∞ (m/s)	$\alpha_{\text{eff.}}$ (°)	Re_c (-)	δ (mm)	δ^* (mm)	θ (mm)	U_e (m/s)	u_τ (m/s)	Π (-)
17	0	1.0×10^6	28	6.7 (6.3)	4.1 (3.9)	15.3	0.45 (0.48)	2.6
34	0	2.0×10^6	27	6.1 (5.3)	3.9 (3.4)	31.5	0.91 (0.94)	2.5
	4 (SS)	2.0×10^6	30	9.0 (8.4)	4.8 (4.7)	31.5	0.69 (0.78)	4.8
	4 (PS)	2.0×10^6	17	3.4 (3.6)	2.8 (2.6)	31.0	1.08 (1.08)	1.4
51	0	3.0×10^6	26	5.5 (4.9)	3.6 (3.3)	47.6	1.35 (1.39)	2.4

tions proposed in Section 6.2.2, is also estimated using the pairs of sensors along the serration centre. The derivative of the phase in the cross-spectrum of the pressure measurements with respect to the frequency (equation 6.12) is used to estimate the convection velocity (U_c), following the work of Romano [56]. In the equation, ψ is the phase in the cross-spectrum and Δx_1 is the distance between the sensors.

$$U_c = 2\pi\Delta x_1 \frac{d\psi^{-1}}{df}. \quad (6.12)$$

Using the pair of sensors at the root of the serration, a relation between convective velocity and the boundary-layer shape factor (H) is obtained by combining the data at different velocities and angles of attack. This relation follows equation 6.13 and the fitting comparisons can be seen in figure 6.6a for the three Reynolds numbers tested in this experiment. The work of Catlett et al. [57] has also proposed a linearly decaying convection velocity with H . The choice for the exponential function in this work follows the limits expected for $H \rightarrow 1$ (uniform flow, $U_c = U_e$), and $H \rightarrow \infty$ ($U_c = 0$).

$$\frac{U_c^o}{U_e} = e^{-\left(\frac{H-1}{1.5}\right)^{3/4}}. \quad (6.13)$$

The measurements of the convection velocity along the serration have indicated that it increases almost constantly from the root to the tip of the serration, as depicted in figure 6.6b. Thus, U_c can be described along the serration following equation 6.14. This empirical relation is used in the remainder of the manuscript in order to produce the corrections described in Section 6.2.

$$\frac{U_c}{U_e}(x_1) = \frac{U_c^o}{U_e} + 0.14 \left(\frac{x_1}{2h} \right). \quad (6.14)$$

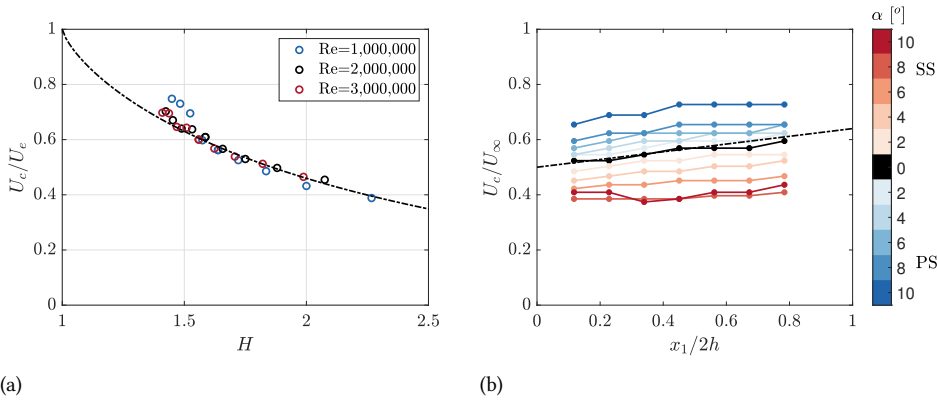


Figure 6.6: Measurements of the convection velocity along the centre of the serration. (a) fit of convection velocity at the root of the serration (equation 6.13) (b) variation of the convection velocity along the serration compared to a linear fit in dotted and dashed line (equation 6.14).

6.4 RESULTS AND DISCUSSIONS

In this section, the proposed analytical models are compared against the data from the experimental campaign to validate the hypotheses formulated and provide ways of predicting the wall-pressure distribution on the surroundings of a serrated trailing edge. The first section describes the effects that are independent of the aerodynamic loading of the serrations while the second section focuses on the particular effects of aerodynamic loading.

6.4.1 WALL-PRESSURE SPECTRUM WITHOUT LOADING

Figure 6.7 shows the measured variations of the pressure spectrum along the serration edge at $Re = 2 \times 10^6$ and $\alpha = 0^\circ$. It is important to highlight that the wall-pressure fluctuations measured are also affected by the scattered acoustic waves at the trailing edge. It is hereby assumed that the variation of the wall-pressure fluctuations over the serration surface is solely an effect of the modifying convective fluctuations. The assumption is based on the much larger wavelength of the acoustic waves in comparison to the aerodynamic ones (in the order of 10 times larger), which are unlikely to vary within the dimensions of the serration.

The effects highlighted in sections 6.2.1 and 6.2.2 can be observed from the graphs. At low frequencies, the wall-pressure spectrum levels decrease from the root towards the tip of the serration. This decrease is, however, bound to no more than 3 dB, as demonstrated with all the measured wall-pressure spectra within the grey region, which represents 3 dB below the most upstream sensor (black curve). The reduction seems to affect strongly the low frequency content ($f < 2,000$ Hz) and it reduces as the frequency is increased.

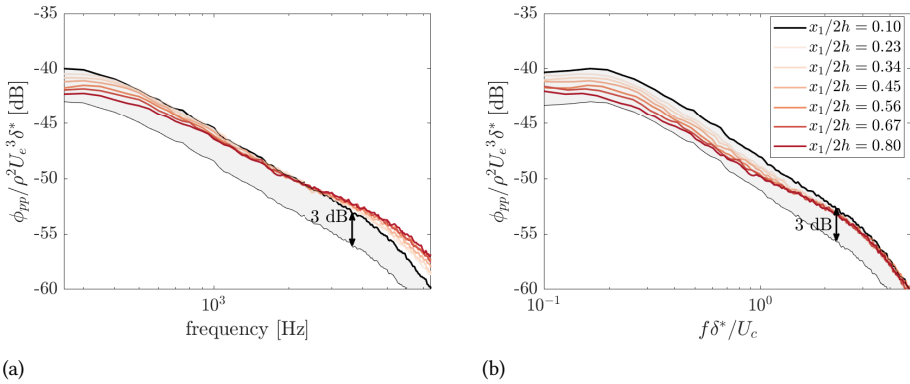


Figure 6.7: Measurements of the wall-pressure spectrum along the centre of the serration for $\alpha = 0^\circ$ and $Re = 2 \times 10^6$. Figure (a) shows the wall-pressure levels with no scaling applied in the frequency and (b) with the frequency scaled with the local convection velocity. The grey area illustrates the maximum possible reduction hypothesized (3 dB) from equation 6.1.

6

At high frequencies ($f > 2,000$ Hz), the opposite trend is noted and the pressure fluctuations increase instead. In figure 6.7b the same plot is shown but the frequency is scaled with the convection velocity estimated at the specific sensor location (following equation 6.14). As it can be seen, this scaling is able to make all the curves collapse at high frequencies. The agreement suggests that the high-frequency increase of the pressure fluctuations observed along the serrations in this experiment is driven solely by the increase of the convection velocity at the inner scales. Other references [16, 17] have observed the same trend of increased levels at high frequencies, which points to the same effect taking place.

The modifications of the wall-pressure fluctuations along the serrations at a given frequency can demonstrate the influence of the underlying mechanisms discussed. Figure 6.8 shows the distribution of the wall-pressure fluctuations over the serration surface for 6 selected frequencies. Figures 6.8 (a to f) depict the experimental results linearly interpolated from the microphone locations while figures 6.8 (g to l) show the respective predictions obtained from equations 6.5 for the impedance change, and 6.7 for the modification of the convective velocity. The predictions of the effect of the impedance modification are performed using a value $C_i = 2.1$, i.e. considering a radius of influence 1.5 times larger than the spanwise correlation length at the specified frequency (according to the formulation of [44], and prediction values of [51]). In equation 6.7, the value $C_3 = 1.1$ is chosen following [46].

At low frequencies, the dominant effect is the impedance change from the wall-bounded to the free region. Given the larger structures at such frequencies,

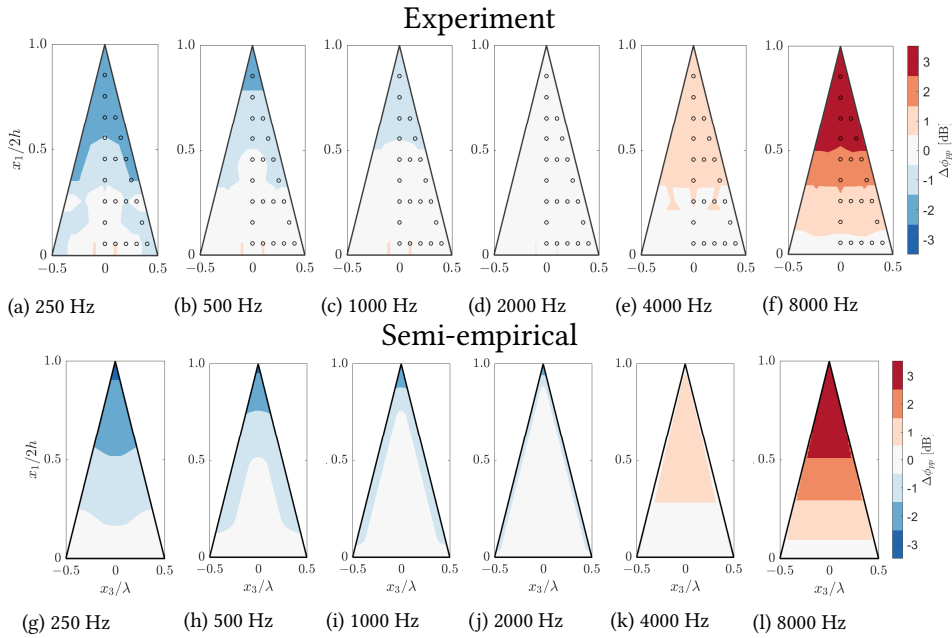


Figure 6.8: Distribution of the wall-pressure fluctuations over the serration surface for $\alpha = 0^\circ$ and $Re = 2 \times 10^6$. Reference is set to the sensor at the centre root of the serration. Figures (a) to (f) show the measured wall-pressure levels and figures (g) to (l) show the predicted distributions.

the radius of influence (l) is also larger and, therefore, the reduction of the wall-pressure fluctuations is gradual and takes over a larger portion of the serration surface. This effect can be seen both for the experimental data (figures 6.8a, b, and c) and for the model predictions (figures 6.8g, h, and i). The predictions proposed in section 6.2.1 can describe well the phenomenon and the discrepancies with the experimental data are within the 1 dB accuracy of the plot.

As the frequency increases, the smaller wavelengths of the turbulent waves restrict the effect of the impedance modification only to the very edge of the serrations, which cannot be captured by the sensors. On the other hand, the modification of the convective velocity is responsible for increasing the wall-pressure levels at the serration tip. This is observed for the two highest frequencies in this measurement ($f = 4000$, and 8000 Hz). The correction proposed in section 6.2.2 produces satisfactory predictions. The hypothesized independence of the spanwise position on the convection velocity can also be noted from the experimental data, where the increase of the wall pressure depends only upon the streamwise location along the serration.

In figure 6.9, the predicted variations with respect to the root pressure fluctuation ($\Delta\phi_{pp}$) are presented (dashed and dotted curves) against the measured ones

(circular marks) for the three speeds tested. Overall, the predictions capture correctly the trends of the experimental results. The agreement confirms the physical mechanisms hypothesized for serrations without aerodynamic loading. Different studies have demonstrated a similar trend of the pressure fluctuations [12, 16–18] and are believed to be affected by the same phenomena.

The proposed corrections are dependent on the Strouhal number and as such, they are shifted towards higher frequencies as the flow speed increases. The wake acceleration correction is also dependent on the Reynolds number as the factor R_t from the Goody model governs the start of the inner scales.

The predictions follow correctly the experimental observations. Deviations from the prediction are overall below ± 1 dB. Following the consistency of the deviations with the sensor location, it is here assumed that the deviations are originated from the model assumptions and not from experimental uncertainties. In comparison, the hypothesis of frozen turbulence would lead to errors in the order of ± 3 dB. Nevertheless, deviations between the predictions and the experimental data arise in the mid-frequency range. These deviations are caused by the selection of $C_i = 2.1$ for the η function and the parameter C_3 that controls the starting of the inner scales in Goody equation.

To summarize, when serrations are tested on an airfoil or flat plate at zero or mild aerodynamic loading conditions, the following observations should be expected for the wall-pressure fluctuations:

- low-frequency fluctuations are higher at the root and reduce towards the tip. This reduction is limited to no more than 3 dB and is caused by the transition between the wall-bounded region to the unbounded one;
- high-frequency fluctuations are higher at the tip and lower at the root. The increase follows the acceleration of the flow near the serration edge and is limited to $50 \log_{10} \left(\frac{U_c(x)}{U_c^0} \right)$ dB.

Further verification of the analytical models against the data presented in the works of Avallone et al. [16, 17] can be seen in Appendix D.

6.4.2 WALL-PRESSURE SPECTRUM WITH LOADING

The effect of increasing aerodynamic loading on the distribution of the wall-pressure fluctuations on the suction side can be observed in figure 6.10 for angles from 0° to 10° at non-dimensional frequencies around $f\delta^*/U_c \approx 0.4$. In the figure, the effect of the wall-pressure fluctuations induced by the vortex pairs for this experiment is apparent for angles of attack above 6° . This effect modifies the previously discussed reduction of the wall-pressure fluctuations at the serration tip and, instead, an increase in the order of 9 dB is captured for the highest angle of attack tested. As

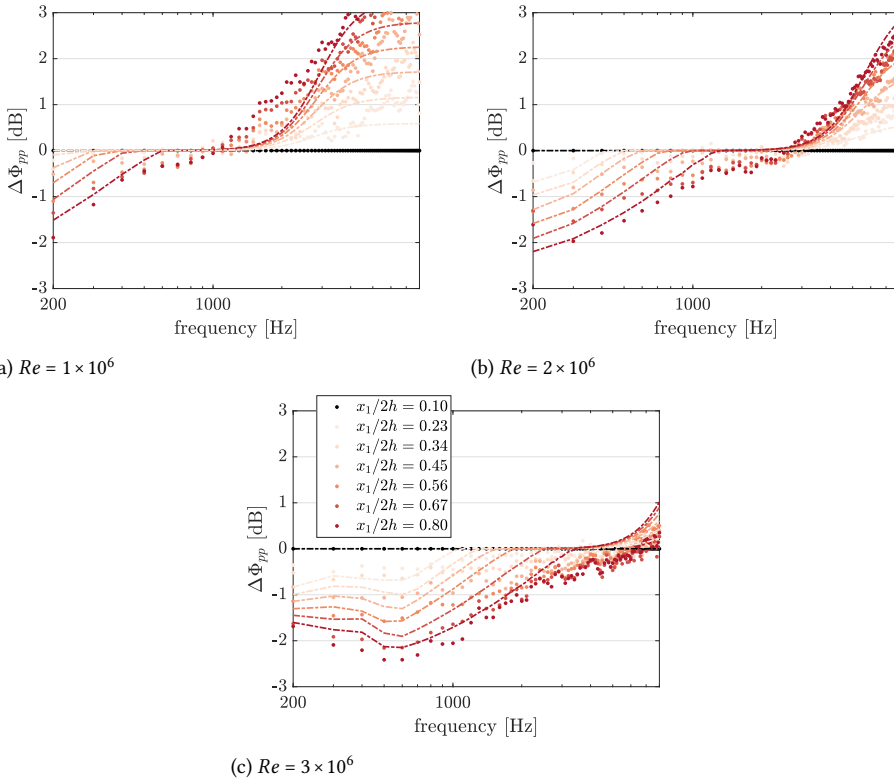


Figure 6.9: Comparison between measured (circular marks) and predicted (dashed-dotted lines) $\Delta\phi_{pp}$ at sensor positions along the centre of the serration for $\alpha = 0^\circ$. Delta values are computed as the difference with respect to the pressure fluctuations measured by the sensor at the centre root of the serration ($x_1/2h = 0.10, x_3/\lambda = 0.0$).

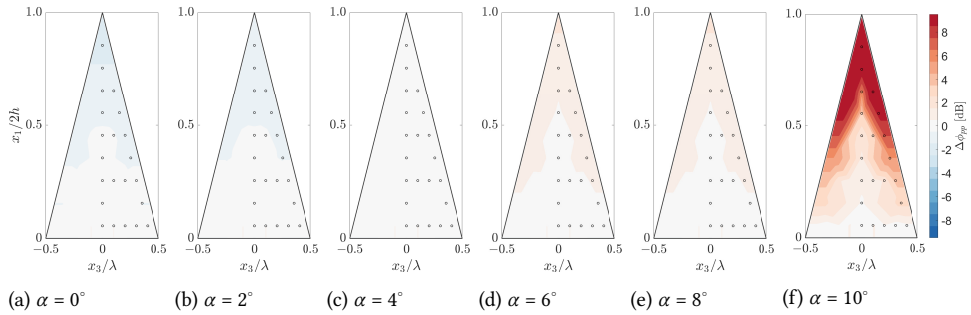


Figure 6.10: Distribution of the wall-pressure fluctuations over the serration surface measured on the suction side at different angles of attack, $Re = 2 \times 10^6$ and $f\delta^*/U_c \approx 0.4$. Delta values are computed as the difference with respect to the pressure fluctuations measured by the sensor at the centre root of the serration ($x_1/2h = 0.10$, $x_3/\lambda = 0.0$) for each angle of attack.

shown in Lima Pereira et al. [109] for this model, the outer rim of the serrations is affected and the pressure fluctuations are increased along this region.

Figure 6.11 details the variation of the spectrum along the serration edge for a highly loaded case ($\alpha = 10^\circ$). From the figures, it is clear that the vortex pairs cause an increase in the pressure fluctuations restricted in a narrow band around $f\delta^*/U_c = 0.4$. This increase is more clearly observed on the pressure side (figure 6.11a), where the smaller pressure fluctuations at low frequencies make the effect of the vortex pairs more prominent. Nevertheless, a small increase in the pressure levels can also be noted for the spectrum on the suction side (figure 6.11b).

Figure 6.11 further shows the results from the semi-empirical model reported in equation 6.10 as dashed-dotted lines. The prediction is obtained using $C_v = 5.1 \times 10^{-3}$, the boundary-layer properties from the suction side, and the convective velocity estimated at the root of the serration at the suction side. The values chosen seem to produce a coherent prediction of the loading effect on both sides, indicating that the interaction of the vortex pairs with the suction side fluctuations (the strongest fluctuations in this frequency range) is dominant. The value of 5.1×10^{-3} is defined to match the spectrum measured at the serration tip. The simplifications of the mean flow considered for the analytical modelling do not allow a description of the spatial distribution of the wall-pressure fluctuations as observed in figure 6.10. Nevertheless, the model predicts correctly the narrowband increase of the wall-pressure fluctuations observed in the experiment, reinforcing the assumption made about this mechanism. Underpredictions are observed in the high-frequency range, which could be driven by the choice of the Gaussian spectrum. Grasso et al. [135] has also observed a faster decay of the predicted pressure fluctuations from the wall-pressure fluctuations modelled with the Gaussian velocity cross-correlation equation in comparison with other velocity cross-correlation models.

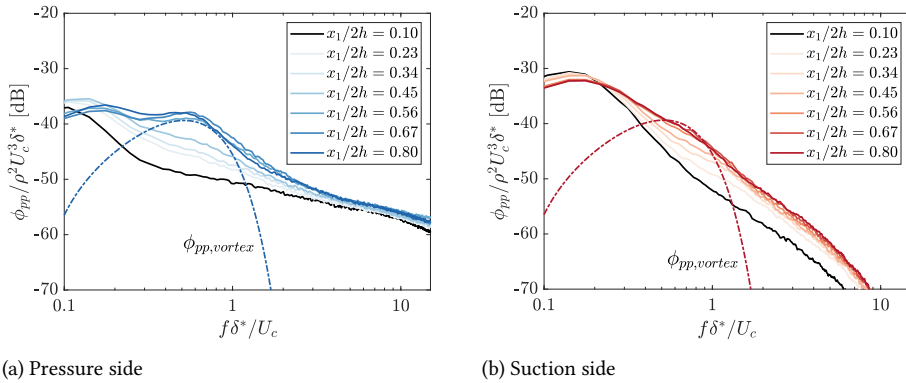


Figure 6.11: Measured variation of the wall-pressure spectrum measured (ϕ_{pp}) along the serration edge for $\alpha = 10^\circ$ and $Re = 2 \times 10^6$. (a) shows the spectrum along the pressure side and (b) along the suction side. Predicted aerodynamic loading effects are presented in dashed and dotted lines ($C_v = 5.1 \times 10^{-3}$).

The proposed analytical model is also compared against the wall pressure captured at the serration tip in figure 6.12 for different airfoil angles of attack. Values are presented again for $C_v = 5.1 \times 10^{-3}$.

The figure depicts how the model describes the narrowband increase measured for the spectrum at the tip of the serration. Also, the variation of the measured wall-pressure fluctuations with the angle of attack is presented. The wall-pressure fluctuations due to the aerodynamic loading for $\alpha \leq 4^\circ$ are well below the ones induced by the turbulent boundary layer and, as such, they do not influence the measured spectrum at such conditions, following the observations from figure 6.10a, b, and c. For higher angles, the pressure fluctuations induced by the aerodynamic loading are of the same order as the ones due to the incoming turbulent boundary layer, and so, the effect of the vortex pairs starts to be part of the observed wall-pressure distribution over the serrations (figure 6.10d, e, and f). This is well in agreement with the predictions from equation 6.10. Nevertheless, an overprediction is observed for the spectrum at $\alpha = 8^\circ$ from both the suction and the pressure side. This can indicate the assumption of linear variation of the induced velocity with the angle of attack (discussed in Appendix C) is not appropriate at such high angles and small serration aspect ratio or that the value of C_v based on the data at 10° overestimates the aerodynamic loading effect at smaller angles. Overall, the model captures the observed trends correctly and, despite the oversimplifications on the description of the flow field and velocity fluctuations, it can be used for estimating the effect and influence of the aerodynamic loading on the wall-pressure spectrum of sawtooth serrations of different sizes.

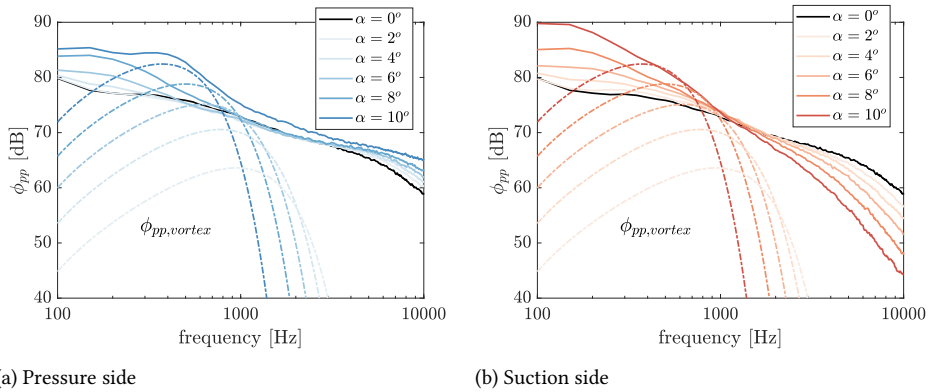


Figure 6.12: Comparison between measured ϕ_{pp} (solid lines) and predicted aerodynamic loading effects (dashed dotted lines) at the sensor located at the serration tip ($Re = 2 \times 10^6$). (a) shows the spectrum on the pressure side and (b) on the suction side.

Finally, figure 6.13 compares the spectrum measured along the serration edge at different angles of attack with the one predicted with the semi-empirical equations proposed. The comparisons are created using the root wall-pressure spectrum as reference and shows the predictions at $x_1/2h = 0.10$, $x_1/2h = 0.56$, and $x_1/2h = 0.80$ along the edges of the serration. The plots are obtained with the contributions from equations 6.5, 6.7, and 6.10 applied to the reference wall-pressure spectrum measured at the centre and root of the serration. It is important to remind that the former two effects are multiplied to the reference spectrum while the latter one is added to it. The agreement for the case of $\alpha = 0^\circ$ was already demonstrated. Figures 6.13(b) and (c) show how the proposed models predict well the experimental wall-pressure spectrum at different angles of attack. In all the figures the effect of the near-wake acceleration can be observed. This effect increases the wall-pressure fluctuations around the tip of the serrations for frequencies above 2 kHz. The predicted spectra at high frequencies are well compared against the measured ones. Discrepancies are slightly larger at high angles of attack, e.g. $\alpha = 8^\circ$, which could be associated with the ω^{-5} scaling assumed by the Goody model. The change of the impedance along the serration has an effect on the wall-pressure fluctuations that varies between the suction and the pressure side. The higher fluctuations on the suction side are reduced from the root to the tip of the serration, as observed in the experiments. However, the opposite trend is captured on the pressure side. On this side, the tip region is affected by both the lower pressure fluctuations from the pressure side but also by the higher fluctuations from the suction side, following equation 6.1. As a result, the levels are expected to increase from the root to the tip, as also observed in the figures. The effect of the vortex pairs can be seen in

the $\alpha = 8^\circ$ case. A hump close to 800 Hz is predicted for all the spectra. This hump agrees with the data outside the serration root. Since the model does not depend on the location over the serration surface, the effect of the vortex pairs overpredicts the spectrum for $x_1/2h = 0.10$ on the pressure side. This error can be avoided by applying the equation only to the prediction of the wall-pressure fluctuations along the edge and tip of the serrations, where the vortex-pair effect is more noticeable.

The results indicate that the semi-empirical models proposed are able to capture the trend of the wall-pressure fluctuations on the surface of the serrated trailing edges under different aerodynamic loading conditions. Variations of the spectrum observed in this experiment ranged from -3 to $+9$ dB, indicating that prediction of trailing-edge noise from the incoming wall-pressure fluctuation is prone to errors of the same magnitude. The semi-empirical models are able to capture this variation consistently throughout different velocities, angles of attack, and locations on the serrations surface.

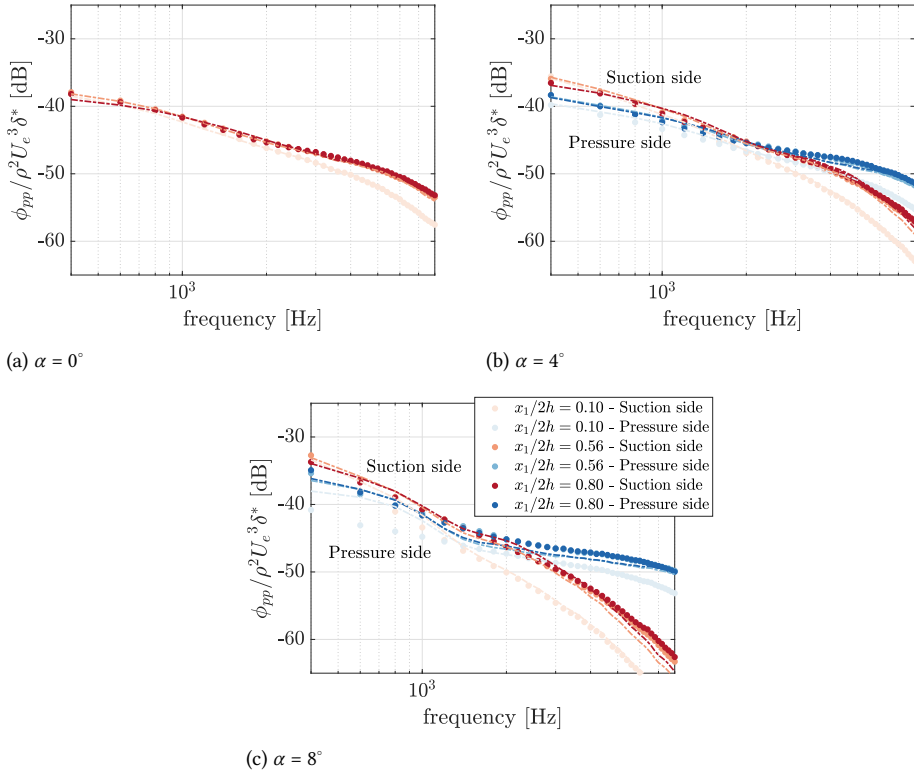


Figure 6.13: Comparison between measured ϕ_{pp} (circular marks) and predicted wall-pressure spectrum (dashed dotted lines) along the serration edge for three different angles of attack ($Re = 2 \times 10^6$). Levels are made non-dimensional with respect to the boundary-layer displacement thickness at $\alpha = 0^\circ$. The analytical predictions are created using the spectrum at the centre and root ($x_1/2h = 0.1$, $x_3/\lambda = 0.0$) of the serration as reference.

6.5 CONCLUSIONS

Physical interpretation and semi-empirical models of the underlying mechanisms behind the observed wall-pressure fluctuations over a sawtooth serration surface are proposed. The interpretation is corroborated with experimental data from measurements of the wall-pressure fluctuations over a symmetric airfoil model at high Reynolds regime. Results compare the semi-empirical models with the measured wall-pressure fluctuations over the serration surface, demonstrating the importance of the three mechanisms described and their effects on the wall-pressure fluctuations over the serration surface.

At low and mild loading conditions, the distribution of the wall-pressure fluctuations is dictated by the transition between bounded and unbounded flow and the flow accelerations in the near wake. The former causes the fluctuations to decrease by no more than 3 dB (in the symmetric case) from the root to the tip. The latter impacts the energy distribution of the small structures in the frequency domain, causing an increase in high frequency at the serration tip. The experimental results show that both phenomena are apparent along the serration surface. Also, the semi-analytical models proposed are able to capture the main tendencies of the experiment with deviations no larger than 1 dB.

At high loading conditions, the accelerations of the mean flow imposed by the vortex pairs formed around the serrations affect the wall-pressure distribution at mid-frequencies ($f\delta^*/U_c \approx 0.4$). A proposed model for the influence of the vortex pairs is created by assuming the stream and spanwise accelerations of the mean flow interacting with the incoming velocity fluctuations dominant. Considering a simple excitation in the form of a Taylor-Green vortex, an analytical model can be derived for the wall-pressure fluctuations generated by a forcing wavenumber excitation of the mean flow in the incoming velocity fluctuations from a turbulent boundary layer. The results show that the derived model can describe the observed trends of serrations under high loading conditions, predicting the observed narrowband increase in the wall-pressure levels around the frequency range and the dependency on the ratio δ/λ . This model still needs to be verified for different serration aspect ratios.

Overall, the results corroborate with the physical understanding and mathematical modelling of wall-pressure fluctuations over serrated trailing edges. The mechanisms highlighted here play an important role in the scattered noise from serrated trailing edges. The hypothesized frozen turbulence has already been proven to fail in many other references [11, 14, 16–18, 38]. In this work, an attempt is made to first model the deviations of the wall-pressure fluctuations mentioned. The proposed analytical approach can be further expanded, without affecting its general validity, to include a more complex wall-pressure spectrum model for the wake acceleration effect or a different description of the vortex pairs surrounding

the serrated edge. The resulting equations from this work can be used to improve the fidelity of noise predictions from serrated trailing-edge configurations.

7

SERRATION GEOMETRY AND ITS IMPLICATION ON THE EMITTED NOISE

7.1 OBJECTIVES

Theoretical models [10, 20–22, 62] have described the main physical mechanism of serrated trailing edges and explained the noise reduction obtained. According to the theory, by creating a non-orthogonal angle between the incoming turbulent flow fluctuations and the trailing-edge direction, serrations promote a weaker scattering of the dominant wall-pressure fluctuation modes, i.e. the spanwise oriented waves ($k_z = 0$). Similarly to the noise of a slanted trailing edge [29], this weaker scattering in comparison to a straight edge is responsible for the noise reduction observed in the far field.

The analytical approaches, however, neglect the modifications of the flow due to the presence of the serrations which, in turn, affect the acoustic response [16, 17, 122]. Throughout the years, researchers have demonstrated that the flow is significantly altered by introducing trailing-edge serrations [12, 15, 109, 110, 133, 137]. In an effort to model such alterations, Lima Pereira et al. [110] has shown that three physical mechanisms dominate the modification of the wall-pressure fluctuations on the surface of a serrated trailing edge. Two of these mechanisms concern the alteration of conditions in the vicinity of the serrations while the last one pertains only to serrations generating aerodynamic loading, i.e. a pressure difference between the upper and lower side of the serration exists. This aerodynamic loading causes a pair of counter-rotating vortices to be formed around the serration edges [15], inducing an increase in the wall-pressure fluctuations over the serrations. The latter is associated with the noise increase from serrated trailing edges at high angles, as shown in Arce Leon et al. [122] and Lima Pereira et al. [111].

The modification of the wall-pressure fluctuations for serrated trailing edges is often described as the main cause of the departure between the predicted and the observed noise reduction spectrum from serrated trailing edges [62, 122, 137]. For example, while models predict an asymptotic noise reduction at high frequencies, experiments and numerical simulations have always demonstrated a cut-off of the noise reduction and even noise increase at high frequencies based on the flow speed (U_∞), and boundary-layer thickness (δ) ($> \frac{U_\infty}{8}$) [16, 17, 122, 133]. Also, analytical models suggest that the higher the serration aspect ratio ($2h/\lambda$) the lower the noise from the serrated trailing-edge. However, Gruber et al. [11] has shown a limit on the serration aspect ratio, where increasing its height ($2h$) or decreasing its wavelength (λ) does not improve the maximum noise reduction and an increase of the high-frequency noise is observed. Gruber et al. [11] has come to the conclusion that, differently from the analytical predictions [10], noise reduction from serrations is more correlated to the ratio $2h/\delta$, and that the aspect ratio ($2h/\lambda$) does not affect noise reduction in the same way as the predictions suggest.

Besides, several serration concepts exist, such as the sawtooth serrations, the

concave-shaped (iron, or ogee-shaped) serrations [16, 64], and the combed-sawtooth serrations [66]. Despite that, there is no consensus on the advantages and disadvantages of each geometry, which is also dependent on airfoil geometry, flow conditions, and installation effects. Therefore, the design of trailing-edge serrations lack general guidelines and still requires dedicated numerical simulations and experimental campaigns for each application.

In this work, design guidelines for trailing-edge serrations are sought. To create these guidelines, a parametric study based on experiments with sawtooth serrations of different scales and other geometries, namely concave-shaped, and combed-sawtooth serrations is carried out. Differently from other parametric studies [11, 38, 65], this work proposes a sensitivity-based approach, based on a reference sawtooth serration geometry, where each parameter of this serration design that affects the trailing-edge noise is varied separately. The trends found are interpreted through the physical mechanisms described in previous research. The model of a benchmark airfoil section [112], the NACA 63₃-018, is selected for the experiments and tested under different conditions of flow speeds and angles of attack to build a complete picture of the acoustic properties of serrated trailing edges. A description of those experiments is presented in Section 4.3 including flow conditions, serration geometries, acoustic measurements, and post-processing techniques. The discussions in the results section (Section 7.2) are based on the analytical description of the scattering at a serrated trailing edge described in 2.5.2 and the physical mechanisms of wall-pressure fluctuations on the serration surface from Chapter 6. Design guidelines and conclusions are shown in sections 7.3, and 7.4 respectively.

7.2 RESULTS AND DISCUSSIONS

In this section, the results of the acoustic measurements are discussed. The first subsection is dedicated to the basic features of the noise reduction from serrated trailing edges. The influence of flow conditions such as the flow speed and angle of attack is discussed. The second subsection is dedicated to the scaling of sawtooth trailing-edge serrations, i.e. the influence of parameters such as the serration height ($2h$), wavelength (λ), and aspect ratio ($2h/\lambda$). The third section describes the modifications of serration geometry in terms of concave and convex-shaped serrations while the last one is dedicated to the effect of introducing combs on the sawtooth serration.

7.2.1 GENERAL CHARACTERISTICS OF TRAILING-EDGE SERRATION NOISE

This section gives a description of the noise reduction obtained from serrated trailing edges. The acoustic results shown in this section describe the noise reduction spectrum of the reference serration design ($2h = 30$ mm, and $\lambda = 15$ mm) and how

it varies with the different flow conditions tested.

At first, the variation of the noise reduction with the flow speed is assessed, as shown in Figure 7.1. In Figure 7.1(a), the dimensional frequencies demonstrate how the noise reduction created by the serrations is shifted from lower frequencies at low speeds to higher ones at high speeds. Following previous works [11, 13, 16, 17], the measured noise reduction from serrated trailing-edges starts at a certain frequency, reaches a maximum, and decays for higher frequencies.

In Figure 7.1(b), the spectrum of the noise reduction is scaled with the Strouhal number based on the boundary-layer displacement thickness of the baseline airfoil (δ^*) and the flow speed. Apart from a minor modification of the amplitude of the maximum noise reduction, the collapse of the curves demonstrates how the choice of Strouhal number is a valid one to describe the spectrum of noise reduction of a certain serration design. This property has already been shown by Gruber et al. [11] and Luesutthiviboon et al. [112]. Discrepancies are observed at high frequencies and are believed to be related to the different proportionality of the high-frequency cut-off due to the wake acceleration effects. Following equation 6.8, the scaling of the wake acceleration with the Strouhal number based on the flow viscosity and friction velocity ($f\nu/u_\tau^2$) creates modifications on the non-dimensional spectral shape between different speeds.

The non-dimensional spectrum shape is expected to vary for different serration geometries. Nevertheless, results and literature [11] have consistently shown that maximum noise reduction is observed around a Strouhal number 0.09, following equation 7.1. This Strouhal number coincides with the one of maximum trailing-edge noise [31]. According to the figure, the noise reduction starts at a Strouhal number of about 0.03 and decays monotonically after the Strouhal number of maximum noise reduction.

$$f_{\max} = 0.09 \frac{U_\infty}{\delta^*}. \quad (7.1)$$

The choice of the boundary-layer displacement thickness for the Strouhal number normalization is more complicated under asymmetric flow conditions, i.e. angles of attack different than 0° or for the flow over asymmetric airfoils. As discussed in Brooks et al. [31], the thick boundary layer on the suction side is responsible for the noise generated at lower frequencies whereas the thin boundary layer on the pressure side is responsible for the noise at higher frequencies. These differences are explored in Figure 7.2(a) which shows how the noise reduction is modified for different angles of attack. Results show that the noise reduction is primarily shifted towards a lower frequency range, indicating that the noise reduction from the suction side is predominant. Nevertheless, as a simplified rule of thumb, this noise reduction can be normalized by the averaged boundary-layer

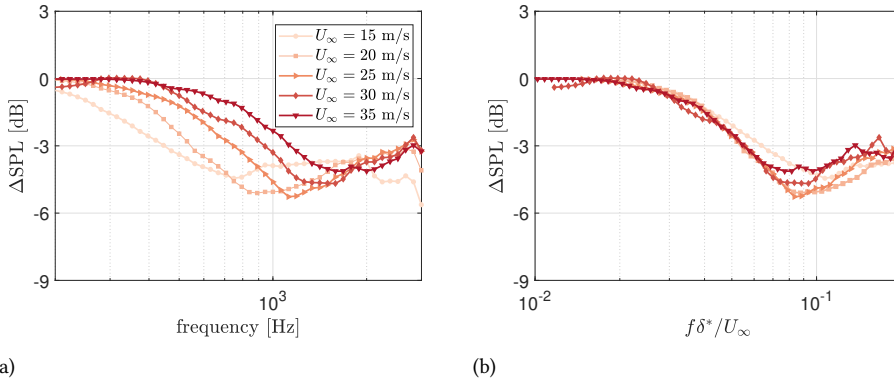


Figure 7.1: Measured noise reduction (ΔSPL) obtained at different flow speeds at $\alpha = 0^\circ$. Figure (a) shows the noise reduction measured against the dimensional frequency, and (b) shows the noise reduction versus the non-dimensional frequency obtained using the boundary-layer displacement thickness.

thickness, i.e. $\frac{1}{2}(\delta_{\text{SS}}^* + \delta_{\text{PS}}^*)$, where δ_{SS}^* is the boundary-layer displacement thickness at the suction side and δ_{PS}^* at the pressure side. Results from the Strouhal scaling are shown in Figure 7.2(b), which produces a fairly good agreement, especially at low Strouhal numbers and small angles of attack.

The non-dimensionalized spectra also show the effects associated with the aerodynamic loading of the serrations at high angles of attack. The aerodynamic loading causes an increase in the noise from the serrations, hampering the noise reduction achieved at high frequencies. This increase of noise is noticeable for angles higher than 8° at a Strouhal number of about 0.40. The value is similar to the one obtained with equation 6.11 of 0.41 for the Strouhal of maximum increase of the wall-pressure fluctuations due to aerodynamic loading. The value is shown in Figure 7.2(b) by the black dashed line in the figure.

7.2.2 SAWTOOTH SERRATION SCALING

DEPENDENCE ON THE SERRATION HEIGHT (CONSTANT $\lambda = 15$ MM)

In this section, the effect of increasing the serration height while keeping its wavelength fixed ($\lambda = 15$ mm) is studied. Four different serration heights are tested and the resulting noise reduction spectrum is shown in Figure 7.3(a) for $\alpha = 0^\circ$, and 7.3(b) for $\alpha = 10^\circ$. These angles are selected because $\alpha = 0^\circ$ represents a condition without aerodynamic loading while $\alpha = 10^\circ$ is a representative high aerodynamic loading case, where no separation is observed at the trailing edge from the pitot-rake measurements.

From the $\alpha = 0^\circ$ condition (Figure 7.3a), it is clear that the higher $2h$ translates

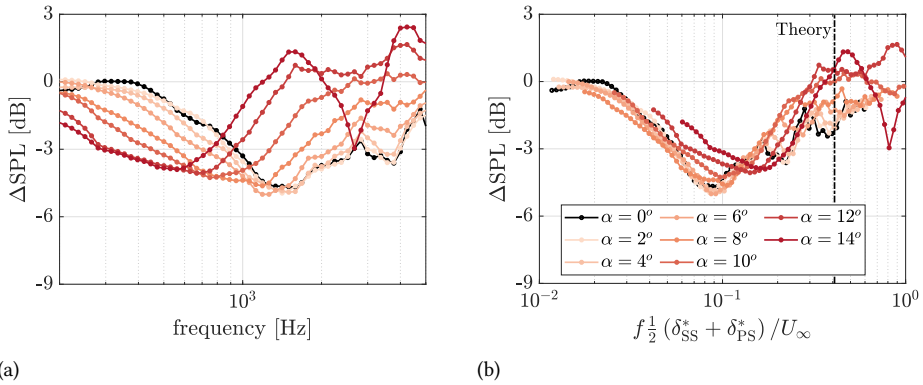


Figure 7.2: Measured noise reduction (ΔSPL) obtained at $U_\infty = 30$ m/s at various angles of attacks. Figure (a) shows the noise reduction measured against the dimensional frequency, and (b) shows the noise reduction versus the non-dimensional frequency obtained using the average boundary-layer displacement thickness. The black-dashed line represents the Strouhal number where the increase of wall-pressure fluctuations due to aerodynamic loading is maximum, according to equation 6.11.

to a higher noise reduction as predicted. Nevertheless, the expected improvement of the noise reduction is limited for serration heights above $2h \geq 12\delta^*$ ($2h \geq 2\delta$). In the figure, the highest serrations ($2h = 30$, and $2h = 40$) yield similar levels of noise reduction, indicating that increasing the height above this limit does not yield any further improvement. This result is also observed in Gruber et al. [11], where the gain in noise reduction between the two serration heights tested is small for conditions where $2h/\delta^* > 8$. The results are opposite to the predictions from theory [20, 137], where the increasing serration height always yields an improvement of the noise reduction. Following Lima Pereira et al. [110], the increase of the serration height is supposed to accentuate the wake acceleration effects, thus intensifying the increase of noise from the serrations at high frequencies. It is believed that this effect is the underlying cause of the observed upper limit for the serration height.

Figure 7.3(a) also shows that the noise reduction starts approximately in the same frequency range. The results agree with the scattering prediction models [20], as the increasing height does not impact the cut-on frequency (equation 2.55).

The effect of modifying the serration height under different angles of attack is seen in Figure 7.3(b), where the small $2h$ serrations present lower noise reduction at low frequencies and higher noise reduction at high frequencies compared to large serrations. The serration of $2h = 40$ mm even demonstrates a noise increase in the order of 3 dB against a straight trailing edge at high frequencies.

According to the theory, the increasing height modifies the sensitivity to the angles of attack. Following Lima Pereira et al. [110], the increasing height decreases the frequency where aerodynamic loading affects the noise from serrations and

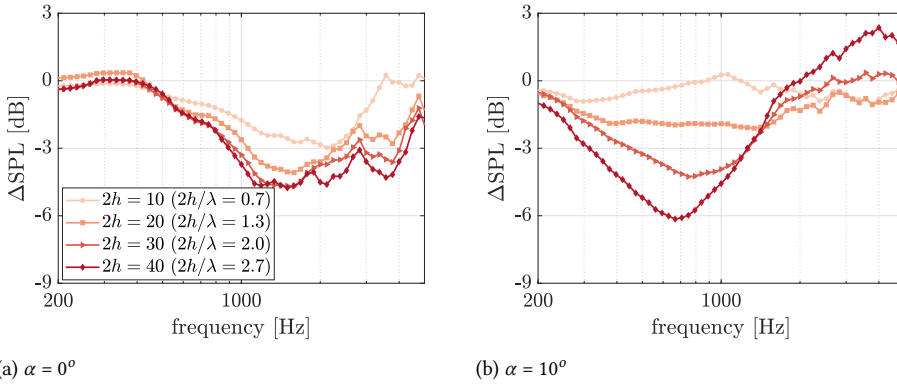


Figure 7.3: Measured noise reduction (ΔSPL) obtained at $U_\infty = 30$ m/s by varying $2h$ while keeping λ constant. (a) $\alpha = 0^\circ$, and (b) $\alpha = 10^\circ$.

increases its associated wall-pressure fluctuations. The results indicate that a higher serration experiences a stronger loss of noise reduction when at an angle than a short one. This means that increasing the serration height beyond the necessary ($2h/\delta^* \gg 12$) does not bring a meaningful increase in the maximum noise reduction and creates a design that is more sensitive to changes in flow conditions, e.g. variations of the angle of attack during the operation.

Nevertheless, following the criteria for serration height ($2h \gtrsim 12\delta^*$), the thicker boundary layer on the suction side indicates that bigger serration heights are preferable at high angles of attack. The results show that the highest serration ($2h = 40$ mm) is significantly more effective to reduce noise at low frequencies than the smaller ones at $\alpha = 10^\circ$. For this particular condition, the highest serration tested is the only design closer to the criteria of $2h \sim 12\delta^*$, i.e. $2h \approx 10\delta^*$.

The trends described before can also be observed in the contour plots of Figure 7.4. In the figures, the x-axis represents the frequency, and the y-axis the change of serration height. Figure 7.4(a) shows the obtained results at $\alpha = 0^\circ$. The black vertical lines represent the cut-on, max, and cut-off frequencies, as described in equations 2.55, 7.1, and 6.8. The horizontal line shows the described limit of $2h = 12\delta^*$. These lines indicate the measured trend from the serrations tested. Noise reduction is 3 dB lower than the maximum around the cut-on frequency ($f_{\text{cut-off}}$), reaches its maximum around f_{max} , and decays for frequencies above $f_{\text{cut-off}}$. At 10° angle of attack (Figure 7.4b), the same trends are observed. Besides, the presence of aerodynamic loading can be observed by the f_{load} curve that describes the frequency where aerodynamic loading causes an increase of the noise from the serrated trailing edges. For this case, the $2h = 12\delta^*$ line is not visible as the thicker boundary layer on the suction side causes the line to be above the highest serration

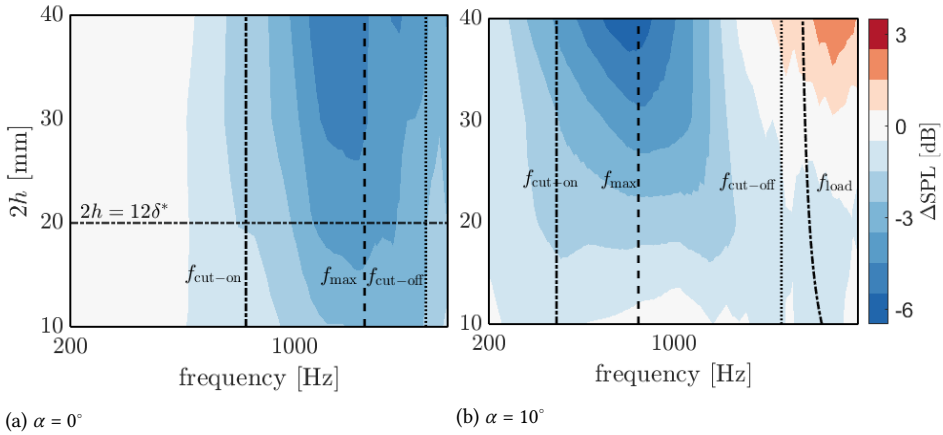


Figure 7.4: Contour plot of the variation of noise reduction for $\alpha = 0^\circ$ (a), and $\alpha = 10^\circ$ (b) at $U_\infty = 30$ m/s with the variation of serration height while the wavelength is kept constant ($\lambda = 15$ mm). Black lines show the theoretical predictions for the cut-on, max, cut-off, and loading noise frequencies.

tested. The increasing boundary-layer thickness causes the frequency of maximum noise reduction to decrease, getting closer to the cut-on frequency.

DEPENDENCE ON THE SERRATION WAVELENGTH (CONSTANT $2h = 30$ MM)

This analysis focuses on the influence of changing the serration wavelength (λ) while keeping a constant serration height ($2h = 30$ mm). In this case, for each angle of attack the non-dimensional quantity $2h/\delta^*$ is kept constant while the serration wavelength is modified, therefore affecting the serration aspect ratio. The noise reduction at $\alpha = 0^\circ$ is shown in Figure 7.5(a) while the one obtained at $\alpha = 10^\circ$ is shown in Figure 7.5(b). The overall trends at zero degrees angle of attack show that the higher wavelength yields a lower noise emission and a lower frequency where maximum noise reduction is observed. At 10° angle of attack, the noise reduction spectra from all the different serrations have a similar spectral shape.

At symmetric conditions ($\alpha = 0^\circ$), the results disagree with the predictions [20, 21], where the increasing wavelength yields less noise reduction (the lower the serration aspect ratio, the lower the noise reduction achieved). The results indicate that a wider serration (lower serration aspect ratio) reduces more noise than a narrow one. This behaviour is only observed in the experimental work of Gruber et al. [11] for the lowest wavelengths tested. Nevertheless, the predicted modification of the frequency range is observed as the increasing wavelength (λ) yields a shift in the noise reduction towards the lower frequencies, as implied in equation 2.55.

It is here speculated that the lower noise reduction from the narrow serrations

is observed due to the small frequency range between the cut-on frequency ($f_{\text{cut-on}}$), the frequency of maximum noise reduction (f_{max}), and the cut-off frequency ($f_{\text{cut-off}}$) for these designs. Following equations 7.1, and 6.8, the maximum noise and cut-off frequencies at $\alpha = 0^\circ$ are around 1600, and 2500 Hz respectively. This is observed in Figure 7.5(a), as the noise reduction decreases for all the serrations at frequencies above 2000 Hz. However, the cut-on frequency prediction from equation 2.55, tells that the serrations of wavelength 5, 10, 15, and 20 mm are meant to start reducing noise for frequencies above 2300, 1200, 800, and 600 Hz respectively. This indicates that the small wavelength designs have a theoretical cut-on frequencies similar to or higher than the predicted frequency where noise reduction is maximum or the one where noise reduction stops. This can be better visualized in Figure 7.6(a), where the contour of the variation of the noise reduction spectrum with serration wavelength is shown. The figure also shows the predicted cut-on, maximum noise, and cut-off frequencies for the different serration wavelengths. These lines follow well the observed trends, i.e. noise reduction is only higher than 3 dB for frequencies above the cut-on frequency, the noise reduction reaches a maximum around f_{max} , and it reduces for frequencies above $f_{\text{cut-off}}$.

Figures 7.5(a), and 7.6(a) indicate that designs where the cut-on, maximum noise, and cut-off frequencies are too close, such as the $\lambda = 5$, and $\lambda = 10$ mm ones, have limited noise reduction. This means that the noise reduction for those designs starts at a frequency close to the ones of maximum noise and of the cut-off frequency, where aerodynamic alterations of the inner scales increase the scattering levels. As a result, the overall achieved noise reduction is significantly reduced. The other two designs show similar noise reduction, although $\lambda = 20$ mm still presents lower noise levels at low frequencies while $\lambda = 15$ mm reduces more noise at high frequencies. By considering that trailing-edge serrations are meant to reduce noise at the regions of maximum noise on a turbulent boundary layer ($f_{\text{cut-on}} < f_{\text{max}}$), it can be inferred that $\frac{\lambda}{\delta} > 5$. This equation represents a first minimum value for the serration wavelength.

At high angles of attack, the improvement of the noise reduction of narrow serrations and the deterioration of the noise reduction of the wider ones cause all the measured serrations to present a similar noise reduction spectrum. The results indicate that the wider serrations are more affected by the angle of attack change, due to their higher surface area and consequent aerodynamic loading generated. The similar noise reduction performance also suggests that the frequency where the aerodynamic loading affects the serration noise is not modified with the serration wavelength, as predicted by the theory. The latter can be also observed in the contour plot in Figure 7.6(b) where the frequency of maximum aerodynamic-loading influence is shown. At this condition, the cut-on frequency does not describe the frequency where noise reduction starts. This behaviour is associated with the small

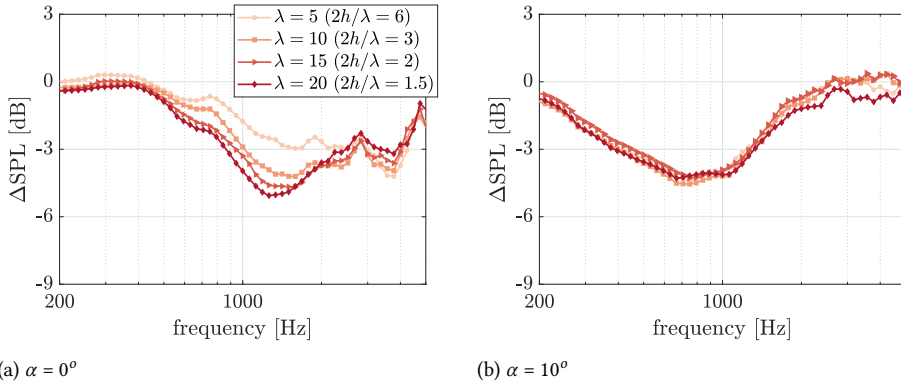


Figure 7.5: Measured noise reduction (ΔSPL) obtained at $U_\infty = 30$ m/s by varying λ while keeping $2h$ constant. (a) $\alpha = 0^\circ$, and (b) $\alpha = 10^\circ$.

difference between the maximum and cut-on frequencies at such conditions.

DEPENDENCE ON THE SERRATION SCALE (CONSTANT $2h/\lambda = 2$)

The last geometric property of the sawtooth design to be assessed is the scaling of the serration with respect to the incoming turbulent scales, i.e. the consequences of keeping the serration aspect ratio constant ($2h/\lambda = 2$) while modifying both the height and wavelength of the serrations. The resulting noise reduction spectrum is observed in Figure 7.7, where Figure 7.7(a) shows the results obtained at $\alpha = 0^\circ$, and Figure 7.7(b) at $\alpha = 10^\circ$.

From the results at zero angle of attack, the serration scale changes both the maximum noise reduction and the frequency of maximum noise reduction. According to the analytical scattering models [20], the scaling of the serrations alters only the frequencies where noise reduction starts. However, the experiments show that the cut-on frequency also affects the maximum noise reduction obtained. From the graphs, serrations with height of $2h = 30$ or $2h = 40$ ($\lambda = 15$, and $\lambda = 20$ mm respectively) show maximum noise reduction in the order of 5 dB. Among them, the changes in height and wavelength only modify the frequency where the maximum noise reduction is reached. The results from this figure suggest again that, for maximum noise reduction performance, the ratio $2h/\delta^*$ must be higher than 12. The two highest serration designs ($2h = 30$, and $2h = 40$ mm) have demonstrated the same level of noise reduction, as predicted by the analytical models. However, the smaller serrations ($2h = 20$, and $2h = 10$ mm) present a lower level of noise reduction.

These results are better illustrated in Figure 7.8, where a contour of the variation of the noise reduction with the serration scale is shown for $\alpha = 0^\circ$, and $\alpha = 10^\circ$. Figure 7.8(a) depicts the predicted cut-on, cut-off and max frequency, based on equations

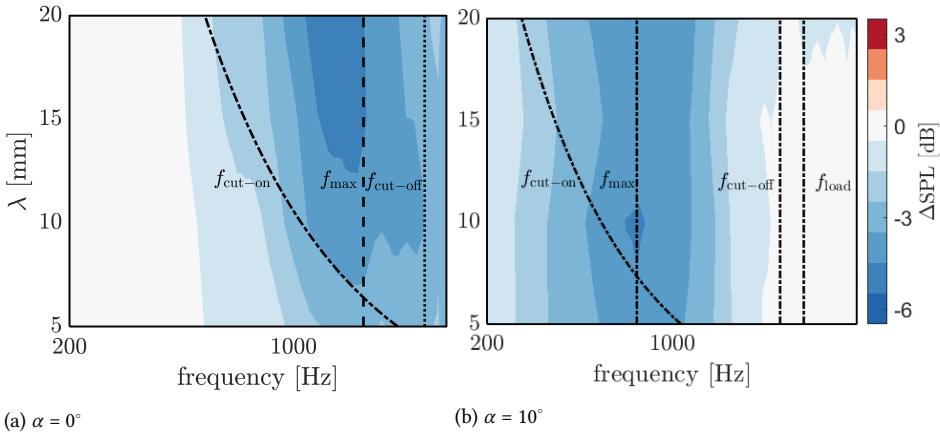


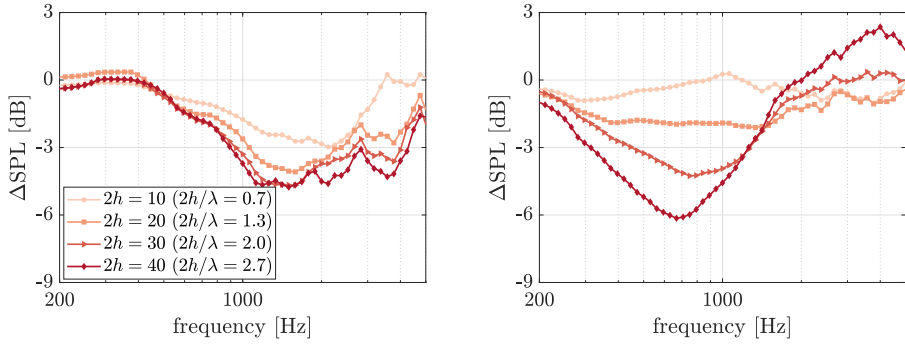
Figure 7.6: Contour plot of the variation of noise reduction for $\alpha = 0^\circ$ (a), and $\alpha = 10^\circ$ (b) at $U_\infty = 30$ m/s with the variation of serration wavelength while the height is kept constant ($2h = 30$ mm). Black lines show the theoretical predictions for the cut-on, max, cut-off, and loading noise frequencies.

2.55, 6.8, and 7.1 respectively. As observed, the Strouhal number of maximum trailing-edge noise ($f\delta^*/U_\infty \approx 0.09$) describes well the region where maximum noise reduction is observed. The cut-on frequency, based on the serration wavelength, can also describe the region where noise reduction is higher than 2 dB (3 dB below maximum noise reduction) for the different wavelengths tested. The cut-off frequency describes the region where noise reduction is decaying below 3 dB. Again, it can be inferred that serrations with small wavelength, such as $\lambda = 5$, and $\lambda = 10$ mm, have a very small frequency range for noise reduction, yielding poorer performance than expected. As discussed in the previous section, in order to satisfy $f_{cut-on} < f_{max}$, the serration wavelength should follow $\frac{\lambda}{\delta^*} > 5$.

The serration height yields a higher sensitivity to the angle of attack, as observed in Figures 7.7(b), and 7.8(b) where noise increasing due to aerodynamic loading is observed for the highest serrations tested. Still, the thicker boundary layer shows the benefits of a larger serration design, achieving higher noise reductions at low frequencies.

7.2.3 SERRATION GEOMETRY

In this section, the effect of the serration geometry is assessed. Convex and concave-shaped serrations are compared against a baseline sawtooth design. In Figure 7.9, the noise reduction spectrum is shown for the different geometries tested. Figure 7.9(a) shows the noise reduction at $\alpha = 0^\circ$. The results demonstrate the beneficial effect of the higher serration root angle, as discussed in Avallone et al. [16]. From the experiments, the concave-shaped serrations have shown a reduction of the

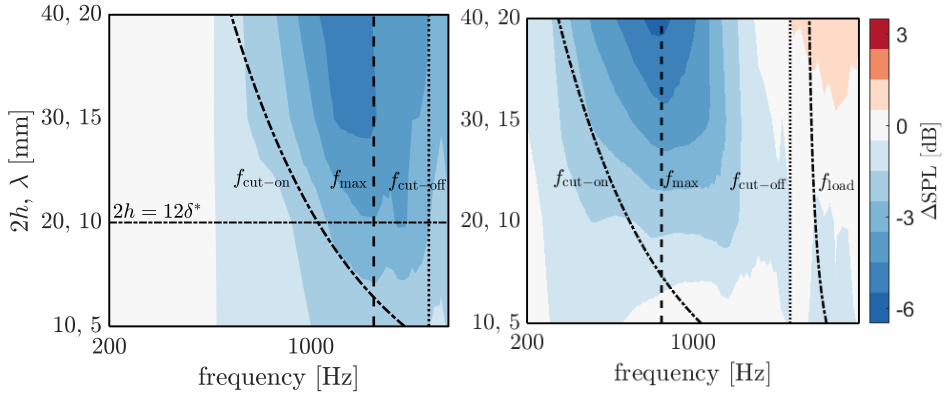


(a) $\alpha = 0^\circ$

(b) $\alpha = 10^\circ$

Figure 7.7: Measured noise reduction (ΔSPL) obtained at $U_\infty = 30$ m/s by varying $2h$ while keeping λ constant. (a) $\alpha = 0^\circ$, and (b) $\alpha = 10^\circ$.

7



(a) $\alpha = 0^\circ$

(b) $\alpha = 10^\circ$

Figure 7.8: Contour plot of the variation of noise reduction for $\alpha = 0^\circ$ (a), and $\alpha = 10^\circ$ (b) at $U_\infty = 30$ m/s with the variation of serration wavelength and height while keeping the aspect ratio constant ($2h/\lambda = 2$). Black lines show the theoretical predictions for the cut-on, max, cut-off, and loading noise frequencies.

noise of about 6 dB, compared to 5 dB from the baseline sawtooth. Avallone et al. [16] attributes the better performance of the concave-shaped serrations to the reduced scattering at the root at low frequencies. Lima Pereira et al. [110] also demonstrates that the low-frequency wall-pressure fluctuations are more intense along the serration root. By creating a higher angle at the root, the concave serrations promote a lower scattering at the region where the wall-pressure fluctuations are more intense, yielding a higher noise reduction. On the other hand, the convex design, which features a lower angle at the root in comparison to the other designs, presents a much poorer noise reduction performance. The concave serrations create a more intense scattering at the tip, where high-frequency fluctuations are more intense. As a result, the noise increases faster at high frequencies for $SF = 0.8$ than for $SF = 0.2$ for frequencies above 3000 Hz. Avallone et al. [16] has also observed that the benefits of concave-shaped serrations are limited to the low-frequency region.

Nevertheless, the advantages of the concave serrations at low angles of attack are balanced at high angles of attack. The larger surface area promotes higher aerodynamic loading when concave serrations are placed at 10° angle of attack. This yields a more intense vortical formation around the edges of the serrations, resulting in a more significant loss of performance at high angles of attack. As a result, the noise reduction obtained at $\alpha = 10^\circ$ (Figure 7.9b) shows similar levels for both the sawtooth and concave-shaped serrations. At this condition, the maximum noise reduction is obtained by the serration with $SF = 0.7$, contrary to the $\alpha = 0^\circ$ condition, where the $SF = 0.8$ presented the highest noise reduction. Besides, at high frequencies, the convex-shaped serration shows the best noise reduction in comparison to the other designs. These results suggest that the optimal serration geometry is different depending on the loading condition and while concave shapes are advantageous for low loading conditions, sawtooth-like and even convex-like shapes are preferable for conditions of high angles of attack.

7.2.4 COMBED SAWTOOTH DESIGN

This section is dedicated to the observed noise reduction obtained when combs are added to the sawtooth serration design. At first, the focus is given to the number of comb teeth and the thickness of these teeth. Figure 7.10 shows the noise reduction spectrum obtained with the different number of teeth (N_{teeth}). From the conditions at a low angle of attack ($\alpha = 0^\circ$), an interesting feature can be observed. None of the combed options (red shades) seems to reduce more noise than the baseline sawtooth (black curve). The results indicate that the introduction of the combs is not beneficial to the serration design. This happens as the tip of the combs are equivalent to a straight trailing edge, and their addition is detrimental to the serration performance, as shown in the analytical work of Azarpeyvand et al. [65]

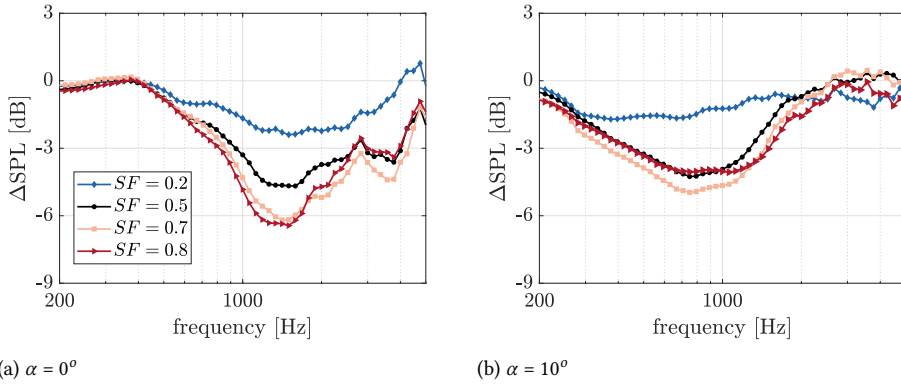


Figure 7.9: Measured noise reduction (ΔSPL) obtained at $U_\infty = 30$ m/s by varying the serration geometry parameterized with the solidity factor SF . (a) $\alpha = 0^\circ$, and (b) $\alpha = 10^\circ$.

for slit-sawtooth serrations. The comb thickness and the number of teeth determine the frequency at which the combed-sawtooth noise reduction departs from the sawtooth one. Thicker combs present a noise reduction curve that deviates from the sawtooth one at lower frequencies. This departure is clear in the figure as $N_{\text{teeth}} = 1$ is less effective than the sawtooth design for $f > 500$ Hz, $N_{\text{teeth}} = 3$ for $f > 1000$ Hz, $N_{\text{teeth}} = 5$ for $f > 1500$ Hz, and $N_{\text{teeth}} = 7$ for $f > 2000$ Hz. This corresponds to a Strouhal number based on the comb thickness ($St = f t_{\text{teeth}}/U_\infty$) around 0.05.

In summary, without the presence of aerodynamic loading, the results indicate that the thinner the combs on the serration are, the more similar the noise reduction is to the regular sawtooth design. The sawtooth serration represents the limit where $t_{\text{comb}} = 0$ mm and it reduces the noise the most in comparison to other combed-sawtooth designs.

These results differ from literature [17] and applied combed-sawtooth serrations on an industrial environment [66], which indicate a significantly better performance of the combed sawtooth concept in comparison with the sawtooth design. A reason for the discrepancies is seen when observing the noise reduction at $\alpha = 10^\circ$. At this condition, the combed-sawtooth designs with $N_{\text{teeth}} \geq 3$ present a higher noise reduction than the sawtooth one. Based on previous studies [17, 109, 110], it is expected that the presence of the combs avoid the formation of the counter-rotating pair of vortices, in turn avoiding the secondary wall-pressure fluctuations observed when sawtooth serrations are placed under aerodynamic loading. Besides, by extending the region of scattering further downstream, the combs also decrease low-frequency noise, with a mechanism similar to the concave serrations, where the scattering happens in the region of lowest wall-pressure fluctuations.

It is important to highlight that the benefits of the combed-sawtooth design are

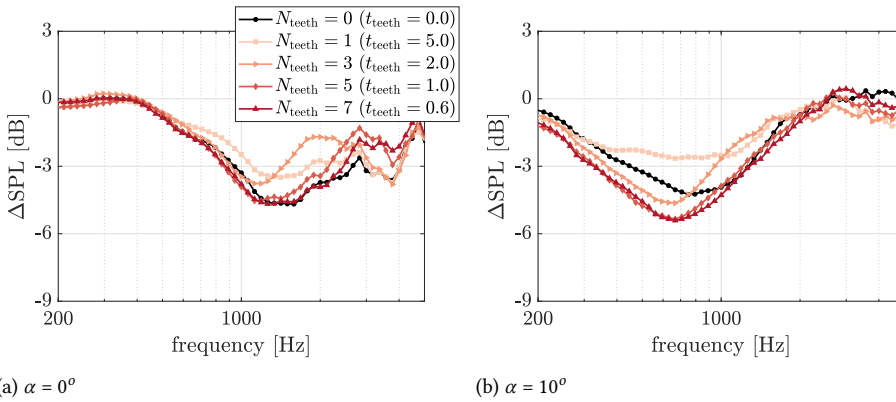


Figure 7.10: Measured noise reduction (ΔSPL) obtained at $U_\infty = 30$ m/s by varying the number of combs (N_{teeth}) in the combed sawtooth design. (a) $\alpha = 0^\circ$, and (b) $\alpha = 10^\circ$.

extended for serrations placed at large angles with respect to the airfoil trailing-edge angle. For example, Avallone et al. [17] demonstrates a better noise reduction from the combed-sawtooth compared to the standard sawtooth serrations mounted on a NACA 0018 airfoil at zero angle of attack. This airfoil shape features a 12° angle between the trailing edge and the airfoil chord line. The work shows that the combs greatly reduce the spanwise deviation of the flow along the serration. In that sense, the combs are a solution to avoid any secondary flow formation along the serration, in turn, creating a design that is more robust to serration installation and aerodynamic loading from changing angles of attack. From the graphs at $\alpha = 10^\circ$, it is possible to observe that the designs with $N_{teeth} = 5$, and $N_{teeth} = 7$ reduce up to 1 dB more noise than the regular sawtooth design.

A second analysis investigates how the solidity factor of the combed serration affects the performance at low and high angles of attack. The serrations tested have 5 teeth per wavelength ($N_{teeth} = 5$) and are differentiated by the thickness of these teeth, respectively $t_{teeth} = 0.6$, 1.0, and 2.0 mm. To achieve these teeth thicknesses, the gap in-between teeth is 2.0, 1.0, and 0.6 mm respectively. The baseline sawtooth serration is also shown as a reference result, which is equivalent to $t_{teeth} = 0$ mm. Figure 7.11 shows the noise reduction spectrum at two angles of attack. By increasing the comb thickness, the scattering is moved to the tip of the serrations, resulting in a higher noise reduction at low frequencies, as observed in Figure 7.11(a) for $\alpha = 0^\circ$. However, following the previous discussions, this benefit is missed at high frequencies, where the thicker combs present a cut-off at lower frequencies.

Still, the main differences are observed for $\alpha = 10^\circ$, where the aerodynamic loading is responsible for decreasing the noise reduction at high frequencies of the

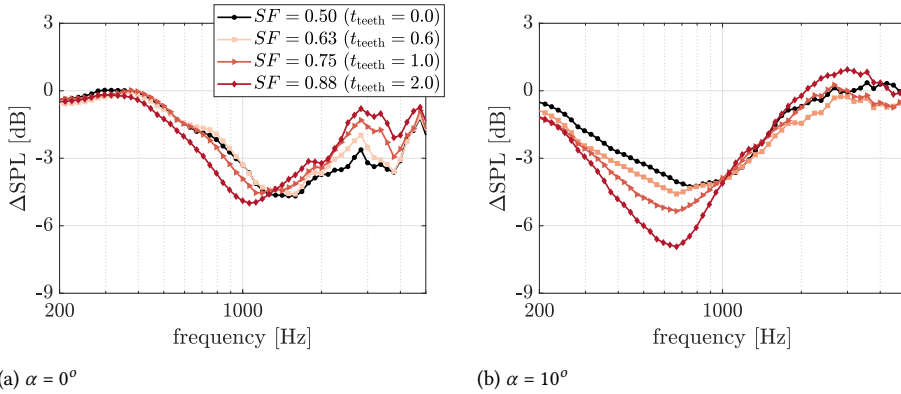


Figure 7.11: Measured noise reduction (ΔSPL) obtained at $U_\infty = 30$ m/s by varying the solidity factor (SF) of the combs in the combed sawtooth design. (a) $\alpha = 0^\circ$, and (b) $\alpha = 10^\circ$.

serrations. Under these conditions, the serration with $t_{teeth} = 1.0$ mm ($SF = 0.75$) presents the best compromise between noise reduction at low frequencies and no increase in noise at high frequencies.

Results suggest that the combs are effective in avoiding the secondary flow features induced by the pressure difference over the serration surface, creating a design that can reduce noise at different conditions of angles of attack, airfoil cambers, and wedge angle between the airfoil and the serration surfaces. However, introducing the combs cause the noise reduction curve to have a lower cut-off frequency, in turn reducing the overall noise reduction from the serration to the sawtooth design. It is expected that the comb size must follow $t_{teeth} < 0.05U_\infty/f_{cut-off}$ to avoid this cut-off to affect the noise reduction. The comb pitch and solidity are another important way of controlling the noise reduction obtained. From the results, the thicker combs ($t_{teeth} = 1.0$ mm, and $t_{teeth} = 2.0$ mm) are the most effective ones at high angles. Nevertheless, the thicker the comb the worse the noise reduction performance is at high frequencies.

7.3 SUMMARY OF PARAMETER DEPENDENCE

This work provides guidelines for the design of trailing-edge serrations. The following paragraphs summarize the results obtained and the impacts expected for each parameter varied in this study:

$2h/\delta^*$: the serration height governs the maximum noise reduction obtained. This is hypothesized in Howe [20]. However, following Gruber et al. [11], a limit is observed for serrations of a certain height. In this work, a maximum noise reduction is reached for serrations of $2h/\delta^* \gtrsim 12$. Results indicate that this value is an optimum for noise reduction, above which no significant improvement is observed. Also, the

height of the serration influences its performance at high angles of attack. Results and theory indicate that the serration height influences the frequency and levels where the aerodynamic loading modifies the noise from the serrations. For high $2h/\delta^*$ serrations, the increase of the noise levels due to aerodynamic loading is stronger, and results from this work have demonstrated up to 3 dB noise increase at 10° angle of attack.

λ/δ^* : the serration wavelength affects mostly the frequency where noise reduction is observed. This is first noted in this work and, according to the theoretical models, the cut-on frequency is inversely proportional to the serration wavelength. Nevertheless, the frequency of cut-off, and of maximum noise reduction are independent of the wavelength. As a consequence, small wavelength serrations reduce noise in a narrower range of frequencies and, at some conditions, cannot reach the maximum noise reduction expected. This is observed in the results where excessively narrow serrations do not reduce noise as wider ones. Considering that the cut-on frequency is desirably below the frequency of maximum generation of broadband noise, the serration wavelength should follow $\frac{\lambda}{\delta^*} \geq 5$. The wavelength does not modify the aerodynamic loading, and results at angle of attack seem to collapse into a similar noise reduction spectrum, indicating that the height of the serration is a more important parameter as long as performance under aerodynamic loading is concerned.

$2h/\lambda$: the serration aspect ratio combines the effect of modifying the wavelength and the height of the serration. Unlike described by Howe [20], increasing the aspect ratio does not necessarily translate into lower noise as alterations of the turbulent flow affect the scattered noise. First, the high-frequency cut-off imposed by the acceleration of the small scales of turbulence limits the noise reduction at certain frequencies. By combining the criteria proposed in the previous two paragraphs, results suggest that an aspect ratio around 2.4 is a valid design as long as both conditions are met concerning the boundary-layer displacement thickness. Besides, the aspect ratio is associated with the sensitivity to the aerodynamic loading. A high aspect ratio serration design is more prone to increasing noise at high frequencies in conditions where the angle between the serrations and the flow direction is high. In this work, meaningful degradation of the high-frequency performance is observed for angles above 10° when considering the sum of the angle of attack (α), the airfoil camber (θ_{TE}), the trailing-edge angle (δ_{TE}), and the serration flap angle with respect to the chord line (δ_{Serr}), i.e. $\alpha + \theta_{TE} + \delta_{TE} + \delta_{Serr} > 10$.

Figure 7.12 summarizes all the modifications of the sawtooth geometry and the impact on the maximum noise reduction (ΔSPL_{min}) achieved. The graph combines the results from every sawtooth serration design, angle of attack, and flow speed assessed. The region of $2h/\delta^* \geq 12$, and $\frac{\lambda}{\delta^*} \geq 5$ is also shown, demonstrating that it contains the designs that achieve maximum noise reduction for this experiment.

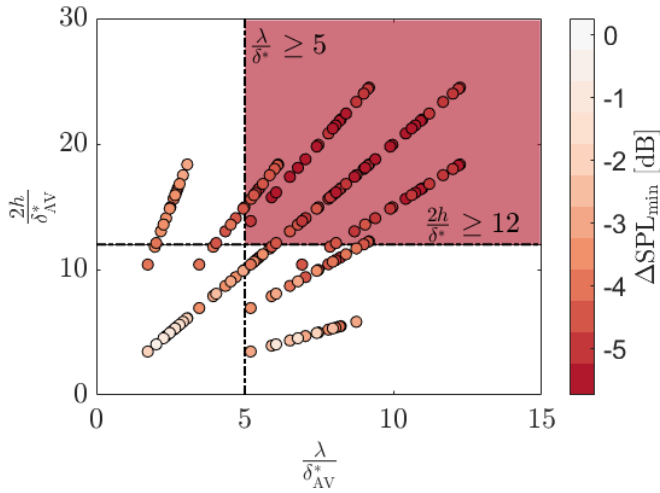


Figure 7.12: Summary scatter plot of maximum noise reduction ΔSPL_{\min} for all sawtooth geometries tested under all angle of attack and flow speed conditions available. The graph also depicts the two criteria for serration design mentioned in this work, i.e. $2h/\delta^* \geq 12$, and $2h/\delta^* \geq 5$

Concave-shaped serrations: the concave-shaped serrations have demonstrated higher noise reduction in comparison to the sawtooth design, as also observed in Avallone et al. [16]. The higher serration angles at the root are responsible for a lower scattering at this region. Studies [16, 17, 110] have shown that the low-frequency wall-pressure fluctuations are more intense at the serration root. It is expected that the less intense scattering at the region of the strongest wall-pressure fluctuations is the underlying phenomenon responsible for the better performance of concave-shaped serrations. On the other hand, the concave-shaped serrations feature a lower angle at the tip. The same studies [16, 17, 110] have also demonstrated that high-frequency wall-pressure fluctuations increase at the tip of the serration. This restricts the advantages of concave-shaped serrations at this frequency range. Besides, the higher associated solidity factor in comparison to the sawtooth serrations is related to a poorer behaviour of the high-frequency noise reduction at angles of attack.

Serration combs: combs are an important feature to reduce secondary flow formations that affect the serration noise. This reduction yield a design that is more robust concerning airfoil camber, angle of attack, and serration wedge angle. It is shown here that, at angles of attack of 10° , the combed serrations reduce as much as 2 dB more noise than the sawtooth design. Nevertheless, the thickness of the comb modifies the high-frequency noise at low angles of attack. It is shown that this thickness is associated with an early cut-off of the noise reduction at

non-dimensional frequencies beyond $ft_{\text{combs}}/U_{\infty} = 0.05$. At higher frequencies, the presence of the combs causes an increase in the noise. This is related to the more intense scattering along the straight edges of the combs. Regarding the thickness of the combs with respect to the gap between them, the results point to an optimal region where the thickness of the combs equals the width of these gaps. Thicker combs yield an increase of noise at high frequencies while smaller ones yield similar behaviour to the sawtooth serrations.

7.4 CONCLUSIONS

This work describes a parametric study of trailing-edge serrations for turbulent boundary layer trailing-edge noise. Several geometries are experimentally tested and results are used to assess the design choices of serration scaling and geometry on the noise reduction obtained. The study is carried out with a one-factor-at-a-time procedure proposed to individually assess the influence of each design parameter on the noise reduction achieved. A series of design modifications are given to a reference sawtooth serration geometry to describe the sensitivity of this design with respect to modifications of the serration height, wavelength, aspect ratio, and of the serration geometry, represented by concave and combed-sawtooth designs. A summary of the main obtained trends is presented, culminating in a guideline on serration design for broadband noise reduction. Two independent physical phenomena are used to carry the discussion about the effects of serration design on noise, namely the acoustic scattering, and the influence on the turbulent flow surrounding the serration. The latter is separated between effects that are observed when serrations are placed at an angle with respect to the flow direction and effects that are present at every condition. The conclusions obtained in this work can be used as a practical guideline for the preliminary design and sizing of serrations for different applications.

8

CONCLUSIONS AND RECOMMENDATIONS

8.1 CONCLUSIONS

The work developed in this thesis explains the physics of broadband noise reduction achieved from serrated trailing edges. The work has first verified the evidence of modifications of the flow on the trailing edge when serrations are added. A detailed investigation of these modifications is carried out in Chapter 5. In this chapter, several measurement techniques are explored to describe the physical mechanisms that influence the alterations of the flow near a serrated trailing edge. The work shows how different behaviours are observed when serrations are under aerodynamic loading or not, and how these affect the scattered noise. These alterations in the flow are investigated in detail in Chapter 6, where a physical description and modelling of the wall-pressure fluctuations over a serrated trailing edge is proposed, describing the conditions for trailing-edge scattering of serrated trailing edges with and without aerodynamic loading. Finally, this interpretation of the physics behind serrated trailing-edge noise is explored in a parametric serration geometry study, where the influence of serration design on the noise reduction obtained is described. The following conclusions can be drawn from the three main scientific questions addressed in this work:

- **Aerodynamic and acoustic properties of serrated trailing edges (Chapter 5):** This work details the wall-pressure fluctuations surrounding serrated trailing edges and its implications on the far-field emissions. The results indicate that, at low aerodynamic loading conditions, two distinct behaviours are observed. At low frequencies, the wall-pressure fluctuations are higher along the root of the serration and reduce at its tip. At high frequencies, the wall-pressure fluctuations are lower along the root of the serration and increase at its tip. Under these conditions, the only observed modification is the increasing of the mean velocity along the wake, which in turn, modifies the convective velocity of the wall-pressure fluctuations. When serrations are placed at an angle with respect to the flow and aerodynamic loading is created, a pair of counter-rotating vortices emerge. This pair of vortices is responsible for diverging the flow outwards on the pressure side of the serration and inwards on the suction side of the serration. It is demonstrated that, as a consequence of the interaction between the incoming turbulence and the mean flow accelerations caused by the vortices, the wall-pressure fluctuations are increased along the outer rim of the serration surface. Acoustic measurements show that the aerodynamic loading is responsible for the degradation of the level of noise reduction achieved. It is demonstrated that analytical predictions using the wall-pressure fluctuations sampled along different locations of the serration surface are better match with the acoustic measurements.

- **Physical description and modelling of the flow over a serrated trailing edge (Chapter 6):** A physical description of the mechanisms that govern the variation of the wall-pressure fluctuations on the serration surface is proposed. This description is broken down into three mechanisms: two observed under every flow condition, and a third one pertaining only to serrations under high aerodynamic loading. The first mechanism is due to the different impedance changes proposed by serrations with respect to a straight trailing-edge. This mechanism causes the wall-pressure fluctuations to naturally reduce from the root to the tip of the serrations. This effect is more pronounced at low frequencies, where the flow coherence is larger. A second physical mechanism observed is the acceleration of the turbulent structures in the inner scales as the wake develops. The acceleration is responsible for shifting the scales that induce wall-pressure fluctuations at the tip of the serration, increasing the high-frequency wall-pressure fluctuations along the tip of the serrations. Finally, a final physical mechanism is described for serrations at angles with respect to the flow. The interaction of the secondary mean flow with the incoming turbulent fluctuations from the boundary layer is responsible for an increase in the pressure fluctuations along the serrations. Semi-empirical models are proposed to describe each of these three mechanisms and comparisons against measurement data and literature studies are used to demonstrate that the mechanisms described represent the underlying physics that governs the wall-pressure fluctuations along serrated trailing edges.
- **Serration geometry and its implication on the emitted noise (Chapter 7):** The design of trailing-edge serrations is explored with respect to the sizing and geometry of the serrations. A parametric study based on a one-parameter-at-a-time approach is proposed in which systematic variations of serration height ($2h$), wavelength (λ), aspect ratio ($2h/\lambda$), and geometry are made, and experimental acoustic results are gathered. The analytical theory of trailing-edge scattering is used along with the proposed physical mechanisms that alter the wall-pressure fluctuations along the serration to create an oriented discussion on the implications of serration design on the noise attenuation achieved. Results demonstrate the effects of the main parameters driving the serration design. It is shown that the wavelength governs the frequency range where noise reduction starts, i.e. wider serrations are designed to reduce noise at lower frequencies while narrow ones reduce noise at higher frequencies. Maximum performance is obtained for wavelengths above 5 times the boundary layer displacement thickness ($\lambda > 5\delta^*$). The height of the serration governs the maximum noise reduction achieved.

Noise reduction is maximal for serration heights above 12 times the boundary layer displacement thickness ($2h > 12\delta^*$). Concerning the serration geometry, concave-shaped serrations are seen to perform better with respect to sawtooth serrations for serrations without aerodynamic loading. When aerodynamic loading exists, the combed-sawtooth geometry yields maximum noise reduction. For the latter, the combs determine the maximum frequency where noise reduction is observed. For such, the comb thickness (t_{teeth}) must follow $t_{\text{teeth}} < 0.05U_{\infty}/f_{\text{cut-off}}$, where $f_{\text{cut-off}}$ is the maximum frequency where noise reduction is desired.

8.2 RECOMMENDATIONS FOR FUTURE WORK

Several lines of work developed during this thesis can have important follow-ups for advancing the the understanding trailing-edge serrations. Below are some suggestions of possible lines of work that can be taken from the discussions of the several chapters of this work.

- Validation of current analytical methods for trailing-edge scattering (Chapter 2):** the recently developed analytical models for serrated trailing edges are yet to demonstrate a consistent prediction against numerical predictions and experiments. This is a difficult test because, first, reliable information on the incoming turbulent flow is required and not always available. Second, the models described in the literature require a mathematical transformation to engineering units, which lack clarity. These two reasons together with the inconsistencies of the assumptions made for predicting serrated trailing edge noise adds to a difficult-to-separate validation and verification of the analytical models. At first, creating numerical and/or experimental verification data is fundamental. This can be achieved by numerical simulations of the diffraction theory, using acoustic solvers, or by experiments using induced wall-pressure fluctuations, in a setup that could be similar to other studies [138]. Besides, generating reliable and well-described acoustic data for the validation of these methods is necessary. Benchmark efforts such as the IEA Task 39 [112] are an important step towards this achievement. Still, data of the incoming wall-pressure fluctuations [109] and numerical simulations for validation are required. This is especially true for a full characterization of the wavenumber-frequency spectrum of the wall-pressure fluctuations.
- The role of coherent structures on the prediction of trailing-edge noise (Chapter 2):** the discussions of the analytical modelling of trailing-edge noise opens the question to the importance of assessing the assumption

of uncorrelation between wavenumbers. For example, coherent structures inside the turbulent boundary layer, such as hairpins or trains of hairpins could have a particular influence on the scattering of serrated trailing edges. Studying the influence of such turbulent structures requires the modelling of the imprint of the wall-pressure fluctuations created by the passing of these structures. Having that determined, the level and phase information of the wavenumber-decomposed wall-pressure fluctuation can be used as input for the analytical formulations, where the importance of considering or not the phase-information can be assessed.

- **Improvement of the scattering models (Chapters 5, and 6):** the semi-analytical models proposed in Chapter 6 can describe the wall-pressure fluctuations on top of the serration surface. In Chapter 5 we have demonstrated that, by inputting the modified wall-pressure fluctuations along the serration surface in the scattering models, yield a more coherent noise prediction. Future work can explore whether the semi-analytical models proposed can produce a more coherent prediction of the scattered noise. By using the predicted wall-pressure fluctuations as input to the scattering predictions, one can observe whether the differences yield improved scattering predictions.

A

VALIDATION OF MEASUREMENT TECHNIQUES AND ACOUSTIC NOISE ESTIMATIONS FROM ISOLATED SERRATIONS STUDY

This appendix provides the analysis of the flow and noise characteristics measured for a straight trailing edge at 0 and 10° flap angle. The boundary-layer properties extracted for this case are used as normalising and scaling terms through the work and the acoustic measurements resulting from this configuration are used for the comparison of the noise against the sawtooth geometry presented in Section 5.2.3.

Domain cropping: first, the required domain cropping is analyzed. The reconstructed data close to the outer domain boundaries (edge of the boundary layer and in- and out-flow surfaces) suffers from increased oscillations caused by the lower particle concentration. The latter typically decays within 5 grid points towards the interior of the computational domain. The data domain used for pressure evaluation is, therefore, a sub-domain with respect to that analysed with VIC+. The criterion for cropping is based on the analysis of the divergence error (mass conservation principle). The components of the velocity divergence in a scatter plot are shown in Figure A.1, where the term with larger uncertainty ($\frac{\partial u_1}{\partial x_1}$) is presented on the horizontal axis. The data dispersion decreases rapidly as one moves from the frontier of the domain towards its interior. Based on the data, the domain volume is cropped by approximately 10% at its borders to avoid the spurious oscillations in the pressure reconstruction scheme, as also suggested in Schneiders and Scarano (2016) [117]. Data in the selected sub-domain falls inside the blue (turbulent boundary

layer) and red (trailing-edge serrations) areas in the graphs, where the error is below 0.002% of the overall mass flow within the measurement region.

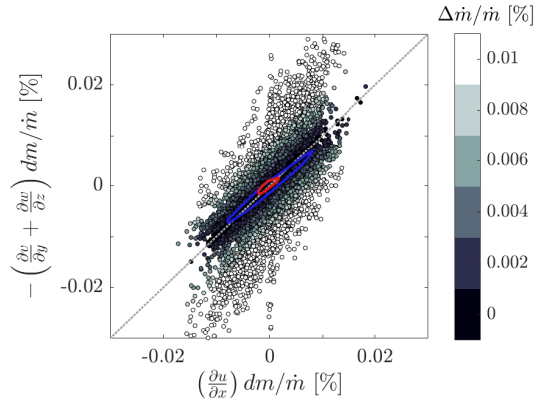


Figure A.1: Mass-flow disparity (distance from the dotted diagonal) obtained from VIC+ for the turbulent boundary layer. Results after domain cropping are represented within the blue (turbulent boundary layer) and red (trailing-edge serrations) areas.

Facility comparison: the mean flow over the trailing edge is presented in Figures A.2a and b. The boundary-layer profiles on both the suction and pressure side is given in Figures A.2c and d. The dashed lines in Figures A.2a and b represent the region of extraction of the boundary-layer quantities. The log and log-wake laws [45] are also included in the graph. Table 4.1 summarizes the relevant boundary-layer quantities measured with the PIV technique. Figures A.2e shows the fluctuating velocity components. Figures A.2c, d, and e also demonstrate measurements with a hot-wire probe performed in the anechoic wind tunnel (A-tunnel) for comparisons against the PIV measurements. Discrepancies between the two measurements are below 0.8 m/s for the mean flow and 0.1 m/s for the root mean square velocity fluctuations, indicating that the characteristics of the incoming boundary layer is similar on both wind tunnels. The pressure gradients are estimated from the variation of the edge velocity along the streamwise direction. Differently from airfoil measurements, where the angle of attack drastically changes the scales between pressure and suction side, at the flat plate the different pressure gradient conditions still yield similar boundary-layer heights. This contributes to the inspection of the different pressure gradient conditions over the loaded serrations as both pressure and suction sides have similar scales and, consequently, produce noise in a similar frequency range.

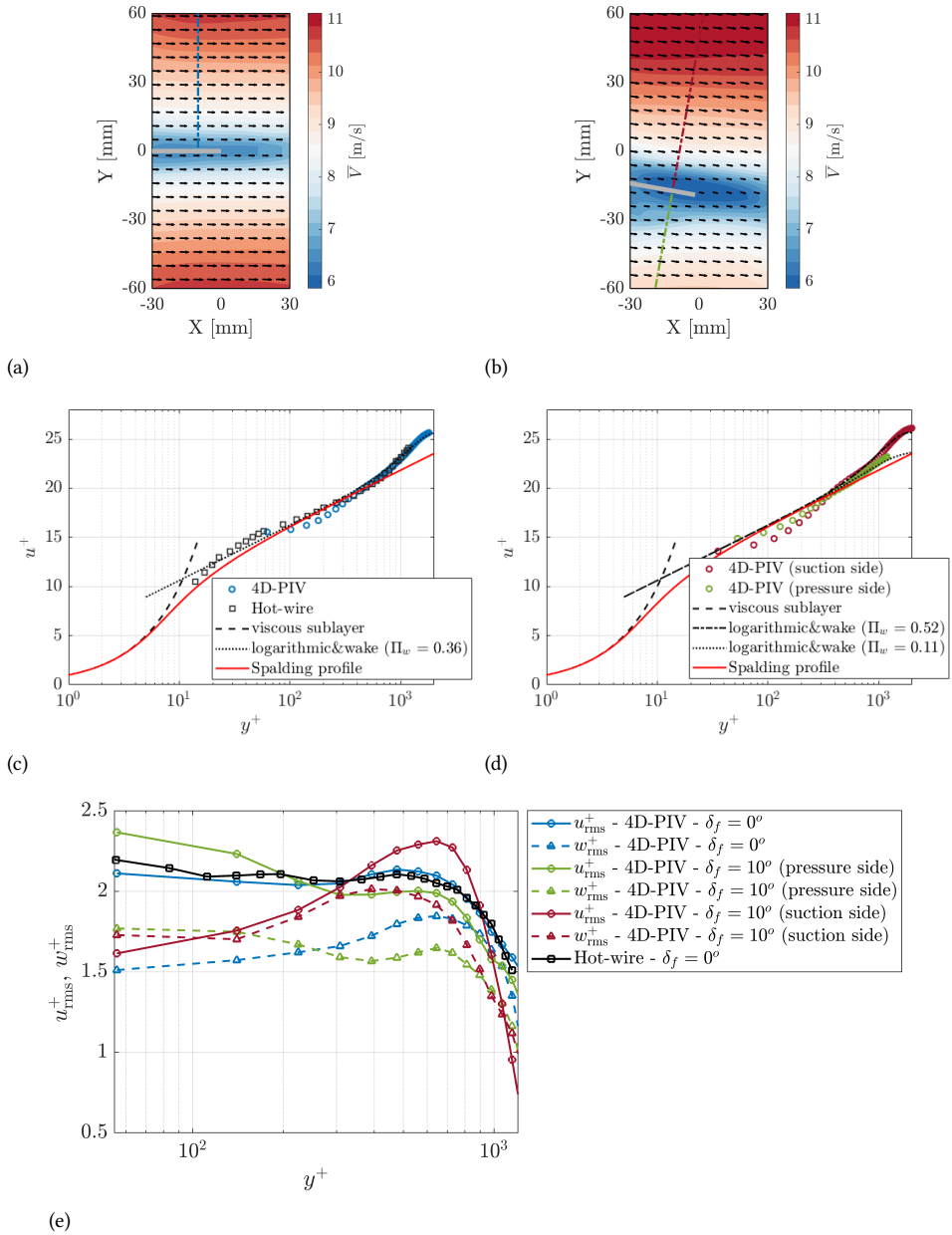


Figure A.2: Mean flow over the trailing edge and boundary-layer mean velocity profile measured at the trailing edge at $\delta_f = 0^\circ$ (a and c respectively) and $\delta_f = 10^\circ$ (b and d respectively) and root mean square (RMS) of the stream and spanwise velocity fluctuations (e). The dashed lines in (a) and (b) represent the region of extraction of the boundary-layer velocity profiles.

Wall-pressure and noise comparisons: first, the wall-pressure spectrum measured with the surface-mounted microphones and the PIV technique is compared against the analytical models from Panton and Linebarger [54]; Goody [48]; Kamruzzaman [50] in Figure A.3. The Kamruzzaman model presented the best agreement with the current set of experimental data among the APG semi-empirical models. For the sake of conciseness, this is the only APG model presented here. The PIV measurements agree with the surface microphones with some underprediction observed at very low frequencies. Nevertheless, the model of Kamruzzaman overpredicts the outer and inner scales for the other conditions, especially for the FPG case. The Goody model overpredicts the frequency where the inner scale starts, what could be caused by the low Δ_* of the boundary layer formed in the flat plate.

The integral model from Panton can rather precisely predict the universal and starting of the inner scales. The model correctly identifies the pressure fluctuations for the ZPG and APG cases, with some over-prediction noted for the FPG one.

Figures A.3e and f show the variation of the spectrum in relation to the ZPG condition. Deviations from the methods are overall large. The increase in the wall-pressure spectrum on the suction side is highly under-predicted and even the results from the Panton model show a deviation in the order of 3 dB with respect to the measurements. Similarly, the pressure side is only mildly considered, and some pressure increase in the mid-frequencies, predicted by both Kamruzzaman and Panton models, is not captured during the experiments.

In order to further analyse the spatial distribution of the wall-pressure structures, it is necessary to estimate the convective speed of such structures. Figure A.4 shows the convection velocity estimated from the microphone and PIV measurements at the trailing-edge sensors. This velocity is within the expected value of 60% of the free stream velocity [44] for the ZPG case. FPG conditions, given the higher associated velocity close to the wall, present an increased convection velocity (68% of the edge velocity, 6.6 m/s). On the suction side, the APG flow experiences a significant decrease in the same parameter (52% of the edge velocity, 5.8 m/s) induced by the smaller velocity gradient along the wall-normal direction at the wall. The table on the right-hand side of the graph compares the values obtained from the microphones and PIV measurements. The slightly higher value of the convection velocity estimated from the PIV measurements may be ascribed to the restrictions of the PIV technique, which limits the estimation within large structures that advect faster.

An estimation of the stream- and span-wise correlation length is presented in Figure A.5 with the microphone measurements. The fitting of the measured coherence between the sensors is plotted against the hypothesised exponential curve in Figure A.5a and b. The results demonstrate the quality of the fitting used for the estimation of the length of the coherent structures. Errors exist at the lowest

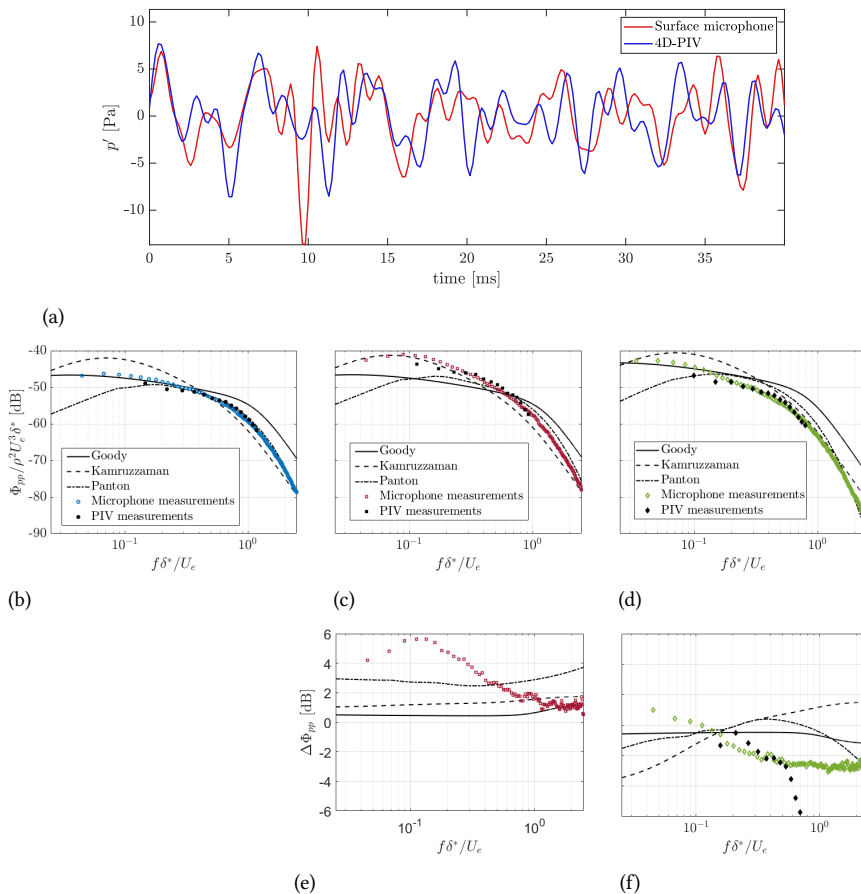
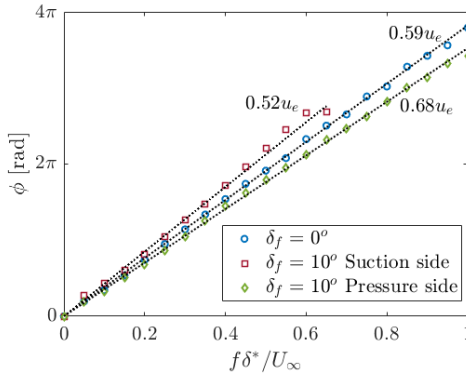


Figure A.3: Comparison between the wall-pressure fluctuations measured by the microphone sensors compared against PIV data and analytical models. The time history of the wall-pressure measured at the boundary layer region is shown in (a). Measurements are given at $\delta_f = 0^\circ$ (b) and $\delta_f = 10^\circ$ (suction and pressure side, c, and d respectively). Measured and estimated changes in the pressure spectrum with respect to the $\delta_f = 0^\circ$ case are presented in (e) and (f).

frequencies, where the coherence levels are higher and the shape of the coherence distribution in space exits the exponential curve [139]. The resulting fitting of Corcos's equation with values by Hu and Herr [51] is also shown in the figure ($\alpha_{x_1} = 0.15$, and $\alpha_{x_3} = 0.71$). According to the reference, the correlation length is seen to be well described as a function of the frequency and the convection velocity only. Predicting the convection velocity at such conditions is keen in obtaining a precise spatial description of the flow fluctuations near the trailing edge. Discrepancies with the model of Hu and Herr [51] are higher for the streamwise correlation



	Microphone	PIV
$\delta_f = 0^\circ$	6.0 m/s	6.1 m/s
$\delta_f = 10^\circ$ (suction)	5.8 m/s	6.0 m/s
$\delta_f = 10^\circ$ (pressure)	6.6 m/s	6.7 m/s

(b)

(a)

Figure A.4: Pressure fluctuations convection velocity estimated from the different angles of the straight trailing edge using the microphone and PIV measurements. In the graph, the markers represent the measured values and the dotted lines show the fitted expression used for the estimation of the convection velocity.

length, where a better fit is obtained with a constant value $\alpha_{x_1} = 0.17$ instead of 0.15.

Predictions of the trailing-edge noise using the model as described in Section 2.4 in the centre of the array location are presented in Figure A.6. The figure shows the measured wall pressure levels ($\Pi_{pp} = \phi_{pp} l_{x_3}$) combined from both sides of the model. The higher fluctuations on the suction side, even when combined with the lower convection speed, still make the suction side the dominant noise source for $\delta_f = 10^\circ$ in low frequencies. At high frequencies, the $\delta_f = 0^\circ$ and the $\delta_f = 10^\circ$ have similar Π_{pp} and are expected to produce similar noise levels. Figure A.6b and c compare the measured far-field noise from the beamforming measurements against the predicted values. Differences in speed are corrected with a scaling of M^5 . Results demonstrate the agreement between the experiment and scattering predictions. Overall, the noise is underestimated by the analytical method for the $\delta_f = 0^\circ$ case, resulting in higher differences between the 0° and the 10° case. Higher errors are observed for low and high frequencies. This is caused by the acoustic measurement technique applied, which is limited at low frequencies due to the large beamwidth of the background sources and at high frequencies due to the contamination of the noise sources by spurious side lobes. Another explanation for the high-frequency bump observed in both cases is the possibility of a remaining shedding from the wake. This would agree with the Strouhal number based on the trailing-edge thickness ($St_t = 0.1$) despite the small thickness of the trailing edge in comparison to the boundary layer one ($t/\delta^* = 0.11$), following the criteria

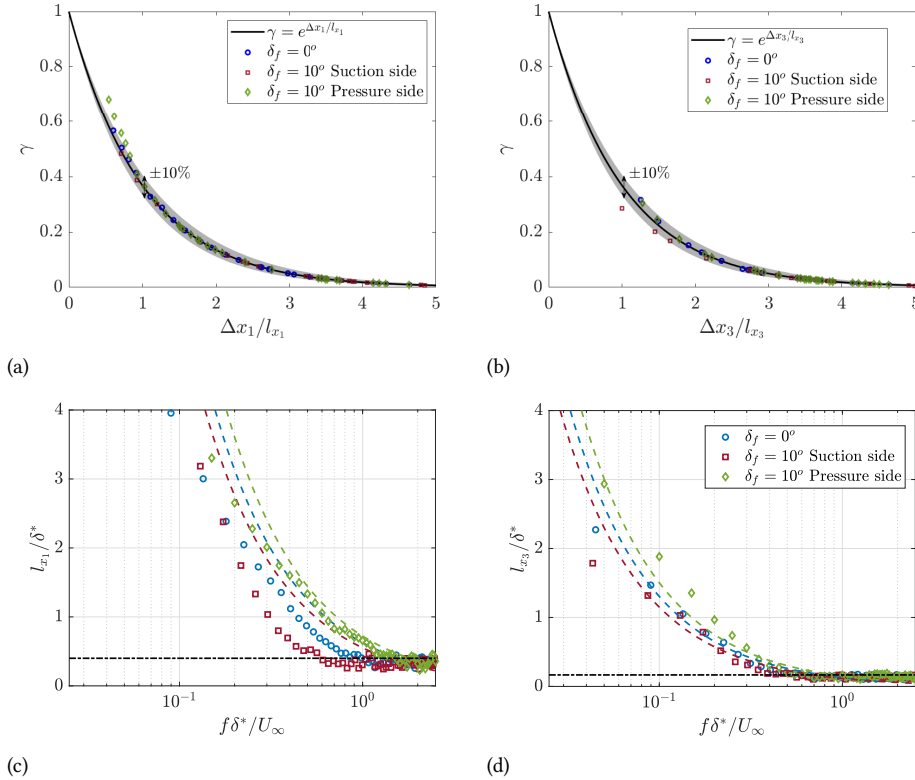


Figure A.5: Measured coherence levels between microphones compared against the proposed exponential coherence curve assumed for the estimation of the streamwise (a) and spanwise (b) correlation lengths. The computed streamwise and spanwise correlation lengths at $\delta_f = 0^\circ$ and $\delta_f = 10^\circ$ are shown in (c) and (d). The markers represent the measured values while the colored dashed curves show the fitting constants present in the work of Hu and Herr [51]. The black dot-dashed lines represent the limit of the measurement technique considering coherence levels below 0.05 for two adjacent microphone sensors.

established in Blake [140].

The experiments with the straight trailing edge indicate that prediction of the trailing-edge scattering noise from measurements of the wall-pressure spectrum is reliable and can well identify the trends observed for different incoming boundary layers. The results support the comparisons made against the noise reduction of the serrated trailing edges, suggesting that major deviations with the analytical comparisons are ascribed to the modelling of the serrated trailing edges and not to the description of the incoming flow conditions and reference straight trailing-edge noise.

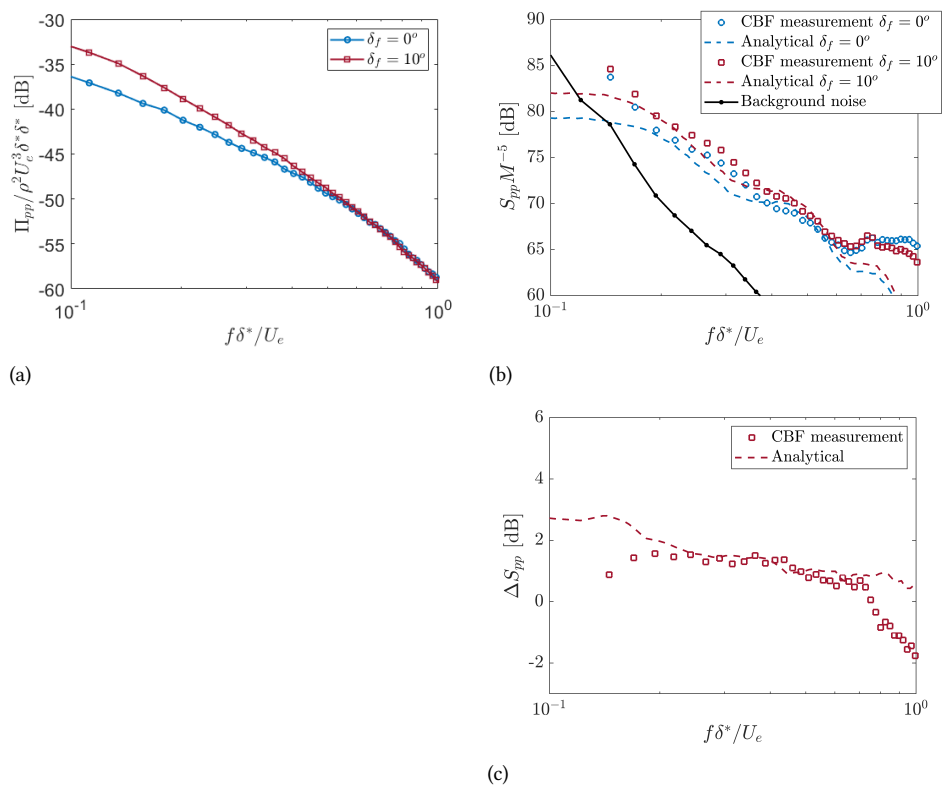


Figure A.6: Wall-pressure spectrum measured by the first pressure sensor of the trailing edge (M09) compared against PIV data and analytical models. Measurements are given at $\delta_f = 0^\circ$ (a) and $\delta_f = 10^\circ$ (suction and pressure side, b, and c respectively). Measured and estimated changes in the pressure spectrum with respect to the $\delta_f = 0^\circ$ case are presented in (e) and (f).

B

RELATION BETWEEN WALL-PRESSURE FLUCTUATIONS AT THE WALL-BOUNDED REGION AND ALONG THE WALL PLANE ON THE NEAR WAKE

This appendix describes mathematically the relation between the pressure fluctuations along the wall plane in the presence (referred as "wall" in the remainder of the equations) and absence (referred as "free" in the remainder of the equations) of a wall. The effect in the pressure fluctuations at $x_2 = 0$ can be seen from the analytical solution of the pressure Poisson represented in equation B.1.

$$\frac{1}{\rho_0} \nabla^2 p = q = -2 \frac{\partial U_i}{\partial x_j} \frac{\partial u_j}{\partial x_i} - \frac{\partial}{\partial x_i \partial x_j} (u_i u_j - \overline{u_i u_j}). \quad (\text{B.1})$$

The equation can be solved with the appropriate boundary conditions using the definition of the Green's function as shown in Lilley [43]. Equation B.2 illustrates the equivalent pressure estimations for the two different conditions illustrated in this work, where $q(\mathbf{y})$ represents the source term in the Poisson equation.

$$\begin{cases} p_{\text{free}}(t, \mathbf{x}, x_2 = 0) = -\frac{1}{4\pi} \int_{-\infty}^{\infty} \int_{-\infty}^{\infty} \int_{-\infty}^{\infty} \frac{1}{|\mathbf{x}-\mathbf{y}|} q(\mathbf{y}, t) d\mathbf{y} \\ p_{\text{wall,upper}}(t, \mathbf{x}, x_2 = 0) = -\frac{1}{2\pi} \int_0^{\infty} \int_{-\infty}^{\infty} \int_{-\infty}^{\infty} \frac{1}{|\mathbf{x}-\mathbf{y}|} q(\mathbf{y}, t) d\mathbf{y} \end{cases} \quad (\text{B.2})$$

The variance of the pressure fluctuations can be used here to represent the effect that the presence of the wall has on the wall-pressure spectrum levels. Since

the integrals along x_1 and x_3 are the same, these two integrals are replaced by $Q(x_2)$ for brevity.

$$\begin{cases} \langle p, p \rangle_{\text{free}}(x_2 = 0) = \frac{1}{16\pi^2} \int_0^\infty \left(\int_{-\infty}^\infty Q(\mathbf{y}, t) dy_2 \right)^2 dt \\ \langle p, p \rangle_{\text{wall,upper}}(x_2 = 0) = \frac{1}{4\pi^2} \int_0^\infty \left(\int_0^\infty Q(\mathbf{y}, t) dy_2 \right)^2 dt \end{cases} \quad (\text{B.3})$$

The estimation of the free field can be modified by separating the integral between the upper ($x_2 \geq 0$) and lower ($x_2 \leq 0$) flow regions and further considering that both sides are uncorrelated. The latter hypothesis should be valid in the vicinity of the trailing edge, where the flow from both sides has not mixed.

$$\begin{cases} \langle p, p \rangle_{\text{free}}(x_2 = 0) = \frac{1}{16\pi^2} \left[\int_0^\infty \left(\int_0^{-\infty} Q(\mathbf{y}, t) dy_2 \right)^2 dt + \int_0^\infty \left(\int_0^\infty Q(\mathbf{y}, t) dy_2 \right)^2 dt \right] \\ \langle p, p \rangle_{\text{wall,upper}}(x_2 = 0) = \frac{1}{4\pi^2} \int_0^\infty \left(\int_0^\infty Q(\mathbf{y}, t) dy_2 \right)^2 dt \end{cases} \quad (\text{B.4})$$

Finally, recognizing that the two terms in the free field estimation correspond to the wall-pressure estimations coming from the upper and lower side of the flow, a relation for the pressure fluctuations at the wall plane at a wall-bounded and free condition can be created (Equation B.5).

$$\langle p, p \rangle_{\text{free}} = \frac{1}{4} \langle p, p \rangle_{\text{wall,upper}} + \frac{1}{4} \langle p, p \rangle_{\text{wall,lower}} \quad (\text{B.5})$$

C

WALL-PRESSURE FLUCTUATIONS INDUCED BY TURBULENT FLOW OVER A SPAN-STREAMWISE OSCILLATING FLOW FIELD

This appendix describes the derivation of the wall-pressure fluctuations created by a wall-bounded turbulent flow excited by the mean flow in particular wavenumbers in span and streamwise directions.

The mean flow excitation is in the form of a Taylor-Green's function following equation 6.9, where $\bar{k}_1 = \pi/2h$, and $\bar{k}_3 = 2\pi/\lambda$. The mean flow is used to derive a source term for the pressure Poisson equation (equation B.1), resulting in equation C.1.

$$q(\mathbf{x}, \bar{\mathbf{k}}) = -2 \frac{\partial U_i}{\partial x_j} \frac{\partial u_j}{\partial x_i} = - \left[\frac{\partial u_1}{\partial x_1} + \frac{\lambda}{4h} \frac{\partial u_1}{\partial x_3} - \frac{4h}{\lambda} \frac{\partial u_3}{\partial x_1} - \frac{\partial u_3}{\partial x_3} \right] \bar{k}_1 A_0 e^{-i\bar{k}_1 x_1} e^{-i\bar{k}_3 x_3} \dots$$

$$- \left[\frac{\partial u_1}{\partial x_1} + \frac{\lambda}{4h} \frac{\partial u_1}{\partial x_3} + \frac{4h}{\lambda} \frac{\partial u_3}{\partial x_1} + \frac{\partial u_3}{\partial x_3} \right] \bar{k}_1 A_0 e^{-i\bar{k}_1 x_1} e^{-i\bar{k}_3 x_3} \quad (\text{C.1})$$

This source function can be extended using the wavenumber decomposition for the velocity fluctuations:

$$\begin{aligned}
 q(\mathbf{x}, \mathbf{k}, \bar{\mathbf{k}}) = & \left(k_1 + \frac{\lambda}{4h} k_3 \right) \left[u_1(x_2, \mathbf{k}) - \frac{4h}{\lambda} u_3(x_2, \mathbf{k}) \right] \bar{k}_1 A_o i e^{-i\bar{k}_1 x_1} e^{i\bar{k}_3 x_3} e^{-ik_1 x_1} e^{-ik_3 x_3} \dots \\
 & + \left(k_1 + \frac{\lambda}{4h} k_3 \right) \left[u_1(x_2, \mathbf{k}) + \frac{4h}{\lambda} u_3(x_2, \mathbf{k}) \right] \bar{k}_1 A_o i e^{-i\bar{k}_1 x_1} e^{-i\bar{k}_3 x_3} e^{-ik_1 x_1} e^{-ik_3 x_3},
 \end{aligned}
 \tag{C.2}$$

where $\mathbf{k} = (k_1, k_3)$, and $\bar{\mathbf{k}} = (\bar{k}_1, \bar{k}_3)$. Following the approach of Willmarth and Roos [39], the Fourier transform along x_1 and x_3 is taken. Since the function is a bilinear combination of two wavenumbers $(\mathbf{k}, \bar{\mathbf{k}})$, a change of variables is necessary, according to the following identity of the Fourier transform:

$$F.G(k_i) = F(k_i - \bar{k}) . G(\bar{k}), \tag{C.3}$$

resulting in the source term for equation C.2:

$$\begin{aligned}
 q(\mathbf{k}, \bar{\mathbf{k}}) = & A_o i \left(k_1 + \frac{\lambda}{4h} k_3 \right) \bar{k}_1 \left[u_1(x_2, \mathbf{k}') - \frac{4h}{\lambda} u_3(x_2, \mathbf{k}') \right] + \dots \\
 & A_o i \left(k_1 + \frac{\lambda}{4h} k_3 - 2\bar{k}_1 \right) \bar{k}_1 \left[u_1(x_2, \mathbf{k}'') + \frac{4h}{\lambda} u_3(x_2, \mathbf{k}'') \right].
 \end{aligned}
 \tag{C.4}$$

where $\mathbf{k}' = (k_1 - \bar{k}_1, k_3 + \bar{k}_3)$, $\mathbf{k}'' = (k_1 - \bar{k}_1, k_3 - \bar{k}_3)$.

The source function can be used to derive a solution for the pressure at the wall. Similarly to Appendix B, this is accomplished by the appropriate selection of the Green's function, represented in equation C.5 for the decomposed wavenumbers in the stream and the spanwise direction. In the equation $k = \sqrt{k_1^2 + k_3^2}$. Therefore, the pressure at the wall ($x_2 = 0$) can be estimated according to equation C.6.

$$G(x_2, X_2, \mathbf{k}) = -\frac{e^{-k|x_2 - X_2|}}{2k} - \frac{e^{-k|x_2 + X_2|}}{2k}, \tag{C.5}$$

$$\begin{aligned}
 p(x_2 = 0, \mathbf{k}, \bar{\mathbf{k}}) = & i\rho_o A_o \int_0^\infty \left\{ \frac{[k_1 + (\lambda/4h) k_3] \bar{k}_1}{k} \left[u_1(\mathbf{k}') - \frac{4h}{\lambda} u_3(\mathbf{k}') \right] + \dots \right. \\
 & \left. \frac{[k_1 + (\lambda/4h) k_3 - 2\bar{k}_1] \bar{k}_1}{k} \left[u_1(\mathbf{k}'') + \frac{4h}{\lambda} u_3(\mathbf{k}'') \right] \right\} e^{-kX_2} dX_2.
 \end{aligned}
 \tag{C.6}$$

The wall-pressure wavenumber spectrum is obtained by the averaging of the multiplication of p by its complex conjugate. The formulation for the spectrum

(ϕ_{pp}) is shown in equation C.7. The equation has two important considerations for simplification. The first considers the contribution from the cross-spectrum of different velocity components negligible with respect to the cross-spectra of the same velocity components [141]. From this assumption, the cross-correlation terms of different velocity components are neglected. The second hypothesis is of homogeneous turbulence, which results in $\phi_{u_1, u_1} = \phi_{u_3, u_3} = \phi_{u, u}$. The work of Lilley [43] discusses that the latter hypothesis suffices for order of magnitude analysis, although the decay of the energy of the smaller structures is underpredicted with respect to experiments. The resulting equation (C.7) depends only on the description of the velocity cross-spectrum along the wall-normal direction.

$$\begin{aligned} \phi_{pp}(\mathbf{k}, \bar{k}) &= \rho_o^2 A_o^2 \frac{[k_1 + (\lambda/4h)k_3]^2 (\bar{k}_1^2 + \bar{k}_3^2)}{k^2} \int_0^\infty \int_0^\infty \phi'_{u,u} e^{-k(X_2 + X'_2)} dX_2 dX'_2 + \dots \\ &\rho_o^2 A_o^2 \frac{[k_1 + (\lambda/4h)k_3 - 2\bar{k}_1]^2 (\bar{k}_1^2 + \bar{k}_3^2)}{k^2} \int_0^\infty \int_0^\infty \phi''_{u,u} e^{-k(X_2 + X'_2)} dX_2 dX'_2. \end{aligned} \quad (C.7)$$

In this study, the most simplistic model of the velocity cross-spectrum, the Gaussian spectrum described in Batchelor [142], is selected. Several other models exist for the evaluation of this quantity [143–145]. Those were ruled out as the modelling aims at a first description of the underlying parameters that govern the wall-pressure fluctuations of serrations under loading. At a later stage, the model can benefit from a more precise description of the mean and fluctuating velocity field along the serrations. Considering more complex vortex models, e.g. the Lamb-Oseen or the Batchelor ones, or a precise description of the decay of energy of the fluctuations and anisotropy are possible ways of improving the predictions. The cross-spectrum considered assumes the form of equation C.8 where L is the characteristic length scale of the flow.

$$\phi_{uu}(\mathbf{k}, x_2, x'_2) = \frac{L^4}{16\pi} \sqrt{u_i^2(x_2) u_i^2(x'_2)} k^2 e^{-\frac{L^2 k^2}{4} - \frac{(x_2 - x'_2)^2}{L^2}} \quad (C.8)$$

The equation is further simplified by considering constant velocity fluctuations in the wall-normal direction, following the work of Kraichnan [40]. Finally, using equation C.8 in the integrals of equation C.7 and solving it, one can obtain a closed-form of the wall-pressure fluctuations due to stream and spanwise accelerations induced by the mean flow (equation C.9).

$$\phi_{pp}(\mathbf{k}, \bar{\mathbf{k}}) = \frac{\rho_o^2 A_o^2 L^5 \overline{uu}}{32 \sqrt{\pi}} (\bar{k}_1^2 + \bar{k}_3^2) \left\{ [k_1 + (\lambda/4h)k_3]^2 k'^2 e^{-\frac{L^2 k'^2}{4}} + \dots \right. \\ \left. [k_1 + (\lambda/4h)k_3 - 2\bar{k}_1]^2 k''^2 e^{-\frac{L^2 k''^2}{4}} \right\} \frac{e^{\frac{L^2 k^2}{4}}}{k^3} \operatorname{erfc}\left(\frac{kL}{2}\right), \quad (\text{C.9})$$

where $k' = \sqrt{(k_1 - \bar{k}_1)^2 + (k_3 + \bar{k}_3)^2}$, and $k'' = \sqrt{(k_1 - \bar{k}_1)^2 + (k_3 - \bar{k}_3)^2}$.

The pressure spectrum can be obtained by considering $k_1 = \omega/U_c$ and integrating over all spanwise wavenumbers, following equation C.10.

$$\phi_{pp}(\omega, \bar{\mathbf{k}}) = \frac{1}{U_c} \int_{-\infty}^{\infty} \phi_{pp}(\mathbf{k}, \bar{\mathbf{k}}) dk_3 \quad (\text{C.10})$$

According to the software of symbolic mathematical handling *Mathematica*, the former equation does not seem to produce a closed analytical solution. Nevertheless, a numerical integration procedure can be used to derive a final and simplified equation that describes fairly well the solution in mid and high frequencies (equation 6.10). The parameters of the equation are converted into simple flow parameters according to the following assumptions:

$$L \propto \delta^* \quad (\text{C.11})$$

$$\overline{uu} \propto U_c^2 \quad (\text{C.12})$$

$$A_o \propto U_c \frac{h}{\lambda} \alpha_s \quad (\text{C.13})$$

Assumptions C.11, and C.12 follow the works of Chase [61] and Blake [42] while assumption C.13 considers the circulation on the serration proportional to the serration area times the angle with respect to the zero-lift condition (potential lift generation). Vortex lift [146] can also have a contribution to the serration lift given the small aspect ratio and the presence of the vortex pairs around the edges of the serration. The latter was ruled out due to the small angles and since the vortex pairs are not formed in the surface of the serration but rather around its corner (see Avallone et al. [15]). Nevertheless, the contribution of the vortex lift could change the linear dependency of α_s in assumption C.13 to α_s^2 at small angles. Further investigations could provide a better insight into the lift generation mechanism of trailing-edge serrations.

D

VERIFICATION OF ANALYTICAL MODELS WITH OTHER DATASETS

This appendix is dedicated to comparisons between the models obtained and available results from the literature.

References [16, 17] are used for the verification of the models describing the effects that modify the wall-pressure fluctuations at low angles of attack, namely the impedance change at the trailing-edge region (Section 6.2.1), and the wake acceleration effect (Section 6.2.2). Given that the references do not provide the variation of the convection velocity over the airfoil, the latter correction was created using the convection velocity equations of this work (equations 6.13, and 6.14).

Figures D.1 and D.2 compares the distribution of the variance of the pressure fluctuations over the serration surface predicted with the simulated one shown in Avallone et al. (2017) [16] (figure 9 from the publication), and Avallone et al. (2018) [17] (figure 17 from the publication) respectively. To create the variance of the fluctuations, the model is integrated over the entire frequency range shown in the references. This process leads to the dominance of the low frequency (high energy) content on the quantity displayed. Thus, the effect of the impedance change dominates the variance of the pressure fluctuations.

Overall, results compare well between the numerical and the semi-empirical models. Discrepancies are not higher than one colour scale and are mostly an overestimation of the levels of the pressure fluctuations by the models. Still, the models are able to describe the tendencies observed among different serration geometries. Both the iron-shaped and the combed-sawtooth serration feature a higher surface area than the sawtooth serration. As a consequence, the reduction of the wall-pressure fluctuations in the different geometries is more concentrated at the serration tip and the difference between the wall-pressure fluctuations around

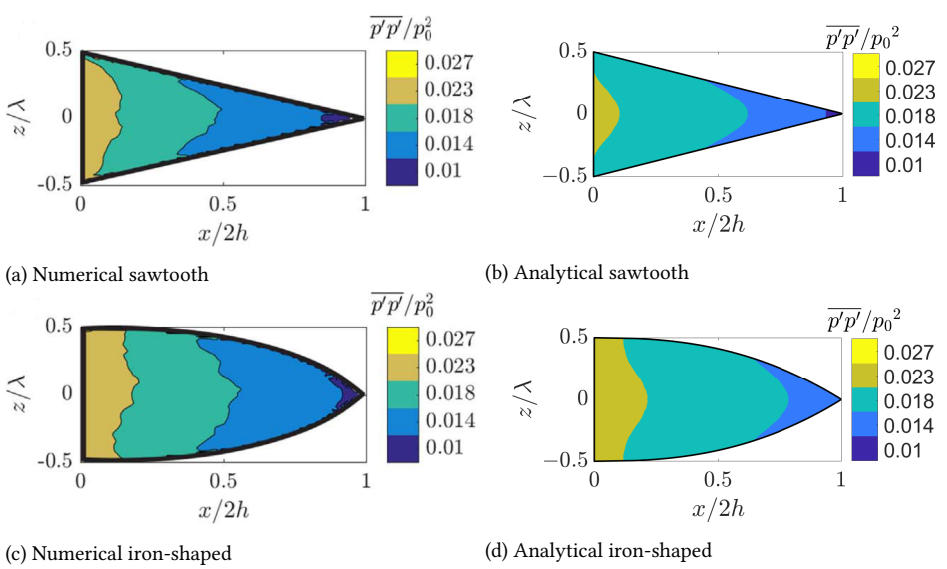


Figure D.1: Simulated distribution of the pressure fluctuations over the serration surface from the work of Avallone et al. (2017) [16] (a and c) compared against the predicted one (b and d). Figures a and b show the sawtooth serration geometry and c and d the iron-shaped serration geometry. Figures a and c are reprinted under the license number 5153050767352.

the centre and the edge of the serration is not as pronounced as the one observed for the sawtooth serrations.

The wall-pressure spectrum measured at the serration root, centre, and tip of the reference sawtooth serration case from the works of Avallone et al. (2017) [16], and Avallone et al. (2018) [17] are shown in figure D.3. In comparison, the predicted wall-pressure spectrum using the root spectrum as reference is shown in dotted-dashed lines. From the graph, it is possible to observe that the semi-empirical models produce an accurate prediction of the varying wall-pressure spectrum on the serration surface. At low frequencies, the impedance change causes a reduction of the wall-pressure fluctuations along the serration tip, well captured by the model. At high frequencies, the increasing convection velocity leads to an increase of the wall-pressure fluctuations at the serration tip, which is also correctly described by the wake acceleration model. Discrepancies seem to be well within 1 dB, as also observed in this work for the experimental dataset. The results are only shown for the sawtooth serration since the wake acceleration model would predict the same modifications for all the geometries tested. This is still in accordance with the results presented in Avallone et al. (2017) [16], and Avallone et al. (2018) [17], where the geometric modifications do not yield significant change of the wall-pressure spectrum at the same locations.

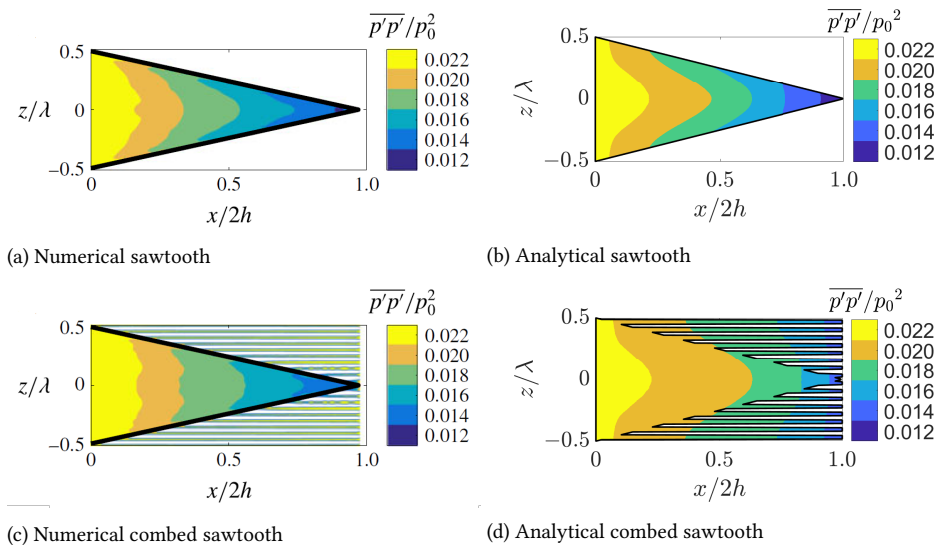


Figure D.2: Simulated distribution of the pressure fluctuations over the serration surface from the work of Avallone et al. (2018) [17] (a and c) compared against the predicted one (b and d). Figures a and b show the sawtooth serration geometry and c and d the combed sawtooth serration geometry. Figures a and c are reprinted under the license number 5153051246667.

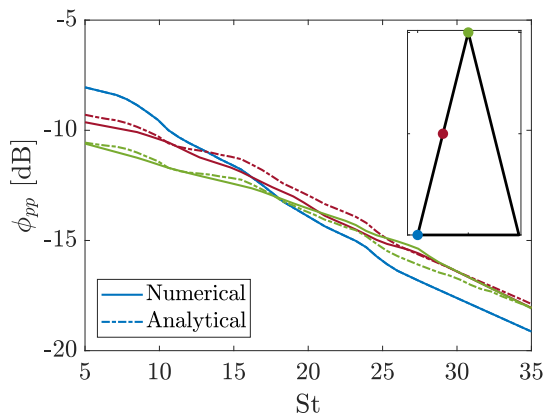


Figure D.3: Comparison between the wall-pressure fluctuations over the sawtooth serration surface presented in the works of Avallone et al. (2017) [16] and Avallone et al. (2018) [17] (solid lines) and the predicted one using the analytical equations described in Section 6.2.1, and 6.2.2 (dashed-dotted lines). The spectrum at the root is taken as a reference for predicting the variations along the serration edge.

In summary, this appendix has demonstrated the ability of two of the proposed analytical models to predict the variation of the wall-pressure fluctuations over the surface of a serrated trailing edge. The impedance change model is seen to correctly describe the low-frequency phenomenon observed on the wall-pressure spectrum and on the variance of the pressure fluctuations over the serration surface. This model can also be applied with other serration geometries and results show a similar trend between the predicted and the simulated distribution of the wall-pressure fluctuations. The wake acceleration effect dominates the observed variations of the wall-pressure spectrum at high frequencies. Predictions of this effect using the variation of the convection velocity estimated for the experimental dataset presented in this work yield good comparisons with the numerical data from the references. It is therefore shown that the effects described in this work are the same that modify the wall-pressure fluctuations over the serration surface of the references used. Moreover, the semi-empirical models proposed and associated empirical quantities (C_i , and C_3) estimated from this work can also be used for different datasets.

BIBLIOGRAPHY

REFERENCES

- [1] BP. Statistical review of world energy. *71st edition*, 2022.
- [2] Siegfried Wagner, Rainer Bareiss, and Gianfranco Guidati. *Wind Turbine Noise*. 1996.
- [3] Stefan Oerlemans and Peter Fuglsang. Low-noise wind turbine design. pages 1–23, 2012.
- [4] Associação Brasileira de Normas Técnicas. NBR-10151. *NBR 10.151 Acústica - Avaliação do ruído em áreas habitadas, visando o conforto da comunidade - Procedimentos*, page 4 pg, 2000.
- [5] Stefan Oerlemans. *Detection of aeroacoustic sound sources on aircraft and wind turbines*. 2009.
- [6] Steven Buck, Stefan Oerlemans, and Scott Palo. Experimental characterization of turbulent inflow noise on a full-scale wind turbine. *Journal of Sound and Vibration*, 385(September 2016):219–238, 2016.
- [7] Daniel Acevedo-Girald, Laura Botero-Bolívar, Lourenço T.L. Pereira, Fernando M. Catalano, Danillo C. Reis, and Eduardo L.C. Coelho. Experimental aeroacoustic and aerodynamic analysis of a large-scale flap side-edge model. *2018 AIAA/CEAS Aeroacoustics Conference*, 2018.
- [8] Stefan Oerlemans, Murray Fisher, Thierry Maeder, and Klaus Kögler. Reduction of Wind Turbine Noise Using Optimized Airfoils and Trailing-Edge Serrations. *AIAA Journal*, 47(6):1470–1481, 2009.
- [9] Siemens Gamesa Renewable Energy S.A. DinoTails Next Generation World-leading noise reduction technology. *71st edition*, 2023.
- [10] M.S. Howe. Aerodynamic noise of a serrated trailing edge. *Journal of Fluids and Structures*, 5(1):33–45, jan 1991.
- [11] Mathieu Gruber, Phillip Joseph, and Tze Chong. On the mechanisms of serrated airfoil trailing edge noise reduction. *17th AIAA/CEAS Aeroacoustics Conference (32nd AIAA Aeroacoustics Conference)*, (June):5–8, 2011.

- [12] Tze Pei Chong and Alexandros Vathylakis. On the aeroacoustic and flow structures developed on a flat plate with a serrated sawtooth trailing edge. *Journal of Sound and Vibration*, 354:65–90, 2015.
- [13] Carlos Arce León, Roberto Merino-Martínez, Daniele Ragni, Francesco Avallone, and Mirjam Snellen. Boundary layer characterization and acoustic measurements of flow-aligned trailing edge serrations. *Experiments in Fluids*, 57(12):1–22, 2016.
- [14] L. E. Jones and R. D. Sandberg. Acoustic and hydrodynamic analysis of the flow around an aerofoil with trailing-edge serrations. *Journal of Fluid Mechanics*, 706:295–322, 2012.
- [15] F. Avallone, S. Pröbsting, and D. Ragni. Three-dimensional flow field over a trailing-edge serration and implications on broadband noise. *Physics of Fluids*, 28(11), 2016.
- [16] F. Avallone, W. C.P. van der Velden, and D. Ragni. Benefits of curved serrations on broadband trailing-edge noise reduction. *Journal of Sound and Vibration*, 400(April):167–177, 2017.
- [17] F. Avallone, W. C.P. van der Velden, D. Ragni, and D. Casalino. Noise reduction mechanisms of sawtooth and combed-sawtooth trailing-edge serrations. *Journal of Fluid Mechanics*, 848(June):560–591, 2018.
- [18] D. Ragni, F. Avallone, W. C. P. van der Velden, and D. Casalino. Measurements of near-wall pressure fluctuations for trailing-edge serrations and slits. *Experiments in Fluids*, 60(1):6, 2019.
- [19] Carlos Arce León, Roberto Merino-Martínez, Daniele Ragni, Francesco Avallone, Fulvio Scarano, Stefan Pröbsting, Mirjam Snellen, Dick G. Simons, and Jesper Madsen. Effect of trailing edge serration-flow misalignment on airfoil noise emissions. *Journal of Sound and Vibration*, 405:19–33, 2017.
- [20] M. S. Howe. Noise produced by a sawtooth trailing edge. *The Journal of the Acoustical Society of America*, 90(1):482–487, 1991.
- [21] Lorna J. Ayton. Analytic solution for aerodynamic noise generated by plates with spanwise-varying trailing edges. *Journal of Fluid Mechanics*, 849(August):448–466, 2018.
- [22] Benshuai Lyu and Lorna J. Ayton. Rapid noise prediction models for serrated leading and trailing edges. *Journal of Sound and Vibration*, 469:115136, 2020.

- [23] J. E. Ffowcs-Williams and L. H. Hall. Aerodynamic sound generation by turbulent flow in the vicinity of a scattering half plane. *Journal of Fluid Mechanics*, 40(4):657–670, 1970.
- [24] N Curle and Proc R Soc Lond A. The influence of solid boundaries upon aerodynamic sound. *Proceedings of the Royal Society of London. Series A. Mathematical and Physical Sciences*, 231(1187):505–514, 1955.
- [25] S. Oerlemans, P. Sijtsma, and B. Méndez López. Location and quantification of noise sources on a wind turbine. *Journal of Sound and Vibration*, 299(4-5):869–883, 2007.
- [26] Roy K. Amiet. High frequency thin-airfoil theory for subsonic flow. *AIAA Journal*, 14(8):1076–1082, 1976.
- [27] R. K. Amiet. Noise due to turbulent flow past a trailing edge. *Journal of Sound and Vibration*, 47(3):387–393, 1976.
- [28] Michel Roger and Stéphane Moreau. Back-scattering correction and further extensions of Amiet’s trailing-edge noise model. Part 1: Theory. *Journal of Sound and Vibration*, 286(3):477–506, 2005.
- [29] Gabriele Grasso, Michel Roger, and Stéphane Moreau. Effect of sweep angle and of wall-pressure statistics on the free-field directivity of airfoil trailing-edge noise. *25th AIAA/CEAS Aeroacoustics Conference, 2019*, (May):1–16, 2019.
- [30] Thomas F. Brooks, Michael A. Marcolini, and Dennis S. Pope. Airfoil Trailing Edge Flow Measurements and Comparisons With Theory, Incorporating Open Wind Tunnel Corrections. *AIAA Paper*, 1984.
- [31] M. A. Brooks, T. F. and Pope, D. S. and Marcolini. Airfoil self-noise and prediction. (August 1989), 1989.
- [32] Hermann Schlichting and Klaus Gersten. *Boundary-Layer Theory*, volume 20. Springer Berlin Heidelberg, Berlin, Heidelberg, 2017.
- [33] Michael J. Kingan and John R. Pearse. Laminar boundary layer instability noise produced by an aerofoil. *Journal of Sound and Vibration*, 322(4-5):808–828, 2009.
- [34] Marlene Sanjose, Prateek Jaiswal, Stéphane Moreau, Aaron Towne, Sanjiva K. Lele, and Adrien Mann. Laminar boundary layer instability noise. pages 243–252, 2017.

- [35] Gyuzel Yakhina, Michel Roger, Stéphane Moreau, Lap Nguyen, and Vladimir Golubev. Experimental and Analytical Investigation of the Tonal Trailing-Edge Noise Radiated by Low Reynolds Number Aerofoils. *Acoustics*, 2(2):293–329, 2020.
- [36] Tze Pei Chong and Phillip F. Joseph. An experimental study of airfoil instability tonal noise with trailing edge serrations. *Journal of Sound and Vibration*, 332(24):6335–6358, 2013.
- [37] William K. Blake. *Hydrodynamically Induced Cavitation and Bubble Noise*, volume 1. 2017.
- [38] Danielle J. Moreau and Con J. Doolan. Noise-Reduction Mechanism of a Flat-Plate Serrated Trailing Edge. *AIAA Journal*, 51(10):2513–2522, 2013.
- [39] W. W. Willmarth and F. W. Roos. Resolution and structure of the wall pressure field beneath a turbulent boundary layer. *Journal of Fluid Mechanics*, 22(1):81–94, 1965.
- [40] Robert H. Kraichnan. Pressure Fluctuations in Turbulent Flow over a Flat Plate. *Journal of the Acoustical Society of America*, 28(3):378–390, 1956.
- [41] Prateek Jaiswal, Stéphane Moreau, Francesco Avallone, Daniele Ragni, and Stefan Pröbsting. On the use of two-point velocity correlation in wall-pressure models for turbulent flow past a trailing edge under adverse pressure gradient. *Physics of Fluids*, 32(10):105105, oct 2020.
- [42] William K. Blake. *Essentials of Turbulent Wall Pressure Fluctuations*, volume 2. 2017.
- [43] G M Lilley and T H Hodgson. On surface pressure fluctuations in turbulent boundary layers. *Advisory Group For Aeronautical Research and Development Paris (France)*, Report 276, 1960.
- [44] G. M. Corcos. Resolution of Pressure in Turbulence. *The Journal of the Acoustical Society of America*, 35(2):192–199, 1963.
- [45] Donald Coles. The law of the wake in the turbulent boundary layer. *Journal of Fluid Mechanics*, 1(2):191–226, 1956.
- [46] Y. F. Hwang, William K. Bonness, and Stephen A. Hambric. Comparison of semi-empirical models for turbulent boundary layer wall pressure spectra. *Journal of Sound and Vibration*, 319(1-2):199–217, 2009.

- [47] Seongkyu Lee and Augusto Villaescusa. Comparison and assessment of recent empirical models for turbulent boundary layer wall pressure spectrum. *23rd AIAA/CEAS Aeroacoustics Conference, 2017*, (June):1–23, 2017.
- [48] Michael Goody. Empirical Spectral Model of Surface Pressure Fluctuations. *AIAA Journal*, 42(9):1788–1794, 2008.
- [49] Yannick Rozenberg, Michel Roger, and Stéphane Moreau. Rotating blade trailing-edge noise: Experimental validation of analytical model. *AIAA Journal*, 48(5):951–962, 2010.
- [50] M. Kamruzzaman, D. Bekiropoulos, Th. Lutz, W. Würz, and E. Krämer. A Semi-Empirical Surface Pressure Spectrum Model for Airfoil Trailing-Edge Noise Prediction. *International Journal of Aeroacoustics*, 14(5-6):833–882, 2015.
- [51] Nan Hu and Michaela Herr. Characteristics of wall pressure fluctuations for a flat plate turbulent boundary layer with pressure gradients. *22nd AIAA/CEAS Aeroacoustics Conference, 2016*, pages 1–18, 2016.
- [52] Seongkyu Lee and Jessica G. Shum. Prediction of airfoil trailing-edge noise using empirical wall-pressure spectrum models. *AIAA Journal*, 57(3):888–897, 2019.
- [53] Yakut Cansev Küçükosman, Julien Christophe, and Christophe Schram. Trailing edge noise prediction based on wall pressure spectrum models for NACA0012 airfoil. *Journal of Wind Engineering and Industrial Aerodynamics*, 175(November 2017):305–IBC, 2018.
- [54] Ronald L. Panton and John H. Linebarger. Wall pressure spectra calculations for equilibrium boundary layers. *Journal of Fluid Mechanics*, 65(2):261–287, 1974.
- [55] S. Remmler, J. Christophe, J. Anthoine, and S. Moreau. Computation of wall-pressure spectra from steady flow data for noise prediction. *AIAA Journal*, 48(9):1997–2007, 2010.
- [56] G. P. Romano. Analysis of two-point velocity measurements in near-wall flows. *Experiments in Fluids*, 20(2):68–83, 1995.
- [57] M. R. Catlett, Jason M. Anderson, Jonathan B. Forest, and Devin O. Stewart. Empirical modeling of pressure spectra in adverse pressure gradient turbulent boundary layers. *AIAA Journal*, 54(2):569–587, 2016.

- [58] A. V. Smol'yakov. A new model for the cross spectrum and wavenumber-frequency spectrum of turbulent pressure fluctuations in a boundary layer. *Acoustical Physics*, 52(3):331–337, 2006.
- [59] Dan Palumbo. Determining correlation and coherence lengths in turbulent boundary layer flight data. *Journal of Sound and Vibration*, 331(16):3721–3737, 2012.
- [60] Alejandro Rubio Carpio, Roberto Merino Martínez, Francesco Avallone, Daniele Ragni, Mirjam Snellen, and Sybrand van der Zwaag. Experimental characterization of the turbulent boundary layer over a porous trailing edge for noise abatement. *Journal of Sound and Vibration*, 443:537–558, 2019.
- [61] D. M. Chase. Modeling the wavevector-frequency spectrum of turbulent boundary layer wall pressure. *Journal of Sound and Vibration*, 70(1):29–67, 1980.
- [62] B. Lyu, M. Azarpeyvand, and S. Sinayoko. Prediction of noise from serrated trailing edges. *Journal of Fluid Mechanics*, 793:556–588, 2016.
- [63] Pavel Kholodov and Stéphane Moreau. Optimization of serrations for broadband trailing-edge noise reduction using an analytical model. (May):1–14, 2019.
- [64] Pavel Kholodov and Stéphane Moreau. Optimization of trailing-edge serrations with and without slits for broadband noise reduction. *Journal of Sound and Vibration*, 490:115736, 2020.
- [65] Mahdi Azarpeyvand, Mathieu Gruber, and Phillip Joseph. An analytical investigation of trailing edge noise reduction using novel serrations. *19th AIAA/CEAS Aeroacoustics Conference*, pages 1–17, 2013.
- [66] Michael J. Asheim, Oriol Ferret Gasch, and Stefan Oerlemans. Rotor blade with a serrated trailing edge, 2017.
- [67] Carlos Arce León, Daniele Ragni, Stefan Pröbsting, Fulvio Scarano, and Jesper Madsen. Flow topology and acoustic emissions of trailing edge serrations at incidence. *Experiments in Fluids*, 57(5), 2016.
- [68] G. I. Taylor. The Spectrum of Turbulence. *Proceedings of the Royal Society of London. Series A - Mathematical and Physical Sciences*, 164(919):476–490, feb 1938.
- [69] Steven L. Garrett. *Understanding Acoustics*, volume 49 of *Graduate Texts in Physics*. Springer International Publishing, Cham, 2020.

- [70] G.R.A.S. Sound and Vibration Website.
- [71] Paul T. Soderman and Stephen C. Noble. Directional microphone array for acoustic studies of wind tunnel models. *Journal of Aircraft*, 12(3):168–173, 1975.
- [72] Pieter Sijtsma. Phased Array Beamforming Applied to Wind Tunnel and Fly-Over Tests. *SAE Technical Papers*, 2010-Octob(October):17–19, 2010.
- [73] Ennes Sarradj. Three-dimensional acoustic source mapping with different beamforming steering vector formulations. *Advances in Acoustics and Vibration*, 2012, 2012.
- [74] Anwar Malgoezar, Mirjam Snellen, Pieter Sijtsma, and Dick Simons. Improving Beamforming By Optimization of Acoustic Array Microphone Positions. *BeBeC*, (January 2017):1–24, 2016.
- [75] William D. Fonseca, Joao P. Ristow, Diogo G. Sanches, and Samir N. Y. Gerges. A Different Approach to Archimedean Spiral Equation in the Development of a High Frequency Array. oct 2010.
- [76] Elias Arcondoulis and Yu Liu. An iterative microphone removal method for acoustic beamforming array design. *Journal of Sound and Vibration*, 442:552–571, 2019.
- [77] S. Luesutthiviboon, A. Malgoezar, M. Snellen, P. Sijtsma, and D. Simons. Improving source discrimination performance by using an optimized acoustic array and adaptive high-resolution CLEAN-SC beamforming. *7th Berlin Beamforming Conference*, pages 1–26, 2018.
- [78] Ennes Sarradj, Gert Herold, Pieter Sijtsma, Roberto Merino Martinez, Anwar Malgoezar, Mirjam Snellen, Thomas F. Geyer, Christopher J. Bahr, Ric Porteous, Danielle J. Moreau, and Con J. Doolan. A microphone array method benchmarking exercise using synthesized input data. *23rd AIAA/CEAS Aeroacoustics Conference, 2017*, (June), 2017.
- [79] R P Dougherty. Functional Beamforming. *5th Berlin Beamforming Conference, February 19-20 2014, Berlin, Germany.*, 2014.
- [80] Lourenço T.L. Pereira, Laura Botero-Bolívar, Matheus T. De Araujo, Fernando M. Catalano, Danillo C. Reis, and Eduardo L.C. Coelho. Experimental and numerical analysis of the aerodynamic and aeroacoustic properties of a 2D high-lift wing model. *2018 AIAA/CEAS Aeroacoustics Conference*, 2018.

- [81] Alan Barlow, Jewel B and Rae Jr, William H and Pope. *Low speed wind tunnel testing*. John wiley & sons, 2015.
- [82] H. C. Garner, E. W. E. Rogers, W. E. A. Acum, and E. C. Maskell. Subsonic Wind Tunnel Wall Corrections. *AGARD Report*, 1996.
- [83] Christopher S. Allen, William K. Blake, Robert P. Dougherty, Denis Lynch, Paul T. Soderman, and James R. Underbrink. *Aeroacoustic Measurements*. Springer Berlin Heidelberg, Berlin, Heidelberg, 2002.
- [84] Odenir de Almeida, Fernando M. Catalano, and Lourenco Tercio Pereira. Improvements of a Hard-Wall Closed Test-Section of a Subsonic Wind Tunnel for Aeroacoustic Testing. *The International Journal of Acoustics and Vibration*, 26(3):248–258, sep 2021.
- [85] Marcel C. Remillieux, Erin D. Crede, Hugo E. Camargo, Ricardo A. Burdisso, William J. Devenport, Matthew Rasnick, Philip Van Seeters, and Amanda Chou. Calibration and demonstration of the new Virginia Tech anechoic wind tunnel. *14th AIAA/CEAS Aeroacoustics Conference (29th AIAA Aeroacoustics Conference)*, (May):5–7, 2008.
- [86] William Devenport, Christian Bak, Kenneth Brown, Aurelien Borgoltz, Jens Osterlund, Peter Davidsson, and S T O. Design and Operation of Hybrid Aeroacoustic Wind Tunnels. *Design and Operation of Aeroacoustic Wind Tunnel Tests for Group and Air Transport*, STO-EN-AVT(January 2019), 2017.
- [87] Martinus P.J. Sanders, Leandro D. de Santana, and Cornelis H. Venner. The sweep angle effect on slat noise characteristics of the 30p30n high-lift model in an open-jet wind tunnel. *Aiaa Aviation 2020 Forum*, 2020.
- [88] Michael Pott-Pollenske and Jan Delfs. Enhanced capabilities of the Aeroacoustic Wind Tunnel Braunschweig. *14th AIAA/CEAS Aeroacoustics Conference (29th AIAA Aeroacoustics Conference)*, (May):5–7, 2008.
- [89] Gerhard Wickern and Norbert Lindener. The audi aeroacoustic wind tunnel: Final design and first operational experience. *SAE Technical Papers*, (724), 2000.
- [90] Roberto Merino-Martínez, Alejandro Rubio Carpio, Lourenço Tércio Lima Pereira, Steve van Herk, Francesco Avallone, Daniele Ragni, and Marios Kotsonis. Aeroacoustic design and characterization of the 3D-printed, open-jet, anechoic wind tunnel of Delft University of Technology. *Applied Acoustics*, 170, 2020.

- [91] Mitsuhiro Murayama, Yuzuru Yokokawa, Hiroki Ura, Kazuyuki Nakakita, Kazuomi Yamamoto, Yasushi Ito, Takehisa Takaishi, Ryotaro Sakai, Keiji Shimoda, Takayuki Kato, and Tomoyuki Homma. Experimental study of slat noise from 30P30N three-element high-lift airfoil in JAXA kevlar-wall low-speed wind tunnel. *2018 AIAA/CEAS Aeroacoustics Conference*, pages 6–13, 2018.
- [92] Michel Roger. Microphone Measurements in Aeroacoustic Installations. (May):1–50, 2018.
- [93] Mohammadreza Kadivar, David Tormey, and Gerard McGranaghan. A review on turbulent flow over rough surfaces: Fundamentals and theories. *International Journal of Thermofluids*, 10:100077, 2021.
- [94] B. Martinez Rocamora Jr., Luciano C. Caldas, Rafael G. Cuenca, Rudner Q. Lauterjung, and Paulo C. Greco. Design of an instrumented stator vane for unsteady pressure measurements using MEMS microphones. *31st Congress of the International Council of the Aeronautical Sciences, ICAS 2018*, 2018.
- [95] Martinus P.J. Sanders, Leandro D. De Santana, Mahdi Azarpeyvand, and Cornelis H. Venner. Unsteady surface pressure measurements on trailing edge serrations based on digital MEMS microphones. *2018 AIAA/CEAS Aeroacoustics Conference*, pages 1–12, 2018.
- [96] Markus Raffel, Christian E. Willert, Fulvio Scarano, Christian J. Kähler, Steve T. Wereley, and Jürgen Kompenhans. *Particle Image Velocimetry*. 2018.
- [97] David Engler Faleiros, Marthijn Tuinstra, Andrea Sciacchitano, and Fulvio Scarano. Helium-filled soap bubbles tracing fidelity in wall-bounded turbulence. *Experiments in Fluids*, 59(3):1–13, 2018.
- [98] Christian Willert. Stereoscopic digital particle image velocimetry for application in wind tunnel flows. *Measurement Science and Technology*, 8(12):1465, dec 1997.
- [99] G. E. Elsinga, F. Scarano, B. Wieneke, and B. W. Van Oudheusden. Tomographic particle image velocimetry. *Experiments in Fluids*, 41(6):933–947, 2006.
- [100] Daniel Schanz, Sebastian Gesemann, and Andreas Schröder. Shake-The-Box: Lagrangian particle tracking at high particle image densities. *Experiments in Fluids*, 57(5):1–27, 2016.

- [101] F. Scarano. Tomographic PIV: Principles and practice. *Measurement Science and Technology*, 24(1), 2013.
- [102] Bernhard Wieneke. Iterative reconstruction of volumetric particle distribution. *Measurement Science and Technology*, 24(2), 2013.
- [103] J. Schneiders, R. P. Dwight, and F. Scarano. Tomographic PIV noise reduction by simulating repeated measurements. *11th International Symposium on Particle Image Velocimetry - PIV15*, (14-16 Sempther), 2015.
- [104] Andrea Sciacchitano, Benjamin Leclaire, and Andreas Schroeder. Main results of the first Data Assimilation Challenge. *14th International Symposium on Particle Image Velocimetry*, 1(1):2–14, 2021.
- [105] Daniele Violato, Peter Moore, and Fulvio Scarano. Lagrangian and Eulerian pressure field evaluation of rod-airfoil flow from time-resolved tomographic PIV. *Experiments in Fluids*, 50(4):1057–1070, 2011.
- [106] Sebastian Gesemann, Florian Huhn, Daniel Schanz, and Andreas Schröder. From Particle Tracks to Velocity and Acceleration Fields Using B-Splines and Penalties. i, 2015.
- [107] N. J. Neeteson, S. Bhattacharya, D. E. Rival, D. Michaelis, D. Schanz, and A. Schröder. Pressure-field extraction from Lagrangian flow measurements: first experiences with 4D-PTV data. *Experiments in Fluids*, 57(6):1–18, 2016.
- [108] Lourenco T. Lima Pereira, Daniele Ragni, Francesco Avallone, and Fulvio Scarano. Pressure fluctuations from large-scale PIV over a serrated trailing edge. *Experiments in Fluids*, 61(3):1–17, 2020.
- [109] Lourenco Tercio Lima Pereira, Francesco Avallone, and Daniele Ragni. Wall-pressure fluctuations over a serrated trailing edge at different angles of attack. In *AIAA/CEAS Aeroacoustics Conference*, pages 1–15, 2021.
- [110] Lourenço Tércio Lima Pereira, Francesco Avallone, Daniele Ragni, and Fulvio Scarano. A physics-based description and modelling of the wall-pressure fluctuations on a serrated trailing edge. *Journal of Fluid Mechanics*, 938:A28, may 2022.
- [111] Lourenco Tercio Lima Pereira, Daniele Ragni, Francesco Avallone, and Fulvio Scarano. Aeroacoustics of sawtooth trailing-edge serrations under aerodynamic loading. *Journal of Sound and Vibration*, 537(April):117202, oct 2022.

- [112] Salil Luesutthiviboon, Lourenço Tércio Lima Pereira, Daniele Ragni, Francesco Avallone, and Mirjam Snellen. {Aeroacoustic Benchmarking of Trailing-edge Noise from a NACA 63\$_3\$-018 Airfoil with Trailing-edge Serrations}. *AIAA Journal*, 2022.
- [113] Eduardo Rodríguez-López, Paul J.K. Bruce, and Oliver R.H. Buxton. On the Formation Mechanisms of Artificially Generated High Reynolds Number Turbulent Boundary Layers. *Boundary-Layer Meteorology*, 160(2):201–224, 2016.
- [114] Francis H. Clauser. The Turbulent Boundary Layer. *Advances in Applied Mechanics*, 4(C):1–51, 1956.
- [115] Philippe R. Spalart and Jonathan H. Watmuff. Experimental and numerical study of a turbulent boundary layer with pressure gradients. *Journal of Fluid Mechanics*, 249(-1):337, apr 1993.
- [116] Fulvio Scarano, Sina Ghaemi, Giuseppe Carlo Alp Caridi, Johannes Bosbach, Uwe Dierksheide, and Andrea Sciacchitano. On the use of helium-filled soap bubbles for large-scale tomographic PIV in wind tunnel experiments. *Experiments in Fluids*, 56(2), 2015.
- [117] Jan F.G. Schneiders, Giuseppe C.A. Caridi, Andrea Sciacchitano, and Fulvio Scarano. Large-scale volumetric pressure from tomographic PTV with HFSB tracers. *Experiments in Fluids*, 57(11):1–8, 2016.
- [118] Sina Ghaemi, Daniele Ragni, and Fulvio Scarano. PIV-based pressure fluctuations in the turbulent boundary layer. *Experiments in Fluids*, 53(6):1823–1840, 2012.
- [119] Kyle Lynch and Fulvio Scarano. A high-order time-accurate interrogation method for time-resolved PIV. *Measurement Science and Technology*, 24(3), 2013.
- [120] Thomas F. Brooks and William M. Humphreys. Effect of directional array size on the measurement of airframe noise components. *5th AIAA/CEAS Aeroacoustics Conference and Exhibit*, (99), 1999.
- [121] W. A. Timmer. Two-dimensional low-Reynolds number wind tunnel results for airfoil NACA 0018. *Wind Engineering*, 32(6):525–537, 2008.
- [122] Carlos Arce León, Daniele Ragni, Stefan Pröbsting, Fulvio Scarano, and Jesper Madsen. Flow topology and acoustic emissions of trailing edge serrations at incidence. *Experiments in Fluids*, 57(5), 2016.

- [123] S. C.C. Bailey, M. Hultmark, J. P. Monty, P. H. Alfredsson, M. S. Chong, R. D. Duncan, J. H.M. Fransson, N. Hutchins, I. Marusic, B. J. McKeon, H. M. Nagib, R. Örlü, A. Segalini, A. J. Smits, and R. Vinuesa. Obtaining accurate mean velocity measurements in high Reynolds number turbulent boundary layers using Pitot tubes. *Journal of Fluid Mechanics*, 715:642–670, 2013.
- [124] Ennes Sarradj, Christoph Fritzsche, Thomas Geyer, and Jens Giesler. Acoustic and aerodynamic design and characterization of a small-scale aeroacoustic wind tunnel. *Applied Acoustics*, 70(8):1073–1080, 2009.
- [125] Lourenço Tércio Lima Pereira, Roberto Merino-martínez, Daniele Ragni, David Gómez-ariza, and Mirjam Snellen. Combining asynchronous microphone array measurements for enhanced acoustic imaging and volumetric source mapping. *Applied Acoustics*, 182, 2021.
- [126] Yannick Rozenberg, Gilles Robert, and Stéphane Moreau. Wall-pressure spectral model including the adverse pressure gradient effects. *AIAA Journal*, 50(10):2168–2179, 2012.
- [127] Benshuai Lyu and Lorna J. Ayton. Serrated leading-edge and trailing-edge noise prediction models for realistic wavenumber frequency spectra. (May), 2019.
- [128] M. S. Howe. A review of the theory of trailing edge noise. *Journal of Sound and Vibration*, 61(3):437–465, 1978.
- [129] A. Haji-Haidari and C. R. Smith. Development of the turbulent near wake of a tapered thick flat plate. *Journal of Fluid Mechanics*, 189:135–163, 1988.
- [130] Sina Ghaemi and Fulvio Scarano. Counter-hairpin vortices in the turbulent wake of a sharp trailing edge. *Journal of Fluid Mechanics*, 689:317–356, 2011.
- [131] Michio Hayakawa and Sei Ichi Iida. Behavior of turbulence in the near wake of a thin flat plate at low Reynolds numbers. *Physics of Fluids A*, 4(10):2282–2291, 1992.
- [132] Y. Zhou and R. A. Antonia. Convection velocity measurements in a cylinder wake. *Experiments in Fluids*, 13(1):63–70, 1992.
- [133] Mathieu Gruber. Airfoil noise reduction by edge treatments by Mathieu Gruber Thesis for the degree of Doctor of Philosophy. 2012.
- [134] William K. Blake. *Noise From Rotating Machinery*, volume 2. 2017.

- [135] G. Grasso, P. Jaiswal, H. Wu, S. Moreau, and M. Roger. Analytical models of the wall-pressure spectrum under a turbulent boundary layer with adverse pressure gradient. *Journal of Fluid Mechanics*, 877:1007–1062, 2019.
- [136] A parametric study of serration design for trailing-edge broadband noise reduction. *Work submitted to Applied Acoustics*, 2022.
- [137] Lorna J. Ayton, Máté Szoke, Chaitanya C. Paruchuri, William J. Devenport, and William N. Alexander. Trailing-edge serrations: improving theoretical noise reduction models. In *AIAA AVIATION 2021 FORUM*, Reston, Virginia, aug 2021. American Institute of Aeronautics and Astronautics.
- [138] A. Juknevičius and T. P. Chong. On the spatial-temporal development of synthetic turbulent boundary layer on a serrated trailing edge. *25th AIAA/CEAS Aeroacoustics Conference, 2019, (May)*, 2019.
- [139] Stefan Pröbsting, Marthijn Tuinstra, and Fulvio Scarano. Trailing edge noise estimation by tomographic Particle Image Velocimetry. *Journal of Sound and Vibration*, 346(1):117–138, 2015.
- [140] William K. Blake. *Noncavitating Lifting Sections*, volume 2. 2017.
- [141] T H Hodgson. *Pressure fluctuations in shear flows*. PhD thesis, Cranfield University, 1962.
- [142] G. K. Batchelor. *The theory of homogeneous turbulence*. Cambridge University Press, 1953.
- [143] H.W. Liepmann, W. Laufer, and K. Liepmann. On the spectrum of isotropic turbulence. Technical report, National Advisory Committee for Aeronautics, 1951.
- [144] Theodore von Karman. Progress in the Statistical Theory of Turbulence. *Proceedings of the National Academy of Sciences*, 34(11):530–539, nov 1948.
- [145] D. K. Wilson. Three-Dimensional Correlation and Spectral Functions for Turbulent Velocities in Homogeneous and Surface-Blocked Boundary Layers. Technical Report July, ARMY RESEARCH LABORATORY, 1997.
- [146] Edward C. Polhamus. A Concept of the Vortex Lift of Sharp-Edge Delta Wings Based on a Leading-Edge Suction Analogy. *National Aeronautics and Space Administration Technical Note, (TN D-3767)*:1–16, 1966.

ACKNOWLEDGMENTS

I find it extremely selfish to credit (or discredit) an entire work of 4 years to the main author. The reality is that all the people that I have been in contact with during this time, work-related or not, have somehow affected this work. If today I am proud of the thesis I delivered, it is because I have been lucky to be surrounded by people that have positively affected my work.

If I have to choose the factor that contributed to this work the most, it would be the different personalities that I had contact with during it. This is well illustrated by my supervisory board, composed of Dr. Daniele Ragni, Dr. Francesco Avallone, and Prof. Dr. Fulvio Scarano. Three completely different personalities that have so much contributed to the outcomes of this thesis and, mostly, to my personal development. Francesco has the clearness of mind and attention to communication that is so required of a modern researcher. I thank you for the important discussions, planning sessions, and friendly conversations. Dani was the executioner of this group. Perhaps with the personality that was closest to mine, he has helped me so much in keeping the work (and fun) on track, assisting in the technical, and administrative tasks. Thanks, Dani! Fulvio sits greatly in the role of the promotor. His curiosity, and ability to fast pick up physical concepts pushed me to always stay sharp and have a clear picture of what I was doing and how to communicate it to others.

Having contact with Siemens Gamesa Renewable Energy has had an important impact on my research. I believe that a Ph.D. in an engineering topic must always have a view on its application, and SGRE has provided me with the motivation to tailor my research toward the reduction of wind-turbine noise. Together we looked after a "serration to rule them all" while trying to make sense of the prospects of this research for wind-energy applications. On this journey were Stefan Oerlemans, Pranav Manjunath, Oriol Ferret Gasch, and Steven Buck. I have always had a big admiration for the technical quality and knowledge of the SGRE group. I really hope my research has improved the understanding, and perhaps the quality, of the applications of serration on a wind-turbine blade. It was always a pleasure to work with and receive guidance from all of you.

This Ph.D. work was part of the H2020 Marie Skłodowska Curie project called SMARTANSWER, managed and supervised by Christoph Schram and Julien Cristoph, to whom I extend my gratitude. During the project, I had the opportunity to get to know, exchange discussions, and have fun with the great group of fellow Ph.D.

candidates of the project. Riccardo, Alessandro, Sergi, Georgios, Ignacio, Felipe, Thanushree, Emanuele, Niloofar, Massimo, Morteza, Chaitanya. Being the latest Ph.D. candidate to enter the consortium, I had the chance to see them all evolving and moving forward to occupy important positions in their fields of research. This is perhaps the smartest of the answers given by the project, and I am very happy to know that they are all succeeding.

Here in Delft, I had the opportunity to work with and meet with some of the people that I like the most. At first, I had the opportunity to collaborate on two projects (and many drinks) with Roberto Merino Martinez. In him, I not only see a friend but also a great and enthusiastic researcher. I also had the opportunity to work with Salil Luesutthiviboon, only the best guy to have during a wind-tunnel campaign. My office mates have also had an important impact on my work, by helping me with technical discussions or by keeping me away from them during the lunch and coffee breaks. In special, Leandro "OCara" Maranhão, with whom I have worked for 6 years, discussing technical issues, or simply humming nonsense music. Also I have to mention Fernanda, a great friend and someone to count on for anything, from drinks to plant-sitting. Some of my greatest friends have been from the aeroacoustics group, including Hugo, Gabs, Edo, Andrea, Manoel, and Christopher. Also, I cannot help but mention the many other fantastic people I met during my Ph.D.: Yanan, Dylan, Livia, Claudia, Rosella, Cristina, Alejandro, Colin, Ruben, Martijn, Nitish, Federica, Blanca, Thomas, Julia, Ming, and Mark.

TU Delft has also provided us with a large network of support that assist us in our daily activities. I would like to acknowledge all the help that I received from Sylvia and Collete, from the technicians Stefan, Emiel, Frits, Dennis, and Peter, and from DEMO Steve Van Herk, Stephan van 't Hof, Danny de Gans, and Chris Swanink.

Outside work, many activities were important during my off-time to refresh my mind. Among them, I rediscover my passion for tennis, perhaps the most ungrateful sport the world has ever created. For that, I would like to thank my many friends that have played with me during this whole time. In special, I would like to highlight the participation in the competitions with Thomas, Mateusz, Ivo, and William, who told us about the importance of stopping losing to start winning. Music was a second side of my past time that I always adored. Having jamming sessions with Dani, Leandro, and Gabs, and with the "to-this-point unknown" band with Andrea, Claudia, Lars, and Emilio was great fun.

The ultimate reason behind my hard work and motivation has always been the family that I love so much and to whom I switch to Portuguese to acknowledge: *Mãe e pai, vocês são e sempre serão o motivo dos meus esforços. Vocês nos ensinaram a importância de escolher trabalhar com aquilo que gostamos, mesmo que vocês tivessem que se sacrificar por isso. Saibam que a gente tem muita sorte de ter vocês e tudo que*

nós fizemos e conquistamos nesse mundo sempre foi para orgulhar vocês. Iti e Lulu, nossos pais sempre nos ensinaram sobre a importância de sermos mais que irmãos, amigos. Saibam que tenho grande orgulho e admiração pelas pessoas que vocês se tornaram e pela amizade que temos. Amo muito todos vocês.

Finally, to Natalia, the love of my life, my best friend. You are the reason why I can feel at home in any place. Every day of work in this thesis has been a day in which you helped me. Helped me to rest, to discuss technical matters, to distract, anything. You have had my back through the worst and best moments of my life and I hope I have also helped you along the way. You are my role model researcher and I will always look after you for that. I love you.

LIST OF PUBLICATIONS

JOURNAL PUBLICATIONS

7. L. T. Lima Pereira, F. Avallone, D. Ragni, and F. Scarano A parametric study of serration design for trailing-edge broadband noise reduction. *Applied Acoustics*, vol. 211, 2023, doi:10.1016/j.apacoust.2023.109470.
6. S. Luesutthiviboon, L. T. Lima Pereira, D. Ragni, F. Avallone, and M. Snellen Aeroacoustic benchmarking of trailing-edge noise from a NACA 63₃-018 airfoil with trailing-edge serrations. *AIAA Journal*, vol. 61, 2023, doi:10.2514/1.j061630.
5. L. T. Lima Pereira, F. Avallone, D. Ragni, and F. Scarano A physics-based description and modelling of the wall-pressure fluctuations on a serrated trailing edge. *Journal of Fluid Mechanics*, vol. 938, 2022, doi:10.1017/jfm.2022.173.
4. L. T. Lima Pereira, D. Ragni, F. Avallone, and F. Scarano Aeroacoustics of sawtooth trailing-edge serrations under aerodynamic loading. *Journal of Sound and Vibration*, vol. 537, 2022, doi:10.1016/j.jsv.2022.117202.
3. L. T. Lima Pereira, R. Merino-Martínez, D. Ragni, D. Gómez-Ariza, and M. Snellen Combining asynchronous microphone array measurements for enhanced acoustic imaging and volumetric source mapping. *Applied Acoustics*, vol. 182, 2021, doi:10.1016/j.aa.2021.108247.
2. L. T. Lima Pereira, D. Ragni, F. Avallone, and F. Scarano Pressure fluctuations from large-scale PIV over a serrated trailing edge. *Experiments in Fluids*, vol. 61, 2020, doi:10.1007/s00348-020-2888-x.
1. R. Merino-Martínez, A. Rubio Carpio, L. T. Lima Pereira, S. van Herk, F. Avallone, D. Ragni, and M. Kotsonis Aeroacoustic design and characterization of the 3D-printed, open-jet, anechoic wind tunnel of Delft University of Technology. *Applied Acoustics*, vol. 170, 2020, doi:10.1016/j.apacoust.2020.107504.

CONFERENCE PUBLICATIONS

3. L. T. Lima Pereira, F. Avallone, D. Ragni, S. Buck, and S. Oerlemans Semi-empirical framework for predicting the noise from wind-turbine blades with serrated trailing edges, *AIAA/CEAS Aeroacoustics Conference*, 2023, doi:10.2514/6.2023-3644.
2. G. V. I. Plaza, A. Fischer, O. Lylloff, C. Bak, A. S. Olsen, F. Bertagnolio, S. Luesutthiviboon, L. T. Lima Pereira, D. Ragni, F. Avallone, A. Suryadi, and M. Herr Benchmarking of the NACA 63₃-018 Trailing-Edge Noise in a Broad Reynolds Number Range as Part of the IEA Task 39, *AIAA/CEAS Aeroacoustics Conference*, 2022, doi:10.2514/6.2021-2179.
1. L. T. Lima Pereira, D. Ragni, F. Avallone Wall-pressure fluctuations over a serrated trailing edge at different angles of attack. *AIAA/CEAS Aeroacoustics Conference*, 2021, doi:10.2514/6.2022-2981.